

Spectroscopic Investigations of Kagome - Honeycomb Quantum Magnets

Von der Fakultät Mathematik und Physik der Universität Stuttgart
zur Erlangung der Würde eines Doktors der Naturwissenschaften
(Dr. rer. nat.) genehmigte Abhandlung

vorgelegt von
Tobias Biesner
aus Hoffnungsthal

Hauptberichter: Prof. Dr. Martin Dressel

Mitberichter: Prof. Dr. Bernhard Keimer

Tag der mündlichen Prüfung: 14.10.2022

Prüfungsvorsitzender: Prof. Dr. Hans Peter Büchler

1. Physikalisches Institut
Universität Stuttgart
2022

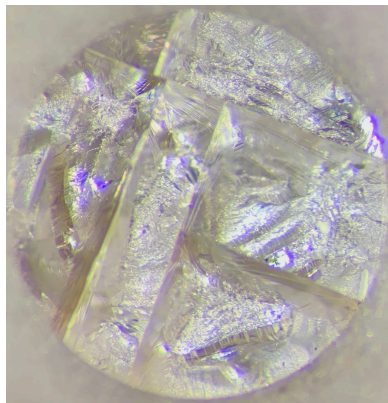
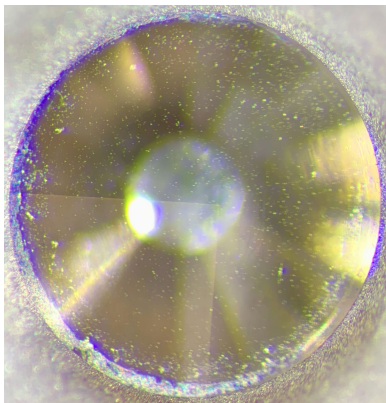


Figure 1: Diamonds used in high-pressure experiment. Left panel: intact diamond (before experiment), right panel: broken diamond (after experiment).

Abstract

In quantum magnets, exotic magnetic properties arise from the antiferromagnetic coupling of often minimal ($S = 1/2$) spins. Here the charge could get localized on the lattice but the spins remain "liquid": they move freely inside the material as spinons. These quantum spin liquids (QSLs) [6] are naturally expected in strongly correlated electron systems: Mott- or charge-transfer insulators. Their magnetic properties are crucially influenced by the underlying lattice geometries. For instance, three antiferromagnetically coupled Heisenberg spins on the corners of a triangle (triangular lattice) evade long-range magnetic order, even in the presence of very strong antiferromagnetic coupling. The magnetic exchange is frustrated. Even stronger frustration can be found on the kagome lattice (star-like arrangement of spins). In this case (as illustrated in this work) even very weak lattice distortion can be used to control the degree of frustration and to tune through a plethora of magnetic phases [7]. As well, the magnetic properties are influenced by other parameters, for instance, disorder or impurities [8]. This complexity opened a wide research field on the interface of condensed matter physics and material design in the recent years [9, 10]. Identifying the exotic magnetic properties in candidate systems is crucial for the general understanding of the interplay of spin, charge, and lattice in quantum states of matter.

In this thesis multiple strongly-correlated antiferromagnetic insulators with a variable degree of structural distortion and magnetic frustration are studied with spectroscopic resolution: Herbertsmithite $\text{ZnCu}_3(\text{OH})_6\text{Cl}_2$, Volborthite $\text{Cu}_3\text{V}_2\text{O}_7(\text{OH})_2 \cdot 2\text{H}_2\text{O}$, Y-kapellasite $\text{Y}_3\text{Cu}_9(\text{OH})_{19}\text{Cl}_8$, and (Zn-)Averievite $\text{Cu}_{5-x}\text{Zn}_x\text{V}_2\text{O}_{10}(\text{CsCl})$. Topics extending over electronic, structural, and magnetic degrees of freedom are covered. A particular focus will be on magnetic excitations at low energies, deep in the *THz gap*. Still, this energy scale of the electromagnetic spectrum is largely *terra incognita*, potentially hiding rich physics. At these low energies magnetic excitations can be disentangled from the dielectric backgrounds, providing valuable insight on the spin degree of freedom.

Overall, the present thesis advances the understanding of light-matter interaction in kagome/ honeycomb quantum magnets. It gives further guidelines for material design of quantum magnets by illustrating the influence of structural distortion on the magnetism. The main results shall be summarized as follows:

The archetype quantum spin liquid candidate on the kagome lattice is **Herbertsmithite** [11]. Albeit strong magnetic exchange, no long-range order was found down to the mK range [12]. Instead, a broad scattering continuum was revealed by inelastic neutron scattering (INS) and attributed to spinon excitations [13]. An optical absorption mechanism for spinons was proposed, resulting in a power-law optical conductivity [14, 15]. This power law was observed for Herbertsmithite [16]; however, only in a very narrow frequency range (20 to 45 cm^{-1}), close to a phonon tail. In this thesis terahertz time-domain spectroscopy (THz-TDS) measurements of the optical absorption coefficient/ optical conductivity of Herbertsmithite down to frequencies as low as 6 cm^{-1} and temperatures of $T = 1.6$ K reveal that the previously proposed spinon induced power-law absorption needs to be reconsidered: Fig. 2. Although above 20 cm^{-1} the spectra agree very well with the previous report [16], by significantly expanding the experimental parameters, a clear deviation from the power-law behavior is found below 20 cm^{-1} . Further magneto-THz measurements show no changes in the spectra under magnetic fields up to $H = 8.3$ T.

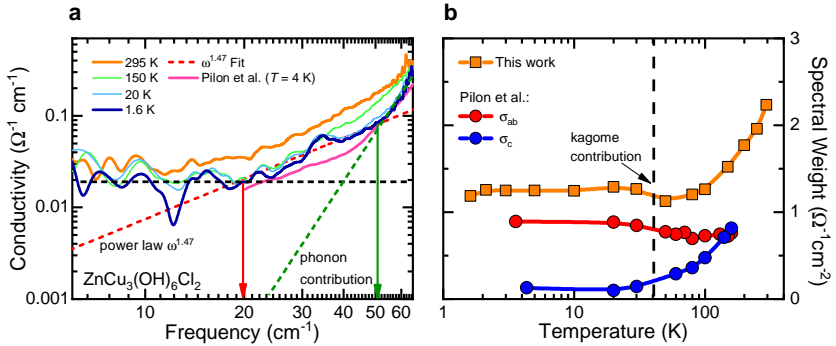


Figure 2: **Investigation of Herbertsmithite.** (a) In the double-log plot of the THz optical conductivity a clear deviation from the proposed power law (Ref. [16], magenta curve) can be seen below 20 cm^{-1} . (b) Spectral weight of this work (orange curve) compared to the results of Ref. [16] (red and blue curves). Dashed line: the hump in spectral weight was ascribed to the kagome contribution.

It is shown that magnetic short-range correlations before the magnetic transition are spectroscopically accessible in the THz range, encoded in the dynamic magnetic susceptibility χ''_m and the integrated absorption coefficient IA . This will be demonstrated utilizing **Volborthite** and can be further traced under a variable degree of structural distortion/ correlation strength in Y-kapellasite and Averievite. In Volborthite the onset of short-range magnetic correlations was previously determined at $T^* \approx 60$ K [17]. Furthermore, a broad maximum in susceptibility was observed at $T_p = 18$ K without any indication for spin freezing at these temperatures. Below $T_N = 1.4$ K Volborthite harbors a magnetic trimer state [18]. The temperature-dependent evolution of THz IA (Fig. 3) is reminiscent of these temperature scales observed in susceptibility. Furthermore, first infrared investigations are presented, unveiling a rich phononic background.

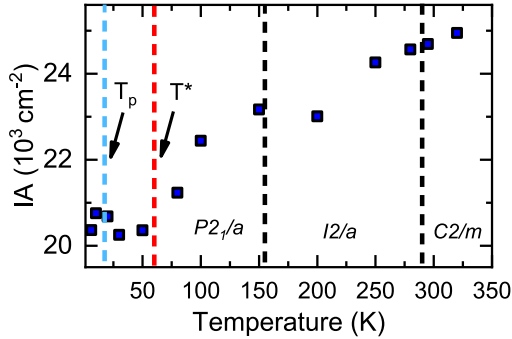


Figure 3: **Investigation of Volborthite.** THz integrated absorption coefficient IA probes short-range magnetic correlations in Volborthite. The peak-like increase (blue dashed line) coincides well with the maximum observed in susceptibility ($T_p = 18$ K) [17]. At $T^* \approx 60$ K the susceptibility starts to deviate from a Curie-Weiss behavior, onset of short-range magnetic correlations [17]. Black dashed lines: structural transitions [19, 20].

Y-kapellasite is an example for a distorted kagome antiferromagnet [21]. Here mild structural distortion leads to an imbalance of three nearest-neighbor antiferromagnetic couplings. A coplanar non-collinear magnetic state with ordering wave vector $\mathbf{Q} = (1/3, 1/3)$ is suggested below $T_N = 2.2$ K [7]: cf. the three distinct magnetic hexagons in Fig. 4a. The magnetism remained intriguing showing indications for spin dynamics and a successive spin freezing [22]. Studying Y-kapellasite, in this thesis, an exotic multi-center magnon absorption (continuum-like contribution at THz frequencies and low temperatures), entangled with the three-fold magnetic symmetry on the distorted kagome lattice is unveiled, Fig. 4b. The multi-center magnons are closely related to magnetic short-range correlations ($T = 30$ K), similar to paramagnons. Further insight is provided by magneto-THz spectroscopy and linear spin wave theory (LSWT). Exploiting the multi-center magnon excitation, in this proof-of-principle experiment it is shown that the spin (magnon) density of states can be accessed in the entire magnetic Brillouin zone with THz light. This releases the $\mathbf{q} \approx 0$ constraint of THz photons and expands the capability of THz-TDS to $\Delta\mathbf{q} \approx 0$: a new aspect to probe magnetism in matter. Further temperature- and pressure-dependent Fourier-transform infrared (FTIR) spectroscopies are presented, illuminating the structural degree of freedom.

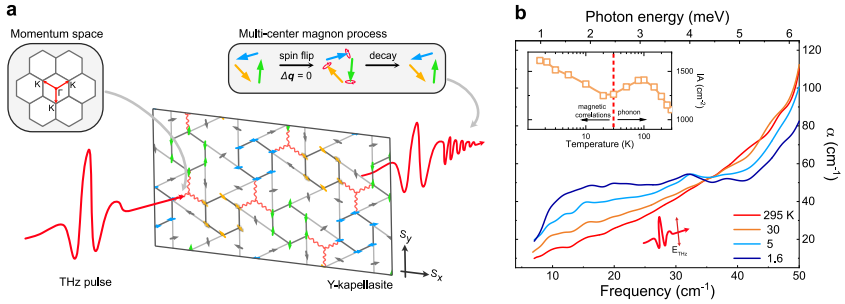


Figure 4: **Investigation of Y-kapellasite.** (a) Y-kapellasite possesses an intriguing $\mathbf{Q} = (1/3, 1/3)$ magnetic order below $T_N = 2.2$ K [7]. The three-fold magnetic symmetry (distinct magnetic sublattices - *centers*: green, blue, and yellow spins) features a multi-center magnon excitations mechanism evading the $\mathbf{q} \approx 0$ constraint of THz photons. (b) The multi-center magnon picture is used to explain the broad, continuum-like THz response, emerging with the onset of short-range magnetic correlations ($T = 30$ K). Inset: integrated absorption coefficient IA . At high temperatures IA is determined by the contribution of the phonon tail over 40 cm^{-1} . Below 30 K the multi-center magnon dominates the response. Adapted with permission from Ref. [1].

In **Averievite**, the degree of structural distortion is enhanced [23]. This system possesses a kagome lattice coupled to a honeycomb layer provoking magnetic interlayer coupling and magnetic order below $T_N = 24$ K. Substituting copper by zinc in the honeycomb layer (Zn-Averievite), the interlayer coupling is suppressed as well as the structural distortion. With the undistorted kagome lattice the system does not show indications for magnetic long-range order. In this thesis multiple sharp magnetic resonances coupling to external magnetic fields are observed below the onset of short-range magnetic correlations for unsubstituted Averievite. By retrieving the high symmetry of kagome lattice in Zn-Averievite and suppressing magnetic order, these resonances can be switched off, leaving only the dielectric background behind. Investigating multiple Zn concentrations, THz *IA* complemented by electron-spin susceptibility gives direct access to contributions from magnetic order, frustration, and structural properties, opening the phase diagram of Averievite, Fig. 5. Furthermore, this work sheds light on how magnetic interaction affects time-domain spectra through magnetization dynamics.

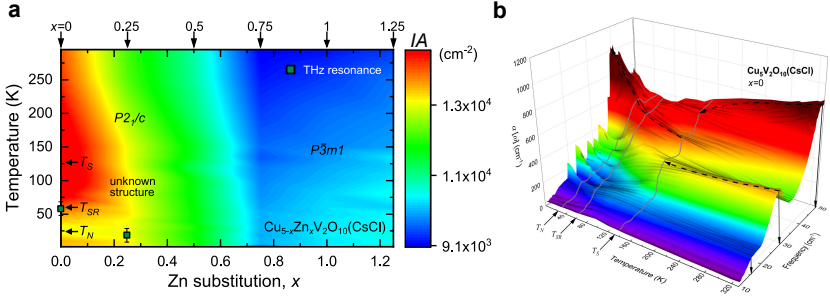


Figure 5: **Investigation of Averievite.** (a) The false-color plot of THz IA resembles the phase diagram (magnetic and structural phases) of $(Zn)_x$ Averievite $Cu_{5-x}Zn_xV_2O_{10}(CsCl)$: $T_S = 127$ K, structural transition ($P2_1/c$ to an unknown structure); $T_{SR} \approx 60$ K, onset of short-range magnetic correlations; $T_N = 24$ K, long-range order. Magnetic THz resonances were observed for the compounds with $x = 0$ and $x = 0.25$ (dark green points). The $P\bar{3}m1$ structure is found for $x = 0$ only for $T > 310$ K while it persists in the entire temperature range for high Zn substitutions. Measured Zn concentrations are indicated by vertical arrows at the top. (b) False-color plot of the absorption coefficient $\alpha(\omega, T)$ spectra for the $x = 0$ sample. Three lines are representing $T_S = 127$ K, $T_{SR} \approx 60$ K, and $T_N = 24$ K, respectively. With the onset of magnetic short-range correlations, sharp magnetic resonances are emerging (see around 20 cm^{-1}). These can be well separated from the phonon modes (28 and 50 cm^{-1}) and are susceptible to external magnetic field. Adapted with permission from Ref. [2]. Copyright (2022) by the American Physical Society.

Kurzfassung

In Quantenmagneten resultieren exotische magnetische Eigenschaften von der Kopplung oft minimaler ($S = 1/2$) Spins. In speziellen Fällen kann die Ladung lokalisiert bleiben und der magnetische Freiheitsgrad verhält sich „flüssig“: Spins bewegen sich frei im Material als Spinonen. Diese Quanten Spin Flüssigkeiten [6], engl. quantum spin liquids (QSLs), sind zu erwarten in stark korrelierten Elektronensystemen: Mott Isolatoren oder Ladungstransferisolatoren. Ihre magnetischen Eigenschaften sind stark abhängig von dem zugrundeliegenden kristallographischen Gitter. Ein Beispiel lässt sich auf dem Dreiecksgitter finden: Trotz starker antiferromagnetischer Wechselwirkung ordnen drei Heisenberg Spins auf den Ecken eines Dreiecks nicht magnetisch. Die magnetische Wechselwirkung ist frustriert. Noch stärkere Frustration kann auf dem Kagomegitter (sternförmige Anordnung der Spins) gefunden werden. In diesen Fällen (wie in der vorliegenden Arbeit veranschaulicht) können selbst kleinste Gitterverzerrungen den Grad der Frustration manipulieren und eine Vielzahl von magnetische Phasen [7] induzieren. Auch sind die magnetische Eigenschaften beeinflussbar durch weitere Parameter, wie beispielsweise Unordnung oder Unreinheiten [8]. Während der letzten Jahre öffnete diese Komplexibilität ein weites Forschungsfeld an der Schnittstelle Physik der kondensierten Materie und Materialdesign [9, 10]. Exotische magnetische Eigenschaften in Kandidatensystemen zu identifizieren ist hierbei essenziell für das generelle Verständnis des Zusammenspiels von Spin, Ladung und Gitter in Quantenzuständen von Materialien.

In der vorliegenden Arbeit werden mehrere stark korrelierte antiferromagnetische Isolatoren mit einem unterschiedlichen Grad an struktureller Verzerrung und magnetischer Frustration mit spektroskopischer Auflösung untersucht: Herbertsmithite $\text{ZnCu}_3(\text{OH})_6\text{Cl}_2$, Volborthite $\text{Cu}_3\text{V}_2\text{O}_7(\text{OH})_2 \cdot 2\text{H}_2\text{O}$, Y-kapellasite $\text{Y}_3\text{Cu}_9(\text{OH})_{19}\text{Cl}_8$ und (Zn-)Averievite $\text{Cu}_{5-x}\text{Zn}_x\text{V}_2\text{O}_{10}(\text{CsCl})$. Dabei sind Themen von elektronischen- und strukturellen bis zu magnetischen Freiheitsgraden abgedeckt. Speziell wird der Fokus auf magnetische Anregungen, welche tief in der sogenannten *THz gap* beheimatet sind, gelegt. Nach wie vor ist dieser Energiebereich des Spektrums weitgehend unerforscht und verbirgt potenziell eine Vielzahl von physikalischen Phänomenen.

Insgesamt treibt die vorliegende Arbeit das Verständnis von Licht-Materie Interaktion in Kagome/ Honigwaben Quantenmagneten voran. Sie illustriert den Einfluss von struktureller Verzerrung auf den Magnetismus

und ist richtungsweisend für das Materialdesign von Quantenmagneten. Die Hauptresultate werden wie folgt zusammengefasst:

Das Urbild eines Quanten Spin Flüssigkeits Kandidaten auf dem Kagomegitter ist **Herbertsmithite** [11]. Selbst bei tiefsten Temperaturen (mK Bereich) konnte trotz starker magnetischer Wechselwirkung keine langreichweitige magnetische Ordnung nachgewiesen werden [12]. Stattdessen ließ sich ein breites Streukontinuum mithilfe von inelastischer Neutronenstreuung (INS) messen und Spinonen zuschreiben [13]. Ein optischer Absorptionsmechanismus für Spinonen wurde vorgeschlagen, resultierend in ein Potenzgesetz für die optische Leitfähigkeit [14, 15]. Dieses konnte für Herbertsmithite experimentell beobachtet werden [16], jedoch nur in einem sehr engen Frequenzbereich (von 20 bis 45 cm^{-1}), nahe eines Phononenschwanzes. In dieser Arbeit zeigen Terahertz Zeitbereichsspektroskopie-, engl. terahertz time-domain spectroscopy (THz-TDS), Messungen des Absorptionskoeffizienten/ der optischen Leitfähigkeit zu niedrigen Frequenzen (6 cm^{-1}) und tiefen Temperaturen ($T = 1.6$ K), dass der Vorschlag eines Potenzgesetzes für die optische Absorption durch Spinonen überdacht werden muss: Abb. 6. Durch eine signifikante Erweiterung der experimentellen Parameter konnte eine klare Abweichung von einem Potenzgesetz unter 20 cm^{-1} gefunden werden. Weitere magneto-THz Messungen zeigen keine Veränderungen in den Spektren unter magnetischen Feldern bis zu $H = 8.3$ T.

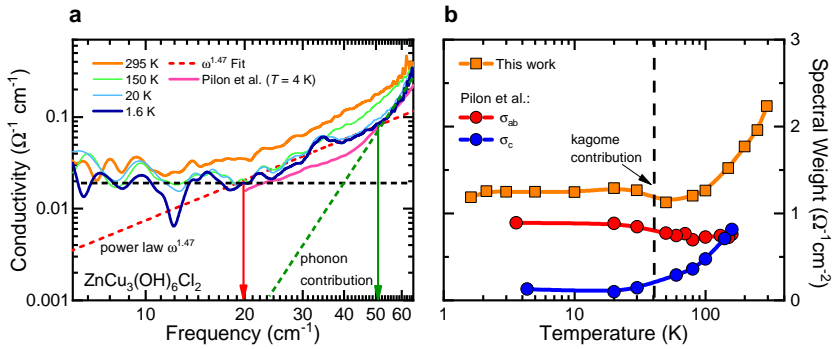


Abbildung 6: **Untersuchungen von Herbertsmithite.** (a) Doppel-Logarithmisches Diagramm der optischen Leifähigkeit. Eine Abweichung vom Potenzgesetz (Ref. [16], magenta Kurve) wird deutlich unter 20 cm^{-1} . (b) Spektrales Gewicht: Diese Arbeit (orange Kurve) verglichen mit Ref. [16] (rote und blaue Kurve). Gestrichelte Linie: Der Buckel im Spektralen Gewicht wurde dem Kagome Beitrag zugeordnet.

Es wird gezeigt, dass kurzreichweitige magnetische Korrelationen noch vor einem magnetischen Übergang spektroskopisch zugänglich sind über die dynamische magnetische Suszeptibilität χ''_m und den integrierten Absorptionskoeffizienten IA im THz Bereich. Dies wird demonstriert am Beispiel **Volborthite** und kann weiter verfolgt werden mit variablem Grad an struktureller Verzerrung und Korrelationsstärke in Y-kapellasite und Averievite. In Volborthite wurde das Einsetzen kurzreichweitiger magnetischer Korrelation zuvor mit $T^* \approx 60$ K bestimmt [17]. Des Weiteren wurde ein breites Maximum in der Suszeptibilität bei $T_p = 18$ K beobachtet, ohne ein Indiz für magnetische Ordnung [17]. Nur unterhalb von $T_N = 1.4$ K zeigt Volborthite einen magnetischen Trimer Zustand [18]. Diese Temperaturskalen ($T > 6$ K) spiegeln sich in der Temperaturabhängigkeit von THz IA (Abb. 7) wieder. Auch werden erste Infrarot Messungen gezeigt, welche einen reichhaltigen Phononen-Hintergrund in dieser Materialklasse enthüllen.

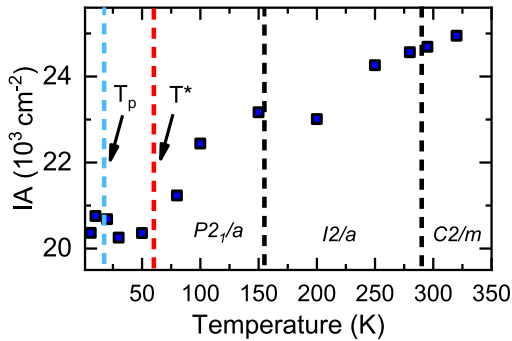


Abbildung 7: **Untersuchungen von Volborthite.** THz integrierter Absorptionskoeffizient IA ist sensitiv zu kurzreichweitigen magnetischen Korrelationen in Volborthite. Die peakartige Zunahme (gestrichelte blaue Linie) fällt zusammen mit einem Maximum in der Suszeptibilität ($T_p = 18$ K). Unter $T^* \approx 60$ K weicht die Suszeptibilität von einem Curie-Weiss Verhalten ab: Beginn der kurzreichweitigen magnetischen Korrelation [17]. Schwarz gestrichelte Linien: Strukturelle Übergänge [19, 20].

Y-kapellasite ist ein Beispiel für einen strukturell verzogenen Kagome-Antiferromagneten [21]. Hier induziert schwache strukturelle Verzerrung ein Ungleichgewicht der drei dominanten antiferromagnetischen Kopplungen, resultierend in magnetischer Ordnung: Unter $T_N = 2.2$ K ist ein koplanarer, nicht-kollinearer magnetischer Grundzustand $\mathbf{Q} = (1/3, 1/3)$ vorgeschlagen [7] (vgl. drei magnetischen Hexagone in Abb. 8a). Der Magnetismus bleibt faszinierend und zeigt Anzeichen für Spin Dynamik und ein aufeinanderfolgendes Ausfrieren des Spin Systems. Bei den Studien von Y-kapellasite wurde eine exotische multi-center Magnon Absorption (ähnlich eines Kontinuums) bei THz Frequenzen und tiefen Temperaturen nachgewiesen, Abb. 8b. Diese wird ermöglicht durch die dreizählige magnetische Symmetrie des verzerrten Kagomegitters. Auch sind die multi-center Magnonen eng verbunden mit kurzreichweitigen magnetischen Korrelationen ($T = 30$ K), zu vergleichen mit Paramagnonen. Weitere Einsicht ist gegeben durch magneto-THz Messungen und linearer Spinwellentheorie (LSWT). Unter Ausnutzung der multi-center Magnon Anregung konnte in diesem Proof-of-Principle Experiment gezeigt werden, dass die Spin- (Magnon-) Zustandsdichte in der gesamten magnetischen Brillouin Zone erreichbar ist über THz Licht. Dies löst die $\mathbf{q} \approx 0$ Beschränkung der THz Photonen und erweitert die Fähigkeiten von THz-TDS zu denen einer $\Delta\mathbf{q} \approx 0$ Methode: ein neuer Aspekt, um den Magnetismus in Materie zu untersuchen. Weitere temperatur- und druckabhängige Fourier-Transform-Infrarotspektroskopien (FTIR) werden präsentiert um strukturelle Aspekte zu beleuchten.

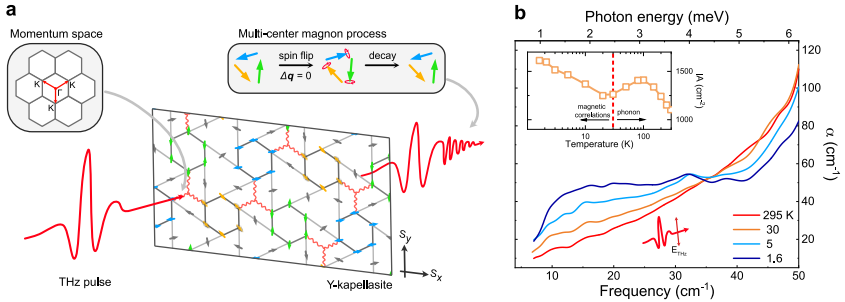


Abbildung 8: **Untersuchungen von Y-kapellasite.** (a) Y-kapellasite zeigt eine faszinierende $\mathbf{Q} = (1/3, 1/3)$ magnetische Ordnung unterhalb von $T_N = 2.2$ K [7]. Die dreizählige magnetische Symmetrie (unterscheidbare magnetische Untergitter - *centers*: grüne, blaue, und gelbe Spins) erlaubt eine multi-center Magnon Anregung über die $\mathbf{q} \approx 0$ Beschränkung von THz Photonen hinaus. (b) Das multi-center Magnon Bild wird benutzt um die breite, kontinuumähnliche THz Antwort (einsetzend mit kurzreichweitigen magnetischen Korrelationen, $T = 30$ K) zu erklären. Einsatz: integrierter Absorptionskoeffizient IA . Bei hohen Temperaturen wird IA bestimmt durch den Beitrag von Phononen (Phonenschwanz über 40 cm^{-1}). Unter 30 K dominiert die multi-center Magnon Absorption. Angepasst von Ref. [1] mit Erlaubnis.

In **Averievite** ist die strukturelle Verzerrung weiter ausgeprägt [23]. Dieses System stellt ein Kagomegitter gekoppelt mit einem Honigwabengitter dar. Interaktion zwischen den Gittern führt zu einer magnetischen Ordnung unterhalb von $T_N = 24$ K. Durch gezielte Substitution von Kupfer mit Zink im Honigwabengitter (Zn-Averievite) kann die magnetische Kopplung zum Kagomegitter und die strukturelle Verzerrung unterdrückt werden. Damit zeigt Zn-Averievite keine Indizien für magnetische Ordnung. In der vorliegenden Arbeit wurden unterhalb des Eintretens magnetischer kurzreichweitiger Korrelationen mehrere scharfe magnetische Resonanzen in nicht substituierten Proben beobachtet. Diese koppeln zudem an externe magnetische Felder. Durch Zink-Substitution können die magnetischen Resonanzen abgeschaltet werden. Studien an Proben mit verschiedenen Zink-Konzentrationen ermöglichen es das Phasendiagramm von Averievite unter Berücksichtigung der Beiträge von magnetischer Ordnung, Frustration und strukturellen Eigenschaften weiter auszufüllen (Abb. 9). Diese Informationen sind in THz *IA* kodiert und werden vervollständigt durch Elektronspin Suszeptibilität. Auch zeigt diese Arbeit den Einfluss magnetischer Interaktionen über Magnetisierungs-Dynamik in THz Zeitdomänen Spektren.

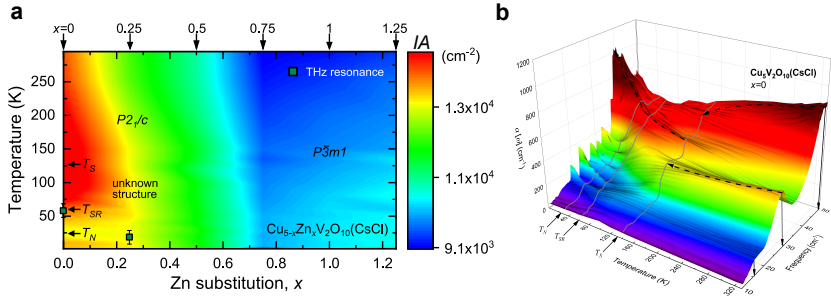


Abbildung 9: **Untersuchungen von Averievite.** (a) Der Falschfarben-Plot (THz IA) gibt das Phasendiagramm (magnetische und strukturelle Phasen) von (Zn-)Averievite $\text{Cu}_{5-x}\text{Zn}_x\text{V}_2\text{O}_{10}(\text{CsCl})$ wieder: $T_S = 127$ K, struktureller Übergang ($P2_1/c$ zu einer unbekannt Struktur); $T_{SR} \approx 60$ K, Beginn von kurzreichweitigen magnetischen Korrelationen; $T_N = 24$ K, magnetische Ordnung. Magnetische THz Resonanzen wurden beobachtet für $x = 0$ und $x = 0.25$ Komponenten (dunkelgrüne Punkte). Die $P3m1$ Struktur existiert für $x = 0$ nur im Bereich $T > 310$ K. Für hohe Zink-Konzentrationen bleibt sie über den gesamten Temperaturbereich erhalten. Gemessene Proben (Zink-Konzentrationen) sind gekennzeichnet mit vertikalen Pfeilen (oben). (b) Falschfarben-Plot des Absorptionskoeffizienten $\alpha(\omega, T)$ für $x = 0$. Drei Linien kennzeichnen $T_S = 127$ K, $T_{SR} \approx 60$ K und $T_N = 24$ K. Mit dem Beginn kurzreichweitiger magnetischer Korrelation treten scharfe magnetische Resonanzen auf (um 20 cm^{-1}). Diese können sehr gut von Phononen (28 und 50 cm^{-1}) separiert werden. Auch lassen sich die Resonanzen durch ein externes magnetisches Feld in ihrer Frequenz verschieben. Angepasst von Ref. [2] mit Erlaubnis. Copyright (2022) American Physical Society.

Publications

Some results of this work are already published in the following contributions:

1. *"Multi-Center Magnon Excitations Open the Entire Brillouin Zone to Terahertz Magnetometry of Quantum Magnets"*
T. Biesner*, S. Roh*, A. Razpopov, J. Willwater, S. Süllow, Y. Li, K. M. Zoch, M. Medarde, J. Nuss, D. Gorbunov, Y. Skourski, A. Pustogow, S. E. Brown, C. Krellner, R. Valentí, P. Puphal, M. Dressel, (*equally contributing)
Adv. Quantum Technol. **5**, 2200023 (2022)
2. *"Magnetic terahertz resonances above the Néel temperature in the frustrated kagome antiferromagnet averievite"*
T. Biesner, S. Roh, A. Pustogow, H. Zheng, J. F. Mitchell, M. Dressel,
Phys. Rev. B **105**, L060410 (2022)
3. *"Pressure-Tuned Interactions in Frustrated Magnets: Pathway to Quantum Spin Liquids?"*
T. Biesner, E. Uykur,
Crystals **10**, 4 (2019)

Other scientific works:

4. *"Generation of THz Vortex Beams and Interferometric Determination of Their Topological Charge"*
S. W. Pinnock, S. Roh, **T. Biesner**, A. V. Pronin, M. Dressel,
to appear in **IEEE Trans. Terahertz Sci. Technol.** (2022)
5. *"Charge localization in strongly correlated κ -(BEDT-TTF)₂Cu[N(CN)₂]I due to inherent disorder"*
O. Iakutkina, L. N. Majer, **T. Biesner**, E. Uykur, J. A. Schlueter, M. Dressel,
Phys. Rev. B **104**, 205127 (2021)
6. *"Spectroscopic trace of the Lifshitz transition and multivalley activation in thermoelectric SnSe under high pressure"*
T. Biesner, W. Li, A. A. Tsirlin, S. Roh, P.-C. Wei, E. Uykur, M. Dressel,
NPG Asia Mater. **13**, 12 (2021)

-
7. *"Photomolecular High-Temperature Superconductivity"*
M. Buzzi, D. Nicoletti, M. Fechner, N. Tancogne-Dejean, M. A. Sentef, A. Georges, **T. Biesner**, E. Uykur, M. Dressel, A. Henderson, T. Siegrist, J. A. Schlueter, K. Miyagawa, K. Kanoda, M.-S. Nam, A. Ardavan, J. Coulthard, J. Tindall, F. Schlawin, D. Jaksch, A. Cavalleri, *Phys. Rev. X* **10**, 031028 (2020)
 8. *"Optical signatures of phase transitions and structural modulation in elemental tellurium under pressure"*
D. Rodriguez, A. A. Tsirlin, **T. Biesner**, T. Ueno, T. Takahashi, K. Kobayashi, M. Dressel, E. Uykur, *Phys. Rev. B* **101**, 174104 (2020)
 9. *"Two Linear Regimes in Optical Conductivity of a Type-I Weyl Semimetal: The Case of Elemental Tellurium"*
D. Rodriguez, A. A. Tsirlin, **T. Biesner**, T. Ueno, T. Takahashi, K. Kobayashi, M. Dressel, E. Uykur, *Phys. Rev. Lett.* **124**, 136402 (2020)
 10. *"Magnetic-order-driven metal-insulator transitions in the quasi-one-dimensional spin-ladder compounds BaFe₂S₃ and BaFe₂Se₃"*
S. Roh, S. Shin, J. Jang, S. Lee, M. Lee, Y.-S. Seo, W. Li, **T. Biesner**, M. Dressel, J. Y. Rhee, T. Park, and J. Hwang, *Phys. Rev. B* **101**, 115118 (2020)
 11. *"CMOS-Compatible Antimony-Doped Germanium Epilayers for Mid-Infrared Low-Loss High-Plasma-Frequency Plasmonics"*
H. Chong, Z. Xu, Z. Wang, J. Yu, **T. Biesner**, M. Dressel, L. Wu, Q. Li, H. Ye, *ACS Appl. Mater. Interfaces* **11**, 19647 (2019)
 12. *"Detuning the honeycomb of α -RuCl₃: Pressure-dependent optical studies reveal broken symmetry"*
T. Biesner, S. Biswas, W. Li, Y. Saito, A. Pustogow, M. Altmeyer, A. U. B. Wolter, B. Büchner, M. Roslova, T. Doert, S. M. Winter, R. Valentí, M. Dressel, *Phys. Rev. B* **97**, 220401(R) (2018)

Contents

Abstract	v
Publications	xxi
Table of contents	xxiii
1 Motivation	1
1.1 Structure of the thesis	5
2 General background	7
2.1 Light-matter interaction	7
2.1.1 Coupling of light to magnons	9
2.1.2 Coupling of light to spinons	15
2.1.3 Optical selection rules	17
2.1.4 Other methods	18
2.2 Introduction to quantum magnetism	20
2.2.1 General properties	20
2.2.2 Experimental detection	22
2.2.3 External stimuli: magnetic field and pressure	25
3 Experimental methods and data analysis	27
3.1 Fourier-transform infrared spectroscopy	27
3.1.1 Reflectance and transmittance measurements	28
3.1.2 Pressure-dependent optical studies	32
3.1.3 Extraction of response functions	35
3.2 Terahertz time-domain spectroscopy	36
3.2.1 Magneto-optical measurements	39
3.2.2 Extraction of response functions	42
3.2.3 Extraction of dynamic magnetic susceptibility	46
3.3 Electron spin resonance	47
3.3.1 Extraction of electron spin susceptibility	49
4 Results I: Herbertsmithite and Volborthite	51
4.1 Introduction of the material	52
4.2 Experimental methods	60
4.3 Sample preparation	61
4.4 QSL response: THz-TDS investigations of Herbertsmithite	62
4.5 Magneto-THz spectroscopy	65
4.6 Pressure-dependent optical studies	66

4.7	The slightly distorted case: experimental studies of Volborthite	71
4.7.1	Structural and electronic aspects	73
4.7.2	Short-range magnetic correlations probed by THz-TDS	77
4.8	Conclusion and outlook	80
5	Results II: Y-kapellasite	83
5.1	Introduction of the material	87
5.2	Experimental methods	89
5.3	Sample growth and structural characterization	92
5.4	(Quasi-) Static response of the magnetic system	94
5.4.1	ESR measurements	96
5.4.2	High-field magnetization	101
5.4.3	AC magnetization	104
5.5	Structural instabilities and phononic properties	105
5.5.1	Pressure-dependent studies	109
5.6	THz time-domain spectra as a probe of spin dynamics	115
5.7	Magneto-THz spectroscopy	119
5.8	Multi-center magnon excitations	121
5.9	Discussion	124
5.10	Conclusion and outlook	126
5.11	Appendix	127
5.11.1	Extended data of THz-TDS	127
5.11.2	Magneto-optical THz-TDS	128
5.11.3	Phase diagram of the distorted kagome antiferromagnet	130
5.11.4	Details of the linear spin-wave theory calculations	130
5.11.5	Linear spin-wave theory calculations over an extended range	132
5.11.6	Calculation of χ_m''	132
5.11.7	Linear spin-wave theory calculations under magnetic field	134
5.11.8	Two-center magnon and three-center magnon excitation	136
6	Results III: Averievite	139
6.1	Introduction of the material	141

6.2	Experimental methods	144
6.3	Structural and magnetic characterization	146
6.4	Phononic and dielectric properties	149
6.5	Kagome and honeycomb copper sites: ESR characterization	158
6.6	Magnetic resonance in Averievite probed by THz-TDS . .	159
6.6.1	Magneto-THz spectroscopy	166
6.7	Discussion	167
6.8	Conclusion and outlook	168
6.9	Appendix	169
6.9.1	Zinc substitution	169
6.9.2	Magneto-THz measurements	170
6.9.3	Pellet preparation and reproducibility	172
7	Conclusion	175
	Acknowledgments	179
	Bibliography	181
	Declaration of originality	207
	Vita	209

1 Motivation

Quantum mechanics generates a plethora of astonishing phenomena and opens problems physicists will never stop to agonize about. One such fruit is zero-point motion or quantum fluctuation, where a system fluctuates in its lowest possible energy state - a consequence of Heisenberg's uncertainty principle. A prominent example is liquid helium, which does not freeze at any observable temperature [24]. Another aspect is quantum superposition, where the system remains in two states at the same time, i.e., Schrödinger's cat. Quantum superpositions and quantum fluctuations have drastic consequences in condensed matter physics as well [25]. Here, the internal degree of the electron, spin can be entangled over large distances in a quantum superposition: valence state, opening the route to quantum spin liquids (QSLs) [6]. In simple terms, these are systems which albeit strong antiferromagnetic interactions do not freeze even at zero temperature but show pronounced quantum fluctuations (the spin system remains "liquid"). A mechanism called geometric frustration, that is, a suitable arrangement of the spins on the crystallographic lattice, can be a main ingredient for suppressing long-range order in candidate systems [26]. Here, fractional excitations, spinons could be found [27]. A spinon resembles a *fraction* of the electron, carrying spin $1/2$ but no charge: fermionic quasiparticle. Even though it is already interesting to study these systems only because of their exotic properties, they give a further, more concrete, motivation: the key to high-temperature superconductivity if the system could be doped to become metallic [28, 29]. Furthermore, a relevance for quantum computing is investigated [30]. In this context, understanding the quantum mechanical processes to precisely manipulate materials [31] could lead to advances mastering many critical global challenges of our modern society. Prominent examples are energy storage and distribution in a world developing toward renewable energy sources and information storage and processing beyond the Silicon Age.

Unfortunately, the topic remains a puzzle with many parts, and the insulating candidate systems need to be cooled to very low temperatures (mK range) to get a glimpse on their fascinating physics. However, in the vicinity of the quantum spin liquid, the frustrated quantum magnet can be found [32]. Here, several contributions to the Hamiltonian might lead to a spin freezing at a finite temperature. This brings good experimental accessibility between the temperature scales of the onset of short-range magnetic correlations and long-range order. As well, interplay of (lattice-)symmetry, quantum-, and thermal fluctuations frequently

generates exotic magnetic phases and interesting properties [7, 33, 34], including triplons [35], valence bond solids [36] and spin nematics [18]. Investigating this variety of magnetic phases including their exotic magnetic excitations and understanding the quantum mechanical processes is of fundamental interest. It might yield information about their tunability in the framework of QSL. Moreover, considering the success of conventional antiferromagnets [37], these properties could be exploited for complex technical applications of the future.

In this context, due to their high geometric frustration, some lattice geometries are of particular interest, for instance, the kagome lattice. Its name originates from the Japanese expressions for a bamboo-basket (kago) and woven pattern (me), where six triangles built a star-like arrangement [38]. These arrangements can be found, for instance, in copper oxide minerals [39, 40]. Magnetic interaction can be provided by different means but most relevant here is a superexchange mechanism along the Cu-O-Cu path, which antiferromagnetically couples $S = 1/2$ Cu²⁺ Heisenberg spins. Trying to place the Heisenberg spins on the kagome lattice results in frustrated magnetic interactions evading long-range order [39]. Another prominent lattice geometry is a honeycomb arrangement. In general, it has relevance for compass-like magnetic structures (Kitaev magnetism) [41]. However, here a particular case where a kagome lattice is coupled to a honeycomb geometry is considered.

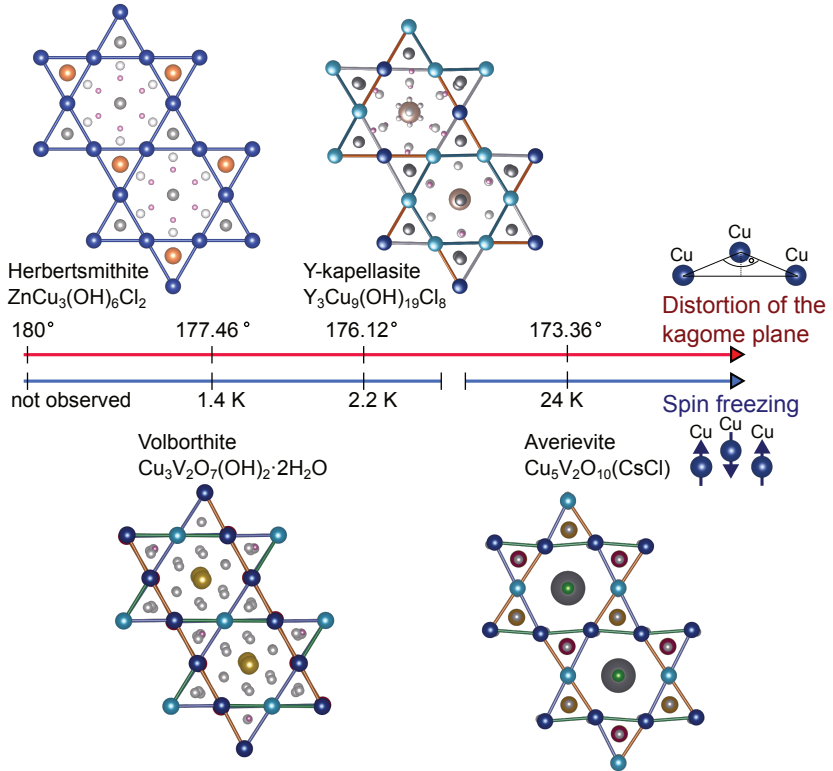


Figure 1.1: **Structural distortion and spin freezing on the kagome lattice.** In this thesis four quantum magnets with kagome (honeycomb) lattice are studied: Herbertsmithite, Volborthite, Y-kapellasite, and Averievite. Structures within the kagome planes are shown. The lattices are organized by their respective degree of structural distortion (deviation of the Cu-Cu-Cu bond angle from 180°) and Néel temperature T_N . Dark blue and light blue spheres: magnetic Cu ions. Structures are based on Refs. [19, 21, 23, 42].

In this thesis, selected quantum magnets (kagome/ honeycomb compounds) with varying degrees of structural distortion/ inherent magnetic frustration, Fig. 1.1 are investigated. The project is intended to experimentally study the influence of the latter two parameters on the magnetism.

Besides the general interest in tuning the magnetic phases, the main questions motivating the research are:

- What properties have the (magnetic) phases at intermediate temperature, between the onset of short-range magnetic correlations and long-range order?
- What is the role of spin dynamics at intermediate temperatures?
- How are the properties at intermediate temperatures connected to the low-temperature states?
- How does structural distortion affect the magnetism?
- How can the contributions from magnetism, structure, and electronic degrees of freedom be disentangled?

Solving these key-questions will give an advanced understanding of the exotic magnetism in this material class.

Although conventionally inelastic neutron scattering (INS) is the method of choice to study magnetic properties, in this thesis (quasi-) optical spectroscopy will be applied to answer these questions. Besides the fact that such an unconventional approach is already of interest solely to map out the fingerprints of magnetic properties in optical spectra (light-matter interaction in quantum magnets), it has several advantages: table-top access without the need of large-scale facilities, advanced energy resolution [43], smaller required sample masses, and no restriction for strong neutron absorbers. As it will be shown throughout this thesis, although optical spectroscopy cannot replace neutron scattering it might be a valuable complementary technique to probe magnetic properties. Hereby, the focus is the low-energy (THz) regime. The *THz gap*, between radio frequencies and infrared (IR) regime, still is *terra incognita* for the present material class, although recently the interest is growing substantially [16, 44–54]. Since this energy scale corresponds to the order of the magnetic superexchanges, magnetic excitations are naturally expected

here. Furthermore, other (stronger) electronic transitions, potentially covering the magnetic responses, are not present deep in the charge/ Mott gap for the insulating compounds. Terahertz time-domain spectroscopy (THz-TDS) is used to map out the dynamic magnetic response of the systems, i.e., *THz-magnetometry*. A particular case, where the natural restriction of optical spectroscopy to the center of the Brillouin zone ($\mathbf{q} \approx 0$ response) is released was found. Furthermore, the spectral shapes of the emergent magnetic features could be extracted. Results will be compared to static magnetization, electron spin resonance (ESR) spectroscopy and nuclear magnetic resonance (NMR) measurements. Advanced theoretical calculations will help to establish a deeper understanding of the physics. Fourier-transform infrared (FTIR) spectroscopy will be employed to map out structural and electronic properties in the infrared regime to complement a comprehensive picture. Furthermore, the influence of external stimuli (external magnetic field and hydrostatic pressure) on magnetism and structure is studied.

Besides the advances in the understanding of the magnetism of the particularly studied systems, the general impact expected from this work is:

- Deepened understanding of the appearance of magnetic excitations of quantum magnets in optical spectra by extracting the spectral shapes, separated from dielectric contributions.
- Establishment of THz-TDS as an important method in the field of quantum magnets: showing a particular case where the $\mathbf{q} \approx 0$ constraint is released.
- Guiding material design by considering the influence of structural distortion on the magnetism.

1.1 Structure of the thesis

The thesis is structured in the following way:

- In the first chapter "Motivation" the reader will receive a concise introduction to the thesis. Furthermore, the motivation for this research is presented. A German and an English abstract can be

found above, summarizing the main results. As well a publication list is included.

- In Ch. 2 "General Background" a broader overview of the relevant research fields is given. It covers the topics light-matter interaction (especially in magnetic materials) and an introductory section to quantum magnetism.
- In Ch. 3 "Experimental Methods and Data Analysis" the variety of experimental techniques is introduced. This includes aspects from the general principles and schematics to more detailed experimental procedures. Here, the goal is, without giving too many details, to allow a reproducibility of the experiments. The focus will be especially on (magneto-) terahertz time-domain spectroscopy (THz-TDS) since it is the first dissertation at the institute using this technique.
- In Ch. 4 "Results I: Herbertsmithite and Volborthite" the first results are presented. Here, experiments on the non-distorted QSL candidate Herbertsmithite and the mildly distorted quantum magnet Volborthite are shown. The reader will see that the case of Herbertsmithite needs to be reconsidered in the sense that the earlier proposed power-law (spinon) optical absorption does not hold down to low energies. Volborthite will serve as an excellent example to investigate magnetic short-range correlations using THz-TDS.
- In Ch. 5 "Results II: Y-kapellasite" the structural distortion of the kagome lattice is increased and the compound Y-kapellasite is investigated by a plethora of experimental and theoretical methods. Exotic multi-center magnon absorption was found deep in the charge gap, releasing the $\mathbf{q} \approx 0$ constraint of THz-TDS.
- In Ch. 6 "Results III: Averievite" the heavily distorted kagome-honeycomb magnet is investigated. Here strong structural distortion/ magnetic interlayer coupling allows to probe sharp magnetic resonances, in contrast to the cases presented before.

Finally, a general conclusion on the distorted kagome/ honeycomb quantum magnets is given before coming to acknowledgments, bibliography, declaration of originality, and vita of the author.

2 General background

In this chapter, an overview of the general theoretical background is given based on cited literature and the author's publications (Refs. [1–3]). The first part covers concepts of light-matter interaction with focus on the coupling of light to the material's magnetic degree of freedom. Concepts of the magnetic THz resonance and optical magnon absorption are going to be discussed. Here an important experimental observable the dynamic spin susceptibility will be introduced. In the second part the reader receives an introduction to the quantum magnetism/ quantum spin liquids, including the concepts geometric frustration and magnetic exchange on the kagome lattice.

The advent of ultrafast lasers and sophisticated detection schemes made dynamical processes in the (sub-) picosecond range attainable in solid state physics over the recent years [55–57] by opening the time domain to spectroscopic methods, for instance, in THz time-domain spectroscopy (THz-TDS) [58]. But new techniques allow not only time-resolved studies. In fact, the control of magnetization dynamics [59–62], including the coherent generation of magnons [63] opens a versatile playground from basic research to practical application. Within this field magneto-optical Faraday or Kerr effects were exploited to probe magnetic material properties [64, 65]. The observation of THz-driven spin precession [66–69] paved the way for THz magnetometry: the optical extraction of magnetic properties [70].

2.1 Light-matter interaction

In the following the fundamentals of light-matter interaction in magnetic materials (permeability $\mu \neq 1$) are going to be reviewed. Fig. 2.1 gives an overview of the relevant energy scales. Mostly, magnetic properties become visible at low energies (THz range) in insulating materials [2, 16, 45, 71–76]. Here the electronic background diminishes and besides magnetic excitations only phonons are expected. However, in some cases, it might be challenging to exactly distinguish between the possible contributions of phonon (-tails), electronic background (i.e., a residual slope in optical conductivity stemming from the higher lying interband transitions), and magnetic excitations. An analysis scheme dealing with these challenges is presented in Sec. 3.2.3.

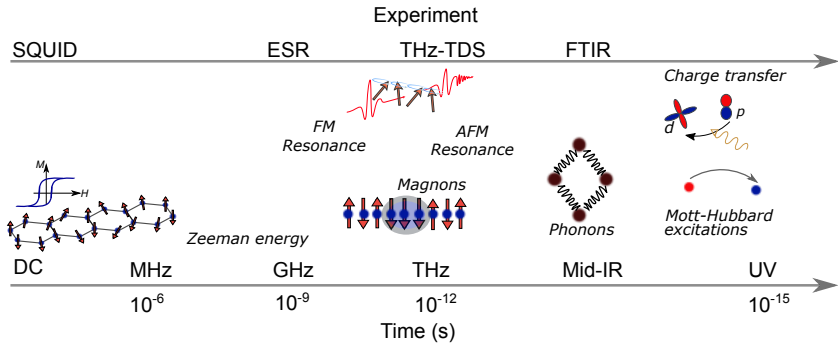


Figure 2.1: **Frequency- and time scales of electronic and magnetic excitations, relevant for this thesis.** Accordingly, the used experimental methods are arranged. Scales are based on [57, 77].

Magnetic properties can be probed with light over several routes. On the first glance, mechanisms exploiting spin-orbit coupling (SOC) are most obvious. Here, the spin degree of freedom of the electron becomes accessible over the electric field component of the light, for instance, in Raman scattering. SOC can be exploited to generate magnons [78] and gives rise to inverse Farady effect [61] or inverse Cotton-Mouton effect [79]. Other mechanisms: magnetoelectric responses, magnetoelastic-, or non-linear coupling are reported in literature [74, 80] but put additional constraints to the material, for instance, a restriction to non-centrosymmetric space groups.

Another route is the direct probe over the coupling to the magnetic field component of the light. This might be challenging at the first glance, considering that electronic dipole-active processes are usually assumed to be much stronger. However, in the THz range, without any other contributions hiding the magnetic response (in insulators), a direct detection (magnetic-dipole interaction [43]) is possible [64, 66–69], for instance, via the free induction decay signal (see the sections below).

For more information, especially on the interaction of light and non-magnetic matter the reader is referred to extensive introductions presented in literature (starting from the Maxwell’s equations and covering all aspects of response functions and material parameters), for instance, the

books [81, 82], reviews [77, 83], and previous theses [84–86].

2.1.1 Coupling of light to magnons

Before considering more concrete cases, in the following, a general mathematical description (detached from any material constraints) of the coupling between an electromagnetic wave and magnetic matter is going to be reviewed from the viewpoint of optical absorption: one photon gets absorbed, creating a spin wave - one-magnon resonance. This elaboration is mainly based on the Refs. [43, 87]. Optical absorption, for instance, in the THz range is sensible to the dynamic susceptibility [43]. This quantity is a tensor with matrix elements $\tilde{\chi}_{\alpha\beta}(\omega) = \tilde{\chi}_{\alpha\beta}^{\text{mm}}(\omega) + \tilde{\chi}_{\alpha\beta}^{\text{ee}}(\omega) + \tilde{\chi}_{\alpha\beta}^{\text{me}}(\omega) + \tilde{\chi}_{\alpha\beta}^{\text{em}}(\omega)$, where α, β run over the Cartesian coordinates. The contributions of the sum are the magnetic, dielectric, magnetoelectric, and electromagnetic susceptibilities, respectively [43, 87]:

$$\tilde{\chi}_{\alpha\beta}^{\text{mm}} = \frac{\mu_0}{\hbar NV} \sum_n \frac{\langle 0 | \Delta M_\alpha | n \rangle \langle n | \Delta M_\beta | 0 \rangle}{\omega_{n0} - \omega - i\delta}, \quad (2.1)$$

$$\tilde{\chi}_{\alpha\beta}^{\text{ee}} = \frac{1}{\hbar NV \epsilon_0} \sum_n \frac{\langle 0 | \Delta P_\alpha | n \rangle \langle n | \Delta P_\beta | 0 \rangle}{\omega_{n0} - \omega - i\delta}, \quad (2.2)$$

$$\tilde{\chi}_{\alpha\beta}^{\text{me}} = \frac{1}{\hbar NV} \sqrt{\frac{\mu_0}{\epsilon_0}} \sum_n \frac{\langle 0 | \Delta M_\alpha | n \rangle \langle n | \Delta P_\beta | 0 \rangle}{\omega_{n0} - \omega - i\delta}, \quad (2.3)$$

$$\tilde{\chi}_{\alpha\beta}^{\text{em}} = \frac{1}{\hbar NV} \sqrt{\frac{\mu_0}{\epsilon_0}} \sum_n \frac{\langle 0 | \Delta P_\alpha | n \rangle \langle n | \Delta M_\beta | 0 \rangle}{\omega_{n0} - \omega - i\delta}. \quad (2.4)$$

Here $\Delta \mathbf{M}$ and $\Delta \mathbf{P}$ are the fluctuation of magnetization and polarization of the material, respectively, under excitation by the light (electric field \mathbf{E}^ω and magnetic field \mathbf{H}^ω) adding the perturbation: $\mathcal{H}' = -\mathbf{H}^\omega \cdot \Delta \mathbf{M} - \mathbf{E}^\omega \cdot \Delta \mathbf{P}$ ¹. They include the magnon creation and annihilation operators in the entire Brillouin. $|0\rangle$ is the ground state with energy E_0 , $|n\rangle$ is the n -th magnetic excitation with energy E_n and pole position $\omega_{n0} = (E_n - E_0)/\hbar$. ϵ_0 and μ_0 are the permittivity and permeability in vacuum, respectively. N is the total number of spins and V is the

¹Note that here \mathbf{P} is assumed to dependent on the spin structure: $\Delta \mathbf{P}$ is induced by the magnetic excitation.

normalized unit volume (per spin). With Eqs. 2.1 - 2.4, the magnetic induction \mathbf{B}^ω and electric induction \mathbf{D}^ω read [87]:

$$\mathbf{B}^\omega = \mu_0[\hat{1} + \hat{\chi}^{mm}(\omega)]\mathbf{H}^\omega + \sqrt{\epsilon_0\mu_0}\hat{\chi}^{me}(\omega)\mathbf{E}^\omega, \quad (2.5)$$

$$\mathbf{D}^\omega = \epsilon_0[\hat{1} + \hat{\chi}^{ee}(\omega)]\mathbf{E}^\omega + \sqrt{\epsilon_0\mu_0}\hat{\chi}^{em}(\omega)\mathbf{H}^\omega. \quad (2.6)$$

Furthermore, inside the material the Maxwell's equations can be rewritten [87]:

$$\mathbf{k} \times \mathbf{E}^\omega = \omega[\mu_0[\hat{1} + \hat{\chi}^{mm}(\omega)]\mathbf{H}^\omega + \sqrt{\epsilon_0\mu_0}\hat{\chi}^{me}(\omega)\mathbf{E}^\omega], \quad (2.7)$$

$$\mathbf{k} \times \mathbf{H}^\omega = -\omega[\epsilon_0[\hat{1} + \hat{\chi}^{ee}(\omega)]\mathbf{E}^\omega + \sqrt{\epsilon_0\mu_0}\hat{\chi}^{em}(\omega)\mathbf{H}^\omega]. \quad (2.8)$$

Here, magnetic permeability $\hat{\mu}$ and electric permittivity $\hat{\epsilon}$ take the form:

$$\hat{\mu} = \hat{1} + \hat{\chi}^{mm}(\omega), \quad (2.9)$$

$$\hat{\epsilon} = \hat{1} + \hat{\chi}^{ee}(\omega). \quad (2.10)$$

Since the forms of refractive index and other quantities such as Faraday or Kerr angle dependent on the selected geometry/ polarization and the magnetic ground state, they will not be shown here. Further information can found in the Refs. [43, 81, 82, 87].

Note that Eqs. 2.1 - 2.4 are general expressions and do not specify the momentum dependence. They sum over all possible states, encoded in $\Delta\mathbf{M}$, $\Delta\mathbf{P}$: magnon creation/ annihilation with an arbitrary wave vector \mathbf{q} , i.e., $\tilde{\chi}_{\alpha\beta}(\omega, \mathbf{q})$. This will be addressed in the following.

Conservation of momentum and energy

Optical absorptions in solid-state physics are governed by conservation of momentum and energy. For instance, electronic transitions have to obey $\Delta E = E_{ph}$ and $\Delta\mathbf{q} = \mathbf{q}_{ph}$, where ΔE and $\Delta\mathbf{q}$ are the energy/ momentum differences between initial and excited states and E_{ph} , \mathbf{q}_{ph} are energy and momentum of the absorbed photon, respectively. While ΔE can be tuned over the electromagnetic spectrum by selecting photons with a matching wavelength λ , $\Delta\mathbf{q}$ is determined due to the small photon momentum $q_{ph} = h/\lambda \approx 0$ ², i.e., the direct electronic transition (electron gets

² $q_{ph} \approx 0$ holds for photons considered in this thesis - THz and infrared photons.

excited into a higher band by absorbing one photon) is a vertical line in the band structure (energy vs. momentum). Since electrons are fermions and follow Fermi-Dirac statistics, they occupy states up to the Fermi energy with momentum k_F . Therefore, direct optical transitions can be probed in the entire Brillouin zone (where the band structure supports it). However, for magnetic excitations (magnons), Bose-Einstein statistics governs the condensation of all magnons in the ground state $|0\rangle$ at $T = 0$ K. In the general description above (Eqs. 2.1 - 2.4) $\Delta\mathbf{M}$ and $\Delta\mathbf{P}$ include the magnon creation and annihilation operators in the entire magnetic Brillouin zone. However, due to the small photon momentum, momentum conservation restricts the accessible magnon states of the one-magnon absorption (one photon gets absorbed, creating one magnon) to the center of the magnetic Brillouin zone, $\mathbf{q} \approx 0$ response [43, 46, 49, 51, 88, 89]. This can be taken into account in Eqs. 2.1 - 2.4 by only summing over states with $|n, \mathbf{q} = 0\rangle$ and rewriting $\Delta\mathbf{M}$ and $\Delta\mathbf{P}$ [43]. With this constraint the dynamic magnetic susceptibility (Eq. 2.1) takes the form [43]:

$$\tilde{\chi}_m(\omega) = \gamma \sum_{\alpha, \beta} h_\alpha h_\beta \tilde{\chi}_{\alpha\beta}^{\text{SS}}(\mathbf{q} = 0, \omega), \quad (2.11)$$

where γ is a constant and h_α, h_β are the magnetic field components of the light along the directions α, β . $\tilde{\chi}_{\alpha\beta}^{\text{SS}}$ is the spin susceptibility, which is related to the spin-spin correlation function $S_{\alpha, \beta}$ at zero temperature: $\text{Im}\{\tilde{\chi}_{\alpha, \beta}^{\text{SS}}(\mathbf{q} = 0, \omega)\} = S_{\alpha, \beta}(\mathbf{q} = 0, \omega)$. Thus, by computing the spin-spin correlation function the dynamic magnetic susceptibility can be obtained.

In fact, the $\mathbf{q} \approx 0$ constraint for magnons is a substantial limitation in optical absorption spectroscopy, for instance, in infrared and THz measurements. Within this thesis a way to overcome this limitation is shown. THz magnetometry via multi-center magnon absorption can be used to overcome the $\mathbf{q} \approx 0$ constraint (see Ch. 5). After introducing a semi-classical picture for the one-magnon excitations, a general theoretical overview for this multi-center magnon absorption will be given.

Magnetic resonances and free induction decay

The optical one-magnon excitation can be viewed in a quantum mechanical picture as a simple spin flip induced by the absorption of a photon,

creating a spin wave at the Γ -point. However, to describe the in THz spectroscopy observed magnetic resonances [59] as well a semi-classical picture could be utilized. As the THz pulse enters a magnetic material, the (sub-) picosecond magnetic field of the light \mathbf{H}_{THz} might tilt the spins (magnetic moment \mathbf{M}) out of their equilibrium positions via a Zeeman torque: $\mathbf{H}_{\text{THz}} \times \mathbf{M}$. This leads to a precession of the spins around the effective field \mathbf{H}_{eff} . The dynamics of the system in the picosecond (ps) range after the excitation can be described by the Landau-Lifshitz-Gilbert (LLG) equation [90]:

$$\frac{\partial \mathbf{M}}{\partial t} = \gamma \mathbf{M} \times \mathbf{H}_{\text{eff}} - \frac{\alpha}{M} \mathbf{M} \times \frac{\partial \mathbf{M}}{\partial t}, \quad (2.12)$$

where the first cross product describes a precession with frequency $\omega = \gamma H_{\text{eff}}$ and the second cross product is a damping term, determining the relaxation back to the equilibrium position, γ is the gyromagnetic ration, α is the Gilbert damping. The resulting spin precession for a particular case (linearly polarized light, $\mathbf{H}_{\text{THz}} \perp \mathbf{M}$) is shown schematically in Fig. 2.2. Such a precession emits magnetic dipole radiation and is detectable as a free induction decay signal, for instance, in THz-TDS [66–69]. Here typical waveforms show late-time oscillations (several tens of ps), separated from the main pulse, in the time-varying electric field [91–93]. As can be seen from Eq. 2.12, the effective magnetic field of the magnetization \mathbf{H}_{eff} is an important parameter and determines the expected frequency of the magnetic resonance. It might contain several contributions [90]: $\mathbf{H}_{\text{eff}} = \mathbf{H}_{\text{ext}} + \mathbf{H}_d + \mathbf{H}_e + \mathbf{H}_a + \dots$, where \mathbf{H}_{ext} is an external magnetic field, \mathbf{H}_d is a demagnetization field (self-interaction of the magnetization field), \mathbf{H}_e the exchange field (containing the magnetic exchange J_i), and \mathbf{H}_a is the anisotropy field. Note that the validation on the LLG equation on the (sub-) picosecond scale and introducing further extensions is object of active research (see, for instance, Ref. [94]).

For conventional ferromagnetic materials, magnetic resonances are expected in the GHz range [59, 95]. However, in antiferromagnets, magnetizations of the distinct magnetic sublattices \mathbf{M}_i need to be taken into account, i.e., staggered magnetization. Here the frequencies of magnetic resonances can be shifted to the THz range [59, 95]. For instance, in the case of the conventional antiferromagnet MnF_2 typical parameters are $g = 2$, $\gamma = 2.8 \text{ GHz/kOe}$, $\mathbf{H}_{\text{eff}} = 93 \text{ kOe}$, resulting in a resonance at 0.26 THz (1.59 THz for FeF_2) [95]. Such a resonance is studied extensively,

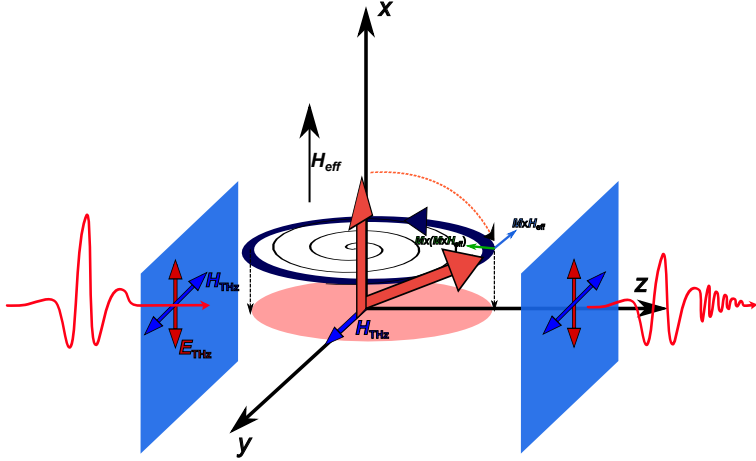


Figure 2.2: **Schematic of THz light induced spin precession and free induction decay signal.** The THz pulse (magnetic field) \mathbf{H}_{THz} adds a Zeeman torque to the system. The spin magnetic moment \mathbf{M} (red arrow) starts to precess around the material's effective internal field \mathbf{H}_{eff} , eventually relaxing back to its equilibrium position. Consequently, a free induction decay signal (pronounced late-time oscillations of the time-varying electric field) is emitted. Based on [66, 69].

theoretically [95, 96] and experimentally, including THz spectroscopy (one-magnon absorption) and Raman spectroscopy (one-magnon scattering) [59, 97–101].

Optical multi-center magnon absorption

Besides a simple one-magnon resonance (see above), more advanced absorption mechanisms can occur. Even in conventional antiferromagnets (FeF_2 , MnF_2 , CoF_2 , and NiF_2) with two magnetic sublattices a two-center magnon absorption was observed: the simultaneous excitation of two magnons, one on each magnetic sublattice, by absorbing one photon [96, 98, 102–106]. Such an absorption process can be described in a simple picture: two magnetic sublattices, \uparrow : spin up, \downarrow : spin down. Considering pairs of magnons with $\sum_n \mathbf{q}_n = 0$, two magnons are generated with

opposite k and $-k$ wave vector and the following four states can occur [96]:

$$|2, +\rangle = |\uparrow k, \uparrow -k\rangle, \quad (2.13)$$

$$|0, +\rangle = |\uparrow k, \downarrow -k\rangle + |\downarrow k, \uparrow -k\rangle, \quad (2.14)$$

$$|0, -\rangle = |\uparrow k, \downarrow -k\rangle - |\downarrow k, \uparrow -k\rangle, \quad (2.15)$$

$$|-2, +\rangle = |\downarrow k, \downarrow -k\rangle. \quad (2.16)$$

$|2, +\rangle$ and $|-2, +\rangle$ are the states corresponding to the two-magnon processes restricted to one sublattice. $|0, +\rangle$ and $|0, -\rangle$ are states that describe the simultaneous excitation of one magnon on each of the magnetic sublattices (two-center magnon). Here, the states $|2, +\rangle$, $|0, +\rangle$, and $|-2, +\rangle$ have positive parity and $|0, -\rangle$ is of negative parity. Thus, in the optical absorption [107], only the latter case is electrical dipole active. In earlier reports three main mechanisms were proposed: dipole-quadrupole interaction between magnetic ions [102], off-diagonal exchange between magnetic ions pairs [103, 108], and phonon-assisted modulation of exchange interaction [109]. For a non-vanishing electric dipole moment especially the removal of centrosymmetry is considered to be necessary [96, 110]. However, from a modern point of view, there is no reason to restrict the absorption solely to electric dipole-active phenomena (see the discussion of the free induction decay mechanism above). At this point no general theoretical picture exists and detailed experimental investigations are desired. The variety of possible magnetic ground states in quantum magnets (see introduction below) might allow observation of exotic excitations. In fact multi-center magnon absorption seems to be enhanced by the low symmetry of the magnetic system especially in non-collinear spin textures/ multiple magnetic sublattices, promoting these systems as suitable candidates.

Note that multi-center absorption process defers from multimagnon scattering often observed by neutron or Raman spectroscopy (neutron/ photon scatters by creating multiple magnons) in quantum magnets. Here, often a magnon decay [111] is discussed (see, for instance, α -RuCl₃ [112]). Under strong quantum fluctuations/ off-diagonal exchange, the single-particle magnon picture is not strictly valid: one-magnon states can be mixed with/ decay in a multiparticle (multimagnon) continuum. This continuum can be traced by Raman [113, 114] or Neutron spectroscopy [115, 116]

but has also relevance for THz absorption [45, 48]. Further information on the scattering mechanisms are summarized in Sec. 2.1.4.

In order to take into account the momentum dependence for the multi-center magnon excitation, Eq. 2.11 needs to be expanded over the entire Brillouin zone:

$$\tilde{\chi}_m(\omega) = \gamma \sum_q \sum_{\alpha, \beta} h_\alpha h_\beta \chi_{\alpha, \beta}^{\text{SS}}(q, \omega), \quad (2.17)$$

where γ is a constant, q is the momentum in the extended Brillouin zone, the summation α and β goes over the Cartesian components, $\chi_{\alpha, \beta}^{\text{SS}}(q, \omega)$ is the spin susceptibility, and h_α is THz magnetic field component. Note that here, for simplicity, no weighting function is included. In general, excitations with lower momentum might be more likely; the probability is not constant over the whole Brillouin zone. However, this would require a more sophisticated model of the multi-center magnon excitation, remaining beyond the scope of the present thesis. Nevertheless, as shown in Ch. 5 already at the present level experiment and theory are well in accordance.

2.1.2 Coupling of light to spinons

Spinons are neutral fermionic quasiparticles, carrying the spin degree of freedom in quantum spin liquids (see introduction in Sec. 2.2). In neutron scattering, they could be distinguished from spin waves by their broad scattering continuum [13, 117]. However, due to their charge neutrality they are believed to not couple directly to the electric field of the light [83]. Instead, for many quantum magnets the frustrated lattice might give rise to magnetoelastic coupling effects [15, 118], spontaneous electric currents correlated with the spin texture [119], generation of electric dipole moments through anisotropic terms [15, 120] or a coupling over virtual charge fluctuations to the emergent gauge electric field [14, 15, 121]. Here, an indirect coupling between photons and spinons is suggested to generate a power-law behavior $\sigma_1 \propto \omega^\beta$ in the sub-gap optical conductivity [14, 15] which could be distinguished from the dielectric background. A power-law behavior was claimed to be observed experimentally for Herbertsmithite in Ref. [16]. This will be further investigated in Ch. 4.

For Herbertsmithite several mechanisms were investigated theoretically, resulting in an exponent of $\beta = 2$ [15]. Here, assuming the case of a U(1) spin liquid, the electric field of the light is suggested to generate virtual charge fluctuation leading to an electric gauge field. Coupling of the external electric field to the gauge electric field gives rise to the Ioffe-Larkin conductivity [15]:

$$\sigma_{\text{IL}}(\omega) \approx 48\sqrt{3}\pi \frac{t^2\omega^2}{U^4} \frac{e^2}{h}, \quad (2.18)$$

where t is the hopping (transfer integral) and U is the on-site Coulomb repulsion, e elementary charge and h Planck's constant. This contribution is estimated to be on the order of $\sigma_{\text{IL}}(1\text{THz}) \sim 10^{-5} \frac{e^2}{h}$ within the kagome layer (two-dimensional conductivity) [15].

Another mechanism yielding a similar powerlaw is magnetoelastic coupling. Since the Cu ions have a net charge, the electric field of the light might introduce a displacement of this. Modulating the hopping along selected bonds, the distortion could introduce a perturbation to the magnetic Hamiltonian. Effectively, for the case of U(1) spin liquids, this generates the optical conductivity [15]:

$$\sigma_{\text{ME}}(\omega) \approx \left(\frac{\omega}{K_{\text{Cu}}a^2}\right)^2 \frac{e^2}{h}, \quad (2.19)$$

where K_{Cu} is the effective spring constant and a is the distance between neighboring Cu sites. This contribution might be even stronger than the Ioffe-Larkin conductivity (for Herbertsmithite $K_{\text{Cu}}a^2 \sim 1$ eV is expected [15]).

An alternative scenario, which does not depend on the gauge field is spin-orbit coupling, leading to Dzyaloshinskii-Moriya (DM) interactions. In a similar manner of the magnetoelastic coupling mechanism, the electric light field could introduce a distortion, modulating the DM interactions. In this case, the electric field generates a spin current perpendicular to it. From this the optical conductivity could arise in the form [15]:

$$\sigma_{\text{DM}}(\omega) \approx \left(\frac{D}{J}\right)^2 \left(\frac{\omega}{K_{\text{eff}}a^2}\right)^2 \frac{e^2}{h} \sigma_s, \quad (2.20)$$

where D is the strength of the DM interaction, J is the exchange constant, K_{eff} is a spring constant taking O an Cu ions into account, σ_s is the spin

conductivity. For the U(1) case, this might be the weakest, however, it could play a role in the Z_2 scenario [15].

Another suggested mechanism to detect spinons by optical spectroscopy is the emergence of cyclotron resonances of spinons under external (static) magnetic field [122]. Here the external magnetic field is suggested to introduce cyclotron quantization of the spinon Fermi surface, leading to characteristic cyclotron resonances in the optical conductivity. However, these evade experimental detection so far.

Besides the indirect coupling to the electric field, coupling to the magnetic light field might be possible. This is argued to result in a broad optical excitation continuum [53]. It was discussed in the context of one-dimensional spin chains (pairwise flip of two spins) [123], but further observation still remains elusive.

2.1.3 Optical selection rules

Selection rules can be a first estimate for possible transitions between two states. In the following some common knowledge from the viewpoint of optical absorption (infrared and THz spectroscopy) is reviewed.

Vibrational modes A transition between two vibrational states $|i\rangle$ and $|j\rangle$ is allowed in infrared or THz spectroscopy (electric dipole active) if the transition matrix element $\langle i|\boldsymbol{\mu}|j\rangle$ (where $\boldsymbol{\mu}$ is the electric dipole operator) does not vanish. This is the case if the transition takes place between states where the vibrational quantum numbers i, j differ by one (only fundamentals are active in first order) and if the dipole moment between the states $|i\rangle$ and $|j\rangle$ changes [124].

Electronic transition For electric dipole transitions in infrared or THz spectroscopy the Laporte rule applies for centrosymmetric systems: here only transitions between states of different parity are allowed [125]. As well, the spin selection rule has to hold: $\Delta S = 0$, i.e., singlet-triplet transitions are spin forbidden.

Magnons Unlike a neutron, a photon does not carry magnetic moment. However, the coupling between photons and spin-waves can be described as a magnetic-dipole active process, where the magnetic field of the light couples to the magnetic moment of the material [43]. A semi-classical picture was introduced above (free induction decay). The determination of selection rules essentially depends on the non-vanishing matrix elements of Eqs. 2.1 - 2.4. In a very simple picture: linear spin chain (alternating $m_s = \pm 1/2$ states) an excitation to the first excited state equals one spin flip, the spin-selection rule $\Delta S = 1$ has to hold [91]. However, the valid selection rules strongly depend on the particular systems [74, 80, 126, 127].

2.1.4 Other methods

In the discussions above, optical absorption in magnetic materials has been reviewed. To emphasize the difference to scattering processes, the basic mechanisms of neutron and Raman scattering are summarized below. As well in the introduction of the magnon absorption above, the term multi-center magnon has been chosen. For instance, the second order Raman scattering process creating two magnons (see below) is called two-magnon scattering, whereas the THz absorption process investigated in this thesis is a multi-center magnon absorption (for the case of two magnons involved it would be a two-center magnon absorption).

Raman scattering

Raman scattering is sensible to magnetic properties and applicable in the field of quantum magnetism [88]. Similar to THz absorption, it is a $\mathbf{q} \approx 0$ method. The Stokes Raman scattering process can be viewed as a virtual excitation of a particle-hole pair by a photon with frequency ω_i . This virtual pair could emit a magnon or spinon and then annihilates by creating a photon of the frequency ω_j [88]. The scattering mechanism for the Raman active one-magnon excitation [128] is an electric dipole-active process [99], where the energy of the incident photon matches to an electronic transition causing a single spin flip (S to $S - 1$) in the presence of spin-orbit coupling. In Raman scattering, furthermore, a two-magnon scattering process $\Delta S = 0$ is known [99]. This is a second order process

where two spin flips occur. For instance, one photon introduces a hop of one electron between neighboring sites with opposite spin states. This causes a double occupancy and a hole. On the double occupancy one electron hops back and emits a photon. This exchange-mediated process creates a pair of magnons with total zero momentum, i.e., two-magnon excitation [129]. Such mechanism was exploited to map out the entire Brillouin zone, $\Delta\mathbf{q} \approx 0$ via Raman scattering [130].

Neutron scattering

Neutron scattering is a powerful method to map out the magnetic structure/ spin-wave dispersion [131]. Due to the magnetic moment of the neutron spin waves can be created ($\Delta S=1$). With the advent of modern triple-axis Neutron spectrometers, not only a wide range of frequencies is accessible but as well the momentum (wave vector \mathbf{q}) is selectable. In inelastic neutron scattering (INS), energy gets transferred by the neutron and creates a spin wave or a phonon. During this process as well the momentum of the neutron changes and the transferred momentum is described by the scattering wave vector. By measuring the scattered neutrons (momentum and energy) the magnetic properties of the sample can be probed. In particular, the scattering function (or spin-spin correlation function) $S_{\alpha,\beta}(\mathbf{q}, \omega)$ can be extracted [43]. Naturally, in the field of quantum magnetism neutron scattering probed particular useful unveiling broad scattering continua of possible spinons [13, 117]. In this field as well a two-magnon scattering process is known. Here within linear spin wave theory two magnons are created with opposite spin by scattering of one neutron ($\Delta S=0$), leading to broad scattering continua [132–134].

2.2 Introduction to quantum magnetism

In the following the principles of quantum magnetism are going to be reviewed. First, some general properties of quantum spin liquids (QSLs) are introduced, including the concept of geometrical frustration. Then the frustrated magnet in the vicinity of QSL is presented. This section is a modified version of the author's publication (Ref. [3]).³

2.2.1 General properties

Quantum spin liquids (QSLs) possess nontrivial ground states, where a local order parameter does not exist. Moreover, despite strong magnetic interactions it is not possible to observe spontaneous symmetry breaking even at very low temperatures. Instead, the system is characterized by quantum mechanical long-range entanglement (topological order) of spins providing persistent spin dynamics. In general, they might be associated with topological phase transitions [135, 136]. Furthermore, it is assumed that QSL can provide an access to high-temperature superconductivity [28] via their quasiparticles. This makes QSL a point of interest, and providing experimental evidences and generating theoretical understanding became a central topic in modern condensed matter physics. In the following, some of the fundamental principles are going to be reviewed, based on Refs. [6, 27, 32]. A more comprehensive introduction can be found in several review articles on this topic [6, 10, 27, 29, 137–141].

QSLs are discussed in the framework of strongly correlated electron systems. For instance, Mott insulators with half-filled electronic bands

³"Pressure-Tuned Interactions in Frustrated Magnets: Pathway to Quantum Spin Liquids?" *Crystals* **10**, 4 (2019)

co-authored with Ece Uykur. Reprinted with permission from Ref. [3]. Copyright CC BY 4.0 (2019) by the authors. Licensee MDPI, Basel, Switzerland. Some passages have been taken verbatim, others are edited/ expanded. There will be no additional citation or other marks in the text for verbatim copied texts or edits from Ref. [3].

Author contributions: T.B. wrote the manuscript. T.B. and E.U. discussed the content.

feature localized electrons retaining their spin degree of freedom. Possessing rich physics and properties, QSLs are subject to extensive experimental and theoretical efforts. The geometrically frustrated materials, where the resonating valence bond (RVB) model [142] is applicable, and the Kitaev QSL candidates, where the Kitaev physics [143] is relevant, are two groups of materials of which the candidates are searched for. Fig. 2.3 shows the archetype of a geometrically frustrated lattice: the kagome lattice [39]. Often the magnetic interaction between two copper sites is based on the superexchange path via the oxygen (Cu-O-Cu). Following the Goodenough-Kanamori rule, the magnetic superexchange J is correlated to the Cu-O-Cu bond angle $\theta_{Cu-O-Cu}$ and to the Cu-O bond length l_{Cu-O} : $J \approx \cos^2(\theta_{Cu-O-Cu})/l_{Cu-O}^n$ with $n \approx 10$ [144, 145]. Although strong magnetic interaction via this exchange path is present, long-range order is suppressed due to the particular lattice geometry of the kagome lattice: geometrical frustration (cf. Fig. 2.3b). By forming valence bonds (VB), which are pairs of spins forming a $S = 0$ singlet: $|\Psi\rangle = \frac{1}{\sqrt{2}}(|\uparrow\downarrow\rangle - |\downarrow\uparrow\rangle)$, the energy can be lowered [6, 27]. The so-called valence bond solid (VBS) is realized, for instance, in $SrCu_2O_3$, $SrCu_2(BO_3)_2$, and CaV_2O_5 [6]. Although this state is characterized by the absence of magnetic long-range order, it does not feature any long-range entanglement or spin dynamics. It is merely a product state of the individual valence bonds and breaks the symmetry. In contrast, the resonating valence bond (RVB) wavefunction is the quantum mechanical superposition of many different valence bond pairs, see Fig. 2.3c for a possible pattern. Consequently, the system's ground state has a large degeneracy. Even in the absence of thermal (classical) fluctuations, the quantum mechanical degeneracy leads to spin dynamics, evading long-range order. In other words, the uncertainty principle exhibits a zero-point motion: quantum fluctuations [6]. By breaking a VB, fermionic quasiparticles can emerge, spinons. They carry fractional spins with their own dispersion expected to give low-lying excitations and can be eventually used to identify the QSL state. Spinons can move on the lattice freely (independent on the charge: spin-charge separation, one electron provides two quasiparticles, a spinon and a holon), simply by rearrangement of the valence-bond pattern, Figs. 2.3c,d. Roughly speaking, the underlying gauge field allows a distinction in two classes: Z_2 or $U(1)$ spin liquids. While the Z_2 might harbor exotic states such as chiral spin liquids [146], it is relevant, for instance, in Kitaev materials with a honeycomb lattice [41]. The $U(1)$

case is assumed to host a Dirac state or a gapless spinon Fermi surface for a simple Heisenberg model on the kagome lattice [27].

In the proximity to QSL, frustrated magnets often realize a form of quantum magnetism with strong short-range magnetic correlations at intermediate temperatures, and exotic (sometimes only partially frozen) long-range order at very low temperatures. Such transitions may be favored, for instance, by unequal superexchange paths due to crystallographically distinct Cu sites, i.e., structural distortion. Recently, the distorted kagome systems were identified as promising hosts: Y-kapellasite ($Q = (1/3, 1/3)$ magnetic structure) [7, 21], Volborthite (spin trimer) [18], $\text{Rb}_2\text{Cu}_3\text{SnF}_{12}$ (pinwheel valence bond solid) [36]. With a rich interplay of lattice geometry, quantum- and thermal fluctuations these systems develop exotic (non-collinear) magnetic phases and offer great tunability [7, 147]. Several examples will be investigated throughout this thesis.

2.2.2 Experimental detection

Several frustrated lattices, such as pyrochlore, triangular, honeycomb, and kagome compounds have been studied in inorganic compounds [6, 10, 137, 138, 140, 141]. However, organic conductors also are promising candidates to search for [83]. The direct detection (*smoking gun* experiment) of a QSL remains elusive even though extensive experimental works [11, 50, 148–150] and theoretical studies [14, 15, 120, 151–154] were carried out in the field, trying to identify fingerprints of QSLs [141]. Technically speaking, it is difficult to identify the QSL state, as one needs to reach absolute zero temperature; that is not achievable. Therefore, within the experimentally reachable limits, temperatures far below (2–3 orders of magnitude) the temperature that identify the magnetic exchange coupling (preferably antiferromagnetic (AFM) spin interactions) are assumed to show properties of the zero-temperature limits.

The first step is to deduce the magnetic exchange coupling constant from the high-temperature behavior of the material via magnetic susceptibility measurements. To identify a QSL state, it is crucial to verify that there is no magnetic ordering or spin freezing down to very low temperatures. Fig. 2.4 compares the susceptibility for a conventional antiferromagnet and a frustrated system. For the conventional antiferromagnet the magnetic

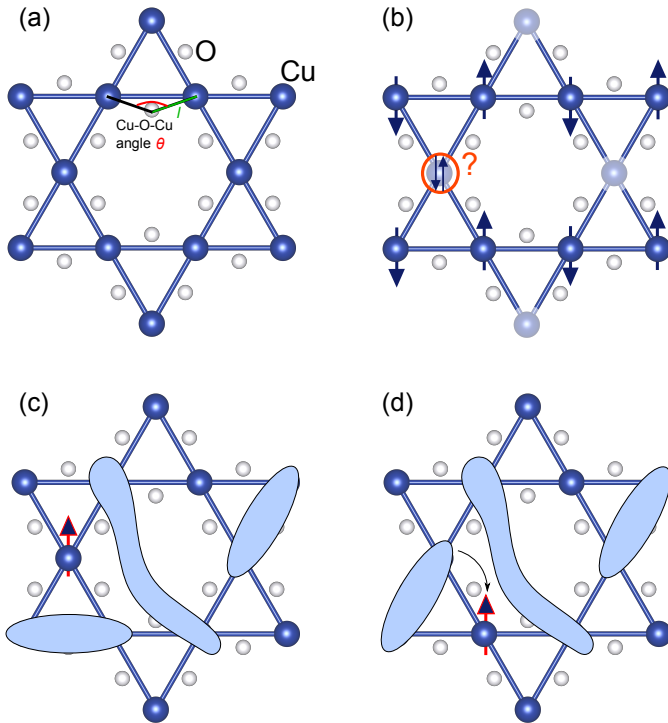


Figure 2.3: **Geometric frustration on the kagome lattice.** (a) Magnetic superexchange (Cu-O-Cu path) depends on the Cu-O-Cu angle, θ and the Cu-O distance, l . (b) The highly effective geometric frustration prevents antiferromagnetic order. (c) Valence bond (VB) pattern, which could be part of the RVB state. By breaking of a VB, fermionic quasiparticles, spinons (red arrow) emerge. (d) Spinons can move by a rearrangement of the VBs. Based on Ref. [6].

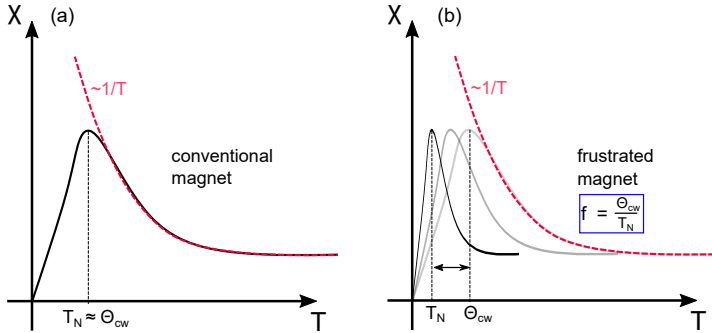


Figure 2.4: **Magnetic susceptibility of a frustrated magnet.** (a) For a conventional magnet, long-range order is observed at $\Theta_{cw} \approx T_N$. (b) For a frustrated magnet, even under strong magnetic interactions, spin freezing might be shifted to very low temperatures, $\Theta_{cw} \gg T_N$. This leaves a wide temperature range for magnetic short-range correlations, between T_N and Θ_{cw} . For the QSL, no long-range order is observed. $f = \frac{\Theta_{cw}}{T_N}$ is the frustration parameter. Grey curves (from right to left) illustrate the increase of f , shift of T_N to lower temperatures. $f \sim 1$: conventional magnet, $f > 5 - 10$: frustrated magnet, $f \rightarrow \infty$: quantum spin liquid. Based on [6, 32].

long-range order develops when the thermal energy is comparable to the scale of magnetic interactions: $\Theta_{cw} \sim T_N$. However, essentially for the frustrated magnet, there is a strong mismatch of freezing temperature and Curie-Weiss temperature: $\Theta_{cw} \gg T_N$, that is, the frustration parameter $f = \frac{\Theta_{cw}}{T_N}$ is high. This might lead to a large temperature window with short-range magnetic correlations and offers an experimental access to study emergent magnetic properties. For $f \rightarrow \infty$, T_N vanishes and the frustrated magnet may host a QSL [6].

A sharp λ -type peak in specific heat is another indication of a phase transition into a long-range order, albeit exceptions may exist in the case of topological phase transitions [155]. Furthermore, entropy releases can be determined yielding valuable information about the ground state. Besides the above mentioned macroscopic probes, more local probes such as muon spin relaxation μ SR and nuclear magnetic resonance (NMR)/ electron spin resonance (ESR), probing the muon relaxation rate, spin-lattice relaxation rate, and electron-spin susceptibility, respectively are usually in play to

investigate the magnetic correlations. Spectroscopic resolution, including the time domain, could be provided by optical spectroscopy, sensitive to electronic and magnetic excitations (see introduction above). Furthermore, broad scattering continua, observed by neutron scattering could help identifying spinons [156]. As well, resonant inelastic x-ray scattering (RIXS) was used to access the magnetic degree of freedom in the cuprates [157] and is recently applied to frustrated magnets [158, 159], even offering access at higher momentum, beyond the zone center excitations. Here a time-resolved extension, trRIXS offers large possibilities [160].

2.2.3 External stimuli: magnetic field and pressure

External pressure can be a very powerful tool to tune the electronic, magnetic, and structural parameters opening a new route in the investigations of QSLs and candidates. For instance, small perturbations to the crystal structure can drive the geometrical frustration factor towards a favorable state. More complicated but possible is a direct tuning of the exchange coupling (Cs_2CuCl_4 [161]). Moreover, unwanted magnetic interactions and fluctuations can be suppressed, leaving room for realization of a pure QSL state. However, it is often difficult to predict the influence of external pressure on magnetic properties of a candidate system. In fact, in few systems pressure induces spin freezing rather than a liquid state (for instance, in $\text{Tb}_2\text{Ti}_2\text{O}_7$ or $\text{Yb}_2\text{Ti}_2\text{O}_7$, see Ref. [3] for a review) or an unfavorable modification of the crystal structure ($\alpha\text{-RuCl}_3$ [5]). Promising are candidates where a magnetic order vanishes before the structural transition as in the case of the iridate systems (see Ref. [3] for an overview). Therefore, there is no easy answer for whether external pressure is always a pathway to introduce spin liquid physics in the candidate systems. Albeit that the end results are unpredictable, exotic states of matter in the vicinity of the QSL state can be investigated.

Another interesting tuning parameter is external magnetic field. It has the advantage to tune the magnetic interactions directly compared to the potentially more complicated detour over the crystal structure with external pressure. However, a comparison of the energy scales: magnetic field energy, superexchange and thermal energy, suggests that often very high magnetic fields are necessary. For instance, for a Cu^{2+} (one unpaired electron) the spin-only moment is $1.73 \mu_B$. At 10 T, this results in a

Zeeman energy of ($10 \text{ T} \cdot 1.73 \mu_B \approx 1 \text{ meV}$). Comparing to a J on the usual order of 150 K (around 13 meV), it becomes clear that only small shifts in the spectra are going to be expected. As well, demagnetization effects need to be considered. Furthermore, the Zeeman energy needs to be larger than the thermal energy $k_B T$. Therefore, in the estimation above, at 10 T, at least temperatures below 12 K (corresponding to about 1 meV) need to be reached. Of course, these are only rough estimates. However, they show that the THz range at very low temperatures, is a good starting point to perform spectroscopic measurements under magnetic field.

3 Experimental methods and data analysis

In this chapter, the extensively used experimental techniques (pressure dependent-) fourier-transform infrared (FTIR) spectroscopy, (magneto-) terahertz time-domain spectroscopy (THz-TDS) and electron spin resonance (ESR) are introduced based on cited literature and the author's publications (Refs. [1–5]). Furthermore, the experimental procedures are described in detail and an overview of the data analysis, including the extraction of the relevant material parameters and response functions is given. Note than further experimental details of the particular measurements presented in the results sections are briefly summarized in the relevant sections as well.

3.1 Fourier-transform infrared spectroscopy

Fourier-transform infrared (FTIR) spectroscopy is a powerful tool to investigate the electrodynamic response (mostly electronic and structural properties) in a broad spectral range (20 cm^{-1} to 25000 cm^{-1} in this thesis) with high spectral resolution (below 1 cm^{-1}) and good signal-to-noise ratio (SNR). This technique allows to measure the optical reflectance and transmittance as a function of frequency. Via a Kramer-Kronig transformation, phase information can be calculated and the frequency-dependent system's response function is obtained, complex permittivity $\tilde{\epsilon}$, among other material parameter such as optical conductivity $\tilde{\sigma}$ [81, 82]. Together with an infrared microscope samples down to the μm range ($50 \mu\text{m} \times 50 \mu\text{m}$ size, depending on the spectral range) can be probed. In general, samples are desired to be optical polished, however, even a difficult surface topography can be canceled out via an *in-situ* gold-evaporation technique [162]. Furthermore, optical pressure cells or superconducting magnets can be incorporated in the experimental setup offering a plethora of research opportunities.

In the following, the principle of FTIR spectroscopy is going to be explained, based on Refs. [81, 163]. Fig. 3.1 illustrates the basic measurement scheme build around a Michelson interferometer. In a table-top setup the beam is provided by a broad-band light source (for instance, Globar). The beam is guided to an IR beamsplitter, where 50 % of the intensity is

deflected to one interferometer arm (fixed mirror) and 50 % is transmitted to the other interferometer arm (movable mirror, scanner). As both beams are reflected back from the mirrors to the beamsplitter they interfere, and the recombined beam is guided on the specimen where it gets reflected or transmitted, depending on the experiment. Successively, the intensity is collected at the detector. Fig. 3.1b shows a possible interferogram (intensity over the path difference). When the interferometer arms are of equal length, i.e., $x = 0$, full constructive interference of the beams yields maximum intensity in the interferogram, that is, center burst. Further intensity maxima and minima are observed as a function of path difference (constructive vs. destructive interference). For the necessary precise measurement of the mirror displacement, a HeNe laser is used. Note that for a broad-band source many frequency components are superimposed in the interferogram. Therefore, the Fast Fourier Transformation (FFT) results in a broad-band spectrum (intensity over frequency), Fig. 3.1c. The spectral resolution depends on the length of the interferometer arm, determining the maximum possible displacement of the movable mirror, eventually allowing to collect a more extended interferogram. The sample's reflectance or transmittance is obtained by dividing through the reference intensity spectrum (mirror or empty hole, respectively).

3.1.1 Reflectance and transmittance measurements

In Tab. 3.1 an overview of the FTIR setups and the optical equipment (beamsplitters, windows, detectors) is given. The spectral ranges are abbreviated as follows: far-infrared (FIR), mid-infrared (MIR), near-infrared (NIR), and visible (VIS). To cover a wide spectral range, multiple measurements utilizing different sets of optical equipment are carried out successively.

Fig. 3.2 shows pictures from the infrared lab. For reflectance (R) measurements in the FIR range a Bruker IFS 113v is used, equipped with a liquid helium flow (LiHe-flow) cryostat and an *in-situ* gold evaporation unit. The beam is guided to the sample mounted in the optical cryostat via a concave mirror. Via an aperture the beamspot can be cut to a minimum diameter of 3 mm to 5 mm. To prevent reflection from the sample holder, the sample is mounted on a copper cone at the cold finger. Because of the wedged geometry, light which is not reflected by

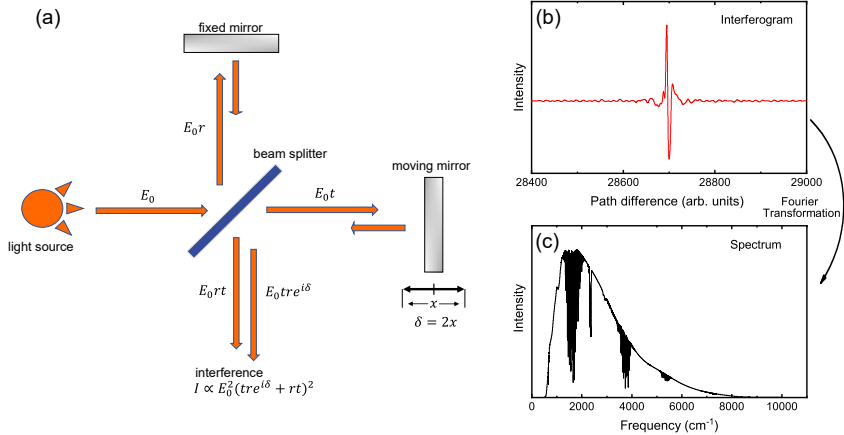


Figure 3.1: **Principle of FTIR spectroscopy.** (a) Infrared light from a broadband light source is guided to a Michelson interferometer. The beam is split into one interferometer arm with a fixed mirror and another arm with a movable mirror. The beams get reflected at the mirror and interfere at the beamsplitter. To map out the full interferogram, the movable mirror is successively shifted and the intensity at every position is collected at the detector. (b) Resulting interferogram, intensity over path difference between the two arms. If both arms are of equal length, the intensity is maximized, i.e., center burst. At positions different from equal length, local maxima and minima are found. (c) Performing the FFT yields the power spectrum (intensity over frequency). Adapted with permission from Ref. [164].

Abbreviation	Range (cm ⁻¹)	Spectrometer	Window	Beamsplitter	Detector	Source	Mirror
FIR	50-700	PP	IFS 113v	Mylar Multilayer	Bolometer	Globar/ Mercury Arc	Au
MIR	500-8000	KBr	Vertex 80v/ IFS 66v/S	KBr	MCT/ PV	Globar	Au
NIR	1800-12000	KBr	Vertex 80v/ IFS 66v/S	CaF ₂	InSb	Tungsten	Au
VIS	7000-25000	KBr/Glass	Vertex 80v/ IFS 66v/S	CaF ₂	Si Diode	Tungsten	Au/ Ag

Table 3.1: **Overview of spectral ranges and optical equipment.** Multiple measurements were carried out successively to cover a wide spectral range. The definitions far-infrared (FIR), mid-infrared (MIR), near-infrared (NIR), and visible (VIS) are not exact as they are adjusted to the approximate ranges of the detectors. All spectra have been obtained in correlation mode and using the relevant non-linear corrections, a Blackman-Harris apodization was used in the FFT. Spectra are corrected by the mirror reflectance. Based on Ref. [84].

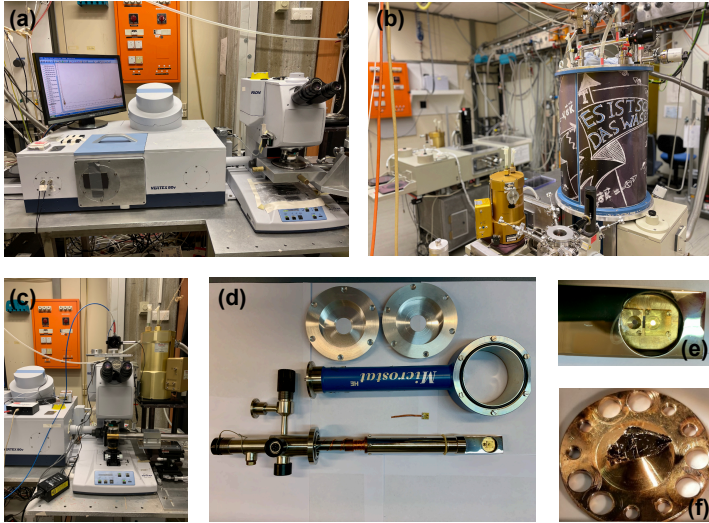


Figure 3.2: **Pictures from the infrared lab.** (a) Bruker Vertex 80v together with a Hyperion 2000 infrared microscope. Under the microscope different optical equipment and LiHe-low cryostats can be mounted. (b) Bruker IFS 113v and superconducting magnet (Spectromag SM4000M-8, Oxford Instruments). The magnet can be coupled to the spectrometer, allowing temperature-dependent reflectance and transmittance measurements under continuous magnetic fields up to $H = 7.5$ T. FIR and MIR spectral ranges are possible with sets of different windows (PP and KBr, respectively). By rotating the magnet, Voigt and Faraday geometries are accessible. The sample is mounted inside a LiHe-flow cryostat on top of a cold finger (base temperature around 5 K). As well a reference can be selected (empty hole or mirror). Besides the magnet, the spectrometer can be operated with a LiHe-flow cryostat and gold evaporation unit, allowing precise measurements of the reflectance in FIR. (c) Hyperion with a screw-driven diamond anvil cell (DAC) and a ruby fluorescence setup (pressure gauge). Right side: Bolometer extension. Pressure-dependent optical spectra can be obtained from FIR to VIS. (d) Small LiHe-flow cryostat (MicrostatHe, Oxford Instruments) with base temperature of around $T = 5$ K. The cryostat has optical access on both sides, allowing reflectance and transmittance measurements. Different windows (PP, KBr, glass) are used to cover the full spectral range. (e) Cold finger of the MicrostatHe with heat shield. Samples are mounted on spring-loaded apertures. In the picture a gold mirror is glued behind the right aperture. The left aperture can be used for the sample. The transmittance reference is collected in the slit between the apertures. (f) Copper cone used in the reflectance measurements with gold evaporation on Bruker IFS 113v. The photos in (a), (b), (f) are reprinted with permission from Ref. [164].

the sample gets scattered away. Also, the gold mirror is mounted on a copper cone, next to the sample. At the first glance the measurement of the gold overcoated sample seems to make a measurement of the gold mirror unnecessary. However, it is still important to reference against the gold mirror. This might cancel out short-time fluctuations and drifts of detector and spectrometer. Gold mirror and sample need to reflect the light under the same angle and should be of similar height. Furthermore, because of the large beamspot a larger area on the sample is illuminated, and the mirror needs to have a similar size. A good alignment of sample and mirror can finally help to reduce any contribution of the PP window. To ensure a good alignment, sample and mirror are aligned by utilizing an alignment laser and several screws.

Measurements were carried out using the following protocol: 1. Temperature-dependent measurement of the sample and gold mirror intensity, I'_s and I'_m , respectively. Dividing resulting in $R'_s = \frac{I'_s}{I'_m}$. Note that measurement of the gold mirror is necessary to cancel out eventual short-time drifts of the setup. 2. Gold evaporation at room temperature: usually evaporating five gold strings with 5 mm length each (250 μm thickness) attached to a tungsten wire (100 μm thickness, 12 loops, total resistance of around 1 Ω) by driving a current with the power of 40 W. 3. Measurement of the overcoated sample and the gold mirror: $R_{sg} = \frac{I_{sg}}{I_m}$. The final reflectance is obtained via the relation

$$R_s = \frac{R'_s}{R_{sg}} \cdot R_g = \frac{I'_s I_m}{I_{sg} I'_m} \cdot R_g \approx \frac{I'_s}{I_{sg}} \cdot R_g, \quad (3.1)$$

where R_g is the reflectance of gold. Since most samples investigated here host strong phonon modes in the FIR range, the transmittance can be neglected in this spectral range. If necessary, a hole was drilled in the copper cone and the sample was mounted on top, to allow a large mismatch of reflected beam and possible backside contribution of the sample holder.

Reflectance and transmittance (Tr) measurements in the MIR to VIS range were carried out using a Bruker Vertex 80v or Bruker IFS 66v/S spectrometer together with a Hyperion 2000 microscope (equipped with two reverses Cassegrain Schwarzschild objectives: Thermo Opticon 15x 0.4 NA 160 mm BFL , 24 mm working distance). The focused beam allows to select a clean and homogeneous surface. Therefore, for samples,

considered in this thesis, no gold evaporation at higher energies was necessary. However, as the present samples have a wide charge gap, they tend to be semi-transparent in the absence of any strongly reflecting phonon mode. In principle, it is possible that the light gets transmitted through the sample and is then reflected back from the sample holder, giving a contribution to the reflectance. To avoid this, the sample was mounted behind an aperture in a LiHe-flow cryostat (Oxford Instruments) with optical access on both sides. This geometry allows a successive measurement of reflectance and transmittance. Furthermore, since the sample is mounted with the aperture, only vacuum is behind it and the reflectance will not be influenced by any backside contribution. Figs. 3.2d,e show the equipment used for such a measurement. Two spring-loaded apertures are used for sample and a reference mirror. The reference mirror is mounted behind the second aperture. This ensure a similar height of sample and mirror to avoid larger shifts and a mismatch of the alignment. To obtain a precise reflectance and avoid any artificial spectroscopic features, sample and mirror have to be aligned under the same angle. This alignment can be carried out with the spring-loaded screws by using an alignment laser. Then the cryostat is mounted and aligned to nearly normal incidence under the microscope by maximizing the reflected intensity on the reference mirror. For the transmittance measurement, the reference (empty space) is obtained by measuring in the slit between the two apertures. In all the measurements the aperture at the microscope determines the beamspot diameter.

3.1.2 Pressure-dependent optical studies

Pressure-dependent optical studies were carried out at the institute and at Synchrotron Soleil, France. In Stuttgart, a screw-driven diamond anvil cell (DAC) from AlmaxEasyLab (CryoDAC-Mega) with type IIa diamonds (800 μm culet) was utilized together with Bruker Vertex 80v spectrometer (see Fig. 3.3 for pictures of the equipment). In the DAC transmittance and reflectance measurements are possible. A ruby fluorescence system consisting of a grating spectrometer (HR2000+, Ocean Optics) and a green laser allowed to collect the pressure-dependent shift of the ruby R1 line, used as a pressure gauge [165, 166]. CuBe gaskets were prepared and pre-indented in the DAC to a thickness between 60 μm to 70 μm ,

depending on the target pressure (60 μm for measurements over 10 GPa, 70 μm for pressures around 5 to 10 GPa). The gasket was drilled using an electrical discharge machine (EDM) for sample compartment (hole of 250 μm diameter in the center of the pre-indented area). Samples were prepared with a surface of 180 $\mu\text{m} \times 160 \mu\text{m}$ and a thickness of about 20 μm thinner than the pre-indentation thickness, i.e., 40 μm to 50 μm . The pressure cell was loaded by gluing the drilled gasket on top of the diamond culet. This sample compartment leaves enough space for the specimen and several small ruby chips. For a reflectance measurement a good contact between sample and diamond should be maintained. CsI_3 was used as pressure transmission medium. It is quasi hydrostatic in the relevant pressure range and transparent down to approximately 100 cm^{-1} . The CsI_3 powder is sprinkled on the sample compartment and solidifies by applying a small force to the screws (about 50 cNm). The reference was either obtained on the gasket (for reflectance measurement) or through the CsI_3 . Sometimes the sample compartment does not allow to measure the reference in transmission geometry with the same size as the sample. In such a case, the signal was scaled by a constant, obtained from geometrical relations between the different sizes.

For temperature-dependent high-pressure FTIR measurements (transmittance) at Synchrotron Soleil (SMIS2 beamline), a membrane pressure cell was utilized, following a similar preparation procedure as introduced above. Here steel gaskets were used, pre-indented to a thickness of 60 μm with a hole of 200 μm . For pressure transmission medium polyethylene (PE) was prepared in FIR, whereas for the MIR measurements NaCl was utilized. The pressure cell was mounted in a LiHe-low cryostat which allows temperature-dependent measurements under increasing pressure (isotherms). The spectra were collected with a ThermoFisher FTIR spectrometer and the horizontal microscope (Cassegrain objectives).

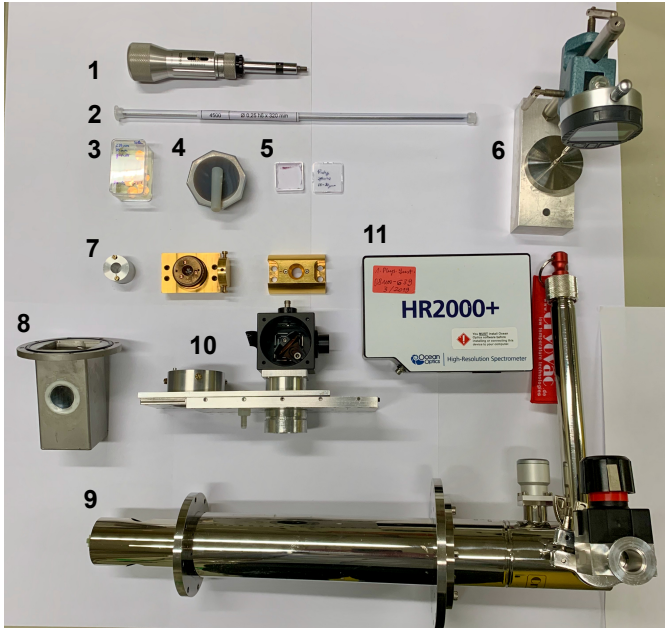


Figure 3.3: **Pictures from the pressure lab.** (1) screwdriver KStools 516.3235 to apply pressure, (2) steel needle h6 diameter 250 μm , No. 4500 (HMTG) for drilling the gaskets, (3) CuBe gasket blanks 250 μm thickness, 10 mm diameter, (4) mortar and pestle to grind CsI_3 , (5) ruby spheres 10 to 50 μm diameter, (6) thickness gauge for controlling pre-indentation thickness, (7) pressure cell CryoDac Mega A68002 (AlmaxEasyLab) and lifting tool (left), (8) cryostat window CsI or KBr 30 mm diameter, 1 mm thickness (Korth Kristalle GmbH) or Mylar foil, (9) LiHe-flow cryostat (CryoVac), (10) beamsplitter for coupling ruby luminescence setup to the infrared microscope: C4W cage cube, AD11F - SM1-threaded adapter, B3CR/M - 30 mm cage cube rotation platform, B5C1 optic mount for 30 mm cage cube (ThorLabs), (11) grating spectrometer HR2000+ (Ocean Optics) for ruby luminescence. Additional components (not shown): optical fiber (Ocean Optics PL100-2-VIS-NIR) and green laser diode (ThorLabs).

3.1.3 Extraction of response functions

With the reflectance and transmittance measurement optical response functions and material parameters can be obtained. The analysis of the data depends on optical properties of the specimen. As $R + Tr + A=1$, where R is reflectance, Tr transmittance and A absorbance has to hold in the absence of any scattering, the following cases can be distinguished:

1. $Tr \ll R$: Here only R is measured and the phase information can be obtained via Kramers-Kronig transformation, allowing the calculation of optical conductivity $\tilde{\sigma} = \sigma_1 + \sigma_2$. See the detailed explanations in Refs. [81, 82]
2. $R \ll Tr$: Here only Tr is measured. For simplicity the absorption coefficient following the well-known Beer-Lambert law [81, 82]: $\alpha = -\frac{1}{d}\ln(Tr)$ is calculated instead of the optical conductivity.
3. $Tr \approx R$: In the semi-transparent case, both R and Tr are measured. For simplicity the absorption coefficient $\alpha = \frac{1}{d}\ln(\frac{(1-R)^2}{Tr})$ is calculated instead of the optical conductivity, depending on R and Tr [4].

Note that for determining the optical conductivity from the sample-diamond reflectance in a pressure experiment, a modified Kramers-Kronig analysis has to be used to take the phase shift due to the diamond into account. This procedure will not be discussed here as the measurements are not shown in the thesis. The results are shown in the author's publication (Ref. [4]). In the case of the pressure-dependent transmittance measurements presented in this thesis, it is sufficient to calculate the standard absorption coefficient: $\alpha = -\frac{1}{d}\ln(Tr)$.

For data analysis and calculations of the response functions/ material parameters the programs Datan (copyright by C. Porter, maintained by D. Tanner), ReFIT (copyright by A. B. Kuzmenko [167]), and WASf (S. Schultz, copyright by University of Stuttgart) were used.

3.2 Terahertz time-domain spectroscopy

Terahertz time-domain spectroscopy (THz-TDS) allows to probe the electronic and magnetic degrees of freedom, including a time resolution. It operates in the so-called THz gap, between the microwave band and the far infrared, which remains difficult to approach by other methods [169]. It is a versatile method offering a wide range of possibilities from technical application to research. In the following the basic principles are going to be introduced, based on the reviews of the method in Refs. [58, 170].

In THz-TDS the oscillating electric field in the picosecond (ps) range is measured directly, containing amplitude and phase information. For resolving the ps time range, a conventional detector such as a bolometer or golay cell is simply too slow. Therefore, a more sophisticated, indirect detection scheme is needed. The high time resolution can be achieved with ultra short laser pulses (femtosecond (fs) range), sampling the THz field. The detection scheme is shown in Fig. 3.4. A fs broad-band NIR laser pulse gets split into two paths by a beamsplitter. In one path the pulse travels to a THz emitter, which is a photoconductive switch (Auston switch). Here, the NIR laser pulse excites a DC biased metal dipole antenna on a gallium arsenide (GaAs) substrate. As the NIR pulse falls on the antenna gap a photocurrent is generated. The driven dipole antenna emits a THz pulse which can be focused on the sample. There are multiple processes which contribute to the THz emission/ photocurrent generation: 1. Charge carriers are generated and accelerated in the bias field until they recombine. 2. The creation of charge carrier causes a drop in the resistivity leading to a response of the bias field, generating a THz field in the antenna. 3. Optical injection of current directly into the antenna by charge carriers generated close to the antenna electrodes. The resulting THz electric field has a power distribution between 2 to 133 cm^{-1} [168] and oscillates in the ps range. The temporal length of the generated THz pulse is determined by the risetime of the photocurrent (approximately the duration of the NIR laser pulse) plus the carrier lifetime. To produce a short THz pulse it is therefore necessary to use photoconductive substrates with a low carrier lifetime, such as the low-temperature grown GaAs (LT-GaAs). In order to improve the coupling of the THz radiation and air and to avoid back reflections due to the impedance mismatch of the GaAs substrate ($n \approx 3.3$) and air, often

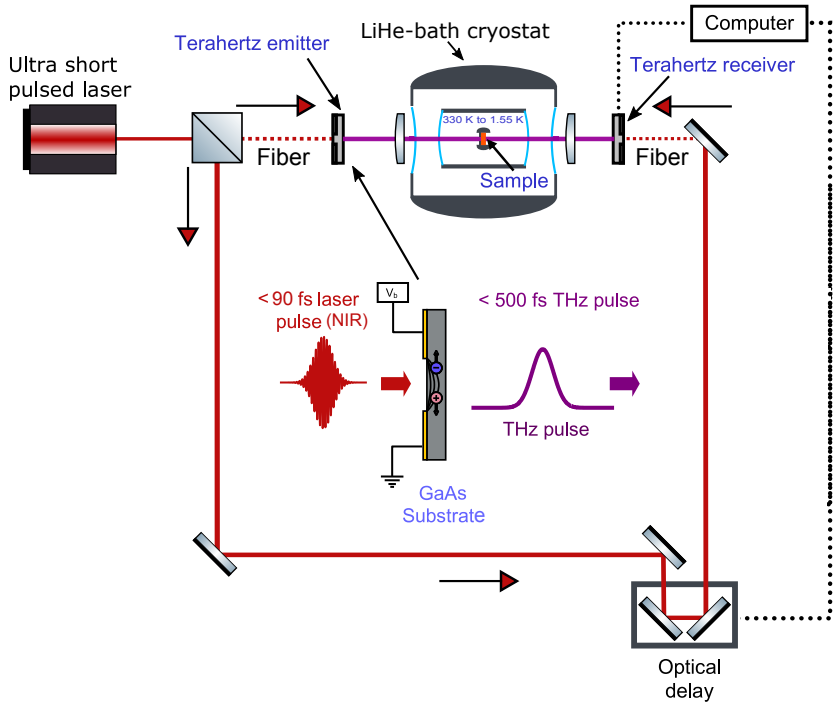


Figure 3.4: **Schematic of the THz-TDS setup.** An ultrafast laser emits the NIR pulse. The pulse is split into a path of the THz emitter, sample, THz receiver and a second path of the optical delay stage, THz receiver. In the THz emitter, the NIR pulse gets converted in a broad-band THz pulse, interacting with the sample, loaded inside an optical cryostat. The transmitted electric field gets detected when the delayed NIR pulse arrives at the THz receiver. The time-resolution is achieved via sampling of the electric field by changing of the optical delay. Based on Ref. [168]. Graphics of the ComponentLibrary (CC BY-NC 3.0, A. Franzen) have been used.

a Si lense is used [171].

The second NIR pulse travels along a mechanical delay line where it gets delayed in time with respect to the other beampath. It is guided to the THz receiver, where the above mentioned process is reversed: the NIR pulse generates an electric bias field in the receiver, allowing to collect the THz electric field coming from the THz emitter/ sample path. As the NIR pulse triggers the receiver, a sampling of the THz electric field in time is achieved by changing the optical delay. Typically, the electric field is plotted over the time delay (ps) or optical delay (mm).

The TeraView TeraPulse 4000 supports two types of manipulating the optical delay: rapid-scan mode, where the optical delay is achieved by a moving mirror or step-scan mode, where a corner-cube retroreflector mirror is moved by a stepper motor [168]. The following parameters have been used to acquire spectra presented in the thesis:

- Scanner: HiResScannerSeries
- Averages: 100 (internal chamber) to 200 (magnet)
- Sample spacing: 0.01
- Sweep speed: 100 to 200 ps/s, depending on the signal
- Split directions: no
- Optical delay offset: 5 (internal chamber with cryostat), 440 (remote heads and LiHe-bath cryostat, two $f = 10$ cm lenses), 2150 (magnet, two $f = 7.5$ cm lenses)
- Apodization in FFT: mostly Tukey for extended time traces, sometimes Blackman-Harris for compact time traces
- Resulting resolution: depends on accessible signal, typically around 0.5 cm^{-1}

In general, TeraView TeraPulse 4000 can be operated using the internal chamber or the remote heads, with corresponding optical delay offsets. While the internal chamber supports a smaller LiHe-flow cryostat, the remote heads support integration in the magneto-optical setup or a larger LiHe bath cryostat. In all cases, the THz beam is linearly polarized. For the internal chamber the beam is focused, whereas for remote heads

additional lenses are used to focus the beam. Fig. 3.5 shows pictures from the THz lab.

3.2.1 Magneto-optical measurements

For magneto-optical measurement the magneto-THz setup has been build. Fig. 3.6 displays a schematic of the setup. Here, the remote heads (THz emitter and THz receiver) are used, coupled to the TeraView TeraPulse 4000. The beam is focused on the sample via a plano-convex polytetrafluoroethylene (PTFE) lens (LAT075, ThorLabs $f = 7.5$ cm). A second lens behind the sample collimates the beam again before it reaches the THz receiver. The sample is mounted in the variable temperature inset (VTI) of the magnet, allowing to adjust the temperature between $T = 295$ K and 1.55 K. The sample holder supports two round apertures of variable size. On one the sample is glued, the other serves as a reference. Sample and reference can be selected by shifting the sample holder up and down. The temperature can be controlled by adjusting the flow of helium from the main reservoir of the magnet through the VTI over the needle valve and the valve to the rotary pump. Above $T = 4.2$ K only a small stream of LiHe from the reservoir is needed to cool the VTI. Here the LiHe evaporates and the sample sits in exchange gas, ensuring a good thermal coupling. For measurements below $T = 4.2$ K, LiHe is condensed in the VTI and the pressure is lowered, such that the helium becomes superfluid. Here the sample is immersed in LiHe. Temperatures are measured directly at the sample holder, next to the sample with a calibrated Cernox sensor (Lake Shore). The magnet has four PP windows and the remote heads can be turned by 90° to switch between Faraday geometry ($\mathbf{k} \parallel \mathbf{H}$) and Voigt geometry ($\mathbf{k} \perp \mathbf{H}$). Furthermore, the heads can be rotated to select, for instance, between vertical and horizontal linearly polarized light. The whole beam path is purged with N_2 gas to avoid atmospheric contributions to the spectra. When the main reservoir is at $T = 4.2$ K, field strengths of up to $H = 10$ T are reached. However, with a lambda fridge refrigerator, fields up to 11.5 T are supported. In order to protect the remote heads against the magnetic stray fields, they are wrapped with several alternating layers of μ -metal (MagnetoShield Flex+, Aaronia AG) and tape, providing an effective shielding.

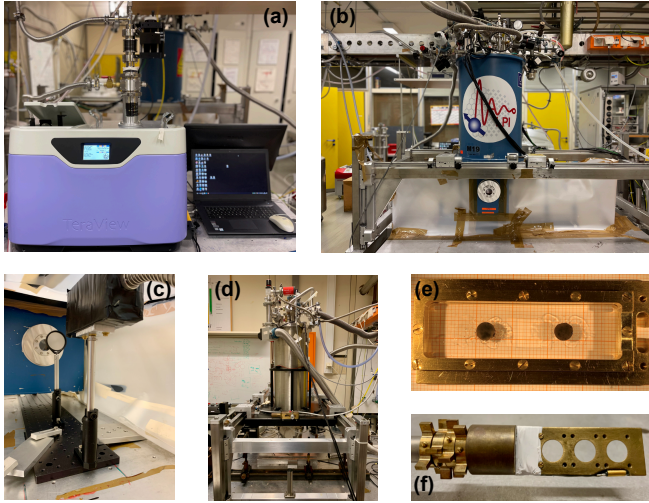


Figure 3.5: **Pictures from the THz lab.** (a) TeraView TeraPulse 4000 spectrometer with a LiHe-flow cryostat (base temperature of $T = 6$ K) mounted in the internal chamber. (b) Magneto-optical setup with a superconducting magnet (Spectromag SM4000-11.5, Oxford Instruments), allowing continuous magnetic fields up to $H = 10$ T. The sample is mounted inside a variable temperature inset (VTI), supporting temperatures between $T = 295$ K and 1.55 K. Helium is used as an exchange gas. The VTI is cooled with a helium stream from the magnet's helium reservoir. Temperatures below 4.2 K are achieved by lowering the pressure in the VTI and condensing liquid helium. Optical windows (PP) on all four sides of the magnet allow usage in Voigt and Faraday geometry. To avoid an atmospheric contribution, the beam path is covered with a N_2 purging box. (c) The beam is guided by remote heads (THz emitter and THz receiver) and gets focused via a plano-convex lens on the sample. A second lens behind the sample is used to collimate the beam. Remote heads are wrapped with several layers of μ -metal to avoid disturbance of the heads by the magnetic stray field. (d) The LiHe-bath cryostat allows temperature-dependent measurements down to $T = 1.55$ K. Similar to the magnet, the temperatures are achieved by immersing the sample in superfluid helium. The beam path consists of two lenses and the remote heads (not shown). (e) Sample holder (slider) for the LiHe-bath cryostat. Two samples can be glued on a thin Mylar foil. On their backsides the foil is cut. In the middle a hole is cut for the reference measurement. The holder can slide during the measurement, allowing to select between samples and the hole. Before the slider an aperture is mounted to determine the spot size. (f) Sample holder for the magnet. The samples are glued directly on an aperture, which is screwed to the sample holder.

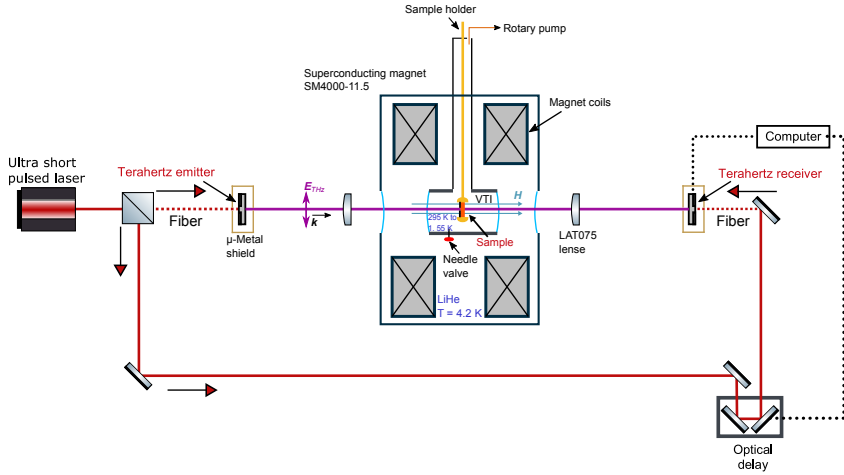


Figure 3.6: **Magneto-THz TDS setup.** For temperature-dependent measurements under continuous magnetic field, the remote heads (THz emitter and THz receiver) are placed next to the superconducting magnet (Spectromag SM4000-11.5, Oxford Instruments). The THz beam is focused on the sample with a plano-convex PTFE lens. An identical lens behind the sample collimates the beam again. The temperature can be controlled in the variable temperature inset (VTI) via the helium flow from the main reservoir (needle valve and valve to rotary pump). In this sketch, the Faraday geometry ($\mathbf{k} \parallel \mathbf{H}$) is shown but the remote heads can be turned by 90° to switch to Voigt geometry ($\mathbf{k} \perp \mathbf{H}$). Graphics of the ComponentLibrary (CC BY-NC 3.0, A. Franzen) have been used.

3.2.2 Extraction of response functions

The transmitted electric field yields amplitude and phase information. From the time-dependent electric field $E(t)$ the frequency-dependent power spectrum $\tilde{E}_{sample}(\omega)$ is obtained via a Fast Fourier Transformation (FFT). Now, the complex transmission (transmitivity) $\tilde{T}r(\omega)$ can be calculated by referencing to the empty hole of the sample holder, $\tilde{E}_{ref}(\omega)$:

$$\tilde{T}r(\omega) = \frac{\tilde{E}_{sample}(\omega)}{\tilde{E}_{ref}(\omega)}. \quad (3.2)$$

For non-magnetic materials ($\mu = 1$), the optical conductivity/ permittivity can be extracted in a straight forward way (see Refs. [81, 82] for the relevant equations, introduced in the following). Considering a plane wave at the interface material (with complex impedance \tilde{Z}_s) and vacuum ($Z_0 = 377 \Omega$) under near-normal incidence, the impedance mismatch at the boarder vacuum-sample causes a separation in reflected and transmitted beam. Utilizing the Fresnel fromulars, the complex transmission coefficient of the plane wave can be written as:

$$\tilde{t} = \frac{2\tilde{Z}_s}{Z_0 + \tilde{Z}_s}. \quad (3.3)$$

Because of material's presence (complex index of refraction \tilde{n}), the plane wave acquires a phase: $\exp\{i\frac{\omega d}{c}\tilde{n}\}$, where d is the sample thickness. Taking into account the complex transmission coefficient at the second border (sample-vacuum): $\tilde{t}' = \frac{2\tilde{Z}_0}{Z_0 + \tilde{Z}_s}$, the transmitted electric field can be written:

$$\tilde{E}_{sample}(\omega) = 4 \frac{Z_0 \tilde{Z}_s}{(Z_0 + \tilde{Z}_s)^2} E_0 \exp\{i\frac{\omega d}{c}\tilde{n}\}. \quad (3.4)$$

Divided by the reference field $\tilde{E}_{ref} = E_0 \exp\{i\frac{\omega d}{c}\}$, the complex transmission reads:

$$\tilde{T}r(\omega) = 4 \frac{Z_0 \tilde{Z}_s}{(Z_0 + \tilde{Z}_s)^2} \exp\{i\frac{\omega d}{c}(\tilde{n} - 1)\}. \quad (3.5)$$

As introduced above, from the FFT of the time-dependent electric field, amplitude and phase of this complex quantity can be obtained directly. A

Newton-Rapson based numerical inversion is used to obtain the complex index of refraction \tilde{n} [172]. From \tilde{n} , optical conductivity/ permittivity can be obtained directly, see Refs. [81, 82].

However, for a magnetic system ($\mu \neq 1$), both permittivity and permeability can contribute to the transmission spectra (especially near the magnetic resonance). Therefore, the four independent quantities (real and imaginary parts of permittivity and permeability) cannot be obtained from transmittance and phase without further assumptions, see discussion in Ref. [80]. The analysis of magnetic systems in this thesis is based on the absorption coefficient α which does not suffer from this since magnetic and electric contributions are considered together in this case. For a transparent material, it can be calculated from the transmittance Tr using the Beer-Lambert law [81, 82]: $\alpha = -\ln\{Tr\}/d$, where d is the sample thickness. The integrated absorption coefficient $IA = \int \alpha d\omega$ is similar to the optical spectral weight $SW = \int \sigma_1 d\omega$. It provides further quantitative access to the spectral features. It is used to describe cumulative changes under external stimulus, such as temperature and external magnetic field. Furthermore, the dynamic magnetic susceptibility can be extracted, as shown in the next section.

During the FFT, the type of apodization function and cut off need to be chosen. In this thesis mostly a Tukey apodization is selected. Depending on the shape of the signal, sometimes as well a Blackman-Harris. As shown in Fig. 3.7, the apodization window influences the final spectra. This can be used to distinguish different contributions and time scales. While phononic and electronic contributions are mostly confined to short time scales in the main echo, sharp magnetic resonances exhibit a pronounced late-time oscillation over several tens of picoseconds, exceeding the main pulse [67–69, 92, 93] (see the spin precession picture introduced above). Moreover, it is important to choose a suitable window, covering the whole signal. At best, at room temperature, the time delay until the next echo (first internal reflection, see Fig. 3.8) is determined. Then the time delay can be chosen until shortly before the first internal reflection. It should be noted that in some cases, i.e., extended late-time oscillations due to magnetic resonances, the first reflected beam can cover the late-time oscillations. In this case, the sample has to be thicker.

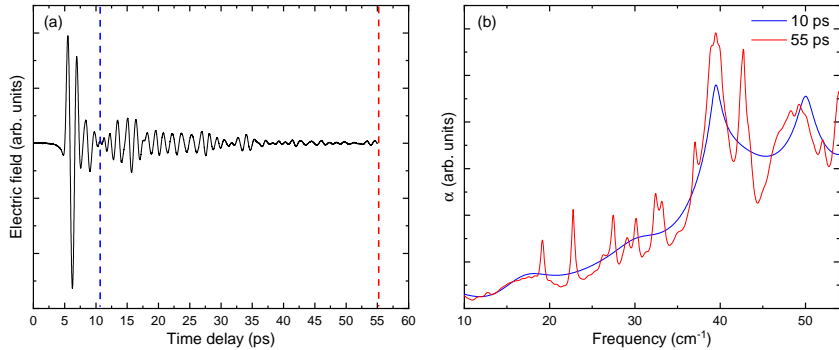


Figure 3.7: **THz spectra for different apodizations of the FFT.** (a) Electric field over time delay. For the case of Averieville (see Ch. 6), the electric field consists of multiple oscillations. By selecting the FFT window with the apodization function, different contributions can be extracted (see blue and red dashed lines) for the absorption coefficient (b). The main pulse, centered at around 5 ps only accounts for the slope of the absorption coefficient and the broad phonon modes at around 40 and 50 cm^{-1} . Including the pronounced late-time oscillations of the electric field (apodization at around 55 ps), several sharp magnetic resonances (see Ch. 6 for further details) are imposed on the spectrum.

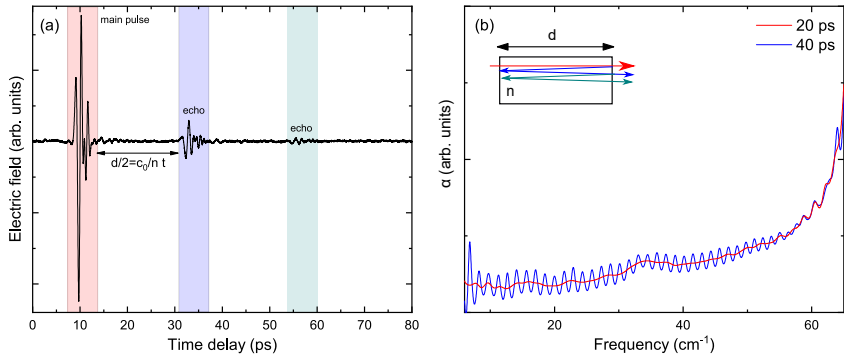


Figure 3.8: **THz spectra for a wide time range.** (a) Electric field over time delay. Besides the main pulse (red shaded area), the first and second internal reflection echos, blue and green shaded areas, respectively are observed. The time shift between the first internal reflection and the main echo is determined by the index of refraction and the thickness of the sample. (b) Resulting absorption coefficient for different apodization windows. Red curve: Cut off at 20 ps, including only the main echo (main pulse). Blue curve: cut off at 40 ps, including main echo and first internal reflection. Including the internal reflection results in artificial oscillation pattern if the number of internal reflections is not considered. Inset: Sketch of the main pulse (red), first internal reflection (blue), second internal reflection (green). For better illustration the internal reflections are shown under an angle with respect to the sample surface.

3.2.3 Extraction of dynamic magnetic susceptibility

This section is part of the author's publication (Ref. [1], supplemental materials).¹

The imaginary part of the dynamic magnetic susceptibility, $\chi_m'' = \text{Im}\{\tilde{\chi}_m(\omega)\}$, can be extracted from the THz data to unveil the natural spectral form of magnetic features by exclusion of the high-temperature dielectric backgrounds, for instance, tails from the phonon modes. It provides quantitative information about the magnetism. Compared to a fit-based subtraction, the following method is advantageous because it offers self-calibration and does not depend on a certain model. Here, the low-temperature magnetic susceptibility $\tilde{\chi}_m$ is extracted from THz-TDS measurements by referencing to the spectra at temperatures above the magnetic ordering (or onset of magnetic interaction). Such an approach was used in Refs. [46, 47, 51, 89, 172, 173] and was proven to be robust in the class of insulating quantum magnets since the electronic contributions are located at much higher frequencies. In the following, $\tilde{\chi}_m(\omega)$ is derived using this approach, based on the more detailed explanation in Ref. [46]. In general, complex transmission through the sample with thickness d , can be written as $\tilde{T}r(\omega) = 4 \frac{Z_0 \tilde{Z}_s}{(Z_0 + \tilde{Z}_s)^2} \exp\{i \frac{\omega d}{c} (\tilde{n} - 1)\}$, where $Z_0 = 377 \Omega$ and $\tilde{Z}_s = \sqrt{\frac{\tilde{\mu}}{\tilde{\epsilon}}}$ is the complex impedance of the sample with permittivity $\tilde{\epsilon}$ and magnetic permeability $\tilde{\mu}$. $\tilde{n} = \sqrt{\tilde{\epsilon} \tilde{\mu}}$ is the index of refraction of the sample [81, 82]. Rewriting the complex transmission in terms of $\tilde{\epsilon}$ and $\tilde{\mu}$ leads to

$$\tilde{T}r(\omega) = \frac{4\sqrt{\tilde{\epsilon}\tilde{\mu}}}{(\sqrt{\tilde{\epsilon}} + \sqrt{\tilde{\mu}})^2} \exp\{i \frac{\omega d}{c} (\sqrt{\tilde{\epsilon}\tilde{\mu}} - 1)\}. \quad (3.6)$$

For the magnetic permeability it can be written: $\tilde{\mu} = 1 + \tilde{\chi}_m$. By assuming $\tilde{\chi}_m \ll 1$ and $\sqrt{\tilde{\mu}} \approx 1 + \tilde{\chi}_m/2$ it reads:

$$\tilde{T}r(\omega) \approx \frac{4\sqrt{\tilde{\epsilon}}(1 + \tilde{\chi}_m/2)}{(\sqrt{\tilde{\epsilon}} + 1 + \tilde{\chi}_m/2)^2} \exp\{i \frac{\omega d}{c} (\sqrt{\tilde{\epsilon}}(1 + \tilde{\chi}_m/2) - 1)\}. \quad (3.7)$$

¹Reprinted with permission from Ref. [1]. Copyright CC BY 4.0 (2022) by the authors. Advanced Quantum Technologies published by Wiley-VCH GmbH. Some passages have been taken verbatim, others are edited/ expanded. There will be no additional citation or other marks in the text for verbatim copied texts or edits from Ref. [1].

It can furthermore be simplified as:

$$\tilde{T}r(\omega) \approx \exp\left\{i\frac{\omega d}{c}(\sqrt{\tilde{\epsilon}}(1 + \tilde{\chi}_m/2) - 1)\right\}, \quad (3.8)$$

since the exponential term is dominating in Eq. 3.7. To extract $\tilde{\chi}_m$ from Eq. 3.8, the dielectric contribution needs to be subtracted. $\tilde{T}r$ can be referenced to a temperature, where $\tilde{\mu} \approx 1$, i.e., above the onset of magnetic interactions. Here, the complex transmission reads $\tilde{T}r_{ref} \approx \exp\left\{i\frac{\omega d}{c}(\sqrt{\tilde{\epsilon}_{ref}} - 1)\right\}$. Under the assumption that the dielectric properties (phononic or electronic contributions) in the THz range do not change considerably below the reference temperature it can be written: $\tilde{\epsilon}_{ref} \approx \tilde{\epsilon}$ and therefore $\frac{\tilde{T}r}{\tilde{T}r_{ref}} \approx \exp\left\{i\frac{\sqrt{\tilde{\epsilon}_{ref}}\omega d}{2c}\tilde{\chi}_m\right\}$. Inverting this leads to:

$$\tilde{\chi}_m(\omega) \approx \frac{2ic}{\sqrt{\tilde{\epsilon}_{ref}}\omega d} \ln\left\{\frac{\tilde{T}r_{ref}}{\tilde{T}r}\right\}. \quad (3.9)$$

The extracted dynamic magnetic susceptibility yields information about the magnetism and can be compared to other probes sensitive to the magnetic correlations. For instance, it is related to the NMR spin-lattice relaxation rate $1/T_1$, which probes the spin fluctuations at a fixed frequency (ω_0): $1/T_1 \propto T|A_{hf}|^2\chi''(\omega_0)/\omega_0$, where A_{hf} is the hyperfine coupling between electron and nucleus [174]. Also, it can be compared to the ESR electron spin susceptibility χ_s^e (see below for further information). In combination, these quantities give a comprehensive picture about the magnetism, well beyond the level of dc or ac magnetization measurements.

3.3 Electron spin resonance

Electron spin resonance (ESR) is an useful technique to probe the magnetism of a system possessing unpaired electrons or any form of magnetic correlations [175]. It measures the absorbed microwave power $P \propto \chi''$ in an external magnetic field \mathbf{H} . Here electrons interact with the field via their magnetic moment $\boldsymbol{\mu}_S = -g\mu_b\mathbf{S}$, where g is the Landé g-factor, μ_b is the Bohr magneton and \mathbf{S} the spin. This interaction releases degeneration

of $m_S + \pm 1/2$ states. The energy shift can be described by the Zeeman Hamiltonian [175]:

$$\mathcal{H} = g\mu_b \mathbf{S}\mathbf{H}. \quad (3.10)$$

If another magnetic field \mathbf{h} with the frequency ν and corresponding energy $h\nu = g\mu_b H$ is applied perpendicular to the static magnetic field \mathbf{H} , transitions between the $m_S = -1/2$ and $m_S = +1/2$ can be excited. Typically, the field strength of \mathbf{H} is swept while \mathbf{h} is kept constant. According to the frequency of the microwave field different frequency bands can be assigned. Here, the X-band ESR ($\nu = 9.8$ GHz) is used. For signal improvement, the static field is often modulated with a small sinusoidal ac field. Via a lock-in scheme the measured signal is the first derivative of the absorbed microwave power with respect to the field \mathbf{H} [176]: dP/dH .

To this end, the ESR signal leads several quantities that can be extracted: line shape, resonance field, g-factor, line width, intensity [177]. They might allow conclusions about the underlying magnetism. Importantly, from the intensity of the ESR line, the electron spin susceptibility χ_s^e can be extracted (see below). This quantity is used together with the magnetization from the SQUID and the NMR spin-lattice relaxation rate $1/T_1$ to probe the onset of (short-range) magnetic correlation. It naturally extrapolates the high frequency THz-TDS measurements.

Measurements were performed using a Bruker (EMXplus) cw-spectrometer in X-band frequency ($f = 9.8$ GHz) together with a LiHe-flow cryostat (Oxford Instruments), see previous theses for further information, for instance, Refs. [176, 177]. The sample mounted in nearly impurity-free suprasil glass holder (spectra have been corrected by the background from the holder prior to analysis). A goniometer is used to rotated the sample with respect to the magnetic fields to probe for any anisotropy. The spectra where collected upon heating using variable temperature slopes.

3.3.1 Extraction of electron spin susceptibility

The absorbed microwave power P is proportional to the imaginary part of the magnetic susceptibility χ'' . Since commonly the derivative of the absorbed microwave power dP/dH is measured, χ'' is obtained by integrating dP/dH over the magnetic field H . Furthermore, the electron spin susceptibility χ_s^e can be obtained by the Kramers-Kronig sum rule [178]: $\chi_s^e = \frac{2}{\pi H_{res}} \int_0^\infty \chi''(H) dH \propto \int_0^\infty P(H) dH = I$. It is proportional to the intensity I of the ESR line and can be either obtained by integration or as well from fits of the line.

4 Results I: Herbertsmithite and Volborthite

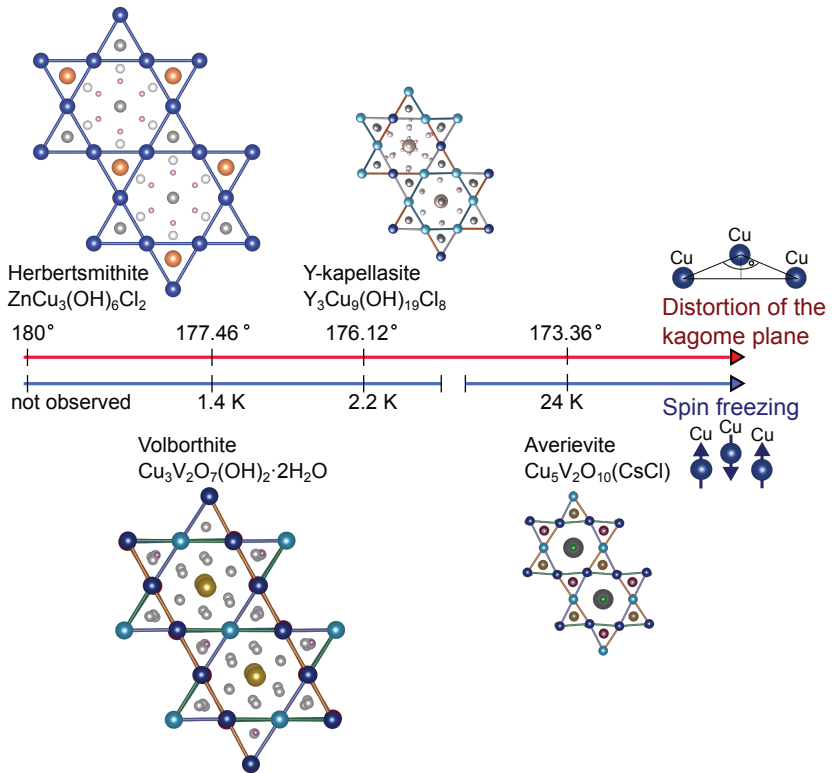


Figure 4.1: **Structural distortion and spin freezing on the kagome lattice.** Structures are based on Refs. [19, 21, 23, 42].

This chapter is focused on the compounds Herbertsmithite and Volborthite. Herbertsmithite features undistorted kagome layers, while Volborthite is only slightly distorted, Fig. 4.1. Both compounds will be introduced by showing recent literature. After these reviews, the results from this thesis are going to be discussed. For Herbertsmithite, at first, THz-TDS is used to probe the putative spinon response in THz range, including the response under external magnetic field. Furthermore, structural aspects will be discussed by showing pressure-dependent optical studies. Having treated the undistorted kagome lattice, the experiments on Volborthite are going to be shown. In contrast to the undistorted kagome lattice, here signatures of short-range magnetic correlations are pronounced in the THz spectra. Further structural and electronic aspects are probed employing FTIR spectroscopy.

4.1 Introduction of the material

Herbertsmithite ($\text{ZnCu}_3(\text{OH})_6\text{Cl}_2$) [42, 179] is highlighted as a QSL candidate with an almost perfect kagome lattice and absence of magnetic long-range order down to the mK range [12]. Its decoupled kagome planes harbor strong antiferromagnetic (afm) exchange along the Cu-O-Cu path ($J \approx 17$ meV or 197 K) [152, 153], see Fig. 4.2 for the structure. Regarding the magnetic ground state, anti-site disorder (on the order of 10% of Cu intercalated at Zn sites, inducing a Curie-like tail in magnetization at low temperatures [180]) appears to be problematic; the impurity spins are even antiferromagnetically coupled [181]. Yet, their influence on the QSL (gapped or gapless state) is still under debate [174, 182].

In the following some relevant findings are going to be reviewed. At first a view on the possible spinon excitations from the perspective of neutron scattering experiments is given. NMR studies will be shown to discuss the influence of disorder on the magnetism. Closely connected with the magnetism, the lattice degree of freedom is going to be introduced by showing pressure-dependent studies. Furthermore, the role of optical investigations will be discussed. Finally, a few open questions in this system will be summarized. Although this list is by far not complete, it should give a brief overview of physics. More extensive reviews can be found, for instance, in Refs. [11, 39].

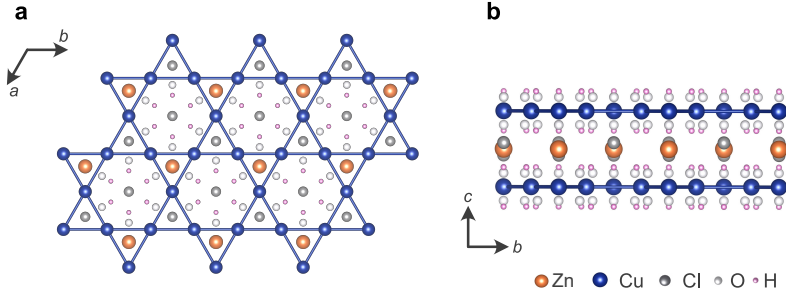


Figure 4.2: **Crystal structure of $\text{ZnCu}_3(\text{OH})_6\text{Cl}_2$.** (a) View within the in-plane (ab) orientation. Herbertsmithite crystallizes in the $R\bar{3}m$ structure and is composed of kagome layers (blue Cu-Cu bonds). (b) The kagome layers are stacked along the c -direction (out-of-plane) and separated by Zn atoms (orange spheres). The picture was prepared using the structural data ($T = 300$ K, single crystal diffraction) of Ref. [42]

Since Herbertsmithite was recognized as a quantum magnet in 2005 [179], a plethora of experimental techniques, such as NMR [183–185], μsr [186], specific heat [12, 187, 188], magnetization [12, 180], x-ray scattering [189], and optical measurements [190–193], and theoretical approaches [152, 153] were employed to study its properties. A remarkable experimental result is the report of a broad scattering continuum at low temperatures which was interpreted as a continuum of fractional excitations (spinons) [13]. Figs. 4.3a-e give an overview of the inelastic neutron scattering investigation of Ref. [13]. The dynamic structure factor $S(Q, \omega)$ at $T = 1.6$ K is displayed for selected energies in Figs. 4.3a-c. A broad continuum contribution (see the green color) persists over a rather wide energy range (at least between 0.25 meV and 11 meV) and wave vector range, indicating a gapless response. It becomes even more visible through cuts along the high-symmetry directions, Figs. 4.3d,e. Integrating $S(Q, \omega)$ over the wave vector, the imaginary part of the dynamic susceptibility χ''_m can be obtained, Figs. 4.3f,g (here measurements of Ref. [194] are shown). Consistent with the magnetization measurements, χ''_m increases at low energies upon cooling. These measurements determine the energy and temperatures scales for forthcoming studies: below 1 meV and lower than 3.5 K.

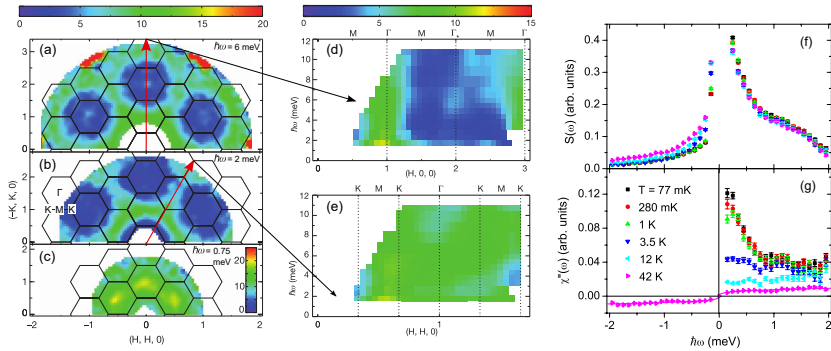


Figure 4.3: **Inelastic neutron scattering on ZnCu₃(OH)₆Cl₂ (Refs. [13, 194])** (a-c) Dynamic structure factor $S(Q, \omega)$ at $T = 1.6$ K plotted for $\hbar\omega = 6$ meV, 2 meV, and 0.75 meV, respectively. The green area features a pronounced scattering continuum. Red arrows: high symmetry directions $(H, 0, 0)$ in (a) and $(H, H, 0)$ in (b). (d, e) Cuts along the $(H, 0, 0)$ and $(H, H, 0)$ directions. Along $(H, H, 0)$ the broad scattering continuum persists (green color). (f) Structure factor $S(\omega)$ for wave vectors $0.5 \leq Q \leq 1.9$ Å. Below 1 meV the structure factor increases significantly. (g) Obtained local dynamic susceptibility $\chi''(\omega) = S(\omega)(1 - e^{-\hbar\omega/k_b T})$, showing an increase at low energies as well. (a-e) Adapted by permission from Springer Nature Customer Service Centre GmbH: Springer Nature, Nature, Ref. [13] Copyright 2012. (f,g) Adapted with permission from Ref. [194]. Copyright (2010) by the American Physical Society.

Furthermore, the theoretical prediction of an optical conductivity, scaling with a power law as a fingerprint of the intriguing spinon Fermi surface opens another perspective [14, 15]. Quasi-optical THz techniques, reaching to very low energies, are of particular interest. Indications for a power-law scaling with an exponent of $\beta \approx 1.4$ were reported for Herbertsmithite [16]. However, the previous reports are limited by a rather narrow frequency and temperature range (down to 20 cm⁻¹ or about 2.5 meV and 4 K).

Although a spinon scattering continuum was concluded in the previous experiments, due to anti-site disorder the extraction of the pure kagome response remains challenging and the results are still under debate [11]. This problem was recently approached employing ¹⁷O NMR [182]. Utilizing the NMR shift, the kagome susceptibility could be distinguished from the disorder contribution. Fig. 4.4a shows the disorder contribu-

tions D_1 and D_2 . The D_1 line was attributed to Cu substituted Zn sites [compare inset (I) and (II)], whereas D_2 is argued to originate from in-plane substitution of Cu by Zn [inset (III)]. Compared to the mostly temperature-independent D_2 , the D_1 shift contributes strongly to the low-temperature magnetic response. Interestingly, it is the weakly coupled out-of plane Cu site, inset (II) which introduces such a strong response. It was argued due to Jahn-Teller driven distortion, introducing a displacement of all six adjacent oxygen sites [182]. The disorder induced shift was cleaned from the data, leaving only the pure kagome susceptibility, Fig. 4.4b. From the temperature dependence of the kagome susceptibility, a gapless QSL scenario was concluded.

However, the previous observations are in stark contrast to a recent ^{63}Cu nuclear quadrupole resonance study [174]. Here the distribution of the spin-lattice relaxation rate, i.e., the histogram $P(1/T_1^{\text{Cu}})$ was determined. From $P(1/T_1^{\text{Cu}})$ two contribution can be discerned: a paramagnetic contribution $1/T_{1,para}^{\text{Cu}} \approx 1000 \text{ s}^{-1}$ of Cu^{2+} spins remaining in a paramagnetic state with short spin-spin correlation length and a so-called singlet contribution $1/T_{1,singlet}^{\text{Cu}}$ (Fig. 4.4c). In contrast to the nearly temperature-independent $1/T_{1,para}^{\text{Cu}}$, the $1/T_{1,singlet}^{\text{Cu}}$ is significantly suppressed below $T = 10 \text{ K}$ and yields a residual value of around $1/T_{1,singlet}^{\text{Cu}} \approx 20 \text{ s}^{-1}$ at the lowest measured temperature. Based on the small floor value of $1/T_{1,singlet}^{\text{Cu}}$, these results were interpreted in favor of a gapped spin-singlet ground state of spin dimers [see inset of Fig. 4.4d]. Furthermore, the fraction of Cu sites involved in the formation of singlets was extracted, Fig. 4.4d. Interestingly, this shows a formation of singlets at relatively high temperatures ($T = 30 \text{ K}$), reaching a value of around 60 % of Cu sites contributing at around $T = 2 \text{ K}$.

Having discussed the recent investigations on the magnetic ground state, now the structural aspects of Herbertsmithite and their connection to the magnetism is further deepened (see introductions in Sec. 2.2). Its structural properties leave open questions: although a perfect threefold symmetry of the kagome lattice was concluded ($R\bar{3}m$ structure) [11, 39], recently indications for a lattice distortion are accumulating [147, 195, 196]. With the close energy scales of gapless/ gapped QSL and valence bond solid impact of a possible lattice distortion on the magnetism eludes the current understanding; more sophisticated theoretical models taking these parameters into account are needed. As the interplay between

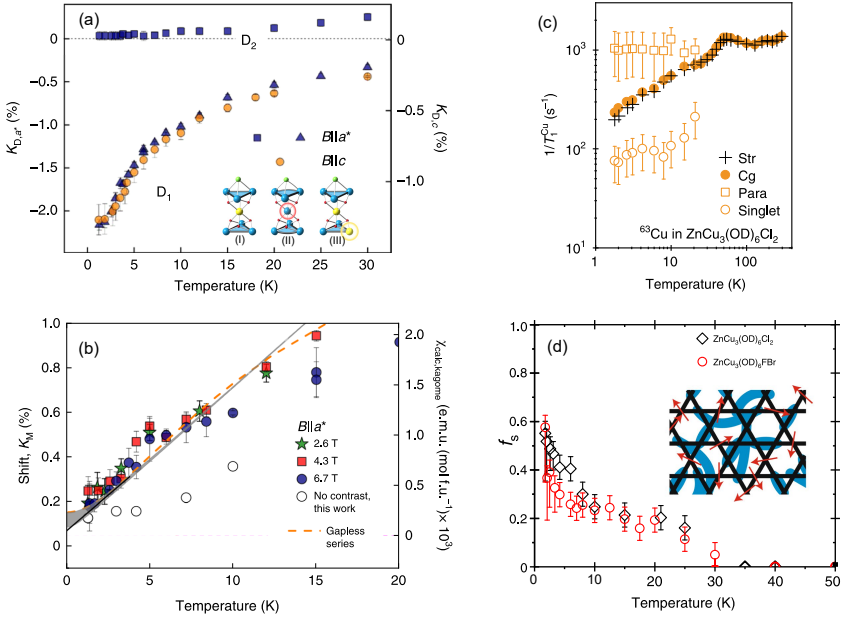


Figure 4.4: **Nuclear magnetic resonance on $\text{ZnCu}_3(\text{OH})_6\text{Cl}_2$** (Refs. [174, 182]). (a) Knight shifts of the D_1 and D_2 lines for several defect contributions, see insets: (I) kagome planes (blue spheres are the Cu ions) are well separated by Zn (yellow sphere), (II) disorder contribution, where Cu/Zn are mixed in the interlayer sites: D_1 line, (III) disorder contribution where Cu/Zn are mixed within the kagome layers: D_2 line. Field along the a -axis corresponds to the right side, along the b -axis to the left side. (b) Cleaning of the disorder-induced shift yields the pure kagome susceptibility interpreted within a gapless QSL picture in Ref. [182] (c) Spin-lattice relaxation rate $1/T_1$. Black crosses: determined from fit of $M(t)$, filled circles: center-of-gravity $1/T_{1,cg}$. From the density distribution (not shown) the contribution of magnetic singlets (open circles) and paramagnetic spins (open squares) can be determined. (d) Fraction of Cu sites which are involved in the formation of spin singlets. Interestingly, the formation of spin singlets is already observed at intermediate temperatures $T \approx 30$ K. Upon cooling the contribution gets enhanced. At the lowest temperature 60 % of Cu sites are contributing to the singlet states. Inset: suggested picture of the gapped magnetic ground state in Ref. [174]. The fluctuating spin singlets are illustrated by blue ovals. Red arrows: paramagnetic spins. Adapted by permission from Springer Nature Customer Service Centre GmbH: Springer Nature, Nature Physics, Ref. [182] (a,b) Copyright 2020 and Ref. [174] (c,d) Copyright 2021.

structure and magnetism becomes more relevant, optical spectroscopies could provide useful information. Indeed, some of the lattice vibrations seem to be magneto-elastically coupled to the spin degree of freedom [191, 193].

To tune the magnetism several strategies haven been tested, including chemical doping [197, 198], external magnetic field [199], and external pressure [144, 200]. In general, external pressure is a clean tuning parameter to alter structural and electronic properties (see introduction in Sec. 2.2.3). In the kagome lattice it might be even used to control the magnetism. For instance, the magnetic superexchange J depends on the Cu-O-Cu bond angle $\theta_{Cu-O-Cu}$ and on the Cu-O bond length l_{Cu-O} : $J \approx \cos^2(\theta_{Cu-O-Cu})/l_{Cu-O}^n$ with $n \approx 10$ [144, 145]. Recently, hydrostatic pressure was applied to Herbertsmithite. Fig. 4.5 summarizes the results of Refs. [144, 200]. Fig. 4.5a displays the lattice parameters. The application of hydrostatic pressure leads to a decrease of the overall unit cell volume, as well as the a -axis (in-plane) and c -axis (out-of-plane) direction. It generates a tilting of the CuO_4 plane of the CuO_4Cl_2 octahedron away from the kagome planes (cf. inset of Fig. 4.5a). Figs. 4.5b,c show distances and angles between several characteristic lattice sites. Up to $P = 2.5$ GPa the Cu-O distance, Fig. 4.5b decreases under pressure and the Cu-O-Cu angle increases. Above $P = 2.5$ GPa the Cu-O distance remains constant and a decrease is observed in the Cu-O-Cu angle. The Cu-Cl distance decreases continuously under pressure, Fig. 4.5c, whereas in the Cu-Cl-Cu angle at first an increase is observed, followed by a nearly constant behavior after $P = 2.5$ GPa. At around 8 GPa a second-order transition to the $P2_1/n$ structure was observed (discontinuity in the unit cell volume in Fig. 4.5d) inducing a monoclinic distortion (see inset of Fig. 4.5d) of the whole kagome plane. In addition, the reduction of the inter-kagome separation (Fig. 4.5e) weakens in this pressure range; and the inter-kagome separation increases again above 12 GPa. These structural modifications have an enormous impact on the magnetism: they induce magnetic long-range order. Figs. 4.5f,g show the corresponding T_N and susceptibility measurements. At $P = 2.5$ GPa spin freezing sets in with a $T_N = 6$ K as the frustration of the kagome lattice gets released [144]. Increasing the pressure further, the Néel temperature decreases, consistent with a reduction of the superexchange due to the decreasing Cu-O-Cu bond angle with nearly constant Cu-O bond length. In the susceptibility measurements of Ref. [200] the weak ordering at $P = 2.5$

GPa (observed in Ref. [144]) cannot be seen. Instead, the order sets in at higher pressure, $P = 6.2$ GPa. The reason for this is not clear and the authors of Ref. [200] argue with non-hydrostatic effects or different sample stoichiometry. However, it seems to be that the magnetic order sets in even before the structural transition. More insight on the type of long-range order was obtained from neutron scattering. Fig. 4.5h shows the neutron diffraction pattern at $T = 1.4$ K and $P = 2.7$ GPa of Ref. [144]. The weak Bragg reflexes were fit to a $\sqrt{3} \times \sqrt{3}$ antiferromagnetic order.

Even though Herbertsmithite has been thoroughly investigated over the recent years, it still puzzles the community. Some of the most interesting questions are not solved and can even be generalized to the whole material class of kagome/ honeycomb quantum magnets. For instance: What is the ground state? What precursor state/ magnetism develops at intermediate temperatures? Is it related to the putative QSL? How are magnetic and structural degrees coupled? How does (even minimal) structural distortion of the kagome lattice affect the magnetism? How and in which direction can the system be tuned? Throughout this thesis some of these questions in the class of kagome/ honeycomb quantum magnets are going to be addressed utilizing different experimental approaches, often complemented by theoretical calculations.

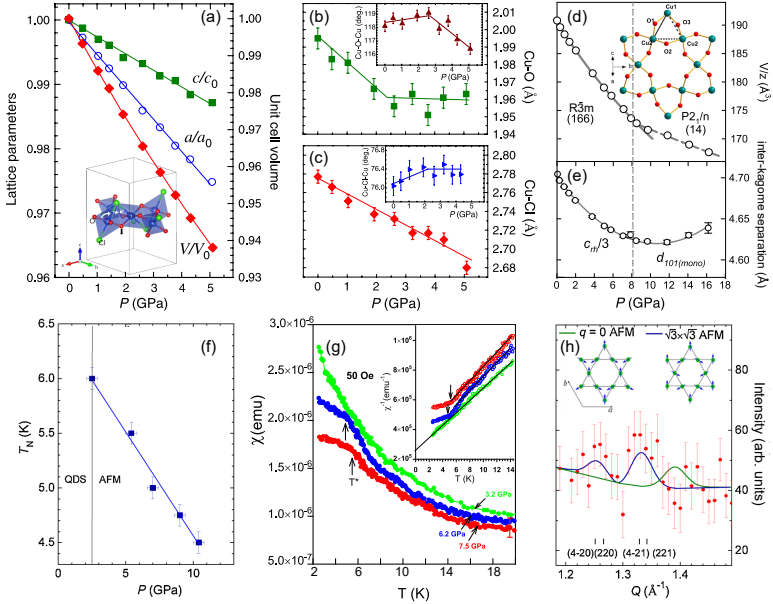


Figure 4.5: **Pressure-dependent studies on $\text{ZnCu}_3(\text{OH})_6\text{Cl}_2$** (Refs. [144, 200]). (a) Lattice parameters (left axis) and unit cell volume (right axis). Inset: Variation of the crystal structure at low pressures ($P \approx 2.5$ GPa) within the $R\bar{3}m$ structure. The CuO_4 plane of the CuO_4Cl_2 octahedron gets tilted away from the kagome plane (see arrows). (b) Cu-O bond length $l_{\text{Cu-O}}$ and Cu-O-Cu bond angle $\theta_{\text{Cu-O-Cu}}$ (inset) crucial for the magnetic superexchange. A discontinuity is observed at $P \approx 2.5$ GPa, leading to a decrease of the magnetic coupling strength J . (c) Cu-Cl bond length and Cu-Cl-Cu angle (inset). (d,e) Structural variations of the high-pressure phase. At around $P \approx 8$ GPa, a second-order transition from $R\bar{3}m$ to $P2_1/c$ induces a monoclinic distortion of the kagome layers (see inset), indicated by a discontinuity in the unit cell volume (d) and a reverse of the inter-kagome separation's pressure dependence. (f) Evolution of the magnetic long-range order T_N as a function of pressure. (g) Magnetic susceptibility χ as a function of temperature for selected pressures. The kink-like structure indicates magnetic order below T^* . Note that the pressure scale, i.e., onset of magnetic long-range order of Ref. [144] (f) is shifted compared to Ref. [200] (g). (h) The neutron diffraction at $T = 1.4$ K and $P = 2.7$ GPa shows weak magnetic Bragg peaks, possibly matching to a $\sqrt{3} \times \sqrt{3}$ order (blue line). For comparison, the green line shows the expectation for $q = 0$. Adapted with permission from Ref. [144] (a-c, f, h) and Ref. [200] (d,e,g). Copyrighted by the American Physical Society.

4.2 Experimental methods

Crystal growth and characterization Single crystals of $\text{ZnCu}_3(\text{OH})_6\text{Cl}_2$ were grown using a hydrothermal method, similar to the reported procedure of Ref. [156] by P. Puphal and C. Krellner. Single crystals of $\text{Cu}_3\text{V}_2\text{O}_7(\text{OH})_2 \cdot 2\text{H}_2\text{O}$ were grown via a hydrothermal method by P. Puphal.

THz-TDS measurements THz-TDS measurements were carried out in transmission geometry ($\mathbf{E}_{\text{THz}} \parallel (a, b)$) at several temperatures between 295 and 1.6 K utilizing a helium bath cryostat, based on the procedure of Ref. [1]. Magneto-optical THz measurements were performed in Voigt geometry ($\mathbf{E}_{\text{THz}} \parallel (a, b)$, $\mathbf{H} \parallel (a, b)$) with static magnetic field strengths up to $H = 8.3$ T and temperatures down to 1.6 K. The absorption coefficient α was calculated from the transmittance Tr by $\alpha = -\ln\{Tr\}/d$, where d is the sample thickness. IA was calculated by integration of α : $IA = \int \alpha d\omega$, and provides a quantitative access to the spectral features.

Pressure-dependent measurements Pressure-dependent transmittance and reflectance spectra (near-normal incidence, $E \parallel (a, b)$) were recorded using a Bruker 80v FTIR setup, equipped with a Hyperion IR-microscope, based on the procedure of Ref. [4]. Pieces with a typical in-plane size of $160 \times 160 \mu\text{m}$ and thickness of $40 \mu\text{m}$ were cut. A diamond anvil cell (Almax easyLab) with Type IIa diamonds ($800 \mu\text{m}$ culet) was utilized to apply pressures up to 10 GPa. CuBe gaskets with a thickness of $60 \mu\text{m}$ and a hole of around $200 \mu\text{m}$ diameter were prepared for sample space. For pressure calibration, ruby spheres were used [165, 166]. CsI_3 was prepared as pressure-transmitting medium. In the investigated spectral range (0 to 12 GPa) this medium ensures a quasi-hydrostatic pressure, and can be used to obtain the reference spectra for transmittance measurements. For reflectance the CuBe gasket served as a reference. Reflectance spectra were subsequently corrected by the reflectance of CuBe. From transmittance data the optical absorption coefficient was calculated over the Beer-Lambert law: $\alpha = -\ln\{Tr\}/d$, where Tr is the transmittance and d is the sample thickness.

4.3 Sample preparation

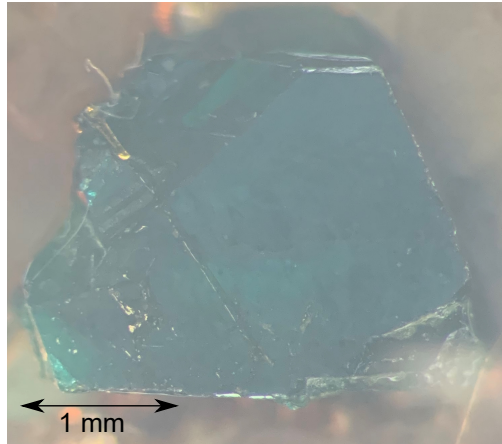


Figure 4.6: **Single crystals of $\text{ZnCu}_3(\text{OH})_6\text{Cl}_2$.** Picture of a polished single crystal (used for THz measurements) showing a large hexagonal surface (about 3×3 mm). Several batches were grown by P. Puphal and C. Krellner using a hydrothermal method.

The hydrothermal synthesis yields large samples with surfaces of approximately 3×3 mm, Fig. 4.6. Unlike Y-kapellasite (see next chapter) Herbertsmithite does not grow in high-symmetry directions, i.e., the facets are not well-defined cuts along kagome planes. Therefore, the crystals were oriented using Laue diffraction and polished on both sides to obtain smooth surfaces. However, a small out-of-plane contribution cannot be excluded.

4.4 QSL response: THz-TDS investigations of Herbertsmithite

Parts of this section are published in the author’s publication (Ref. [1], supplemental materials).¹

The transmitted time-domain electric fields ($\mathbf{E}_{THz} \parallel (a, b)$) are displayed in Fig. 4.7a. The entire time trace is confined to short time scales, below 5 ps, i.e., pronounced extended-time oscillations of the electric field are absent. Cooling to $T = 1.6$ K, it continuously increases without any significant changes of its shape. Fig. 4.7b shows the corresponding absorption coefficient α . At $T = 295$ K, the absorption coefficient is dominated by the tail of the lowest in-plane phonon mode (centered at around 85 cm^{-1} [193]). Focusing on the low temperature response, the phonon tail shifts to higher frequencies; leading to a monotonic response below 40 cm^{-1} at the lowest measured temperature. However, a small peak-like feature (35 cm^{-1}) evolves below $T = 50$ K, and further gains intensity reaching to $T = 1.6$ K. Comparing with the calculated phonon frequencies [193] and considering the weak intensity, a phononic origin seems unlikely. Furthermore, the first electronic transitions are only observed above 1 eV [192]. To this end, its origin remains unknown. To further quantify the low-energy response, IA was calculated (below 45 cm^{-1}), Fig. 4.7c. Upon lowering the temperature, IA decreases strongly until reaching $T = 100$ K. This is most likely caused by the contribution of the phonon tail (sharpening and shifting of the low-energy phonon modes upon cooling). At around $T = 50$ K, a minimum is reached, followed by a slight increase approaching $T = 40$ to 30 K. Below $T = 30$ K, IA remains nearly constant. Interestingly, the slight increase of IA has a similar temperature scale compared to the NMR results of Ref. [174] (onset of spin-singlet formation), suggesting an involvement of the spin degree of freedom. Overall, these observations are in stark contrast to the measurements on the distorted kagome lattice (Y-kapellasite), see next chapter.

¹Reprinted with permission from Ref. [1]. Copyright CC BY 4.0 (2022) by the authors. Advanced Quantum Technologies published by Wiley-VCH GmbH. Some passages have been taken verbatim, others are edited/ expanded. There will be no additional citation or other marks in the text for verbatim copied texts or edits from Ref. [1].

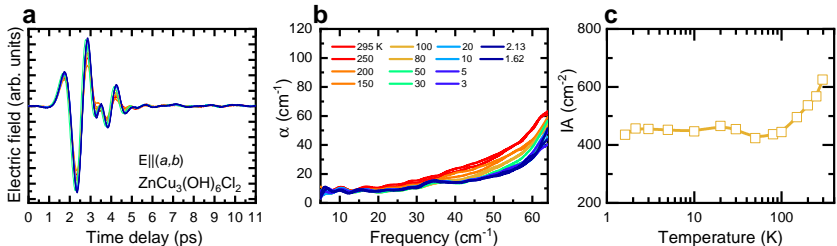


Figure 4.7: **THZ-TDS on $\text{ZnCu}_3(\text{OH})_6\text{Cl}_2$.** (a) Time-domain electric field and absorption coefficient for the in-plane $\mathbf{E} \parallel (a, b)$ (b) Corresponding absorption coefficient α . (c) Integrated absorption coefficient IA (up to 46 cm^{-1}) as a function of temperature. Reprinted with permission from Ref. [1].

As introduced above, a power-law response due to spinon absorption was suggested and previously reported for Herbertsmithite [16]. To compare to the previous report, the optical conductivity and spectral weight were calculated, assuming $\mu = 1$. Overall, the spectra show a quantitatively and qualitatively good agreement with the previous report (cf. magenta line in Fig. 4.8a). However, the small peak-like contribution (35 cm^{-1}) was not observed previously. The low-energy response can be further analyzed in the double-log plot, Fig. 4.8a. Here a power law of the form $\sigma_1 = a\omega^\beta$ (a and β are constants) appears as a straight line. Focusing on the $T = 1.6 \text{ K}$ spectrum, three distinct slopes in the optical conductivity can be seen: between 6 cm^{-1} and 20 cm^{-1} the conductivity is nearly frequency independent (the small spectroscopic features, i.e., oscillations at low frequencies, are due to the decreased signal-to-noise ratio in this spectral range). From 20 cm^{-1} , that is, the end of the data presented in Ref. [16], to 50 cm^{-1} the $T = 1.6 \text{ K}$ spectrum fits well to a power-law conductivity: $\sigma_1 = 0.00025 \text{ } \Omega^{-1} \omega^{1.47}$. Above 50 cm^{-1} , the slope changes again due to the phonon tail. To estimate the influence of a possible out-of-plane contribution, the spectral weight is compared to the previous study, Fig. 4.8b. While the c -axis response (Ref. [16]) decreases upon cooling and nearly vanishes below $T = 40 \text{ K}$, the in-plane spectral weight slightly increases at low temperatures. Even with the possibility of a c -axis contribution at room temperature in this study, the in-plane contribution is clearly distinguishable below $T = 100 \text{ K}$.

Having compared the present results with Ref. [16], by expanding the frequency range from 20 cm^{-1} to 6 cm^{-1} , it becomes clear that the power-law contribution does not extrapolate to zero frequency. This challenges the current interpretation towards a spinon-induced optical absorption. However, it could be that the optical response is gapped, $\Delta \approx 20 \text{ cm}^{-1}$ (2.5 meV, 29 K). Although the investigate frequency and temperature range has been expanded in this study, the small sample size (1.8 mm aperture size) is close to the diffraction limit at 6 cm^{-1} ($\lambda \approx 1.7 \text{ mm}$); the data were cut at 6 cm^{-1} . Here investigations on significant larger samples ($\approx 1 \text{ cm}^2$) at very low temperatures using more powerful terahertz sources might add valuable information in the future. From the local dynamic susceptibility (neutron structure factor, Fig. 4.3), it becomes clear that a least frequencies below 4 cm^{-1} and temperatures colder than $T = 1.5 \text{ K}$ need to be reached.

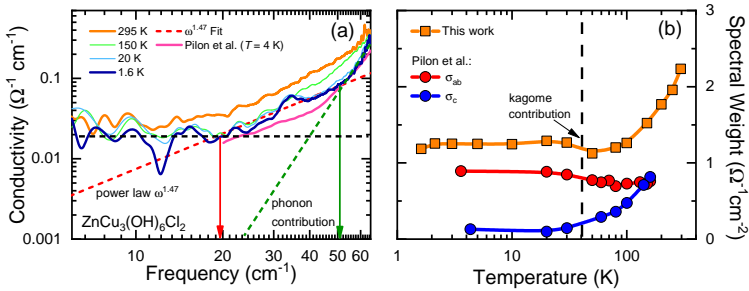


Figure 4.8: **THz-TDS on $\text{ZnCu}_3(\text{OH})_6\text{Cl}_2$.** (a) Optical conductivity σ_1 for selected temperatures. To compare with the previous results of Ref. [16], σ_1 was obtained from THz-TDS by assuming $\mu = 1$. In the double-log plot several contributions with distinct slopes are apparent. 6 cm^{-1} to 20 cm^{-1} : nearly frequency independent conductivity (c.f. black dashed line). 20 cm^{-1} to 50 cm^{-1} : power-law behavior ($\sigma_1 = 0.00025 \Omega^{-1} \omega^{1.47}$), see the fit (red dashed curve). Above 50 cm^{-1} : phonon tail (green dashed line). The $T = 4 \text{ K}$ spectrum of Ref. [16] is the magenta curve. (b) Optical spectral weight (integration of σ_1 over the frequency up to 46 cm^{-1}) of this work (orange curve) and Ref. [16] (red and blue curves, in-plane and out-of-plane conductivity, respectively). The out-of plane contribution diminishes upon cooling, while the in-plane response gains spectral weight.

4.5 Magneto-THz spectroscopy

To investigate any magnetic field dependence of the terahertz response, magneto THz-TDS was performed. Samples were probed in Voigt geometry [$\mathbf{E}_{THz} \parallel (a, b)$, $\mathbf{H} \parallel (a, b)$], see method section for more details. Fig. 4.9a displays the time-domain electric field at $T = 1.68$ K. The time-domain spectra do not show any significant modification up to $H = 8.3$ T. The corresponding absorption coefficient is shown in Fig. 4.9b. These observations are in accordance with Ref. [16]. Note that the small oscillations are spectroscopic features due to the decreased signal-to-noise ratio of a magneto-THz measurement. Considering the expected energy scales the absence of any change under magnetic field becomes clear: the magnetic field energy of $H = 8.3$ T corresponds to $\mu_B \cdot 8.3 \text{ T} \approx 0.48 \text{ meV}$. While this is larger than the thermal energy at $T = 1.68 \text{ K}$ ($\approx 0.14 \text{ meV}$), it is only 2.8 % of the magnetic exchange energy in Herbertsmithite ($J \approx 17 \text{ meV}$). Therefore, if there is no mechanism facilitating the breaking of putative spinons under external magnetic field or another strong coupling mechanism, for instance, due to paramagnetic/ impurity spins, no change is expected at low fields ($17 \text{ meV}/\mu_B \approx 294 \text{ T}$). In fact, the first 1/3 magnetization plateau (i.e., first spin flip in the kagome layer) was recently observed at $H \approx 150 \text{ T}$ for Herbertsmithite [201]. This sets the magnetic field scale for further investigations.

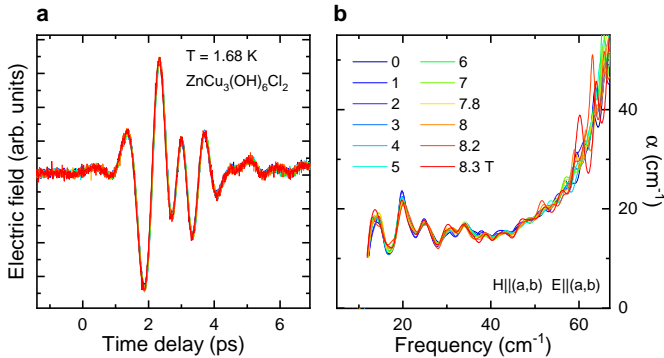


Figure 4.9: **Magneto-THz measurements of $\text{ZnCu}_3(\text{OH})_6\text{Cl}_2$.** Voigt geometry [$\mathbf{E}_{THz} \parallel (a, b)$, $\mathbf{H} \parallel (a, b)$] up to $H = 8.3$ T at $T = 1.68$ K. (a) Time-domain electric field and (b) absorption coefficient.

4.6 Pressure-dependent optical studies

In order to illuminate the structural aspect, pressure-dependent optical studies have been performed. Even for the thin samples (40 μm thickness), in transmittance some of the modes are saturated. Therefore, reflectance and transmittance were recorded in the mid-infrared range. The experimental details are summarized in the method section. Figs. 4.10a-c show the absorption coefficient obtained from transmittance measurements in in-plane direction [$\mathbf{E} \parallel (a, b)$]. Several phonon modes exhibit an interesting pressure dependence. Focusing on the far-infrared measurements [panel (a)], mode m_1 and m_2 undergo a redshift (decrease of center frequency) with increasing pressure. Furthermore, the modes at around 1500 cm^{-1} [panel (b)] show red-shifting and blue-shifting (increase of the center frequency) behavior. Mode m_9 (2900 cm^{-1}) shows a splitting between $P = 2.4$ GPa and 3 GPa. The phonons at around 950 cm^{-1} and 3400 cm^{-1} are saturated due to large absorption. Here additional information can be obtained from the reflectance, Figs. 4.10d,e. Especially the mode at around 950 cm^{-1} is distinct (cf. Fig. 4.10d). It broadens significantly above $P = 3$ GPa. These trends are further quantified in Fig. 4.11, phonon frequencies as a function of external pressure.

The out-of-plane measurements, Figs. 4.12a-e show a similar pressure dependence, with red-shifting and blue-shifting phonons and a splitting between $P = 2.4$ GPa and 3 GPa. In general, a red-shifting phonon mode is correlated with an increase of the bonding length (decrease of bonding force). At the first glance, such a pressure dependence is unexpected since hydrostatic pressure often results in a decrease the bonding length. Therefore, commonly a blueshift of phonons is observed. The different shifts are occurring even for phonons with a similar energy (around 1500 cm^{-1} , modes m_3, m_4, m_5), suggesting a complicated pressure evolution. Previously, the modes between 826 to 3201 cm^{-1} were assigned to OH vibrations [193]. Following such an assignment, the red- and blue-shifting behavior would indicate the distortion of the crystal field environment (CuO_4 tetrahedron) under pressure. This is in accordance with the monoclinic distortion observed in previous studies (Refs.[144, 200]). Furthermore, the small splitting between $P = 2.4$ GPa and 3 GPa (2900 cm^{-1} mode, m_9) fits to the pressure range, where the onset of $\sqrt{3} \times \sqrt{3}$ magnetic order ($T_N = 6$ K) was found ($P = 2.5$ GPa

[144]). The exact assignment of this mode based on literature remains difficult since only the reflectance of Herbertsmithite is reported so far (Refs. [191, 193]); the 2900 cm^{-1} mode was not observed in previous studies. However, the energy range at around 3000 cm^{-1} suggest the involvement of lighter atoms, for instance, O and H sites (see Ref. [193]) as well. A phonon splitting at such a lattice site could fit to the previously observed modifications of the octahedral coordination and variation of the crystal field environment [144].

Overall, the pressure-dependent optical study illustrates the tunability of the kagome lattice. It demonstrates that this lattice geometry is prone to structural distortion even at (unexpected) low pressures. Since magnetic and structural degrees of freedom are closely intertwined on the kagome lattice, abundant physics could emerge by increasing the structural distortion. However, considering the small sample sizes necessary in high-pressure measurements ($\sim 150\text{ }\mu\text{m}$) and the difficulty of focusing THz beams, pressure-dependent optical studies in this range are obscured by the diffraction limit (2 THz corresponds to $\lambda \approx 150\text{ }\mu\text{m}$) and remain elusive so far. Therefore, systems with varied degree of distortion are desired. Examples for such systems will be presented throughout the following chapters of this thesis.

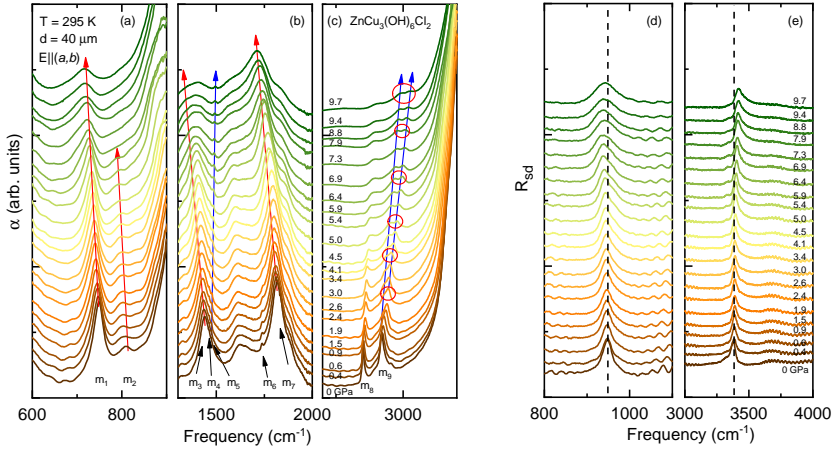


Figure 4.10: **Pressure-dependent optical spectra of $\text{ZnCu}_3(\text{OH})_6\text{Cl}_2$ [in-plane, $\mathbf{E} \parallel (\mathbf{a}, \mathbf{b})$].** The spectra are stacked. (a-c) Absorption coefficient for selected pressures at $T = 295$ K. Several phonon modes with an interesting pressure dependence are marked: m_1 to m_9 . With increasing pressure, red- and blue-shifting modes are observed (see the colored arrows). Between $P = 2.4$ GPa and 3 GPa mode m_9 (2900 cm^{-1}) shows a subtle splitting into two modes. (d,e) Reflectance at the sample-diamond interface R_{sd} . For spectral ranges with a large absorption phonon modes are saturated. Here, instead of the transmittance, reflectance can be used.

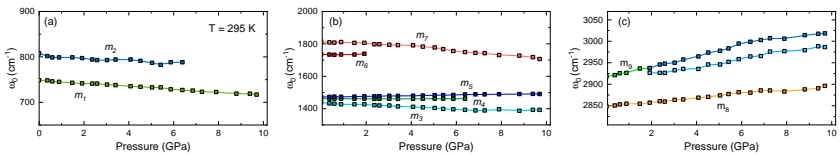


Figure 4.11: **Pressure dependence of selected phonon modes.** (a-c) Center frequencies ω_0 for selected in-plane modes. Some of the modes undergo a redshift, while others are blueshifting under pressure. Mode m_9 splits between $P = 2.4$ GPa and 3 GPa.

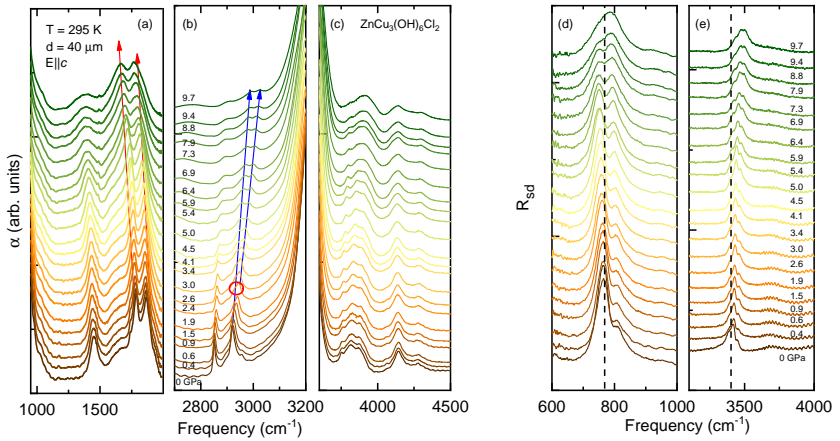


Figure 4.12: **Pressure-dependent optical spectra of $\text{ZnCu}_3(\text{OH})_6\text{Cl}_2$ [out-of-plane, $E \parallel (c)$].** The spectra are stacked. (a-c) Absorption coefficient for selected pressures at $T = 295$ K. (d,e) Reflectance at the sample-diamond interface R_{sd} . For spectral ranges with a large absorption phonon modes are saturated. Here, instead of the transmittance, reflectance can be used.

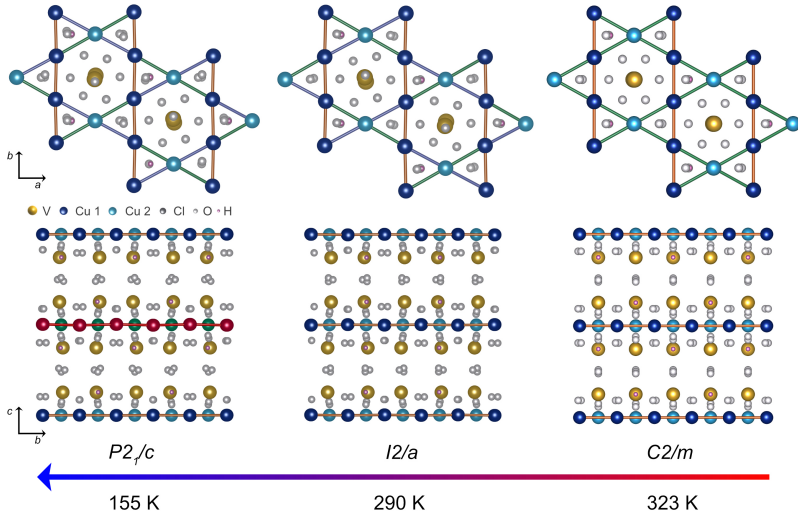


Figure 4.13: **Crystal structure of $\text{Cu}_3\text{V}_2\text{O}_7(\text{OH})_2 \cdot 2\text{H}_2\text{O}$.** Note the distinct crystallographic Cu sites (dark blue, light blue, and red spheres). The $C2/m$ structure at high temperatures undergoes a first order transition to $I2/a$ at $T = 290$ K. At around $T = 155$ K, a second-order transition takes place to $P2_1/c$. Pictures are based on the structures of Refs. [19, 20].

4.7 The slightly distorted case: experimental studies of Volborthite

Introducing crystallographic distortion on the kagome lattice, the magnetism can be altered. Different kind of distortions are possible. In general, even small changes in the Cu-Cu bond distances might result in distinct crystallographic Cu sites, heavily affecting the relevant exchange paths and eventually releasing frustration in favor of a dominating path. Such cases will be discussed in the later chapters. A more subtle distortion is the stretching or compression of the CuO_6 octahedron itself, which will be discussed now.

Volborthite ($\text{Cu}_3\text{V}_2\text{O}_7(\text{OH})_2 \cdot 2\text{H}_2\text{O}$) is particular in that it harbors two distinct Cu^{2+} sites: Cu(1) sits in between the edge-sharing Cu(2) chains. Fig. 4.13 illustrates the crystal motives found for different temperatures. Note that different structures are reported for the $T = 300$ K: $C2/m$ and $C2/c$, where the latter features even three distinct copper sites [20, 202]. The transition to $I2/a$ at around room temperature is first order succeeded by a second order transition to $P2_1/c$ at around 155 K [19, 20]. In $P2_1/c$ slightly modified kagome layers are present (see the red-colored spheres in Fig. 4.13). Overall, the Cu-O-Cu angle is different for the distinct Cu sites. However, crucial for the magnetism is that the Cu(1) O_6 octahedra are stretched towards the VO_4 tetrahedra at low temperatures. In this configuration an antiferromagnetic trimer phase is stabilized below $T_N = 1.4$ K [18, 19] by strong antiferromagnetic interaction ($J = 252$ K) via the Cu(1)-O-V-O-Cu(1) path, dominating the Cu(2)-O-Cu(2) exchange [203].

The magnetic properties of Volborthite are summarized in Fig. 4.14 based on Refs. [17, 18, 202]. At intermediate temperatures, the onset of magnetic short-range correlations was observed [17], indicated by an increase in susceptibility/ deviation from Curie-Weiss law below $T^* \approx 60$ K with a broad maximum centered at around $T_p = 18$ K (cf. Fig. 4.14a and Fig. 4.14b). At this temperature, there is no lambda-like feature in specific heat (Fig. 4.14b), indicating the absence of spin freezing. Only below $T_N = 1.4$ K, the antiferromagnetic trimers form via the Cu(1)-O-V-O-Cu(1) path, Fig. 4.14c [18, 19]. They are interacting over competing ferromagnetic ($J_1 = -34.9$ K) and antiferromagnetic ($J_2 =$

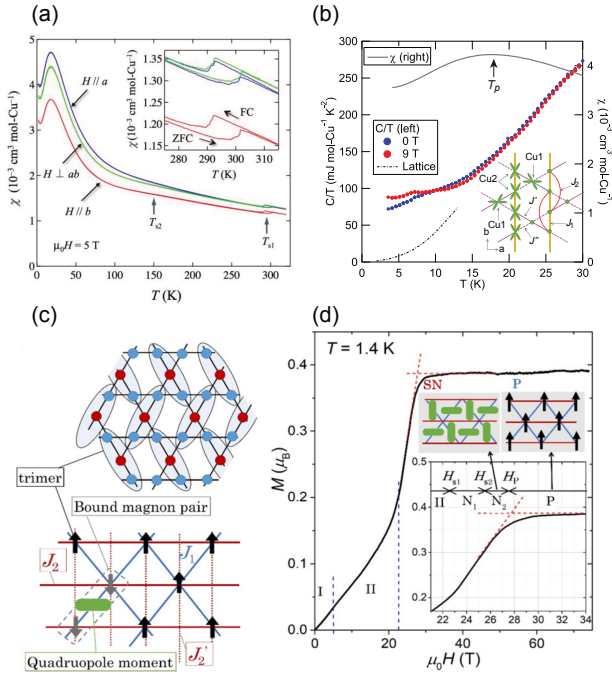


Figure 4.14: **Magnetic properties of $\text{Cu}_3\text{V}_2\text{O}_7(\text{OH})_2 \cdot 2\text{H}_2\text{O}$** (Refs. [17, 18, 202]) (a) Magnetic susceptibility for different crystallographic orientations under field-cooling (FC) and zero-field cooling (ZFC) at a field of 5 T. The structural transitions are indicated by T_{s1} and T_{s2} . Upon cooling an increase of susceptibility was observed, resulting in a peak-like contribution below 30 K. This is attributed to the magnetic short-range order. (b) Specific heat (left axis) and susceptibility (right axis) below 30 K. The broad contribution in susceptibility is centered at $T_p = 18$ K. Here no indications of spin freezing can be seen in specific heat. (c) Sketch of the magnetic trimer state ($T_N = 1.4$ K). The trimers can be mapped on an effective square lattice of $S_{\text{eff}} = 1/2$ spins (black arrows). Under external magnetic field the S_{eff} spins can be flipped ($S_{\text{eff}} = -1/2$): condensation of bound magnon pairs (see dashed gray area). For each pair a quadrupole moment can be assigned (green bar). (d) Magnetization curve with several regimes: (I) Unknown low-field phase (II) incommensurate spin-density wave (SDW). Over 30 T a broad magnetization plateau is observed (c.f. inset), corresponding to the full polarization of the S_{eff} spins. Approaching the magnetization plateau two magnetic phases, N_1 and N_2 can be distinguished. N_2 is identified as a spin nematic (SN) phase. Adapted with permission from Ref. [202] (panel a - Copyright 2019 American Chemical Society), Ref. [17] (panel b), Ref. [18] (panels c,d).

36.5 K) exchange [203]. Magnetization measurements (Fig. 4.14d) show an unknown intermediate phase under magnetic field and an incommensurate spin-density wave ($4.5 \text{ T} < H < 22.5 \text{ T}$) [18, 19]. Further increasing the field, bound magnons (essentially pairs of trimers, exhibiting an effective quadrupole moment) start to condense. This phase was discussed in terms of a spin nematicity. For fields over 27.5 T, a broad plateau between 0.3 and 0.4 μ_B was observed, indicating the full polarization [18].

4.7.1 Structural and electronic aspects

FTIR spectroscopy was performed in order to illuminate structural and electronic aspects. Fig. 4.15 and Fig. 4.16 show the optical conductivity in the FIR range along the in-plane principal axes. Comparing the phonons over the measured temperature range, the structural transitions can be clearly recognized. Some of the stronger modes (for instance, around 200, 450, 550 cm^{-1} in Fig. 4.15) are persisting from room temperature down to $T = 3.2 \text{ K}$. However, many new modes are evolving upon cooling [cf. panels (a-b)]. Especially at low frequencies 80 cm^{-1} to 120 cm^{-1} , a pronounced set of sharp modes is emerging in the low-temperature structure, below $T = 150 \text{ K}$ (see panel (c) in Fig. 4.15), indicating a redistribution of the electric dipole moment.

Fig. 4.17a shows the electronic contributions at high energies. Around 20000 cm^{-1} the onset of the optical gap can be seen: strong increase of the absorption coefficient. Inside the gap (9000 to 17000 cm^{-1}), weaker electronic transitions appear. At $T = 320 \text{ K}$ only one broad transition is resolved; at lower temperatures (cf. $T = 10 \text{ K}$) three peak-like structures can be distinguished. A comparison with the electronic transitions of Herbertsmithite and Y-kapellasite gives information about the origin of the these. Herbertsmithite and Y-kapellasite are characterized by the onset of a charge gap (transfer of one oxygen p -electron to the copper $d_{x^2-y^2}$ orbital) at around 25000 cm^{-1} [192], slightly higher than in the present case. Furthermore, local $d-d$ transitions were observed (Fig 4.17b, see Ref. [192]) around 11500 cm^{-1} . These electronic properties explain the blue color of the crystals. On the other hand, the green color of Volborthite is caused by a shift of the gap towards lower energies (18000 cm^{-1} equals 555 nm). Fig 4.17c displays the crystal field splitting for Cu 3d⁹ in the center of the O₆ octahedron (see Ref. [205] for further

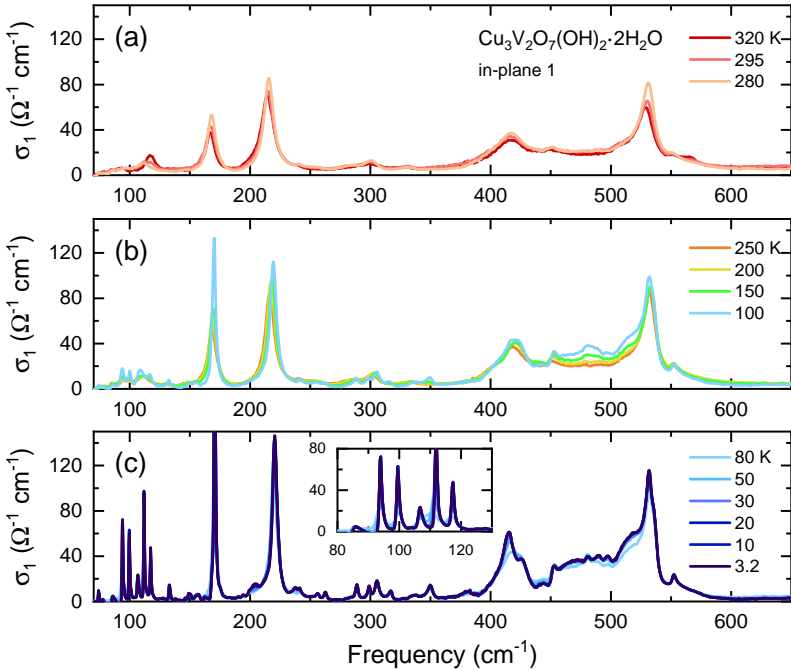


Figure 4.15: **Optical conductivity of $\text{Cu}_3\text{V}_2\text{O}_7(\text{OH})_2 \cdot 2\text{H}_2\text{O}$ in the FIR range (in-plane, principal axis 1).** (a) First-order structural transition $C2/m$ to $I2/a$ at $T = 290$ K. (b) $I2/a$ structure below $T = 290$ K and second-order structural transition $I2/a$ to $P2_1/c$ around $T = 155$ K. (c) Low-temperature structure, $P2_1/c$. Data recorded with the help of T. Zeh [204].

details). For elongation (compression) of the O_6 octahedron, d -orbitals with a z -contribution decrease (increase) in energy. For the case of Herbertsmithite/ Y-kapellasite such a distortion is comparably weak: the t_{2g} orbitals are close in energy. Here two transitions were observed: from d_{xy}, d_{xz}, d_{yz} to $d_{x^2-y^2}$ and from d_z^2 to $d_{x^2-y^2}$ [192]. In the case of Volborthite distortion of the CuO_6 octahedron is strong [203]. This explains the three peak structure between 9000 to 17000 cm^{-1} at $T = 10$ K: t_{2g} levels are more separated. However, at $T = 320$ K only one broad peak is observed. This is in contrast to the results of Ref. [192], where the two peaks are separated even at room temperature. Additional broadness

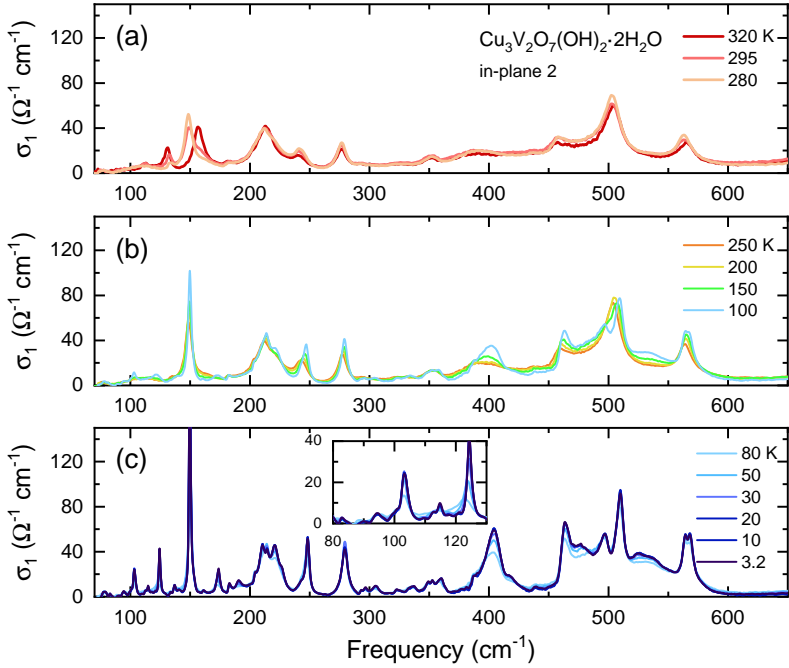


Figure 4.16: **Optical conductivity of $\text{Cu}_3\text{V}_2\text{O}_7(\text{OH})_2 \cdot 2\text{H}_2\text{O}$ in the FIR range (in-plane, principal axis 2).** (a) First-order structural transition $C2/m$ to $I2/a$ at $T = 290$ K. (b) $I2/a$ structure below $T = 290$ K and second-order structural transition $I2/a$ to $P2_1/c$ around $T = 155$ K. (c) Low-temperature structure, $P2_1/c$. Data recorded with the help of T. Zeh [204].

might be related to the unique orbital switching transitions observed in Volborthite, see Fig 4.18 [20]. In the high-temperature structure Cu1 possess an unpaired electron in d_z^2 (Cu2 is of $d_{x^2-y^2}$ type). Therefore, many transitions in a similar energy rang might cause the broadness of the high temperature peak-like contribution. At low temperatures, the distortion of the ligands promotes the $d_{x^2-y^2}$ for Cu1 as well. Here the electronic structure might be simpler, as illustrated in Fig 4.17c.

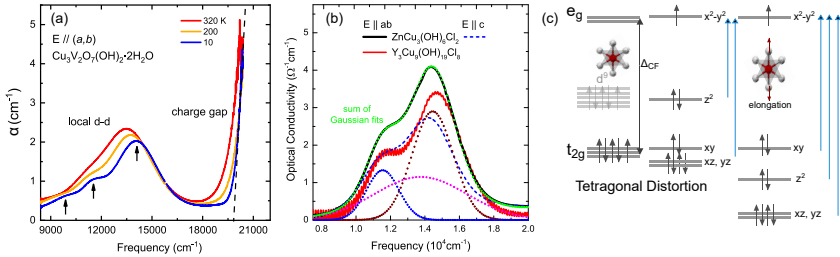


Figure 4.17: **Electronic properties of the kagome lattice.** (a) Measurements of the absorption coefficient α of Volborthite. The compound shows the onset of an optical gap at around 20000 cm^{-1} and electronic transitions (likely local $d-d$ transitions) between 9000 and 17000 cm^{-1} . At 10 K three transitions are distinguishable. Data recorded with the help of T. Zeh [204]. (b) Local $d-d$ transitions in Herbertsmithite and Y-kapellasite at a similar energy range (300 K measurements). Here only two transitions are resolved. Adapted with permission from Ref. [192]. Copyrighted by the American Physical Society. (c) Crystal field splitting with tetragonal distortion, based on Ref. [205]. Under elongation of the CuO_6 cage, d -orbitals with z contribution will decrease their energy. Small black arrows: electron population. For a slight distortion of the CuO_6 octahedron (the case of Herbertsmithite and Y-kapellasite) only two transitions (blue arrows) are resolved in the optical spectra: the degeneracy of t_{2g} is only slightly lifted. For a strong distortion, three transitions can be observed due to the clear separation of the d -orbitals in energy: three peaks in (a).

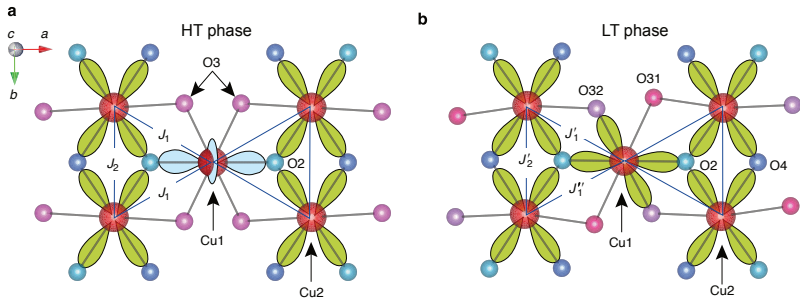


Figure 4.18: **Orbital switching transition in $\text{Cu}_3\text{V}_2\text{O}_7(\text{OH})_2 \cdot 2\text{H}_2\text{O}$ (Ref. [20]).** (a) In the high-temperature phase Cu1 has one unpaired electron in the d_{z^2} orbital. At the Cu2 site one unpaired electron sits in $d_{x^2-y^2}$. (b) At low temperatures, distortion (elongation) of the Cu1O_6 octahedron lowers the energy of d_{z^2} , resulting in an unpaired electron in $d_{x^2-y^2}$: Orbital switching transition. Adapted by permission from Springer Nature Customer Service Centre GmbH: Springer Nature, Nature Communications, Ref. [20] Copyright 2012.

4.7.2 Short-range magnetic correlations probed by THz-TDS

Having analyzed the electronic and structural properties, now the magnetic degree of freedom is going to be considered. Fig. 4.19 displays the THz-TDS spectra, electric field [panels (a,b)] and resulting absorption coefficient α [panels (c,d)]. For both in-plane axes, at room temperature several broader contribution (widths of 5 to 10 cm^{-1} for axis 1, 30 cm^{-1} for axis 2) are observed on the tail of the far-infrared phonons. Comparing with the the electric field (selecting different cut offs for the FFT apodization) it becomes clear that these features are encoded in the main pulse, that is, oscillations below 4 ps. Most likely they are weak phonon contributions. Upon cooling, the main pulse is not significantly affected by temperature. Starting from 50 to 20 K, several weak oscillation components are impose on the signal at times above 4 ps. These result in the sharp features in the THz spectrum, between 70 and 100 cm^{-1} . Integrating the THz response, IA in the insets of Figs. 4.19c,d is obtained (see method section for further information). In the vicinity of the structural transition temperatures, IA exhibits kink-like responses

for both axes. At around $T = 30$ K, together with the onset of magnetic short-range correlations, an increase in IA with a maximum between 10 K and 20 K is observed. It corresponds to the maximum in susceptibility ($T_p = 18$ K) [17]. This correlations of the temperature ranges indicates a magnetic origin of the sharp features, i.e., magnetic resonances. However, they are not well distinguishable from the phonons, as for instance, in Averievite (see Ch. 6). Furthermore, a coupling of phonons and magnetic degree of freedom, as observed for Herbertsmithite or Y-kapellasite is possible. A better data quality could provide more insight. Here the synthesis of larger single crystals (the spectra a recorded with apertures of only about 2 mm diameter) is necessary, but this is beyond the scope of the present thesis. With larger crystals magneto-THz investigations could be performed as well, shading light on the origin of these sharp features.

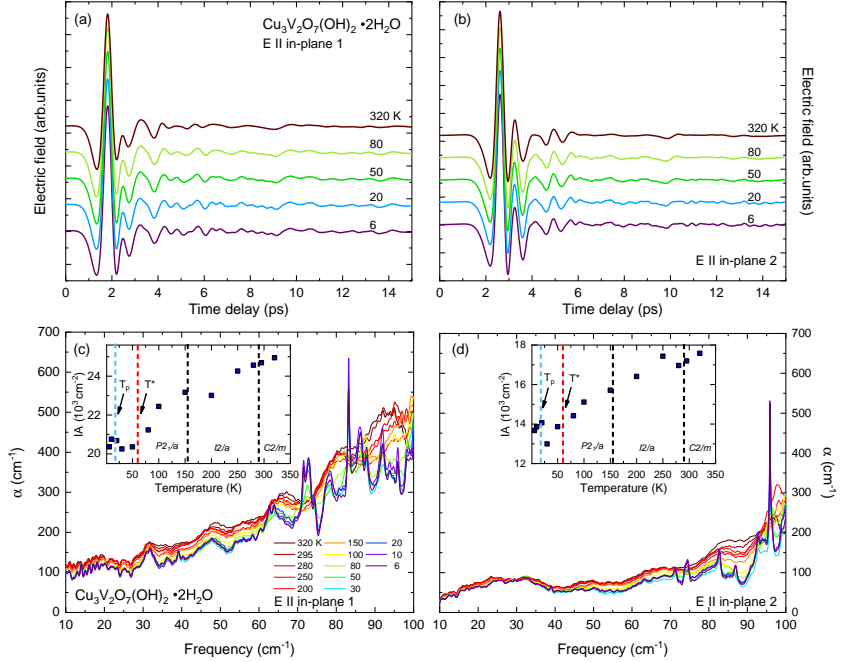


Figure 4.19: **THz-TDS measurements of $\text{Cu}_3\text{V}_2\text{O}_7(\text{OH})_2 \cdot 2\text{H}_2\text{O}$.** (a,b) Electric field as a function of time delay for selected temperatures and both axes. Main pulse: below 4 ps, containing the phononic response. Upon cooling small oscillations are imposed on the spectra above 4 ps. The main pulse is not significantly changed by lowering the temperature. (c,d) Resulting absorption coefficient α . Insets: integrated absorption coefficient IA . Several characteristic temperatures are highlighted by dashed lines $T = 280$ K, $T = 155$ K: structural transitions, $T^* \approx 60$ K onset of short range magnetic correlations. $T_p = 18$ K: Maximum in static magnetic susceptibility. Data recorded by M. Benke and A.-C. Oeter in a Blockpraktikum under supervision of T. Biesner with the help of T. Zeh. First presented in Ref. [204].

4.8 Conclusion and outlook

In this chapter the compounds Herbertsmithite and Volborthite have been investigated. Herbertsmithite hosts a putative QSL ground state on the undistorted kagome lattice. THz-TDS spectroscopy has been used to investigate possible excitations, including the theoretically suggested power-law response of a gapless spinon Fermi surface, i.e., $U(1)$ QSL [14, 15]. Corroborating the previous report [16], a power-law optical conductivity with an exponent of $\beta = 1.47$ has been found down to a frequency of 20 cm^{-1} . However, by expanding the frequency- and temperature range of the previous report (20 cm^{-1} and 4 K) to 6 cm^{-1} and 1.62 K , respectively, a clear deviation from the power-law behavior has been observed below 20 cm^{-1} . This is in contradiction with a gapless picture. A possible spin gap: 2.5 meV or 29 K , extracted from the optical response would be large, considering that NMR studies claim a spin gap on the order of 10 K [185] (cf. 12.1 K of κ -(BEDT-TTF) $_2$ Cu $_2$ (CN) $_3$ [8]). Furthermore, a spin gap was not observed in the neutron scattering experiments [13, 194]. Comparing with the neutron scattering data, it might be that the response in the accessible THz range is not induced by spinons, but has other origin. Here it is worth to note that the temperature scale of the formation of spin singlets at 30 K with spatially varying gaps (Ref. [174]), matches remarkably well with the increase of spectral weight/ IA in the THz data. Measurements below 4 cm^{-1} and 1.5 K , that is, when the $\chi''(\omega)$ increases (cf. Fig. 4.3), might allow further conclusions. Such measurements, requiring significant larger crystal sizes, more powerful terahertz sources, and sophisticated optical cryostats, remain as a challenge for further studies.

Volborthite has been introduced as an example of a weakly distorted kagome lattice. It features a trimer ground state below $T_N = 1.4 \text{ K}$ and a wide area of magnetic short-range correlations at intermediate temperatures [17–19, 202]. Together with the maximum in the susceptibility ($T_p = 18 \text{ K}$), a kink in the integrated absorption coefficient IA has been observed. In the THz range, several sharp features at these temperatures, with a possible magnetic origin have been identified. However, here additional measurements on larger single crystals and under external magnetic field are necessary to verify this interpretation. Nevertheless, by increasing the structural distortion (cf. featureless response of Herbertsmithite),

short-range magnetic correlations can be probed with THz-TDS.

5 Results II: Y-kapellasite

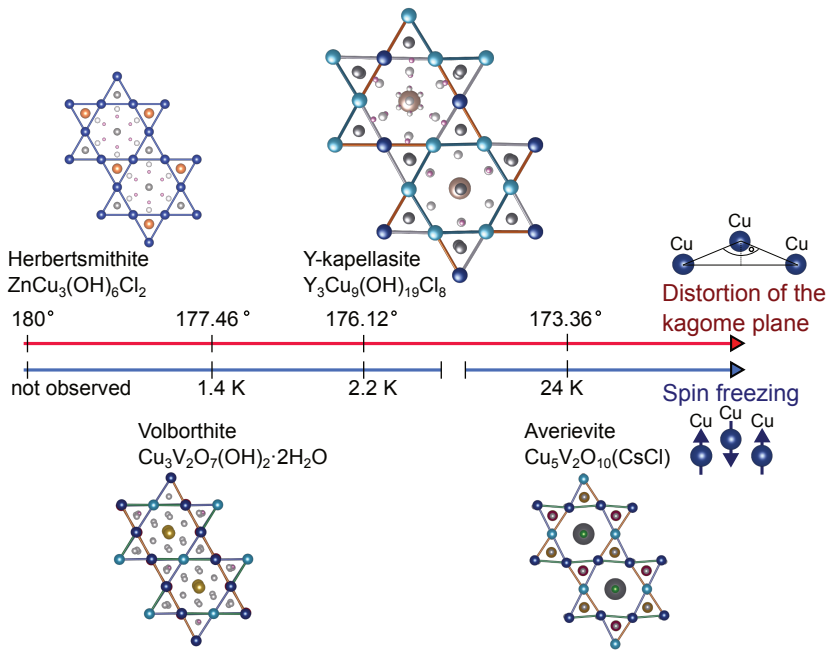


Figure 5.1: **Structural distortion and spin freezing on the kagome lattice.** Structures are based on Refs. [19, 21, 23, 42].

This chapter is a modified version of the author's publication (Ref. [1], main text and supplemental materials).¹

In this chapter research on the quantum magnet Y-kapellasite ($\text{Y}_3\text{Cu}_9(\text{OH})_{19}\text{Cl}_8$) [21] is going to be reported. Y-kapellasite serves as an example for a distorted kagome system, Fig. 5.1. The focus will be on the (magneto) THz-TDS, unveiling continuum-like excitations at THz frequencies. Together with theoretical calculations a possible picture for these is given: multi-center magnons. It will be shown that multi-center magnons yield information about the full magnetic Brillouin zone (BZ) although the THz light is conventionally believed to only probe the center of BZ. Additional experiments, probing the static magnetic responses, are going to be shown. Furthermore, structural aspect will be discussed with pressure- and temperature-dependent FTIR and XRD experiments.

Abstract: Due to the small photon momentum, optical spectroscopy commonly probes magnetic excitations only at the center of the Brillouin

¹"Multi-Center Magnon Excitations Open the Entire Brillouin Zone to Terahertz Magnetometry of Quantum Magnets", *Adv. Quantum Technol.* **5**, 2200023 (2022)

co-authored with Seulki Roh, Aleksandar Razpopov, Jannis Willwater, Stefan Süllow, Ying Li, Katharina M. Zoch, Marisa Medarde, Jürgen Nuss, Denis Gorbunov, Yurii Skourski, Andrej Pustogow, Stuart E. Brown, Cornelius Krellner, Roser Valentí, Pascal Puphal, Martin Dressel.

Reprinted with permission from Ref. [1]. Copyright CC BY 4.0 (2022) by the authors. Advanced Quantum Technologies published by Wiley-VCH GmbH. Some passages have been taken verbatim, others are edited/ expanded. There will be no additional citation or other marks in the text for verbatim copied texts or edits from Ref. [1].

Author contributions: These authors contributed equally: T.B. and S.R.

T.B., S.R. performed the spectroscopic measurements (THz/ ESR) and analyzed the data. P.P., K.M.Z, C.K. grew the crystals. P.P., J.W., S.S., D.G., Y.S., M.M. performed the magnetic characterization. J.N. performed the structural characterization. A.P., S.E.B. did the NMR measurements. A.R. performed the LSWT analysis. Y.L. calculated the phonon dispersion. T.B. performed the FTIR measurements and A.P. contributed the high-energy extrapolation. T.B., S.R., P.P. wrote the manuscript with input from all authors. P.P., T.B., S.R. initiated the project. M.D. and R.V. supervised the project.

Additional material in this chapter: Pressure-dependent optical measurements were performed in Synchrotron Soleil on SMIS 2, proposal 20201579, by Tobias Biesner (main proposer), Seulki Roh (co-proposer), Jens Jakschik, Guratinder Kaur, Francesco Capitani (local contact). Pressure-dependent single crystal x-ray diffraction was performed in ESRF on ID27 by Tobias Biesner, Pascal Puphal, Björn Wehinger (local contact). A manuscript reporting these results is in preparation.

zone; however, there are ways to override this restriction. In the case of the distorted kagome quantum magnet Y-kapellasite, $\text{Y}_3\text{Cu}_9(\text{OH})_{19}\text{Cl}_8$, under scrutiny here, the magnon density of states can be accessed over the entire Brillouin zone through three-center magnon excitations. This mechanism is aided by the three different magnetic sublattices and strong short-range correlations in the distorted kagome lattice. The results of THz time-domain experiments agree remarkably well with linear spin-wave theory. Relaxing the conventional zone-center constraint of photons gives a new aspect to probe magnetism in matter.

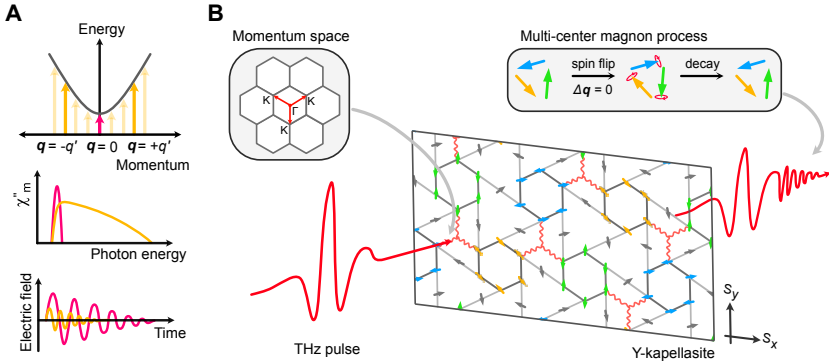


Figure 5.2: **Three-center magnon process in Y-kapellasite.** (a) Comparison between the one-magnon (red) and two-center magnon absorption (yellow). The top panel describes the excitations in the spin dispersion curve. While the one-magnon excitation only takes place near the zone center ($q \approx 0$), the two-center magnon excitations can extend over the entire Brillouin zone ($\Delta q \approx 0$ excitation). Here, the summed momenta of the participating magnons need to vanish, $0 \approx \sum_n q_n$, to ensure momentum conservation. The middle and bottom panel show the corresponding response in energy/ frequency-dependent magnetic susceptibility χ''_m and electric field as a function of time, respectively. A one-magnon excitation shows a sharp peak in χ''_m , due to comparably long lifetimes (20-40 ps). A multi-center magnon process, however, is restricted to shorter time scales, correlated with a broad, continuum-like feature in χ''_m . (b) Schematics of three-center magnon absorption in Y-kapellasite and calculated ground state, $\mathbf{Q} = (1/3, 1/3)$. The simultaneous magnetic absorption occurs through three different magnetic sublattices (green, blue, and yellow hexagons in real space). The excited spin waves fall back to the initial state via a free induction decay resulting in oscillations of the outgoing THz pulse at extended time. Reprinted with permission from Ref. [1].

5.1 Introduction of the material

Y-kapellasite has attracted attention recently due to its intriguing magnetic ground state ($T_N = 2.2$ K), suggested in Fig. 5.2b [7]. Here, the magnetic supercell is comprised of three hexagons rotated by 120° . Due to the three possible arrangements, each hexagon is defined as a magnetic sublattice and is given one of the colors: green, blue, or yellow. In Y-kapellasite, a distorted kagome lattice is formed by two distinct Cu sites, as depicted in Fig. 5.3a. The magnetic superexchange is governed along three different Cu-O-Cu paths with nearest-neighbor couplings of $J = 154.4$ K, $J_\square = 134.2$ K, and $J' = 8.7$ K [7, 21] (see appendix of this chapter for further information, Fig. 5.31). The distorted kagome planes stack along the c -direction (Fig. 5.3b). Strong short-range magnetic correlations and persistent spin dynamics below the ordering temperature (down to $T = 20$ mK) were reported previously [21, 22]. In this thesis, the THz transmission of Y-kapellasite was measured over a wide temperature and magnetic field range. At low temperatures ($T < 30$ K), magnetically active, continuum-like excitations were found decaying through oscillations of the transient electric field during an extended time period of around 5 ps. By comparison to the linear spin-wave theory, it is concluded that the THz χ_m'' encodes the spin (magnon) density of states (SDOS) through a multi-center magnon absorption (Fig. 5.2a), three-center magnon, augmented by the distinct magnetic ground state of Y-kapellasite, as described in Fig. 5.2b. THz magnetometry via multi-center magnon absorption is proposed as a method to overcome the conventional zone-center restriction providing access to magnetism over the entire Brillouin zone.

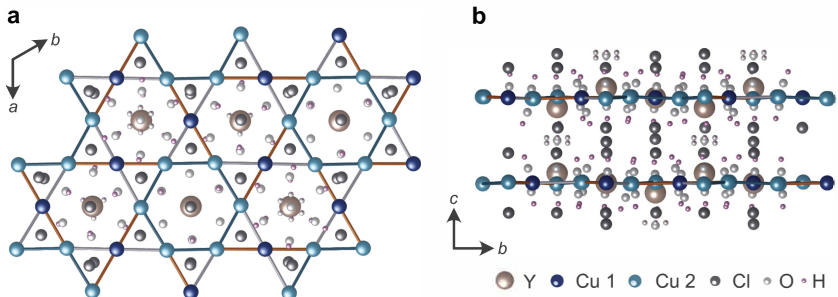


Figure 5.3: **Crystal structure of Y-kapellasite ($T = 173$ K).** (a) In-plane, (a, b) -direction and (b) out-of-plane (c -axis) crystal structure. Different copper sites, inducing the distorted kagome bonds (blue, red, grey) are depicted in cyan and dark blue. Adapted with permission from Ref. [1].

5.2 Experimental methods

Crystal growth and characterization Crystals were grown via a horizontal external gradient growth method. This optimized synthesis leads to nearly perfect defect-free single crystals with large facets (kagome-planes between 2 and 3 mm and thickness of around 0.5-1 mm, see below). The results of X-ray diffraction are presented below.

THz-TDS measurements THz time-domain spectroscopy (THz-TDS) measures the time-dependent electric field [58]. Through a Fast Fourier Transformation (FFT), intensity and phase can be obtained. This allows to directly calculate the optical response functions [81, 82]. A typical time-trace of the transient electric field shows an oscillating behavior with a strong pulse at early times (main pulse). Due to their short lifetime, electronic transitions or phononic resonances are, in general, contained in the main pulse. However, phenomena with a longer lifetime, such as magnetic resonances, can extend to longer times (over several tens of ps), exceeding the main pulse [67–69, 92, 93].

THz-TDS measurements were carried out in transmission geometry on oriented single crystals [$\mathbf{E}_{THz} \parallel (a, b)$] at several temperatures between 295 and 1.6 K with a helium bath cryostat. Magneto-optical THz measurements were performed in Faraday geometry [$\mathbf{E}_{THz} \parallel (a, b)$, $\mathbf{H} \parallel c$] with static magnetic field strengths up to $H = 10$ T and temperatures down to 1.7 K. The absorption coefficient α was calculated from the transmittance Tr by $\alpha = -\ln\{Tr\}/d$, where d is the sample thickness. The integrated absorption coefficient $IA = \int \alpha d\omega$ resembles the optical spectral weight and provides a quantitative access to the spectral features. The frequency-dependent magnetic susceptibility $\chi_m'' = \text{Im}\{\tilde{\chi}_m(\omega)\}$ was calculated by referencing to the high-temperature dielectric response [46, 51, 89, 173], i.e., the $T = 80$ K spectrum, see Sec. 3.2.3 for further information. This quantity encodes the SDOS, as previously shown for the $\mathbf{q} \approx 0$ case [51].

FTIR measurements For reflectance measurements samples with large facets (kagome-planes between 2 and 3 mm and thickness of around 0.5-1 mm) were used. Infrared-measurements in the far-infrared spectral range

were performed in reflection geometry [near-normal incidence, $E \parallel (a, b)$, $E \parallel (c)$], using a Bruker 113v FTIR spectrometer equipped with an *in-situ* gold evaporation unit and LiHe-flow cryostat. For the mid-infrared up to 20000 cm^{-1} a Bruker Vertex 80v together with a Hyperion infrared microscope is utilized. Measurements over the accessible spectral range were successively carried out using MCT, InSb, and Si detectors. The spectra were referenced against a gold mirror. Data are corrected by the mirror reflectance. A Kramers-Kronig transformation was used to obtain the optical conductivity, σ_1 [81, 82].

Pressure-dependent measurements Pressure-dependent transmittance spectra [near-normal incidence, $E \parallel (a, b)$] were recorded at the SMIS 2 beamline (Synchrotron Soleil, France) using the Horizontal microscope together with a ThermoFisher FTIR spectrometer. For pressure-dependent measurement pieces with a typical in-plane size of $160 \times 160 \mu\text{m}$ and thickness of $20 \mu\text{m}$ were cut. A membrane diamond anvil cell (DAC) with Type IIa diamonds ($800 \mu\text{m}$ culet) loaded in a LiHe-flow cryostat was utilized to apply pressures at variable temperatures (isotherms). Stainless steel gaskets with a thickness of $60 \mu\text{m}$ and a hole of around $200 \mu\text{m}$ were prepared for sample space. Ruby spheres were used for pressure calibration [165, 166]. In the far-infrared polyethylene was prepared as a pressure transmitting medium, whereas for the mid-infrared measurements NaCl was utilized. In the investigated spectral range (0 to 12 GPa) these ensure quasi-hydrostatic pressure and can be used to obtain the reference spectra. From transmittance data the optical absorption coefficient was calculated via the Beer-Lambert law: $\alpha = -\frac{1}{d} \ln \{Tr\}$, where Tr is the transmittance and d is the sample thickness.

Pressure-dependent single crystal x-ray diffraction was performed at the ID27 beamline (ESRF, France). A membrane diamond anvil cell was loaded with small sample pieces (in-plane sizes of about $10 \times 10 \mu\text{m}$ and thickness of a few μm). The culet size was $500 \mu\text{m}$. For sample compartment a stainless steel gasket with a thickness of $100 \mu\text{m}$ and a hole of $280 \mu\text{m}$ was utilized. He gas served as quasi hydrostatic pressure medium (39 bar gas loading pressure). The cell was rotated from -32° to 32° (opening angle of the DAC is 64°), while keeping the sample in center of rotation to collect sufficient amount of x-ray reflexes. EIGER2 X CdTe

9M served as detector. Data were analyzed using CrysAlis (Rigaku) and Olex2 (OlexSys).

ESR measurements Temperature-dependent electron spin resonance (ESR) measurements in the X-band frequency were carried out employing a Bruker EMXplus spectrometer equipped with a LiHe-flow cryostat (Oxford Instruments, ESR 900). The in-plane response was determined with a microwave field $\mathbf{h} \parallel c$ and external magnetic field $\mathbf{H} \parallel (a, b)$.

NMR characterization Nuclear magnetic resonance (^1H -NMR) experiments were performed on a $3 \times 3 \times 1 \text{ mm}^3$ sized Y-kapellasite single crystal with magnetic field ($H = 0.98 \text{ T}$) aligned parallel to the kagome layers [$\mathbf{H} \parallel (a, b)$]. The spin-lattice relaxation rate $1/T_1$ was measured by non-selective excitation of the full line. $1/T_1$ was determined through saturation-recovery using single-exponential fits. Temperature control in the range from 4 to 200 K was achieved using a ^4He cryostat with a variable-temperature insert.

High-field magnetization The high-field magnetization was determined between $T = 0.5$ and 30 K in pulsed magnetic fields up to 55 T for in-plane and out-of-plane orientations. Measurements were performed at the high field laboratory in Dresden, Germany (HLD-EMFL).

DFT and LSWT calculations The phonon frequencies were calculated using a combination of the PHONOPY package [206, 207] and Density Functional Theory (DFT) as implemented in the Vienna Ab-Initio Simulation Package (VASP) code [208–210]. The magnon dispersion was determined by using linear spin-wave theory (LSWT) as implemented in SpinW 3.0 [211].

5.3 Sample growth and structural characterization

In the following the single-crystal growth of Y-kapellasite ($\text{Y}_3\text{Cu}_9(\text{OH})_{19}\text{Cl}_8$) and the structural characterization are described. The crystal growth of Y-kapellasite was originally reported in Ref. [21], where 0.59 g Y_2O_3 , 0.82 g CuO, and 0.89 g $\text{CuCl}_2 \cdot 2(\text{H}_2\text{O})$ were heated up in 10 ml H_2O to the dissolution point of Y_2O_3 , followed by a slow cooling to crystallize (sketched in Fig. 5.4a). However, these crystals suffered from small CuO inclusions since the growth takes place on the surface of the polycrystalline CuO starting material. Furthermore, the average size of $1 \times 1 \times 1 \text{ mm}^3$ was not suitable for optical spectroscopy in the THz range. Thus the synthesis was optimized via a horizontal external gradient growth method in a thick-walled quartz ampule by slowly dissolving CuO in a $\text{YCl}_3\text{-H}_2\text{O}$ solution and transporting it to the cold end as depicted in Fig. 5.4b. Here, the inclusion free hexagonal single crystals had an average size of $3 \times 3 \times 1 \text{ mm}^3$ up to $3 \times 3 \times 3 \text{ mm}^3$. The pictures of a single crystalline Y-kapellasite are displayed in Fig. 5.4c and d, which show in the given thickness a transparent specimen without any visible impurity inclusions.

The structure of $\text{Y}_3\text{Cu}_9(\text{OH})_{19}\text{Cl}_8$ was reported in Ref. [21], while for deuterated powder samples a different result was found in Ref. [22]. Here, in contrast to the single crystal structure, the O1 site has no deuterium leading to the stoichiometry of $\text{Y}_3\text{Cu}_9(\text{OD})_{18}\text{OCl}_8$. As well, a recent report described a synthesis of inclusion free crystals using LiOH, $\text{Y}(\text{NO}_3)_3 \cdot 6\text{H}_2\text{O}$ and $\text{CuCl}_2 \cdot 2\text{H}_2\text{O}$ with another slightly different structure, where a partial occupation of Y in the kagome plane is present [212]. This likely is a phase mixture with $\text{YCu}_3(\text{OH})_6\text{Cl}_3$ leading to a magnetic transition around 11 K.

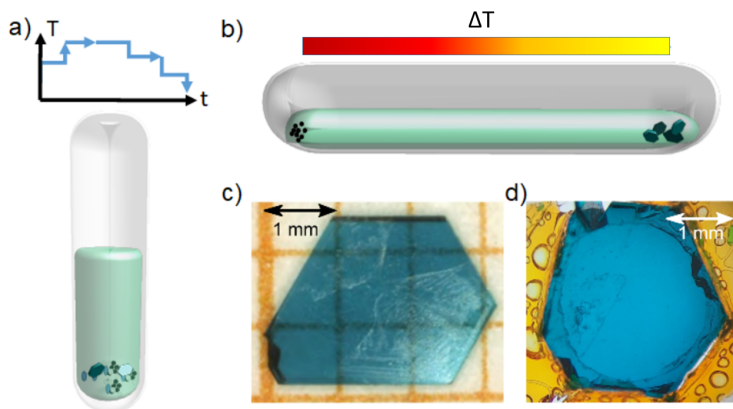


Figure 5.4: **Improvement of the growing method of Y-kapellasite.** (a) Sketch of a thin-walled ampoule that was heated and subsequently cooled in an autoclave. (b) Sketch of the lying thick-walled quartz ampoule that was exposed to an external gradient. Obtained Y-kapellasite single crystals: (c) A single crystalline sample of Y-kapellasite with $3 \times 3 \times 1 \text{ mm}^3$ size. (d) A sample used in THz-TDS measurements, fixed on the sample holder. Reprinted with permission from Ref. [1]. Crystals were grown by P. Puphal, K. M. Zoch, C. Krellner.

For the large inclusion free single crystals used in this thesis, single crystal diffraction was performed to shed light on the various forms of reported structure. A crystal was broken under high viscosity oil and a $150 \mu\text{m}$ piece was mounted with grease on a loop made of Kapton foil (Micromounts, MiTeGen, Ithaca, NY). Diffraction data were collected with a SMART APEX II CCD X-ray diffractometer (Bruker AXS, Karlsruhe, Germany) using graphite-monochromated Mo- K_{α} radiation ($\lambda = 0.71073 \text{ \AA}$) at low temperature $T = 100(2) \text{ K}$. Fig. 5.5 shows the XRD maps of the $(hk0)$, $(h0l)$, and $(0kl)$ reciprocal lattice planes of the $\text{Y}_3\text{Cu}_9(\text{OH})_{19}\text{Cl}_8$ single crystal. The single crystal diffraction confirms the published $\text{Y}_3\text{Cu}_9(\text{OH})_{19}\text{Cl}_8$ structure [21] with a goodness of the fit of 1.1. Refined parameters are shown in Tab. 5.1. Furthermore, no disorder on the Y site was found. The crystal under investigation showed reticular merohedral twinning (reverse-obverse twin). This was taken into account during structure refinement, the twin volume fractions were determined

as 0.847(2) and 0.153(2), respectively.

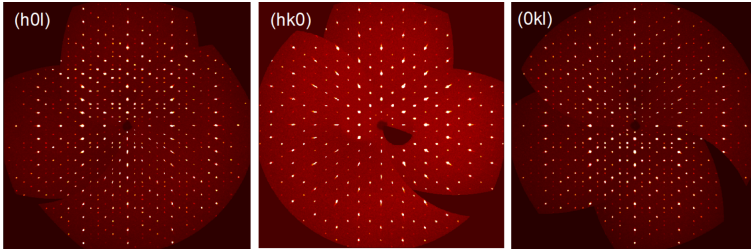


Figure 5.5: **Single crystal diffraction.** XRD maps of the (h0l), (hk0), and (0kl) planes of the investigated $\text{Y}_3\text{Cu}_9(\text{OH})_{19}\text{Cl}_8$ crystal. Reprinted with permission from Ref. [1]. Performed by J. Nuss.

$\text{Y}_3\text{Cu}_9(\text{OH})_{19}\text{Cl}_8$	
Space group:	R3 (No. 148)
Volume:	1983.2(4) \AA^3
a	11.5498(10) \AA
b	11.5498(10) \AA
c	17.167(2) \AA
α	90°
β	90°
γ	120°

Table 5.1: **Structural parameters.** Refined crystal structure parameters for single-crystal $\text{Y}_3\text{Cu}_9(\text{OH})_{19}\text{Cl}_8$ at $T = 100$ K, $\lambda = 0.71073$ \AA . Provided by J. Nuss, P. Puphal.

5.4 (Quasi-) Static response of the magnetic system

Next, the (quasi-) static response of the spin system was investigated. The in-plane magnetic susceptibility [$\mathbf{H} \parallel (a, b)$] down to temperatures as low as $T = 400$ mK is presented in Fig. 5.6a. Focusing on the

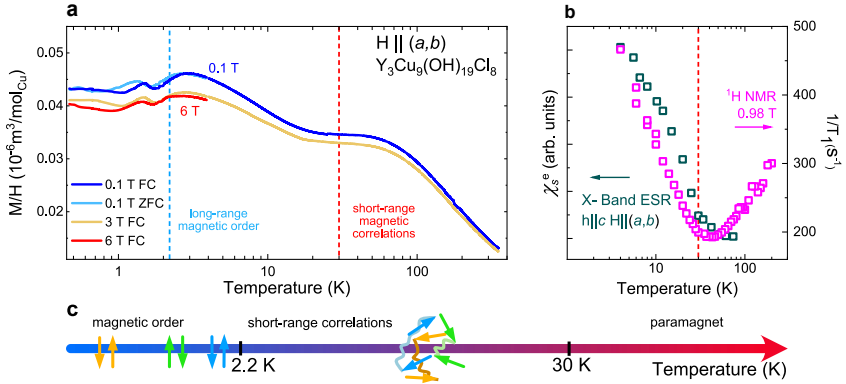


Figure 5.6: **(Quasi-) Static magnetic response.** (a) The temperature-dependent dc magnetic susceptibility M/H (FC - field cooled, ZFC - zero field cooled), under several in-plane magnetic fields is shown. The red dashed line correspond to the onset of short-range magnetic correlations, the light blue dashed line indicates the onset of long-range magnetic order. (b) Spin-lattice relaxation rate $1/T_1$ (^1H NMR, right axis) and electron spin susceptibility χ_s^e (ESR, left axis). Red dashed line: Onset of short-range magnetic correlations. (c) Extracted temperature ranges, onset of short-range magnetic correlations (30 K) and long-range magnetic order (below 2.2 K). Adapted with permission from Ref. [1]. Magnetization: P. Puphal, M. Medarde, NMR: A. Pustogow, S. E. Brown.

$H = 0.1$ T measurements, upon cooling, the magnetization first saturates in a plateau at intermediate temperatures ($T = 50$ K) and continues to rise below $T = 30$ K. At around $T = 3$ K a maximum develops, followed by a smaller peak at lower temperature ($T = 1.5$ K). While the maximum at $T = 3$ K is consistent with the previously reported $T_N = 2.2$ K [21], also observed in heat-capacity measurements, the additional smaller peak suggests a successive freezing of the magnetic texture at lower temperatures. This is in accordance with the recent μSR study on polycrystalline samples [22], reporting persistent spin dynamics down to the mK range. Furthermore, a weak hysteresis between field cooled (FC) and zero field cooled (ZFC) measurements was observed below $T = 3$ K, whereas the cooling protocol does not affect the susceptibility noticeably at higher temperatures, indicating the contribution of uncompensated spins at low temperatures. Increasing the external magnetic field, the

magnetization is slightly suppressed and the 3 K-peak shifts to lower temperatures, implying dominant antiferromagnetic interactions. This result suggests two different characteristic temperatures in Y-kapellasite, around $T = 30$ K and $T_N = 2.2$ K.

For additional information, the magnetic properties of Y-kapellasite were further investigated using nuclear magnetic resonance (NMR) and electron spin resonance (ESR). Starting with the ^1H -NMR characterization (Fig. 5.6b), the in-plane spin-lattice relaxation rate $1/T_1$ first decreases upon cooling and increases again near $T = 30$ K. This crossover indicates the onset of short-range magnetic correlations. A similar temperature scale is found by ESR measurements as shown in Fig. 5.6b, left axis (see below for extended ESR spectra). Simultaneously with the onset of magnetic correlations at around $T = 30$ K, the electron spin susceptibility χ_s^e (see below for further explanation) starts to rise, advocating the close relation between the ESR absorption and the short-range magnetic interactions. The range between $T_{SR} \approx 30$ K (short-range magnetic correlations) and $T_N \approx 2.2$ K offers experimental access for investigating the emergence of magnetism on the kagome lattice above T_N , as sketched in Figure 5.6c.

5.4.1 ESR measurements

More details of the temperature-dependent electron spin resonance (ESR) measurements are presented in the following. Measurements were performed in the X-band frequency ($f = 9.8$ GHz) employing a Bruker (EMXplus) cw-spectrometer and an Oxford Instruments LiHe-flow cryostat. Several geometries were probed, see Fig. 5.7.

For the in-plane measurements, the external magnetic field was applied within the kagome planes $\mathbf{H} \parallel (a, b)$ and the microwave field \mathbf{h} was oriented along the c -axis. The results are shown in Fig. 5.8. Here, a broad contribution evolves in the derivative of the absorbed microwave power dP/dH below the onset of short-range magnetic correlations, $T_{SR} \approx 30$ K. Further cooling results in a strong increase of the overall amplitude and a shift of the contribution to lower magnetic fields. The broad feature agrees well with the derivative of a Lorentzian (the red dashed line is the fit). Additional small resonances develop upon cooling, most likely

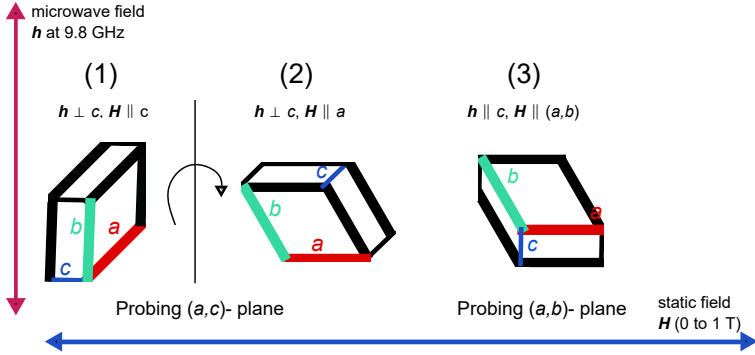


Figure 5.7: **Geometries for X-band ESR measurements.** Three different geometries were probed. (1) Static field $\mathbf{H} \parallel c$ and microwave field $\mathbf{h} \perp c$ can be rotated using a goniometer to (2) $\mathbf{H} \parallel a$, $\mathbf{h} \perp c$. For (3) $\mathbf{H} \parallel (a, b)$, $\mathbf{h} \parallel c$ the crystal was flipped on the sample holder.

related to tiny magnetic impurities in the sample. The good agreement between the temperature scales of the NMR measurements (see Fig. 5.6) and the ESR investigation suggests short-range magnetic correlations to be the main source of the broad ESR feature.

To provided quantitative access, the electron spin susceptibility χ_s^e was calculated from the data. In general, the absorbed microwave power is proportional to the imaginary part of the magnetic susceptibility, $P \propto \chi''$. Hence, χ'' was obtained by integrating the measured derivative of the absorbed power dP/dH over the magnetic field H (inset of Figure 5.8a). χ_s^e (Fig. 5.8b, as shown in Fig. 5.6b), is directly proportional to the intensity of the ESR absorption line by the Kramers-Kronig sum rule: $\chi_s^e \propto \int_0^\infty P(H)dH = I$ [178] and therefore obtained from the intensity of the Lorentz fits of dP/dH .

For out-of-plane measurements, the sample was rotated from $\mathbf{H} \parallel c$ to $\mathbf{H} \parallel a$, keeping $\mathbf{h} \perp c$, using a goniometer. Fig. 5.9 displays the results. In general, the broad Lorentzian contribution is absent. Instead several small resonances can be observed upon cooling, Fig. 5.9a. They have comparable intensities with the small features in in-plane (cf. Fig. 5.9b) and therefore might originate from magnetic impurities as well. At $T = 4$ K several angles $\mathbf{H} \parallel a, c$ were probed (Figs. 5.9c,d), leaving an

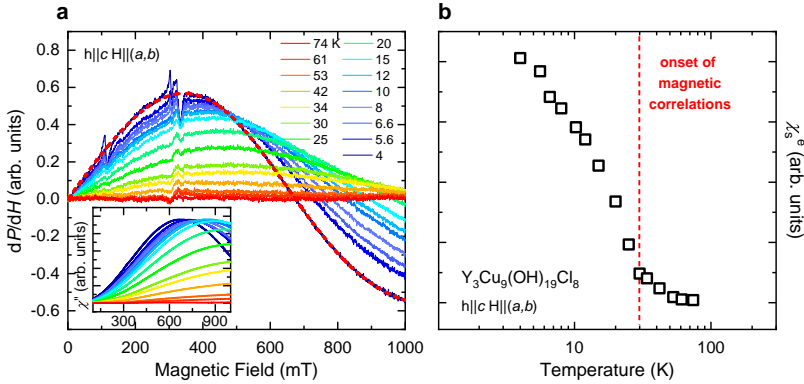


Figure 5.8: **X-band ESR measurements of Y-kapellasite (in-plane)**. (a) Derivative of the absorbed microwave power with respect to the magnetic field: External magnetic field $\mathbf{H} \parallel (a, b)$ with microwave field ($f = 9.8$ GHz) $\mathbf{h} \parallel c$. Upon cooling below the onset of short-range magnetic correlations, a large Lorentzian feature starts to develop. Red dashed line: Fit of the Lorentzian derivative for $T = 4$ K, for example. Inset of (a): χ'' obtained by the integration of dP/dH . (b) Electron spin susceptibility χ_s^e , obtained from the Lorentzian analysis of dP/dH . A strong increase can be seen at the onset of short-range magnetic correlations (vertical red dashed line). Reprinted with permission from Ref. [1].

anisotropic response, in contrast to the isotropic in-plane spectra.

Furthermore, for small features, dependence on the cooling speed was found. In general, all measurements were performed upon heating, after cooling from $T = 300$ K to $T = 4$ K. Here, the speed of the cooling seems to determine shape/ appearance of some of the small resonances. Fig. 5.10 compares the measurements with slow cooling (10 K/ min) and fast cooling (60 K/ min). The resonance at around 200 mT disappears in the spectra collected after fast cooling. This might point to a quenching of magnetic interactions when cooling fast through the temperature range of magnetic short-range correlations $T_{SR} \approx 30$ K. Note that the broad Lorentzian feature did not show any dependence on the cooling rate.

Finally, the amount of magnetic impurities is going to be estimated. Although all spectra were corrected by subtracting the sample holder

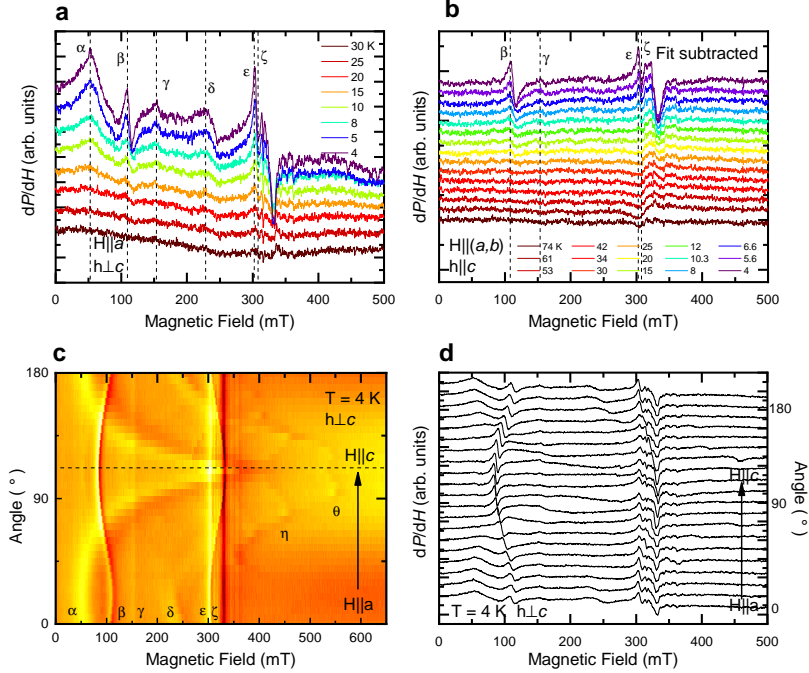


Figure 5.9: **X-band ESR measurements of Y-kapellasite (out-of-plane and in-plane).** (a) Derivative of the absorbed microwave power with respect to the magnetic field: external magnetic field $\mathbf{H} \parallel a$ with microwave field ($f = 9.8$ GHz) $\mathbf{h} \perp c$. Upon cooling several small resonances develop, comparable with the in-plane results. Spectra are stacked. (b) Stacked in-plane spectra. The broad Lorentzian contribution is subtracted, leaving only small (impurity) resonances. (c,d) Probe of the (a, c) -plane at $T = 4$ K. By rotating the sample $\mathbf{H} \parallel a$ to $\mathbf{H} \parallel c$ an anisotropic response can be seen in the false-color plot, stacked spectra, respectively.

(suprasil)/ cavity contribution (see Fig. 5.11a), a residual background contribution at around 300 mT cannot be fully excluded. In fact, the small resonances ϵ and ζ (Fig. 5.9) might be affected by this since suprasil causes resonances at these fields. However, compared to the broad Lorentzian feature, observed in in-plane, the sample holder/ cavity contribution remains small and temperature independent. To estimate the amount of

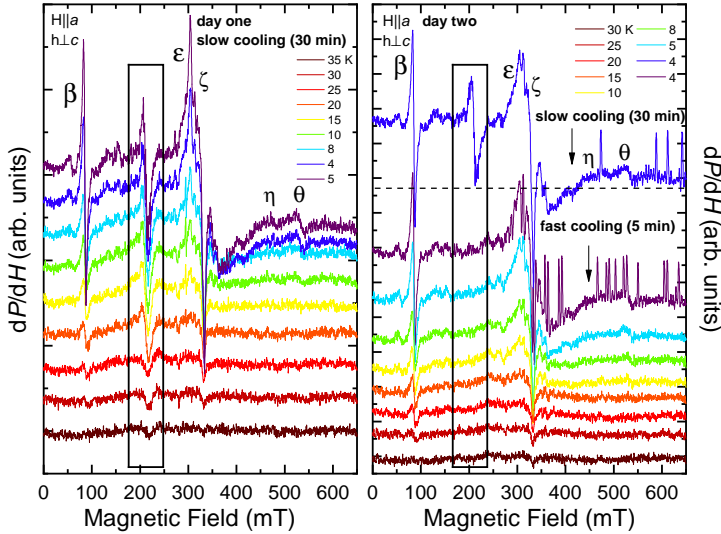


Figure 5.10: **Cooling dependence of ESR spectra.** $H \parallel a, h \perp c$, day one (a), and day two (b), spectra are stacked. On day two spectra were recorded after slow cooling (10 K/ min) and after fast cooling (60 K/ min) from $T = 300$ K to $T = 4$ K. After fast cooling, the resonance at around 200 mT (black frame) was suppressed.

intrinsic magnetic impurities, $\chi_{s,imp}^e$ was obtained by double integration of the small resonances (Figs. 5.9a,b), assuming an impurity origin. A comparison between the different contribution is shown in Fig. 5.11b. Overall, the impurity contribution is less than 1% of the in-plane response. Even though this is a rough estimate, compared to Herbertsmithite, the impurity contribution to magnetism of Y-kapellasite seems to be negligible small.

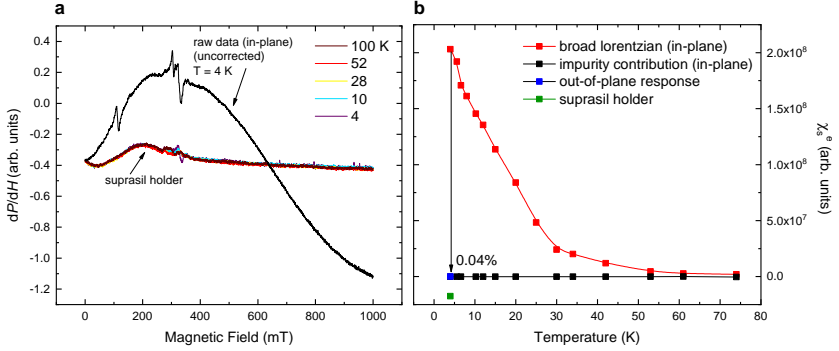


Figure 5.11: **Estimation of impurity contribution.** (a) Temperature-independent background: empty suprasil holder/ cavity contribution and in-plane raw data ($\mathbf{H} \parallel (a, b)$, $\mathbf{h} \parallel c$). Although the contribution of the background is visible in the raw data (see distortion of the lineshape around 200 mT), the background is much smaller compared to the in-plane response and can be easily subtracted. (b) Estimation of the impurity contribution $\chi_{s,imp}^e$. For in-plane ($\mathbf{H} \parallel (a, b)$, $\mathbf{h} \parallel c$, black squares), the broad Lorentzian was subtracted, leaving only the small resonances. Blue squares: out-of-plane response ($\mathbf{H} \parallel c$, $\mathbf{h} \perp c$). Note that the suprasil holder/ cavity response (green square) was subtracted from the spectra. Overall, the impurity contribution compared to the in-plane signal is less than 1%.

5.4.2 High-field magnetization

In order to investigate the low-temperature magnetic transitions further, high-field magnetization measurements were performed. For the measurements with a field parallel to the kagome plane, a single crystal with a total mass of 7.2 mg was aligned in a Laue diffractometer to confirm high crystalline quality. In order to assemble enough material for the configuration with the magnetic field perpendicular to the kagome plane (parallel to the c -axis), an array of seven small single crystals with a total weight of 6.8 mg was prepared. The magnetization was measured as a function of temperature and of field up to 5 T with a commercial SQUID-magnetometer. Subsequently, the magnetization was measured at the high field laboratory in Dresden (HLD-EMFL) at temperatures between 0.5 K and 30 K with fields up to 55 T. A coaxial pick-up coil

system [213] was used to measure the relative magnetization. Absolute values were scaled by using the data from the SQUID measurements.

The high-field magnetization measurements are presented in Fig. 5.12. Above $T = 5$ K the response shows a close-to-linear dependence on the external magnetic field with subtle features developing as the temperature approaches $T_N \approx 2.2$ K. Below T_N , a clear magnetization plateau is formed slightly above 15 T, which can be seen in both in-plane and out-of-plane measurements, with plateau values of $0.21 \mu_B$ for the a, b -plane and $0.18 \mu_B$ for the c -axis at $T = 1.5$ K, Figs. 5.12a,c. Increasing the field further, the magnetization rises again by deviating from the plateau response. The differential magnetization (Figs. 5.12b,d) reveals a small change of the slope between 40 to 45 T, suggesting another magnetization plateau with $0.37 \mu_B$ for the a, b -plane and $0.33 \mu_B$ for the c -axis. While the lower field plateaus are robust even in the ^3He measurements, probing down to $T = 0.49$ K, the more subtle slope changes at high fields are hard to observe here. Considering the similar magnetization for in-plane and out-of-plane orientations, the measurements show that the magnetic anisotropy is rather weak for Y-kapellasite.

The emergence of two plateau-like features at low temperatures around $1/6$ and $1/3$ of full magnetization suggests an involvement of the spins in the hexagon of the kagome lattice in intermediate magnetic phases before the saturation. Similar observations were made, for instance, in the distorted kagome magnet Volborthite (see Fig. 4.14) [18, 203]. Here, the magnetic trimer state gets lifted under magnetic field. For Cd-kapellasite, a series of magnetization plateaus was found and interpreted as crystallization of localized magnons [214]. As well more generalized theoretical models, describing intermediate magnetic phases of the kagome quantum magnet are discussed [215–217]. On the other hand, a microscopic picture of the magnetization plateaus/ intermediate magnetic phases remains elusive for Y-kapellasite.

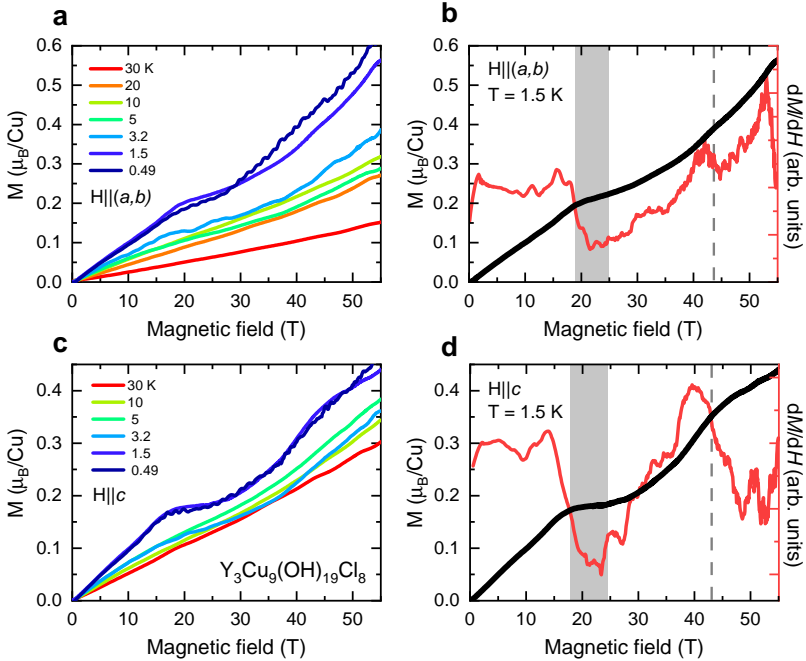


Figure 5.12: **Magnetization of Y-kapellasite in pulsed magnetic fields up to 55 T.** (a) Magnetization M in the a, b -plane, $\mathbf{H} \parallel (a, b)$. (b) Magnetization M (black line, left axis) in comparison to differential magnetization dM/dH (red line, right axis) at $T = 1.5$ K. (c,d) Results for the c -axis, $\mathbf{H} \parallel c$. Reprinted with permission from Ref. [1]. Measured by J. Willwater, S. Süllow, D. Gorbunov, Y. Skourski.

5.4.3 AC magnetization

Results of the ac magnetization measurements are shown in Fig. 5.13. With increasing the frequency of the in-plane ac magnetic field of 0.38 mT the imaginary part of the magnetization M'' starts to rise, Fig. 5.13a. Reaching a frequency of around 10 kHz, M'' shows a broad contribution between 30 K and 100 K, centered at $T = 50$ K, independent of the cooling protocol. Around $T = 2$ K, Figs. 5.13a,b a small kink becomes visible for increased frequencies (333-1024 Hz), possibly related to the onset of magnetic ordering. Further cooling results in a strong frequency-dependent behavior. While frequencies below $f = 800$ Hz lead to comparable temperature dependence, at $f = 1024$ Hz M'' increases below 0.8 K. The enhancement of M'' at low temperatures and the broad contribution above $T = 30$ K imply the occurrence of an absorption mechanism for oscillating fields, connected to the long-range magnetic order and the onset of short-range magnetic correlations.

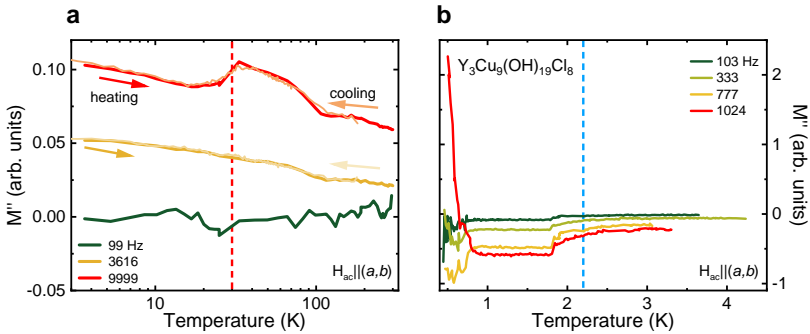


Figure 5.13: **AC magnetization of Y-kapellasite.** Imaginary part of the magnetization M'' with an in-plane oscillating field [$\mathbf{H}_{ac} \parallel (a, b)$] of 0.38 mT for various oscillation frequencies. (a) With increasing the frequency, M'' starts to rise. The broad contribution between 100 K and 30 K might be related to the onset of short-range magnetic correlations (red dashed line), $T_{SR} \approx 30$ K. (b) At low temperatures, M'' starts to increase for $f = 1024$ Hz below $T_N = 2.2$ K (blue dashed line). Reprinted with permission from Ref. [1]. Measured by P. Puphal, M. Medarde.

5.5 Structural instabilities and phononic properties

Having discussed the (quasi-) static magnetic properties in Y-kapellasite, the structural degrees of freedom (FTIR measurements) are shown in the following. Here, a particular focus will be on the coupling between magnetic and structural properties.

In Figs. 5.14a,b the reflectance spectra for in-plane and out-of-plane, respectively, are shown. Comparing these to the performed density functional theory (DFT) calculations (upper and lower panels in Fig. 5.14), the relevant phonon modes can be assigned. For Y-kapellasite $\Gamma = 33A_u + 33\ 1E_u + 33\ 2E_u$ infrared-active phonon modes are expected in the $R\bar{3}$ structure [21, 218]. Here, the dipole moment for A_u is only non-vanishing in the out-of-plane projection and for E_u within the kagome layers. At first the low-energy modes (below 1000 cm^{-1}), mostly involving variations of the Cu-O-Cu angle, are discussed. This angle determines the magnetic superexchange (see Ch. 2). Thus, the spins are susceptible to a transient modulation of the crystallographic lattice, in particular of the CuO_4Cl_2 octahedra, via phonons (see the case of Herbertsmithite [193]). Naturally, such an effect is expected to be important for the low-energy vibrations, $h\nu \ll J$.

Fig. 5.15 shows the optical conductivity σ_1 of the first in-plane phonon modes. These modes are on top of a strong one-magnon contribution (see below and in Ref. [1]) and, therefore, are expected to couple strongly to the magnetism. Figs. 5.15b,c display the fit parameter of the Lorentz analysis. Upon cooling the 3E_u (78.9 cm^{-1}) mode shows a non-thermal redshift possibly related to negative Grüneisen parameter/ lattice instability. Furthermore, an anomalous broadening, effectively decreasing the phonon intensity can be seen upon cooling below 50 K, Fig. 5.15c. It occurs simultaneously with the growing of magnetic short-range correlations ($T_{SR} \approx 30\text{ K}$, see discussion above), implying a magneto-elastic coupling scenario, similar to the case of Herbertsmithite [193]. Fig. 5.15d shows the calculated in-plane projection of 3E_u mode. Indeed, this modes involves pronounced vibrations of the O sites and subtle adjustments of the Cu positions, inducing a modulation of the Cu-O-Cu angle, i.e., of the magnetic superexchange.

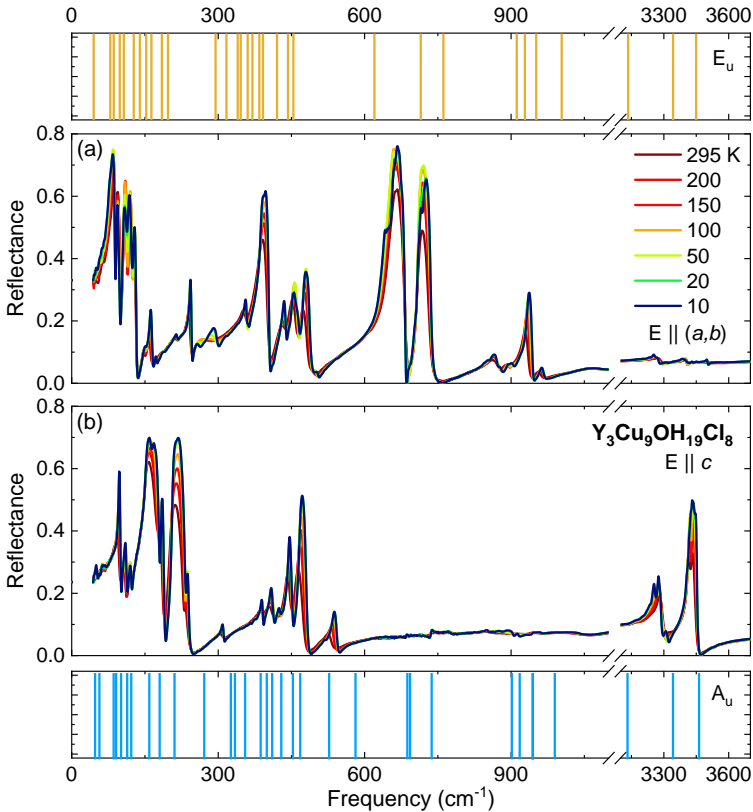


Figure 5.14: **Infrared spectra (FTIR measurements) and expected phonon frequencies (DFT calculation)**. The reflectance is dominated by multiple phononic contributions: (a) in-plane measurements $\mathbf{E} \parallel (a, b)$ and (b) out-of-plane $\mathbf{E} \parallel c$ response. Upper and lower panels: calculated E_u and A_u phonon mode frequencies, respectively. Overall, measured and calculated phonons agree well. DFT calculations were performed by Y. Li.

The temperature dependence of phonons is further analyzed in Fig. 5.16. Comparing to the DFT calculations, these modes correspond to vibrations involving mostly O and H sites. Between $T = 50$ K and $T = 20$ K, close to the onset of short-range magnetic correlations, slight splitting of some modes can be observed (see especially the mode at around 650

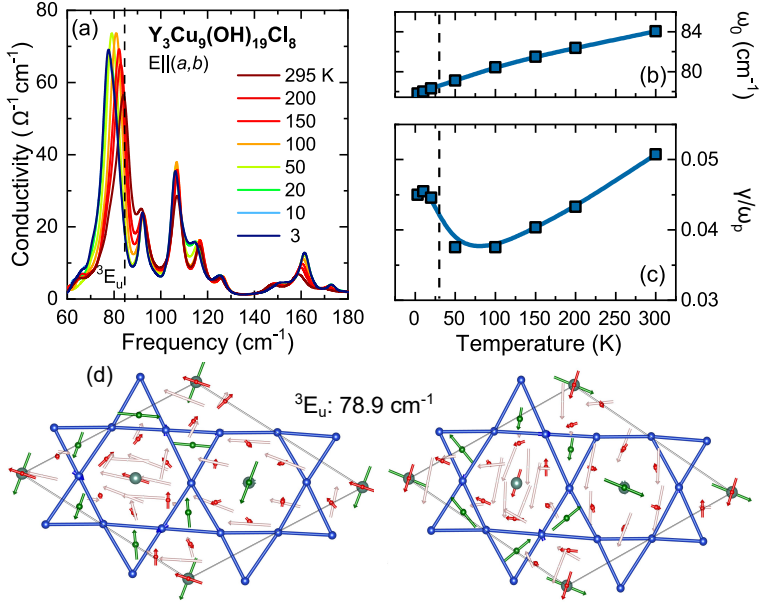


Figure 5.15: **Phonon modes in the far-infrared range.** (a) The far-infrared phonons exhibit an anomalous temperature dependence (3E_u mode at around 80 cm^{-1}). (b,c) Parameters of the Lorentz fit for 3E_u mode, center frequency ω_0 and ratio of linewidth/ plasma frequency (γ/ω_p), respectively. Dashed lines: onset of the magnetic short-range correlations, $T_{SR} \approx 30 \text{ K}$. (d) Arrows: calculated atomic motions of the 3E_u mode. The mode is degenerate. DFT calculations were performed by Y. Li.

cm^{-1}). In agreement with the specific heat data (P. Puphal et al., not presented), showing a small kink at around $T = 30 \text{ K}$, this might point to a small structural variation. As well the onset of short-range magnetic correlations coincides with this temperature scale. At this point the connection between a possible lattice instability and magnetic short-range order is not fully clear and further experimental work, for instance, a measurement of thermal expansion, is necessary.

Furthermore, measurements under external magnetic field (Voigt geometry, $\mathbf{E} \parallel (a, b)$, $\mathbf{H} \parallel (a, b)$) were performed. Here, the relative spectra $I_s(H)/I_s(0)$ (reflected intensity under field divided by reflected intensity

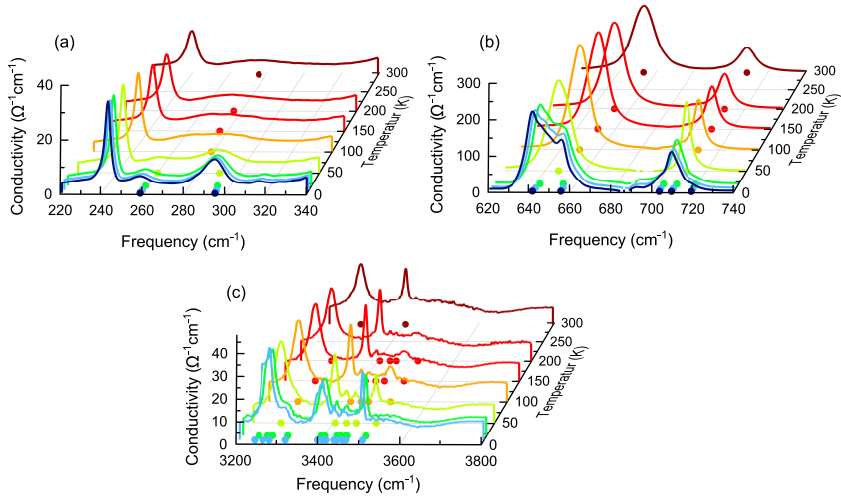


Figure 5.16: **Temperature-dependent optical conductivity of the phonons.** The selected modes correspond mostly to vibrations of O and H. Center frequencies are indicated as colored dots. Between $T = 50$ K and $T = 20$ K several subtle splittings can be seen. Other modes gain intensities upon cooling and are visible only at low-temperatures.

at zero field) at $T = 7$ K are shown in Fig. 5.17a (FIR range). The corresponding changes in the reflectance are calculated by multiplying $I_s(H)/I_s(0)$ with the reflectance spectrum (referenced to the gold mirror) at 0 T, Fig. 5.17b. Figs. 5.17c,d display measurements in the MIR range. In general, no significant changes under magnetic field were observed within the experimentally accessible field range, 0 T to 7 T. Note that the changes in the relative spectra, Figs. 5.17a,c are mostly coinciding with the minima of the phonon lines; exhibiting a worse SNR.

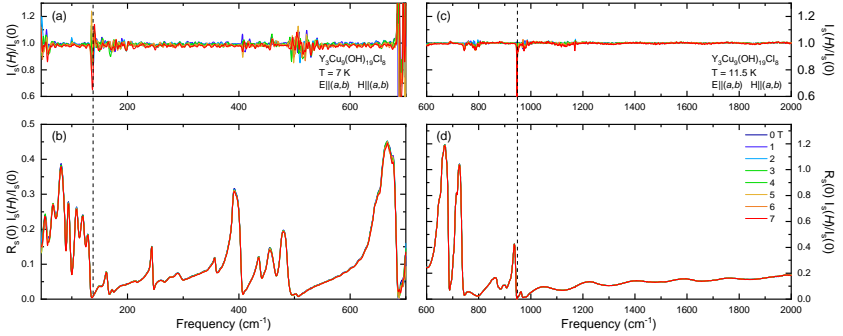


Figure 5.17: **FTIR measurements under external magnetic fields.** (a) Relative spectra under magnetic field: $I_s(H)/I_s(0)$ (reflected intensity under field divided by reflected intensity at zero field) at $T = 7\text{ K}$ in the FIR range. (b) Reflectance under magnetic field, obtained by multiplication of the zero-field reflectance $R_s(0)$ with the relative spectra: $R_s(0) \cdot I_s(H)/I_s(0)$. (c,d) Spectra in the MIR range at $T = 11.5\text{ K}$. Dashed lines: larger changes under magnetic field due to a worse SNR at the minima of the phonon modes.

5.5.1 Pressure-dependent studies

Results of the vibrational spectroscopy under pressure, the 100 K and 20 K isotherms, are shown in Fig. 5.18 and Fig. 5.19, respectively. In general, a rich pressure evolution can be seen, where several modes show a redshift while others are blueshifting with increasing pressure, for instance, for the 500 cm^{-1} and 600 cm^{-1} , the 720 cm^{-1} and 867 cm^{-1} modes. This implies while most of the bonds are shrunk, some of them are stretched. In the following, the pressure evolution of the most interesting modes is going to be described. For instance, between 400 and 500 cm^{-1} the appearance of a new mode, m_2 , at around 440 cm^{-1} was observed with a critical pressure of $P_c \approx 3\text{ GPa}$ (see Fig. 5.18b). Furthermore, in Fig. 5.19c two nearly merged modes, m_5 and m_6 move apart. While m_5 is redshifting, the m_6 is blueshifting with increasing the pressure. Between 3 and 4 GPa, m_5 strongly broadens and splits into three modes as the pressure increases further. A similar splitting was observed for the OH-vibrations, around 3400 cm^{-1} , see Fig. 5.19d. Furthermore, the pressure-dependent evolution of the center frequency of m_7 changes its trend from a redshift to a nearly constant evolution at around 3 GPa. Above 8 GPa, the modes starts

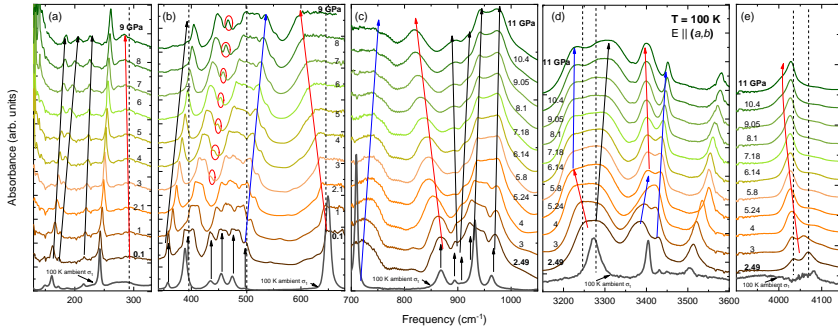


Figure 5.18: **Pressure-dependent absorption spectra ($T = 100$ K isotherm).** (a-e) Absorbance in spectral range of interest in far- and mid-infrared range. Multiple blue and redshifting modes are marked by arrows. Several phonon modes show an unusual pressure evolution, i.e., redshift under pressure. Red circles: Newly appearing phonon modes. Spectra are stacked. The optical conductivity at 100 K, ambient pressure (black line) is shown for comparison. Measurements were performed at Synchrotron Soleil, France (SMIS 2 beamline).

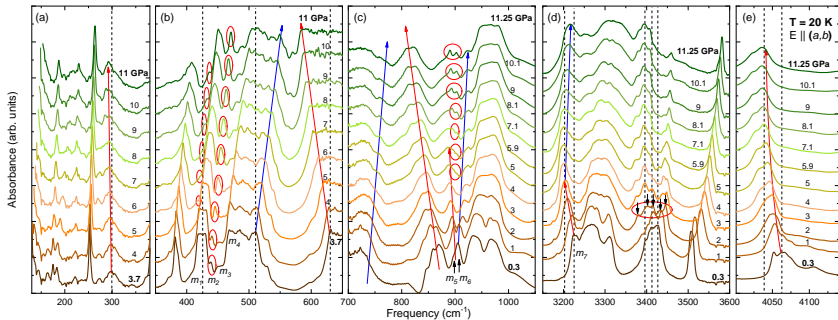


Figure 5.19: **Pressure-dependent absorption spectra ($T = 20$ K isotherm).** (a-e) Absorbance in spectral range of interest in far- and mid-infrared. Several phonon modes show an unusual pressure evolution, i.e., redshift under pressure (marked by red arrows). Red circles: Newly appearing phonon modes. Spectra are stacked. Measurements were performed at Synchrotron Soleil, France (SMIS 2 beamline).

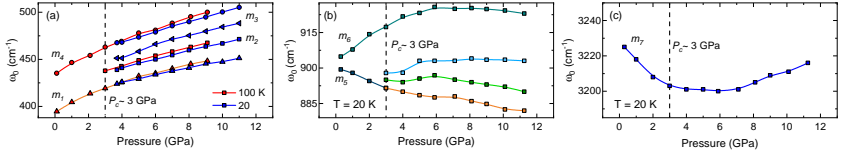


Figure 5.20: **Center frequencies, ω_0 of several modes under pressure.** (a) At a pressure $P_c \approx 3$ GPa, modes m_2 and m_3 are appearing. (b) In addition, mode m_5 broadens and starts to split. (c) At a similar pressure range, mode m_7 changes its pressure dependence (shift of center frequency) from redshifting to blueshifting behavior. Measurements were performed at Synchrotron Soleil, France (SMIS 2 beamline).

to blueshift again. These changes were further analyzed by extracting the center frequencies of the relevant phonons as a function of pressure (Fig. 5.20). The simultaneous appearance of a new mode, splitting of a mode, and a change of the pressure-dependence of the mode frequency at a very similar pressure range supports a structural modification with $P_c \approx 3$ GPa. Furthermore, at around 8 GPa, the structure might undergo further modification, indicated by the non-monotonous pressure evolution of mode m_7 . These changes, furthermore, are corroborated by the pressure evolution of Herbertsmithite (see Ch. 4). Here, similar critical pressures were observed.

To further analyze the high-pressure response, the measurements with $P \approx 11$ GPa are shown in Fig. 5.21. In general, a strongly reduced temperature evolution under pressure was observed. Compared to the ambient pressure results, most modes undergo only subtle changes in sharpness and intensity: any pronounced shifts in the center frequencies are absent. Interestingly, the temperature-induced redshift of some modes at ambient pressure is suppressed for the high-pressure spectra. Such a reduced temperature evolution of the phonons at high pressures might indicate a stabilization of the structure.

For further insight on the structural modifications under pressure, high-pressure single crystal x-ray diffraction experiments were carried out. Fig. 5.22a displays the extracted structural parameter under pressure at $T = 295$ K. As the pressure increases, the lattice constants (in-plane and out-of-plane) monotonously decrease causing a decrease of the unit

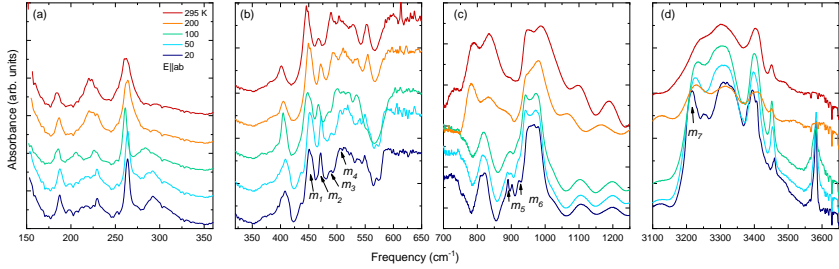


Figure 5.21: **Absorption spectra at high pressures for several temperatures.** (a-d) Absorbance in spectral range of interest in far- and mid-infrared. Overall, at high pressure, the phonons lose their pronounced temperature dependence observed at ambient-pressure. Curves are stacked. The highest pressure point from each isotherm measurement (295 K to 20 K) is shown. Pressures from top to bottom curve: (a,b) 11.12 GPa, 11.4, 9.1, 11, 11; (c,d) 11.3 GPa, 11.56, 11, 11.1, 11.25. Note that the slight deviation in intensity of the orange curve from the overall trend in panel (d) is explained by a small change in the baseline. However, this does not affect the mode frequencies. Measurements were performed at Synchrotron Soleil, France (SMIS 2 beamline).

cell volume. Note that here no indication of a structural transitions was observed. The pressure-dependent unit cell volume can be fitted using the Birch-Murnaghan equation of states [144, 219]:

$$P = \frac{3}{2}B_0(x^{-7/3} - x^{-5/3})\left[1 + \frac{3}{4}(B' - 4)(x^{-2/3} - 1)\right], \quad (5.1)$$

where P is pressure, $x = V/V_0$ is normalized unit cell volume (the zero pressure volume is V_0), $B_0 = -VdP/dV$ is bulk modulus, and B' is its first derivative with respect to pressure. The fit yields: $B_0 = 68.5$ and $B' = 19.3$. Compared to Herbersmithite [144, 200], the bulk modulus is nearly equal, however, the derivative is about five times higher here. Y-kapellasite becomes stiffer under pressure, compared to Herbersmithite. This observation corroborates the vanishing temperature-dependence of the phonon modes in the 11 GPa isobar (Fig. 5.21). Focusing on the averaged Cu-Cu-Cu angle θ_{Cu-Cu} , Fig. 5.22b, under pressure up to around 4 GPa an increase is observed, indicating that mild pressures shift the compound towards a more symmetric kagome lattice. θ_{Cu-Cu} remains nearly pressure independent over a relatively wide pressure range, up to around 7 GPa. It drops again at higher pressures, indicating an increase

of structural distortion. This non-monotonous trend is reminiscent of the pressure dependence of the phonon mode m7 (see Fig. 5.20c).

After having established a picture of the general structural changes, next an estimate of the magnetism under pressure is given. As discussed in Ch. 2, Cu-O-Cu angles $\theta_{Cu-O-Cu}$ and the corresponding Cu-O distances l_{Cu-O} determine the magnetic superexchanges along the Cu-O-Cu paths: $J \approx \cos^2(\theta_{Cu-O-Cu})/l_{Cu-O}^n$ with $n \approx 10$ [144, 145]. Fig. 5.22c shows the three distinct angles and the average distances, which correspond to the magnetic couplings $J = 154.4$ K (greenish curves), $J_{\square} = 134.2$ K (blueish curves), and $J' = 8.7$ K (reddish curves) (see appendix of this chapter and DFT calculations in Ref. [7]). As the pressure increases, $\theta_{Cu-O-Cu}$, contributing to J_{\square} , continuously decreases. $\theta_{Cu-O-Cu}$, corresponding to J , stays nearly constant up to 5 GPa and decreases slightly at higher pressures. The lowest angle, corresponding to J' is independent on pressure over the entire investigated range. Furthermore, all Cu-O distance l_{Cu-O} behave similar, as they decrease with increasing pressures.

Based on the structural parameters, in Fig. 5.22d the resulting magnetic couplings are shown. Although the simple geometrical treatment of the exchange couplings leads to a reversed strength of the two leading couplings (compared to the calculations), i.e., J_1 corresponds to J_{\square} , J_2 to J , J_3 to J' , they can be nevertheless used to give a rough estimate of effect of pressure on the magnetism. Under pressure the the weakest coupling J_3 , continuously increases but remains always significantly smaller than J_1 and J_2 . These two (J_{\square} and J in the DFT calculations) determine the magnetism of the system at zero pressure [7]. As the pressure increases, the structural data suggest that J_2 increases steeper than J_1 , yielding almost equal leading exchanges at around 5 to 6 GPa. Comparing to the phase diagram of Ref. [7], these structural changes are expected to further stabilize the magnetic $Q = (1/3, 1/3)$ order and thus might result in an increase of T_N . Although, in principle an increase in J_3 might shift Y-kapellasite towards the phase boundary of the classical spin liquid, the suggested pressure evolution seems to be too weak to induced such a ground state in the investigated pressure range. Further increasing the pressure, J_1 and J_2 reverse their strength, potentially destabilizing the magnetic order again. This reminds of the pressure evolution of Herbertsmithite, where at first magnetic order is induced and at higher pressures T_N is lowered again [144, 200]. However, to obtain

quantitative information, further DFT calculations with the pressure-dependent structures might be necessary.

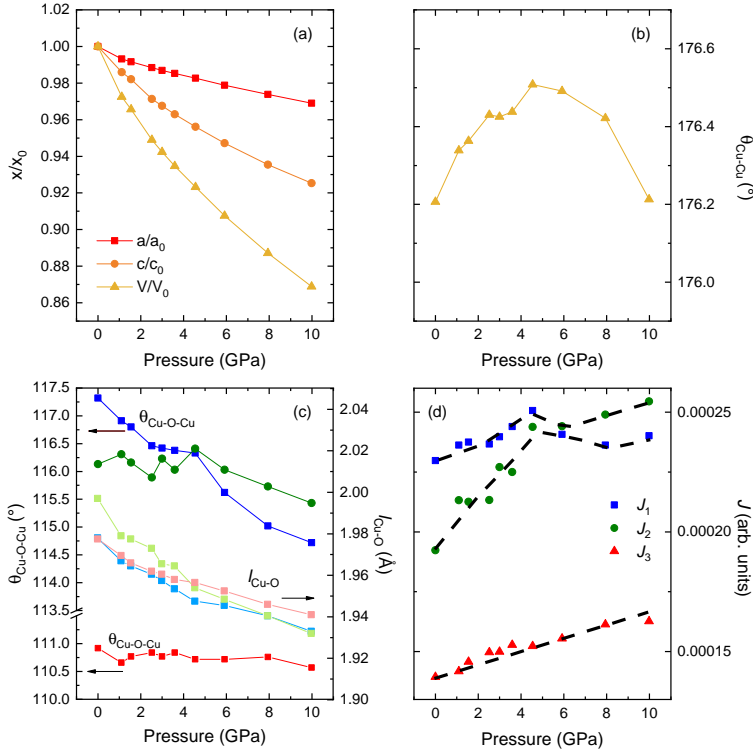


Figure 5.22: Structural parameters of Y-kapellasite under pressure
 (a) Relative changes of the lattice constants $a = b$ (in-plane), c (out-of-plane), and unit cell volume V under pressure. (b) Average of the two Cu-Cu-Cu angles θ_{Cu-Cu} as a measure of the structural distortion. Undistorted kagome plane: $\theta_{Cu-Cu} = 180^\circ$. For Y-kapellasite there are two distinguishable angles. (c) Pressure dependence of the Cu-O-Cu angles $\theta_{Cu-O-Cu}$ (left axis) and corresponding averaged Cu-O distance l_{Cu-O} (right axis), see greenish, blueish, and reddish colors for corresponding pairs. (d) Estimate of the magnetic superexchange based on the geometrical parameters. J_1 corresponds to J_\square , J_2 to J , J_3 to J' of the DFT calculations in Ref. [7]. Measurements were performed at ESRF, France (ID27 beamline). Structures were refined by P. Pupal.

5.6 THz time-domain spectra as a probe of spin dynamics

After the comprehensive structural and magnetic characterization presented above, the results of THz time-domain spectroscopy (THz-TDS) are going to be discussed in the following. Temperature-dependent THz-TDS measurements were carried out in transmission geometry employing a TeraView TeraPulse 4000 THz-TDS spectrometer along with a He-bath cryostat on oriented single crystals (see Ch. 3 for a description of the experimental procedure). In Fig. 5.23 the raw data of the THz-TDS recorded in the *ab*-plane are plotted. At high temperatures, the in-plane time-domain signal of the transient electric field (Fig. 5.23a) consists of only the main pulse ranging from 0 to 4 ps. With cooling, the intensity of this pulse decreases, but in addition a pronounced oscillating electric field develops over an extended time ranging from 4 to 10 ps. Note, for conventional one-magnon excitations, a similar time-domain signal was reported but on a significantly longer time scale (several tens of ps) [67–69, 92, 93], see the introduction (Ch. 2) for a summary of the relevant literature.

To gain more insight into the underlying physical processes, a Fourier transformation was performed and the frequency-dependent absorption coefficient α was calculated, plotted in Fig. 5.23b. At room temperature, only the tail of the lowest in-plane phonon mode contributes notably to the THz absorption. Upon cooling, the phonon contribution first increases slightly and then becomes weaker together with a suppression of the main pulse in the time-domain signal (see above for the results of infrared spectroscopy and DFT calculations of the phonons). As the temperature drops below $T = 30$ K, the low-frequency absorption rises, resulting in a broad continuum-like contribution much stronger than the phonon (in this frequency range). This corresponds to the enhancement of the electric field oscillations at extended times as illustrated in Fig. 5.23a. The feature increases strongly with further cooling and finally dominates the entire THz response down to the lowest temperature measured. Furthermore, for $T < 5$ K, two weaker, but noticeable, peak-like contributions were observed between $30 - 40$ cm^{-1} . Despite the increase of intensity, no qualitative difference was found in measurements below T_N . An extended data set of all measured temperatures is presented in the appendix of

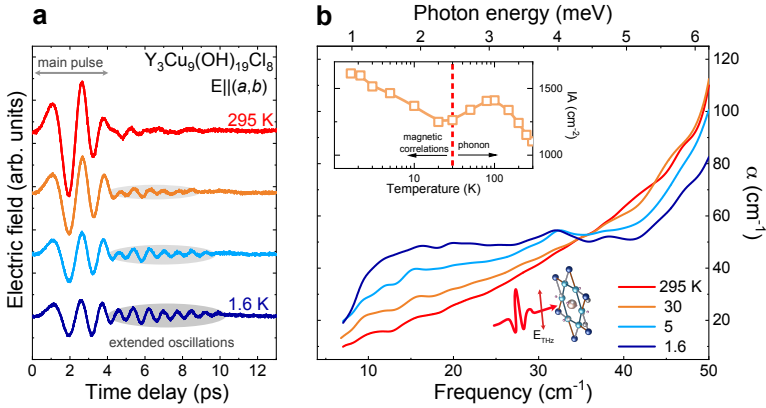


Figure 5.23: **Temperature-dependent THz spectra.** (a) THz electric field, transmitted through Y-kapellasite as a function of time delay and (b) resulting absorption coefficient α for the in-plane direction, as depicted [$\mathbf{E}_{THz} \parallel (a, b)$]. At $T = 295$ K, the main pulse (0 to 4 ps) contains most of the THz responses (phononic properties). Below the onset of short-range magnetic correlations, $T = 30$ K, the THz electric field pronounces extended-time oscillations (4 to 10 ps, shaded area), while the main pulse loses its intensity. As a result the continuum-like absorption develops in α , followed by two additional peak-like features at 32 and 37 cm^{-1} . Inset: Integrated absorption coefficient IA (up to 40 cm^{-1}). The red dashed line represent the onset of short-range magnetic correlations, $T = 30$ K. Above $T = 30$ K, changes in IA are mostly caused by the lowest in-plane phonon mode. Below the onset of short-range magnetic correlations, the IA continuously increases. Reprinted with permission from Ref. [1].

this chapter (Fig. 5.28). From the comparison with DFT calculations, a phononic origin of the low-energy features can be excluded. Also electronic contributions are unlikely for the highly insulating Y-kapellasite (bandgap of 3.6 eV) [21, 192].

These trends become even more obvious when looking at the integrated absorption IA (similar to the spectral weight, see Ch. 3), displayed in the inset of Fig. 5.23b. The crossover range in $IA(T)$ matches well with the onset of short-range magnetic correlations at around $T_{SR} = 30$ K as observed in the NMR spin-lattice relaxation rate and ESR susceptibility (Fig. 5.6). This good agreement between the temperature scales strongly

suggests that the THz continuum-like absorption is caused by short-range magnetic correlations even above T_N .

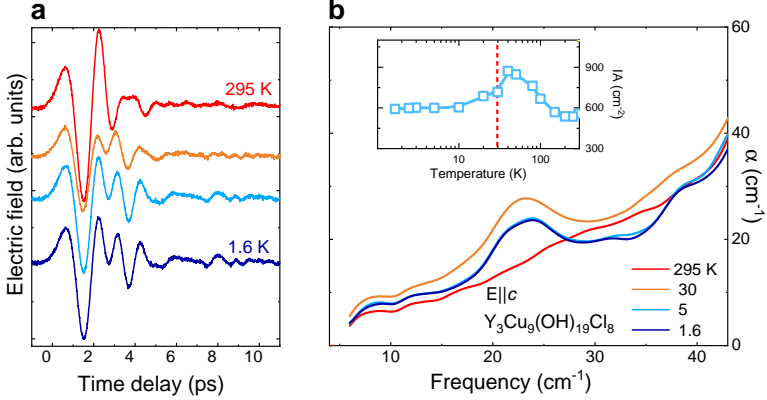


Figure 5.24: **Temperature-dependent THz spectra.** (a) THz electric field, transmitted through Y-kapellasite as a function of time delay and (b) resulting absorption coefficient α for the out-of-plane direction [$\mathbf{E}_{THz} \parallel c$]. The out-of-plane response is restricted to the main pulse (0 to 4 ps). Over the full temperature range, no pronounced extended-time oscillations of the electric field are visible. The absorption coefficient shows a peaklike structure emerging at around 22.5 cm^{-1} between $T = 50 \text{ K}$ and $T = 30 \text{ K}$. Inset: Integrated absorption coefficient IA (up to 40 cm^{-1}). The red dashed line represent the onset of short-range magnetic correlations, $T = 30 \text{ K}$. Above $T = 30 \text{ K}$, changes in IA are mostly caused by the lowest out-of-plane phonon mode. Around the onset of short-range magnetic correlations, the IA drops.

Furthermore, the out-of-plane response [$\mathbf{E}_{THz} \parallel (c)$] was measured. Results are shown in Fig. 5.24. In contrast to the in-plane results, the electric field in out-of-plane does not show pronounced late-time oscillations. In fact, the response is confined to the main pulse mostly (Fig. 5.24a). Focusing on the absorption coefficient, Fig. 5.24b, at room temperature the spectrum is featureless and dominated by the tail of the lowest out-of-plane phonon mode (50 cm^{-1} , see above for FTIR measurements and DFT calculations). Upon cooling below $T = 50 \text{ K}$, a peak-like structure of unknown origin emerges at around 22.5 cm^{-1} . It further gets more pronounced at $T = 30 \text{ K}$ and below, but no qualitative difference was found below T_N . The IA (inset of Fig. 5.24b) shows an increase upon

cooling, stemming from the phononic contribution, similar to the IA in in-plane direction. However, around the onset of short-range magnetic correlations ($T_{SR} \approx 30$ K), the IA drops and continues to decrease upon further cooling.

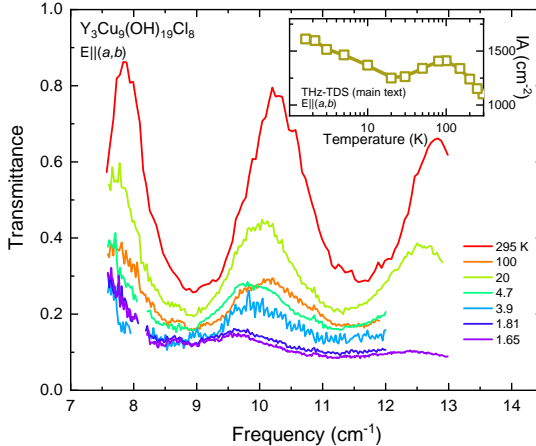


Figure 5.25: **THz-FDS measurements.** The temperature-dependent evolution of the transmittance is in good agreement with the IA obtained by THz-TDS (inset). The oscillation pattern in THz-FDS measurements originates from multiple internal reflections, as the transparent sample serves as a Fabry-Perot resonator, an etalon. Reprinted with permission from Ref. [1].

In addition, THz frequency-domain spectroscopy (THz-FDS) was carried out using a frequency-tunable backward-wave-oscillator (BWO), generating continuous, coherent, and monochromatic THz radiation with a Goly cell serving as a detector and a He-bath cryostat for temperature control [220]. The transmittance was measured by recording the intensity of the THz radiation transmitted through the sample and referenced to the empty hole of the sample holder. Results are shown in Fig. 5.25. In THz-FDS, a series of single frequency measurements were repeated to cover the frequency range between 7.5 to 13 cm^{-1} which lacks the time resolution compared to the THz-TDS. Multiple reflections of the incident light between the parallel surfaces of the transparent sample generate the pronounced Fabry-Perot oscillation pattern in Fig. 5.25. In the THz-TDS, this effect can be avoided by controlling the time window. Nevertheless,

the THz-FDS measurements are in good qualitative agreement with the THz-TDS results. Upon cooling to $T = 100$ K, the transmittance gets suppressed supporting the increase in the integrated absorption coefficient IA for the in-plane orientation (c.f. inset of Fig. 5.25). From $T = 100$ K to $T = 20$ K, the transmittance rises again corresponding to a drop of the IA . Further cooling down to $T = 1.65$ K, a strong suppression of the transmittance is observed, in accordance with a rise of the IA .

5.7 Magneto-THz spectroscopy

To clarify the origin of observed continuum-like absorption in THz range, magneto-THz measurements were carried out. A superconducting magnet (Oxford Instruments) was used to apply a static external magnetic field up to $H = 10$ T in Faraday geometry ($\mathbf{E}_{THz} \parallel (a, b)$, $\mathbf{H} \parallel c$) with temperatures down to $T = 1.7$ K. With ramping up the magnetic field, the continuum-like feature loses its intensity beginning at the low-frequency end, as displayed in Fig. 5.26a (Fig. 5.29 for an extended data set). This can be nicely seen in Fig. 5.26b where the IA is plotted as a function of H . Exceeding a critical field of $H_c = 3$ T, $IA(H)$ decreases considerably; at a field strength of $H = 10$ T the intensity is reduced by almost 10 %. This quantitative change seems reasonable since the magnetic energy corresponds to roughly 10 % of the exchange energy: $\mu_B H = 0.1 k_B \Theta_{CW} \approx 0.1 J$, where $\Theta_{CW} \approx -100$ K is the Curie-Weiss temperature and $J \approx 13$ meV is the dominating exchange energy (μ_B is Bohr magneton, k_B is Boltzmann constant) [7, 21]. The phonon tail above 40 cm^{-1} is affected as well: it weakly shifts towards lower energies. In addition to these obvious changes in the spectrum, some more subtle variations inside the continuum-like absorption can be identified. Slight shifts of the $30 - 40 \text{ cm}^{-1}$ peaks become clearer in the contour plot of the normalized absorption coefficient $\alpha(H)/\alpha(0 \text{ T})$, presented in Fig. 5.26c. Interestingly, the onset of the continuum-like absorption shows a stronger change under magnetic field, compared to the $30 - 40 \text{ cm}^{-1}$ peaks, c.f. grey arrows in Fig. 5.26c. Note the reduced signal-to-noise ratio of a magneto-optical measurement leads to somewhat noisy features below 20 cm^{-1} ; nevertheless, the magneto-optical THz results strongly support the magnetic origin of the continuum-like feature.

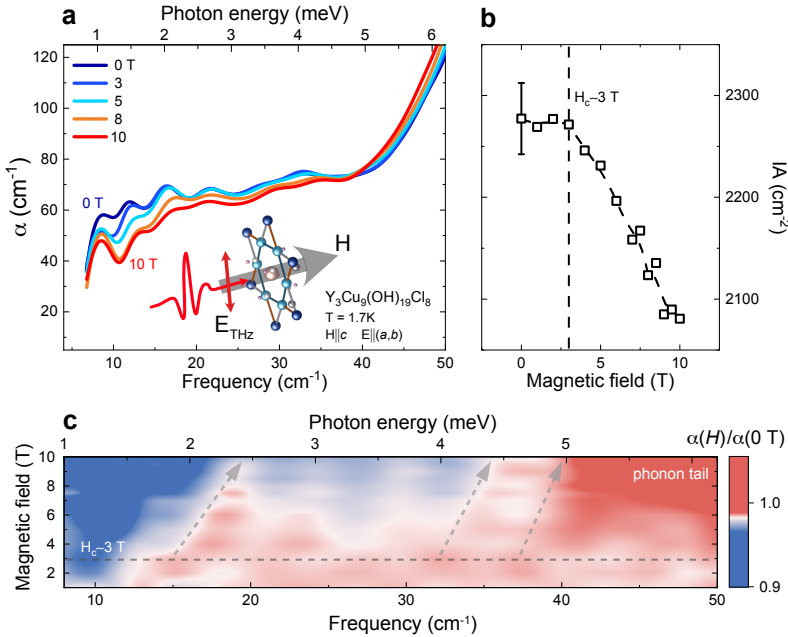


Figure 5.26: **Result of magneto-THz spectroscopy at $T = 1.7$ K.** (a) Absorption coefficient α under magnetic field in Faraday geometry, as depicted ($\mathbf{E}_{THz} \parallel (a, b)$, $\mathbf{H} \parallel c$). The THz continuum-like absorption decreases with increasing magnetic fields, confirming its magnetic origin. (b) Integrated absorption coefficient IA (up to 40 cm⁻¹), exposing a critical magnetic field of $H_c \sim 3$ T. (c) Contour plot of the relative absorption coefficient under magnetic field $\alpha(H)/\alpha(0 \text{ T})$, normalized to zero field. The grey arrows indicate the field evolution of the onset of the continuum-like absorption and of the two peak-like features at 32 and 37 cm⁻¹. Reprinted with permission from Ref. [1].

5.8 Multi-center magnon excitations

In a next step the magnetic contributions are going to be separated from the dielectric ones in order to reveal their natural spectral form in the THz absorption. With the fair assumption that the dielectric properties do not change drastically at low temperatures, the magnetic susceptibility χ_m'' can be obtained from the THz spectra (Fig. 5.23) by referencing to the 80 K-spectrum (see Sec. 3.2.3 for further information). The results are shown in Fig. 5.27a. The extraction of χ_m'' unveils an asymmetric shape of the magnetic continuum-like feature with a maximum at around 12 cm^{-1} and a width of about 30 cm^{-1} followed by two peaks at 32 and 37 cm^{-1} at the lowest temperature, $T = 1.6 \text{ K}$.

To learn more about the origin of the magnetic THz response and the magnetic ground state, the spin-wave dispersion for Y-kapellasite was calculated with linear spin-wave theory by assuming a coplanar non-collinear $\mathbf{Q} = (1/3, 1/3)$ magnetically ordered ground state as suggested by recent *ab-initio* DFT calculations [7] (see appendix for technical details). This ordered state comprises three different magnetic sublattices of hexagons (shown as green, blue, and yellow in Fig. 5.2b). Within each hexagon, the spins are antiferromagnetically coupled and neighboring hexagons are coupled to each other via spins (shown in grey in Fig. 5.2b) whose directions are fully determined by the neighboring hexagons (slave spins) [7].

Figs. 5.27b, c contain the calculated spin (magnon) density of states (SDOS) and the corresponding spin-wave dispersion in the relevant energy range, below 6 meV (1 meV corresponds to 8.065 cm^{-1}). Several energies with a density of states, corresponding to characteristic energy scales of the THz χ_m'' , are marked by dashed lines. The spin-wave dispersion of Y-kapellasite is gapless and degenerated at the Γ -point (Goldstone mode); possible one-magnon excitations are outside the investigated THz spectral range (cf. Fig. 5.27c, see appendix for further information, Fig. 5.32). As introduced above, a one-magnon process only measures the response at the zone center; in stark contrast to multi-center magnon excitations that can expand over the entire Brillouin zone. For the latter case, due to momentum conservation, the total wavevector of the participating magnons must be zero, $\sum_n \mathbf{q}_n \approx 0$, which is accomplished by the simultaneous magnon excitations in three distinct magnetic sublattices. Within

this picture, the steady development of the continuum-like absorption without any additional features across T_N can be explained by multi-center magnon absorptions. The one-magnon excitations are outside the accessible spectral range and only the multi-center magnons are observed. As illustrated in Fig. 5.27d, the spin-wave dispersion beyond the Γ -point gets accessible via such excitations. Indeed, towards the K-direction the degeneracy is lifted and the lowest band exhibits a parabolic shape (Fig. 5.27c). Around 2.7 meV the band flattens and reaches a maximum. This shape of the dispersion yields a large number of available states in the low-energy range and generates the maximum in the SDOS at 2.7 meV which is related to the peak at 1.5 meV (12 cm^{-1}) in χ_m'' . At higher energies, around 4.8 meV, the density of states increases again with the next two higher-lying bands reaching their maxima. At 5 meV the number of available states drops significantly before it peaks again at around 5.2 meV (parabola minima of the next higher bands). Indeed, these states are related to the peak-like contributions between 32 and 37 cm^{-1} (4 and 4.6 meV) in χ_m'' (Fig. 5.27a). There is a small offset of about 1 meV between experimental results and calculations, probably due to a small mismatch in parameters between experiment and theory.

Overall, including the multi-center magnon picture, the SDOS from the linear spin-wave theory calculations shows a remarkable agreement with the experimental result, χ_m'' . Furthermore, based on the SDOS, the expected χ_m'' is calculated, validating the observed spectral shape (cf. Fig. 5.33). The agreement with theory even extends to the magnetic field dependence. Fig. 5.27b displays the change of the SDOS with magnetic field. Under external magnetic field, the spin dispersion becomes gapped and the weight of the SDOS shifts up in energy (cf. appendix, Fig. 5.34). In addition, the 2.7 meV maximum reveals a strong shift under magnetic field, it is slightly different than the one obtained for the 4.8 meV and 5.2 meV peaks. Note that the calculations overestimate the magnetic field scale compared to that of the experiment, perhaps due to demagnetization effects. Still, these trends under external magnetic field are corroborating the result of magneto-THz spectroscopy.

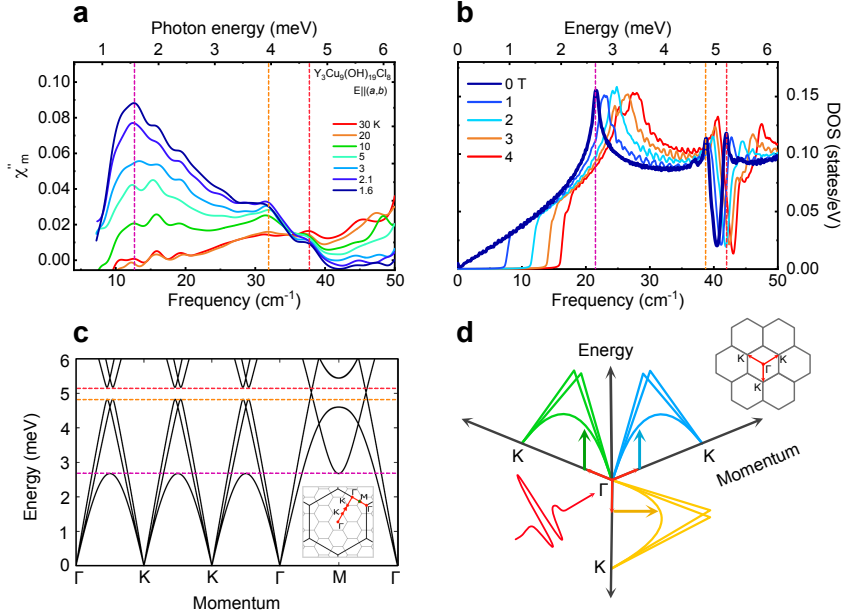


Figure 5.27: **Three-center magnon excitations and theoretical spin-wave dispersion of Y-kapellasite.** (a) The frequency-dependent imaginary part of the magnetic susceptibility χ''_m obtained from THz-TDS exposes the natural spectral form of the three-center magnon excitations. Three distinctive features are marked by vertical dashed lines. (b) Spin (magnon) density of states (SDOS) obtained from linear spin-wave theory calculations with and without magnetic field. The SDOS shows three characteristic energies below 6 meV with a high density of states (vertical dashed lines). (c) Spin-wave dispersion of Y-kapellasite. Horizontal dashed lines: Corresponding to the energies in (b). Inset: Calculated path in the extended Brillouin zone (black hexagon). (d) The three-center magnon process in momentum space, i.e., three spin excitations in the different magnetic sublattices (green, blue, and yellow color code) with $0 \approx \sum_n \mathbf{q}_n$. Reprinted with permission from Ref. [1]. (b,c) Calculated by A. Razpovov and R. Valentí.

5.9 Discussion

The THz study allows to directly probe the spin density of states via optical spectroscopy; by utilizing multi-center magnon absorption the SDOS becomes accessible over the entire Brillouin zone, i.e., THz magnetometry. In Y-kapellasite, strong short-range magnetic correlations lead to spin fluctuations over a wide temperature range. The paramagnonic behavior is aided by these fluctuations explaining the development of the THz continuum-like absorption together with the onset of short-range magnetic correlations. The lattice distortion, on the other hand, lowers the spatial symmetry and generates three magnetic sublattices. This distortion is decisive for multi-center magnon excitations to occur. In particular, the magnetic superstructure favors simultaneous $3N$ magnon excitations where each of the participating magnon excitations occurs, respectively, at one of the three magnetic sublattices, i.e., three-center magnon, while in total the net momentum is conserved ($\Delta\mathbf{q} = \mathbf{q}_{ph} \approx 0$), as illustrated in Fig. 5.2b (see appendix for further discussion, Fig. 5.36). The role of distortion could be further verified in other kagome lattice materials [7, 17, 221, 222]. But for the case of Y-kapellasite, the distortion seems to be crucial for the multi-center magnon absorption given that Herbertsmithite, which is considered as a perfect kagome structure [11], does not reveal any signature of multi-center magnons (Fig. 4.7) [15, 16].

Such a symmetry breaking can also be phonon-assisted [223, 224]. Note that similar suggestions were made for the parent compound of cuprates with an underlying square lattice. In those cases, the observed features were associated with the coupling between magnons and phonons leading to enhanced excitation frequencies in the mid-infrared range [225, 226]. The magnetoelastic coupling may be represented in the temperature dependence of the phonon modes. In the present case, an unusual redshifts and anomalies of the infrared-active phonons is observed, accompanied by the development of short-range magnetic correlations (see above, Fig. 5.15).

Overall, the comparison of the experimental results with linear spin-wave theory calculations suggests that for a proper description a multi-center magnon picture, beyond simple magnetic modes, is required in order to explain the THz excitations. In fact, the multi-center magnon

absorption in Y-kapellasite resembles the conventional two-center magnon absorption observed in classical antiferromagnets: FeF_2 , MnF_2 , CoF_2 , and NiF_2 [96, 98, 102–106]. Utilizing Dexter’s theory of cooperative optical absorption [107], earlier reports proposed several mechanisms [102, 103, 109], where the removal of centrosymmetric points is supposed to be particularly necessary for the non-vanishing electric dipole moment [96].

The former studies confined the two-center magnon absorption as electric dipole active phenomena; but there is no reason for this limitation. Recently, a direct coupling between the magnetic state and light was proposed; the detection takes place over the free induction decay [66–69]. As well, accounting for the two magnetic sublattices in conventional antiferromagnets, traditionally only a two-center absorption was considered. Moreover, the optical selection rule for the three-center magnon excitation might differ from the conventional one-magnon picture ($\Delta S = \pm 1$, the spin difference between initial and excited state). For example, the two-center magnon excitation was discussed before with an altered optical selection rule [227, 228]. All these now turn into limiting factors when a more detailed and generalized microscopic picture has to be established for the multi-center magnon absorption. Together with a refined understanding, the presented approach might be applicable in a large pool of materials.

Furthermore, the relation of the THz multi-center magnon absorption to similar multimagnon processes observed in other quantum magnets of low symmetry should be discussed. For quantum magnets, often a virtual process via the magnon decay [111] is discussed, which has been observed in Raman/ neutron scattering [113–116]. Note that multimagnon scattering (photon/ neutron scatters by creating multiple magnons) and THz multi-center magnon absorption (multi-center magnon: one photon gets absorbed, simultaneously creating multiple magnons in different magnetic sublattices) need to be discerned with distinct optical selection rules [96]. Moreover, the higher-order magnon contributions beyond linear spin-wave theory are as well discussed in THz absorption [45]. However, these are different from the multi-center magnon absorption, subject of the present study. Regarding higher-order magnons, mixing of one-magnon branches with multimagnon states can occur as a result of the low symmetry of the spin interactions as in $\alpha\text{-RuCl}_3$ [48, 112]. A further

example can be found in the case of $\text{Yb}_2\text{Ti}_2\text{O}_7$, showing a field-induced decay of the one-magnon branch into a two-magnon continuum [115]. In Y-kapellasite, however, neither geometrical frustration nor anisotropic spin interactions seem to be present in the system [7] excluding the magnon decay processes from the present case. Nevertheless, note that a multi-center magnon based extraction of the SDOS with THz spectroscopy, as presented in this work, might be possible even in the presence of a decay mechanism.

There are several issues concerning the magnetic properties of Y-kapellasite which should be addressed in future investigations. One particularly interesting issue remaining is the persistent spin dynamics in the magnetically ordered state below $T_N = 2.2$ K [22] which might be related to the successive spin freezing observed in the susceptibility, Fig. 5.6. For optical measurements, such a low temperature (mK range) is still challenging. Hence, complementary experimental techniques are required to scrutinize this exotic behavior. In addition, an investigation of the microscopic origin of the short-range magnetic correlations much above T_N could be a focus of further studies.

5.10 Conclusion and outlook

In conclusion, in a proof-of-principle experiment, THz time-domain spectroscopy is established as a method to directly probe the spin (magnon) density of states by expanding its capability from $\mathbf{q} \approx 0$ to $\Delta\mathbf{q} \approx 0$ excitations over the entire Brillouin zone: THz magnetometry. The three-center magnon absorption in the exotic magnetic superstructure of Y-kapellasite is the key mechanism behind this observation. Driven by short-range magnetic interactions, the absorption persists well above the magnetic ordering temperature, i.e., paramagnons. The multi-center magnon absorption allows easy access to the spin density of states for suitable magnets, in particular in systems with low symmetry.

5.11 Appendix

In this appendix additional information (mainly from Ref. [1]) are presented. This contains extended data sets of the (magneto) THz-TDS measurements, technical details of the LSWT calculations, calculations of the dynamic magnetic susceptibility, LSWT under magnetic field, and further details regarding the multi-center magnon excitation (two-center vs. three-center magnon). Furthermore, an overview of the phase diagram of the distorted kagome antiferromagnet (Ref. [7]) is given.

5.11.1 Extended data of THz-TDS

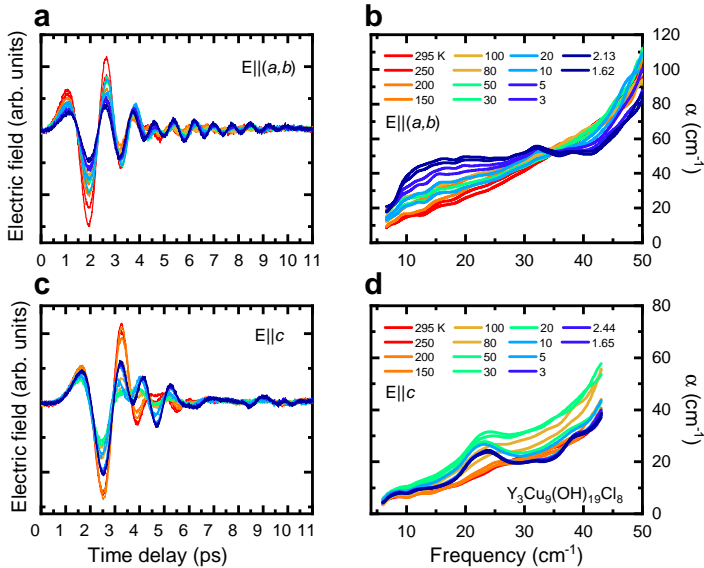


Figure 5.28: **THz-TDS result for all measured temperatures.** (a,b) Time-domain electric field and absorption coefficient for the in-plane $\mathbf{E} \parallel (a, b)$ response, respectively. Adapted with permission from Ref. [1]. (c,d) Response along the c-axis, $\mathbf{E} \parallel c$, time-domain electric field and absorption coefficient, respectively.

Temperature-dependent THz-TDS measurements were carried out in transmission geometry employing a TeraView TeraPulse 4000 THz-TDS spectrometer along with a He-bath cryostat on oriented single crystals. The time-domain electric fields, which are directly measured from the THz spectrometer, are displayed in Fig. 5.28. By performing the Fast Fourier Transformation (FFT), the frequency-dependent power spectrum $\tilde{E}_{sample}(\omega)$ was obtained. Then, the complex transmission $\tilde{T}r(\omega)$ was calculated by referencing to the empty hole of sample holder, $\tilde{E}_{ref}(\omega)$: $\tilde{T}r(\omega) = \tilde{E}_{sample}(\omega)/\tilde{E}_{ref}(\omega)$. The absorption coefficient of the sample is related to the transmittance $Tr(\omega)$ (real part of $\tilde{T}r$) via the Beer-Lambert law: $\alpha(\omega) = -\ln\{Tr(\omega)\}/d$, where d is the thickness of the sample. The absorption coefficient spectra for all measured temperatures are shown in Fig. 5.28.

The integrated absorption coefficient, which is used to analyze the spectra in the main text, $IA = \int \alpha(\omega) d\omega$, is proportional to the optical spectral weight $SW = \int \sigma(\omega) d\omega$ with the relation $\alpha(\omega) = 4\pi\sigma(\omega)/n(\omega)$, where σ is optical conductivity and n is index of refraction [82, 83].

5.11.2 Magneto-optical THz-TDS

Fig. 5.29 shows the time-domain electric fields and the corresponding absorption coefficient over the full magnetic field range (for Faraday geometry, $\mathbf{E}_{THz} \parallel (a, b)$, $\mathbf{H} \parallel c$). With increasing the magnetic field, the main pulse (below 4 ps) increases, while the extended-time oscillations lose intensity, c.f. Fig. 5.29a. In the absorption coefficient, Fig. 5.29b, this field dependency corresponds to a decrease of the continuum-like feature and the peak-like contributions between $30 - 40 \text{ cm}^{-1}$ as expected from the spin-wave theory. As well, the phonon-tail (above 40 cm^{-1}) slightly shifts to lower frequencies. The measurements were repeated in Voigt geometry ($\mathbf{E}_{THz} \parallel (a, b)$, $\mathbf{H} \perp \mathbf{k}_{THz}$), see Fig. 5.30. In general, a similar field dependence but significant weaker compared to the Faraday geometry was observed.

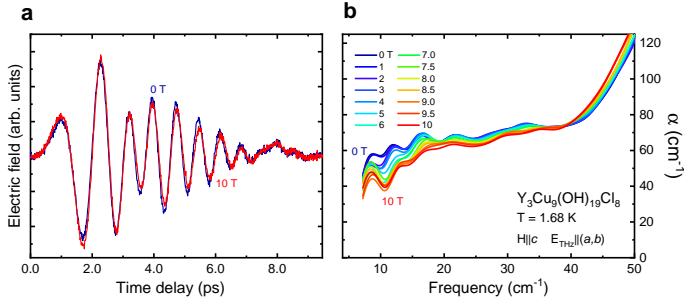


Figure 5.29: **Magneto-optical THz-TDS result over the full magnetic field range.** (a,b) Time domain electric field and absorption coefficient in Faraday geometry ($\mathbf{E}_{THz} \parallel (a, b)$, $\mathbf{H} \parallel c$) at $T = 1.68$ K, respectively. Reprinted with permission from Ref. [1].

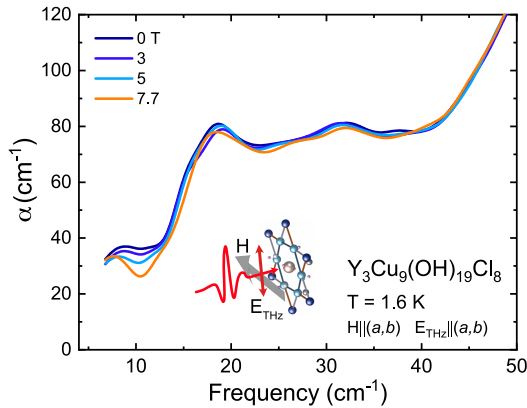


Figure 5.30: **Magneto-optical THz-TDS result in Voigt geometry.** Absorption coefficient in Voigt geometry ($\mathbf{E}_{THz} \parallel (a, b)$, $\mathbf{H} \perp \mathbf{k}_{THz}$) at $T = 1.6$ K. A qualitatively similar field dependence compared to measurements in Faraday geometry is observed. However, the suppression is significantly weaker compared to the previous results. Due to technical reasons the maximum field strength is around 8 T in this geometry.

5.11.3 Phase diagram of the distorted kagome antiferromagnet

The distorted $S = 1/2$ kagome model was investigated in Ref. [7] using a model of three nearest-neighbor antiferromagnetic Heisenberg couplings: J , J_{\square} , J' , Fig. 5.31a. By varying the coupling strengths the theoretical study predicts a rich magnetic phase diagram (see Fig. 5.31b), including $Q = (1/3, 1/3)$, $Q = 0$ phases, and a classical spin liquid. Fig. 5.31c depicts the non-collinear coplanar $Q = (1/3, 1/3)$ phases in the two limits within $J' \rightarrow 0$. For $J_{\square} = J$ the spins are alternating around the hexagons in certain patterns: green, blue, and red spins. Neighboring hexagons are coupled to each other via slave spins (whose directions are fully determined by the neighboring hexagons). In the limit $J \gg J_{\square}$ a $\sqrt{3} \times \sqrt{3}$ trimer phase stabilizes. For $J, J' \gg J_{\square}$ a collinear $Q = 0$ phase is characterized by a parallel alignment of spins within the hexagons and an anti-alignment of other spins. In between these phases a classical spin liquid, that is, a degenerate manifold of non-coplanar ground states is located.

5.11.4 Details of the linear spin-wave theory calculations

Linear spin-wave theory (LSWT) was performed by A. Razpopov and R. Valentí to calculate the magnon dispersion and magnon density of states (SpinW 3.0 [211]). For Y-kapellasite the effective Hamiltonian is given by a spin-1/2 Heisenberg Hamiltonian [7]:

$$H = \sum_{\langle i,j \rangle} J_{i,j} \mathbf{S}_i \mathbf{S}_j, \quad (5.2)$$

where the sum goes over the first nearest neighbors (NN). Lattice distortions lead to three distinct nearest-neighbor couplings: $J = 154.4$ K, $J_{\square} = 134.2$ K, and $J' = 8.7$ K. These were calculated via DFT+U and the total energy mapping analysis [7]. As introduced above, the obtained classical ground state is given by a coplanar state with an ordering vector $Q = (1/3, 1/3)$. The magnon energy dispersion was calculated on 1000

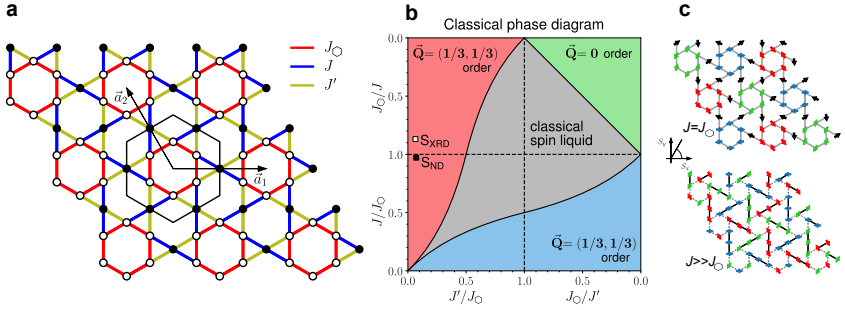


Figure 5.31: **Magnetic phases of the distorted kagome antiferromagnet (Ref. [7]).** (a) Crystallographic distortion introduces three distinct nearest-neighbor coupling: J , J_O , J' . (b) Varying these couplings, a rich magnetic phase diagram opens, including $Q = (1/3, 1/3)$, $Q = 0$ phases and a classical spin liquid. The non-collinear coplanar $Q = (1/3, 1/3)$ phases are stabilized for the case $J' \rightarrow 0$ (red area) or $J \rightarrow 0$ (blue area). For $J, J' \gg J_O$ a collinear $Q = 0$ order evolves. Two coupling sets for Y-kapellasite are depicted by empty and filled squares within the $Q = (1/3, 1/3)$ order. S_{ND} corresponds to powder structure data [22] and S_{XRD} is the single crystal set [21]. (c) Magnetic $Q = (1/3, 1/3)$ order, upper panel: $J_O = J$ (corresponding to red area in the phase diagram), lower panel: $J \gg J_O$. Adapted with permission from Ref. [7].

k-points along the path Γ -K-M- Γ . Furthermore, the magnon density of states was calculated on a $100 \times 100 \times 100$ k-mesh by the definition:

$$DOS(E) = \frac{1}{N} \sum_i^N \delta(E - E_i), \quad (5.3)$$

where E is the energy and E_i is the magnon energy with momentum \mathbf{q} . The Dirac delta function was approximated by a Lorentzian function

$$\delta_\epsilon(x) = \frac{1}{\pi} \frac{\epsilon}{x^2 + \epsilon^2}, \quad (5.4)$$

with $\epsilon = 0.01$ and energy resolution of 0.01 meV.

Note that for simplicity, no excitation probabilities or similar weighting factors for different positions in the BZ have been used. For instance, in the Raman two-magnon process it is assumed that the excitation

probability decreases for higher momenta [96], resulting in an asymmetric spectral shape. Nevertheless, there is a remarkable agreement between experiment and theory already at this level.

5.11.5 Linear spin-wave theory calculations over an extended range

Fig. 5.32 shows the spin dispersion and spin density of states over an extended energy range obtained from linear spin-wave theory (LSWT). Besides the three-peak structure mentioned above, there are several high-energy peaks in the SDOS. For the comparison between the $\mathbf{q} \approx 0$ excitation and multi-center magnon excitation ($\Delta\mathbf{q} \approx 0$), the corresponding SDOS curves ($\mathbf{q} = 0$ and over the entire Brillouin zone) are displayed in Fig. 5.32 (left panel). The $\mathbf{q} = 0$ SDOS mainly consists of three excitations ($E = 0$ meV, i.e., Goldstone mode, around $E = 7.4$ meV, and $E = 8.4$ meV). Note that no excitations are expected in the experimental range (1 - 6 meV) within the $\mathbf{q} = 0$ limit which calls for the multi-center magnon picture facilitating the $\Delta\mathbf{q} = 0$ process. The latter two, $\mathbf{q} = 0$ magnons, $E = 7.4$ meV and $E = 8.4$ meV, are located in the energy-range of the far-infrared phonon modes. They might be related to spin-phonon coupling as suggested above.

5.11.6 Calculation of χ_m''

To confirm the spectral shape of the multi-center magnon and further compare directly between experiment and theory, the imaginary part of the frequency-dependent magnetic susceptibility $\chi_m'' = \text{Im}\{\tilde{\chi}_m(\omega)\}$ expected for the multi-center magnon absorption was calculated using the following relation [43]:

$$\text{Im}\{\tilde{\chi}_m(\omega)\} = \gamma \sum_q \sum_{\alpha,\beta} h_\alpha h_\beta \text{Im}\{\chi_{\alpha,\beta}^{SS}(q, \omega)\}, \quad (5.5)$$

where γ is a constant, q is the momentum in the extended Brillouin zone, the summation α and β goes over the Cartesian components, $\chi_{\alpha,\beta}^{SS}(q, \omega)$ is the spin susceptibility, and h is the orientation of the THz magnetic

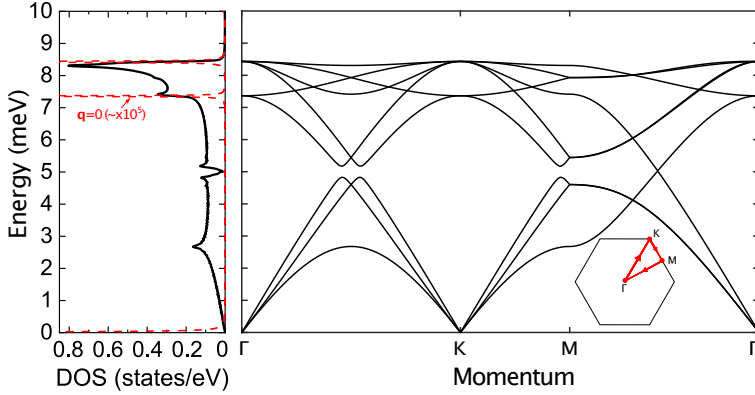


Figure 5.32: **LSWT calculations.** Left panel: DOS, black line: Integrated over the full Brillouin zone and red dashed line: $\mathbf{q} = 0$ contribution (scaled by a factor of $\sim 10^5$). Right panel: LSWT dispersion over an extended energy range. The inset shows the first Brillouin zone. The magnon dispersion has been calculated along the red arrows. Reprinted with permission from Ref. [1]. Calculated by A. Razpopov and R. Valentí.

field. At zero temperature the imaginary part of the spin susceptibility is related to the spin-spin correlation function $S_{\alpha,\beta}$:

$$\text{Im}\{\chi_{\alpha,\beta}^{SS}(q, \omega)\} = S_{\alpha,\beta}(q, \omega), \quad (5.6)$$

where the spin-spin correlation function was computed within the SpinW 3.0 framework [211]. The energy resolution of $\text{Im}\{\tilde{\chi}_m(\omega)\}$ is 0.1 meV with broadening of 0.1. Note that the Eq. 5.5 contains the sum over the full BZ. This is necessary to compare with the multi-center magnon picture. For instance, in the case of a multimagnon decay mechanism, see Ref. [45], only the limit $q \rightarrow 0$ was considered. Results are shown in Fig. 5.33. As discussed above, the experimental and theoretical energy scales are slightly shifted with respect to each other (about 1 meV). In the calculation, a pronounced, asymmetric peak (at around 2.7 meV), corresponding to the first peak in SDOS (same energy) is well-reproduced. Comparing within the experimentally accessible range, the overall shape shows a nice agreement including the double peak/ dip-like structure (around 4 to 4.6 meV in experiment, 5 meV in calculation) validating the multi-magnon scenario once more. The calculation shows a low-energy

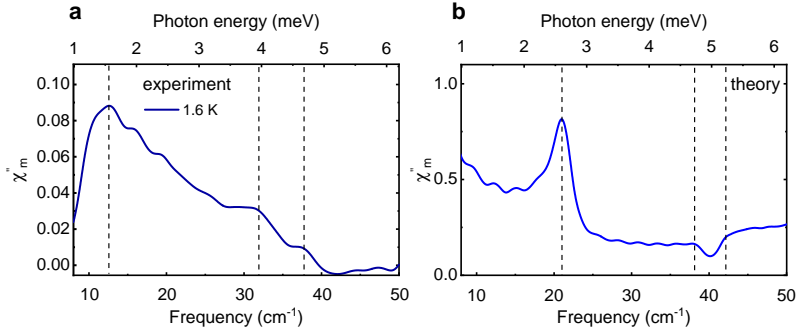


Figure 5.33: **Comparison between (a) experimentally and (b) theoretically determined dynamic magnetic susceptibility χ''_m .** All experimental features are reproduced by the calculation. Note that the energy scale between experiment and theory is shifted by a small offset of about 1 meV. Reprinted with permission from Ref. [1]. (b) Calculated by A. Razopopov and R. Valentí.

contribution (below 2 meV). This feature is outside the experimental range, but perhaps the extra broadening of the experimental peak might already contain the effect of this contribution.

5.11.7 Linear spin-wave theory calculations under magnetic field

Fig. 5.34 shows the calculated spin dispersion under external magnetic field. With increasing magnetic fields, the low-energy dispersion (0 to 3 meV) becomes gapped at the Γ and K points and shifts to higher energies, partially lifting the degeneracy of the three lowest magnon bands. As well, shifts of the characteristic energy scales (between 3 and 6 meV, colored dashed lines), discussed above, to higher energies are observable. The corresponding SDOS is shown in Fig. 5.35. Here, the shifting of the weight to higher energies for increased magnetic field is evident. In addition to the discussion above, here the changes at the higher energies (between 6 and 10 meV) should be considered. At $H = 0$ the SDOS shows a sharp peak at around 8.3 meV. Under magnetic field the peak gets suppressed and its weight gets distributed over a larger energy range

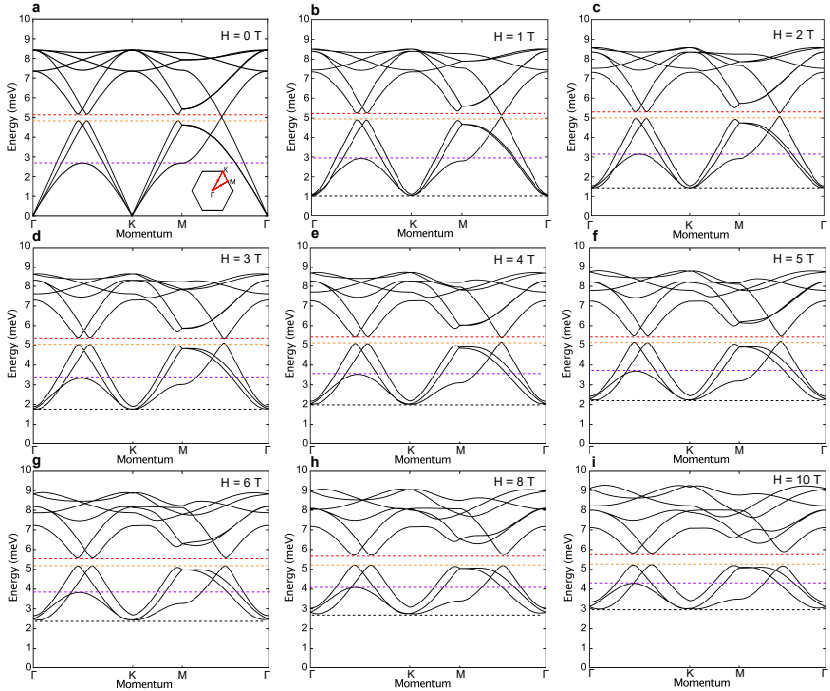


Figure 5.34: **LSWT calculations with magnetic field.** (a-i) Dispersion in the first Brillouin zone (see inset of (a) for calculated path) with selected magnetic fields. Characteristic energy scales, discussed in the main text, are highlighted by colored dashed lines. Black dashed line: Minima of the Γ and K points. Reprinted with permission from Ref. [1]. Calculated by A. Razpopov and R. Valentí.

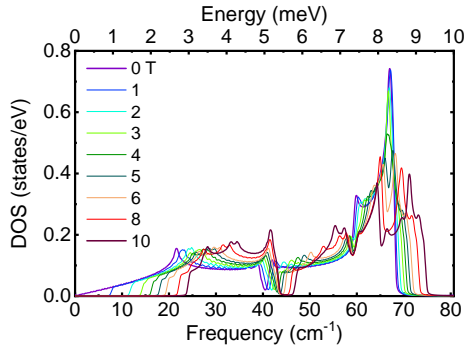


Figure 5.35: **SDOS with magnetic field.** Under magnetic field the SDOS becomes gapped and weight shifts to higher energies. Furthermore, between 6 and 10 meV, the weight gets distributed over a wider energy range. Reprinted with permission from Ref. [1]. Calculated by A. Razpopov and R. Valentí.

leading to an increase of the SDOS at around 6.8 meV / 55 cm⁻¹, i.e., the range of the lowest phonon tail. This field evolution might explain the shift of the phonon tail under magnetic field to lower energies, as observed in the magneto-THz experiment (see above).

5.11.8 Two-center magnon and three-center magnon excitation

For multi-center magnon absorption, i.e., the simultaneous flip of multiple spins by one photon, possible absorption can be either two-center or three-center magnon excitations. For each case, the spin selection rule for linearly polarized THz light ($\Delta S = 0$ [229, 230]) in the magnetic ground state of Y-kapellasite are going to be considered. The two-center magnon excites two magnons simultaneously (left panel of Fig. 5.36). Two scenarios are considered: two magnon excitations in one hexagon or two magnon excitations in different hexagons. Within a single hexagon, the $\Delta S = 0$ selection rule is satisfied if two spins of opposite sign are flipped simultaneously. However, excitations comprising two different hexagons are forbidden. Here, the non-collinearity of the magnetic ground state results in $\Delta S = \pm 1$. For the three-center magnon, the situation is

reversed (right panel of Fig. 5.36). Three spin flips inside a single hexagon cannot satisfy the selection rule but result in spin momentum changes of higher order. However, if one spins in each of the three different hexagons is flipped, the net spin momentum does not change.

Therefore, for linearly polarized light the spin selection rule allows two cases: two-center magnon in one hexagon or three-center magnon that involves three different hexagons. Between these two, flipping one spin in each hexagon (three-center magnon) seems to be energetically more favorable. The high-field magnetization experiment (see above) supports this idea by showing a $1/6$ plateau. Hence, three-center magnon, involving one spin-flip in each of the three different hexagon, is most likely the main contribution of the THz absorption. In order to fully exclude contributions from the spin-allowed two-center process, complete theoretical considerations of the involved selection rules are necessary. This remains the focus of a future study.

Although considering the spin selection rule further insight on the multi-center magnon absorption can be gained, it is not fully clear at this point whether such selection has to hold in general. For instance, magnon generation is not necessary bound to spin selection, as recently proved [79]. However, such a deep theoretical understanding needs a revised theoretical picture and therefore remains for further studies.

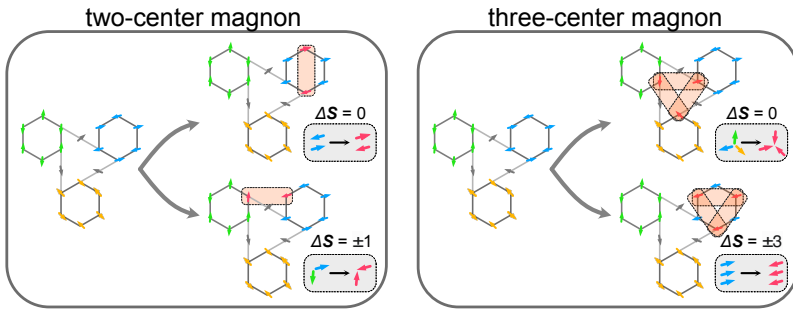


Figure 5.36: **Possible multi-center magnon absorptions: two-center and three-center magnon in Y-kapellasite.** Left panel: two-center magnon (red-shaded area) involving the simultaneous creation of two magnons (spin flips, grey-shaded inset) in one hexagon with $\Delta S = 0$ or a creation of two magnons in two different hexagons, $\Delta S = \pm 1$. Right panel: three-center magnon. Here, the creation of three magnons in three different hexagons gives $\Delta S = 0$, whereas three magnons in the same hexagons yield $\Delta S = \pm 3$. Note that for the $\Delta S = \pm 1$ / $\Delta S = \pm 3$ cases only one of the two possible spin-flip pictures is sketched. Reprinted with permission from Ref. [1].

6 Results III: Averievite

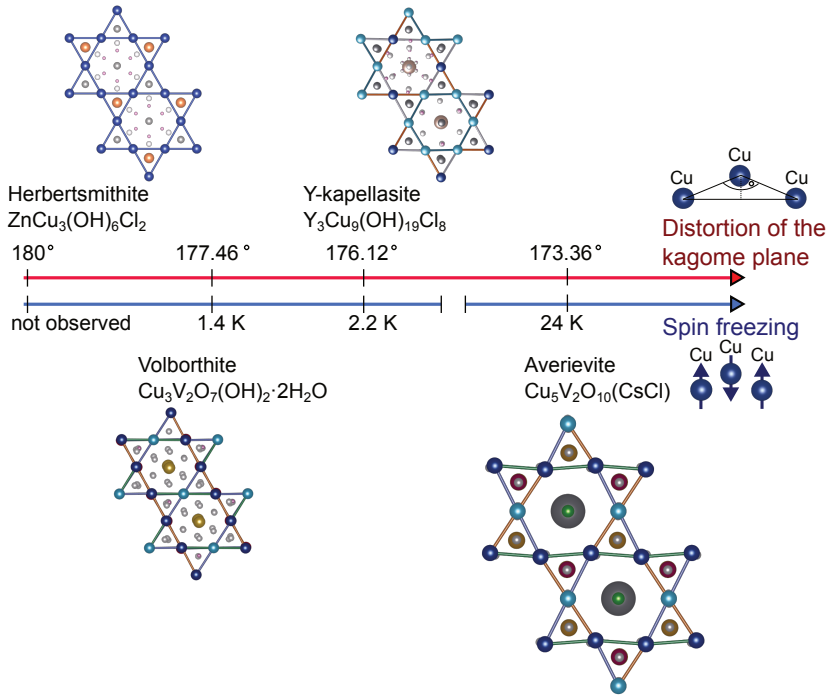


Figure 6.1: **Structural distortion and spin freezing on the kagome lattice.** Structures are based on Refs. [19, 21, 23, 42].

This chapter is a modified version of the author's publication (Ref. [2], main text and supplemental materials).¹

Increasing the distortion of the kagome lattice further, see Fig. 6.1, in this chapter, the physics of $\text{Cu}_{5-x}\text{Zn}_x\text{V}_2\text{O}_{10}(\text{CsCl})$ is explored by employing THz time-domain spectroscopy (THz-TDS). Of particular interest here are magnetic resonances [232, 233] that are induced by the magnetic field of the THz light over a Zeeman torque. When probed by THz-TDS these excitations show up as a free induction decay with a characteristic time scale [62, 66–69, 93, 234, 235]. For $x = 0$, $\text{Cu}_5\text{V}_2\text{O}_{10}(\text{CsCl})$, multiple sharp resonance modes were observed that develop with the onset of short-range magnetic interactions ($T_{\text{SR}} \approx 60$ K) with pronounced extended-time oscillations, a fingerprint of magnetic THz resonances [68, 69]. The magneto-THz investigation further clarifies the magnetic origin of these features. As frustration disturbs the ordered ground state in Zn-substituted Averievite (undistorted kagome lattices), magnetic resonances get suppressed, leaving a featureless response (other than the electronic/phononic background) reminiscent of quantum spin liquids [15, 16]. The false-contour plot of THz IA in Fig. 6.2d summarizes the results. It will be shown that THz IA captures magnetic and structural phases successfully. Note that if not particularly indicated, measurements are performed on powder samples.

Abstract: Time-domain magneto-THz spectroscopy is utilized to study

¹"Magnetic terahertz resonances above the Néel temperature in the frustrated kagome antiferromagnet averievite", *Phys. Rev. B* **105**, L060410 (2022)

co-authored with Seulki Roh, Andrej Pustogow, Hong Zheng, John F. Mitchell, Martin Dressel.

Reprinted with permission from Ref. [2]. Copyright (2022) by the American Physical Society. Some passages have been taken verbatim, others are edited/ expanded. There will be no additional citation or other marks in the text for verbatim copied texts or edits from Ref. [2].

Author contributions: T.B. performed the THz and ESR measurements and analyzed the data. T.B. and S.R. performed the magneto-THz measurements. J.F.M, H.Z. grew the samples and did the structural/ magnetic characterization. A.P., J.F.M. initiated the project. T.B. wrote the manuscript with input from all authors. S.R., M.D. supervised the project.

Additional material in this chapter: Infrared measurements were performed within the scope of Veit Kilian Kutzner's Bachelor's thesis [231], supervised by Tobias Biesner. Dielectric measurements were performed by Tobias Biesner. Additional magnetic and structural characterizations are provided by John F. Mitchell.

the frustrated magnet Averievite $\text{Cu}_{5-x}\text{Zn}_x\text{V}_2\text{O}_{10}(\text{CsCl})$. Pronounced THz resonances are observed in unsubstituted samples ($x = 0$) when cooling below the onset of short-range magnetic correlations. The influence of external magnetic effects confirms the magnetic origin of these resonances. Increasing Zn substitution suppresses the resonances, as frustration effects dominate, reflecting the non-magnetic phases for $x > 0.25$ compounds. The temperature evolution of the THz spectra is complemented with electron spin resonance spectroscopy. This comparison allows a direct probe of the different contributions from magnetic order, frustration, and structural properties in the phase diagram of Averievite. The results illustrate the effect of magnetic interactions in THz spectra of frustrated magnets.

6.1 Introduction of the material

Averievite, $\text{Cu}_5\text{V}_2\text{O}_{10}(\text{CsCl})$, constitutes a very particular case [23, 236–238] because a frustrated $\text{Cu}_3\text{O}_2\text{Cl}$ kagome layer is sandwiched between CuVO_3 honeycomb sublattices [see Figs. 6.2a-c]. The coexistence of a second distinct layer offers two distinguishable copper sites with a square planar and a trigonal bipyramidal coordination for the kagome and honeycomb layers, respectively. Above $T = 310$ K, the trigonal $P\bar{3}m1$ structure features an isotropic kagome network. However, upon cooling, the system enters a monoclinic $P2_1/c$ spacegroup, distorting the kagome geometry. The second transition occurs, below $T_S = 127$ K, to an unresolved structure [23]. Susceptibility measurements reveal strong antiferromagnetic couplings with a Curie-Weiss temperature of $\Theta_{CW} = 185$ K.

However, the compound freezes into long-range order only below $T_N = 24$ K, suggesting a moderate degree of frustration and the onset of short-range magnetic correlations well above T_N (see Fig. 6.2d). The magnetic entropy assigned with this transition ($\Delta S_{mag} = 1.1$ J/mol K) represents only 3.8 % of the expected $R \ln(2)$, pointing to remaining spin fluctuations even in the ordered phase. Moreover, susceptibility measurements do not show any dependence on the cooling protocol (field-cooled/ zero-field-cooled data), excluding the possibility of a spin-glass transition [23]. Theoretical investigations suggest a herringbone

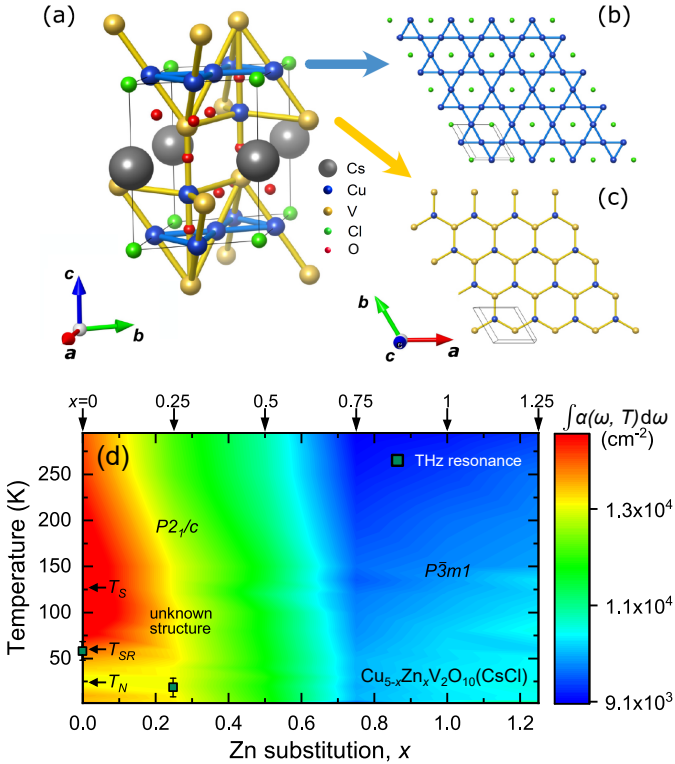


Figure 6.2: **Phases of the Averievite $\text{Cu}_{5-x}\text{Zn}_x\text{V}_2\text{O}_{10}(\text{CsCl})$.** The $P\bar{3}m1$ structure is found for $x = 0$ only for $T > 310$ K while for $x = 1$ in the entire temperature range. (a) A single unit cell representation. Two different in-plane (ab) sheets are stacked along the c direction. One is the kagome structure (b) composed of Cu atoms and the other is a honeycomb lattice (c) consisting of V and Cu. Overall, Averievite crystallizes in alternating kagome and two honeycomb lattices. (d) Structural and magnetic properties of Averievite. $T_S = 127$ K, structural transition; $T_{SR} \approx 60$ K, onset of short-range correlations; $T_N = 24$ K, long-range order. False-color plot is based on the integrated absorption coefficient $\int \alpha(\omega, T) d\omega$ obtained for different Zn concentrations (indicated by vertical arrows at the top). Dark green points: Onset of magnetic THz resonances. Reprinted with permission from Ref. [2]. Copyright (2022) by the American Physical Society.

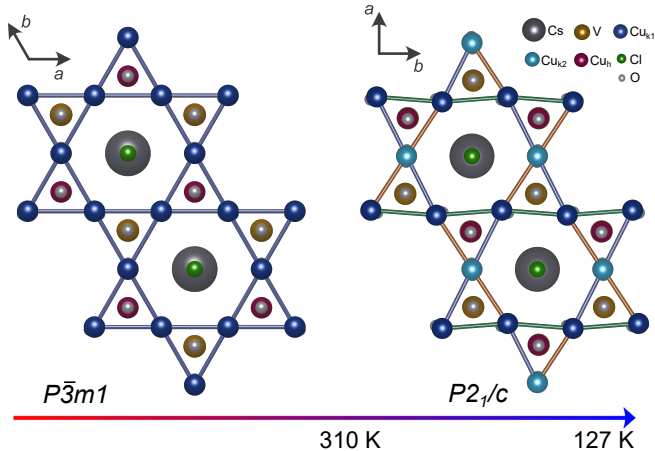


Figure 6.3: **Crystal structures and temperature-dependent phases of $\text{Cu}_5\text{V}_2\text{O}_{10}(\text{CsCl})$.** Upon cooling below $T = 310$ K, the crystal structure ($P\bar{3}m1$) undergoes a monoclinic distortion to $P2_1/c$ structure. Below $T_S = 127$ K there is an unknown structure. Structures are based on Ref. [23].

valence band solid [147, 239]. Magnetic nearest-neighbor coupling was calculated to be the dominant magnetic exchange of $J_1 = 227.8$ K within the kagome layer (in-plane) and one along the out-of-plane, between kagome and honeycomb lattice, as $J_2 = 51.7$ K [239], consistent with the experimentally determined Curie-Weiss temperature [23]. Further magnetic coupling between the two kagome layers is sufficiently suppressed due to intercalated CsO_2 sites.

An additional degree of freedom is provided by chemical substitution; to that end different strategies were explored theoretically and experimentally [23, 239, 240]. Among them, exchanging Cu by non-magnetic Zn in $\text{Cu}_{5-x}\text{Zn}_x\text{V}_2\text{O}_{10}(\text{CsCl})$ was found to replace the copper ions in the honeycomb layers. This substitution reduces the magnetic interlayer coupling preserving the highly frustrated $S = 1/2$ kagome physics with no indication of long-range order or spin-glass behavior down to $T = 2$ K. Furthermore, in $\text{Cu}_4\text{Zn}_1\text{V}_2\text{O}_{10}(\text{CsCl})$ ($x = 1$) the monoclinic distortion upon cooling is absent, such that the compound remains in the more symmetric $P\bar{3}m1$ structure with an undistorted kagome lattice down

to the lowest measured temperature [cf. Fig. 6.2d]. The specific heat shows a gapless behavior with a $C_p/T \sim T^2$ temperature dependence below $T = 10$ K [23]. This not only promotes Zn-substituted Averievite as a QSL candidate, but the entire Averievite family can be taken as a platform for investigating the magnetic ground state under frustration.

6.2 Experimental methods

Powder preparation Averievite powders of various substitution rates ($x = 0, 0.25, 0.50, 0.75, 1, 1.25$) were prepared and characterized by J.F. Mitchell and H. Zheng as described previously [23]. For THz measurements pellets with a typical thickness of $100 \mu\text{m}$, weight of 10 mg and diameter of 5 mm were pressed from fine powder (see appendix for further information). For FTIR reflectance measurements thicker pellets (around 4 mm thickness, 18 mg weight and 3 mm diameter) were prepared. Dielectric measurements were performed on thicker samples as well (around 2 mm thickness, 10 mg weight and 3 mm diameter).

Single crystal synthesis The single crystals were provided by Pascal Puphal (Max Planck Institute for Solid State Research, Stuttgart, Germany). The synthesis remains to be published.

THz-TDS measurements The THz measurements were performed in transmission geometry. All specimens were measured with a time-domain THz spectrometer (TeraView TeraPulse 4000) attaching a homemade He-bath cryostat and a superconducting magnet (Oxford Instruments). The magneto-THz experiments were performed in Faraday geometry (see appendix for further information). The recorded time varying electric fields were further analyzed by fast Fourier transformation (FFT) to obtain the frequency-domain spectra. From that the absorption coefficient $\alpha(\omega)$ is calculated via the well-known Beer-Lambert law: $\alpha(\omega) = -\ln\{Tr(\omega)\}/d$, where Tr is the transmittance and d the sample thickness [82]. The integration of $\alpha(\omega)$ over frequency, $\int \alpha(\omega) d\omega$, thus is proportional to the optical spectral weight [81].

ESR measurements Furthermore, electron spin resonance (ESR) measurements were conducted via a continuous-wave X-band spectrometer (Bruker EMXplus) equipped with a He-flow cryostat (Oxford Instruments, ESR 900) at 9.8 GHz. The spin susceptibility χ_s^e is obtained by double integration of the derivative of the microwave power with respect to the magnetic field, dP/dH , typically recorded as a function of temperature T .

FTIR measurements FTIR measurements were performed in reflection geometry (nearly normal incidence) on thick pellets (several mm thickness) employing a Bruker Vertex 80v spectrometer, equipped with an Hyperion infrared microscope, and a custom-made LiHe-flow cryostat (330 K to 10 K). Measurements over the accessible spectral range were successively carried out using a Bolometer and MCT, InSb, and Si detectors. The spectra were referenced against a gold mirror up to the near-infrared range and a silver mirror above in order to avoid the plasma edge of gold. Data are corrected by the mirror reflectance. A Kramers-Kronig transformation was used to obtain the optical conductivity, σ_1 [81, 82].

Dielectric measurements Dielectric spectroscopy was performed in the range 40 Hz to 10 MHz using an Agilent 4294A complex impedance analyzer together with a LiHe-flow cryostat (325 K to 6 K). The samples were sandwiched between electrodes (gold wires and silver paste), i.e., dielectric in a capacitor. Spectra were corrected by the relevant compensation curves.

6.3 Structural and magnetic characterization

A comprehensive structural and magnetic characterization is presented in Ref. [23] and is summarized above. Here, additional details, provided by J.F. Mitchell, are going to be presented. Corroborating the THz-TDS measurements (vanishing magnetic resonance for $x > 0.25$), the magnetic characterization shows two distinct regimes with a crossover in between $x = 0.25$ and $x = 0.5$ (see the Curie-Weiss temperature for different Zn substitutions in Fig. 6.4).

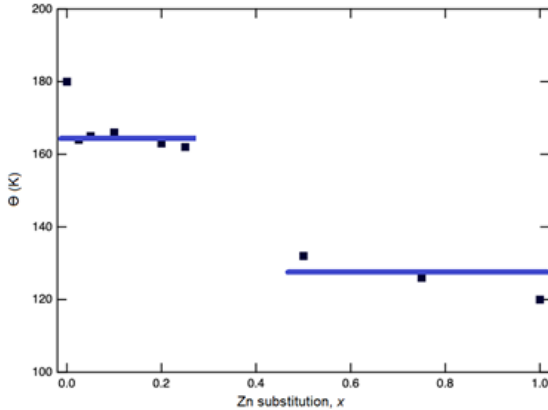


Figure 6.4: **Curie-Weiss temperature extracted from the susceptibility measurements.** The magnetic characterization shows a clear drop in the Curie-Weiss temperature for $x > 0.25$, in accordance with the THz-TDS study. Provided by J. F. Mitchell.

In Fig. 6.5 and Fig. 6.6 results of synchrotron x-ray powder diffraction experiments are shown. At room temperature, the $P2_1/c$ phase appears in the diffraction patterns through $x = 0.25$ (peaks around $2\Theta \approx 6.3^\circ$, Fig. 6.5). It is absent at $x = 0.5$ and above. However, samples beyond $x = 0.2$ are biphasic, making an exact determination of the phase boundaries complicated. Nevertheless, based on the diffraction data at $T = 100$ K the unknown low-temperature phase is unlikely for $x > 0.2$. For higher

Zn concentrations, the $P\bar{3}m1$ phase persists in the whole temperature range.

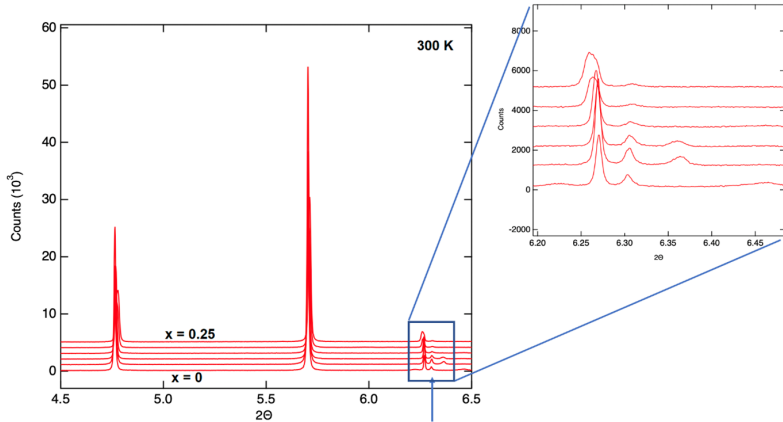


Figure 6.5: **Synchrotron x-ray powder diffraction data at $T = 300$ K.** Shown are different Zn substitutions ($x = 0, 0.025, 0.05, 0.1, 0.2,$ and $x = 0.25$). At 300 K, the $P2_1/c$ phase appears through $x = 0.25$ ($2\theta \approx 6.3^\circ$) and is absent for $x = 0.5$ and above (not shown). Provided by J. F. Mitchell.

The phase diagram, deduced from synchrotron x-ray powder diffraction, Fig. 6.7 resembles the color coding of the IA -based false-color plot (Fig. 6.2). Since the IA is sensitive to structural properties through spectral weight shifts, the false-color plot can trace the phase transitions.

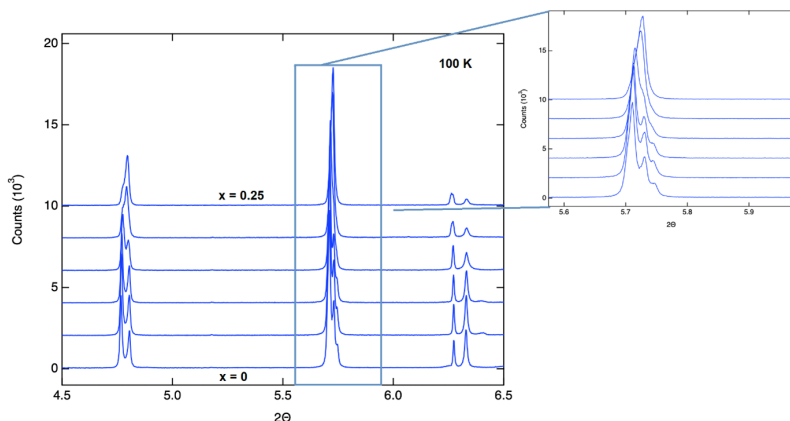


Figure 6.6: **Synchrotron x-ray powder diffraction data at $T = 100$ K.** Shown are different Zn substitutions ($x = 0, 0.025, 0.05, 0.1, 0.2$, and $x = 0.25$). Beyond $x \approx 0.2$, the unknown low-temperature phase disappears. Provided by J. F. Mitchell.

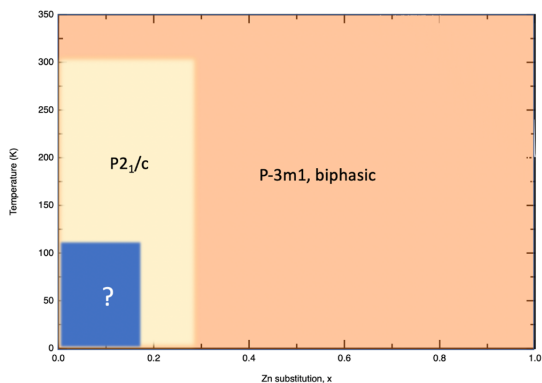


Figure 6.7: **Structural phases for different Zn substitutions as seen from x-ray powder diffraction.** The blue area represents the unknown low-temperature phase. Provided by J. F. Mitchell.

6.4 Phononic and dielectric properties

Results of the FTIR spectroscopy are shown in Fig. 6.8 and Fig. 6.9. Focusing on the far-infrared reflectance, Fig. 6.8 several phonon modes were observed. They exhibit no pronounced temperature dependence, but small blueshifts and sharpening upon cooling. As well, no clear change through the structural transitions ($T = 127$ K, 310 K) in the infrared range nor any indication of Brillouin zone folding, i.e., splitting/ newly appearing modes in the ordered phase ($T_N = 24$ K) were observed for the $x = 0$. Furthermore, there are minor variations for increasing Zn concentrations (modes around 200-300 cm^{-1}), i.e., a small blueshift of the modes around 200 cm^{-1} and suppression of a mode at around 300 cm^{-1} . Perhaps, this might originate from the different space group for $x = 1$ samples.

Fig. 6.9 displays reflectance and obtained optical conductivity in the entire measured frequency range. Besides the phonons in the far-infrared range, the first electronic transitions can be seen at around 6000 cm^{-1} (0.74 eV) with an onset at around 2500 cm^{-1} (0.3 eV). However, comparing the optical conductivity with the calculated bandstructure of Ref. [23] the calculated bandgap (assuming an onsite Coulomb repulsion of $U = 6$ eV): 1.4 eV for $x = 0$ and 1.7 eV for $x = 2$ Averievite does not match with the experimental observation. This could have several reasons. For instance, the onsite Coulomb repulsion could be overestimated in the calculation. On the other hand, it might be possible that the observed electronic transition at 0.3 eV is in fact related to ingap states. Note that the intensity (below 200 $\Omega^{-1} \text{cm}^{-1}$) is comparably low for an intersite transition/ optical gap. However, at this point scattering effects due to the powder cannot be excluded. While at low energies (far-infrared and THz range) scattering should not be involved, at higher energies, the wavelength can be on the order of the grain size (10000 cm^{-1} corresponds to 1 μm). Furthermore, there are several small features at around 1500, 1860, 2835, 2913, 3250 cm^{-1} . It is possible that these stem partially from the vibrations of the lighter ions (O, Cl). Moreover, there are atmospheric contributions, for instance, H_2O , CO_2 in this frequency range as well. It is likely, even after thorough evacuation of the cryostat, that the powder still contains small concentrations of these.

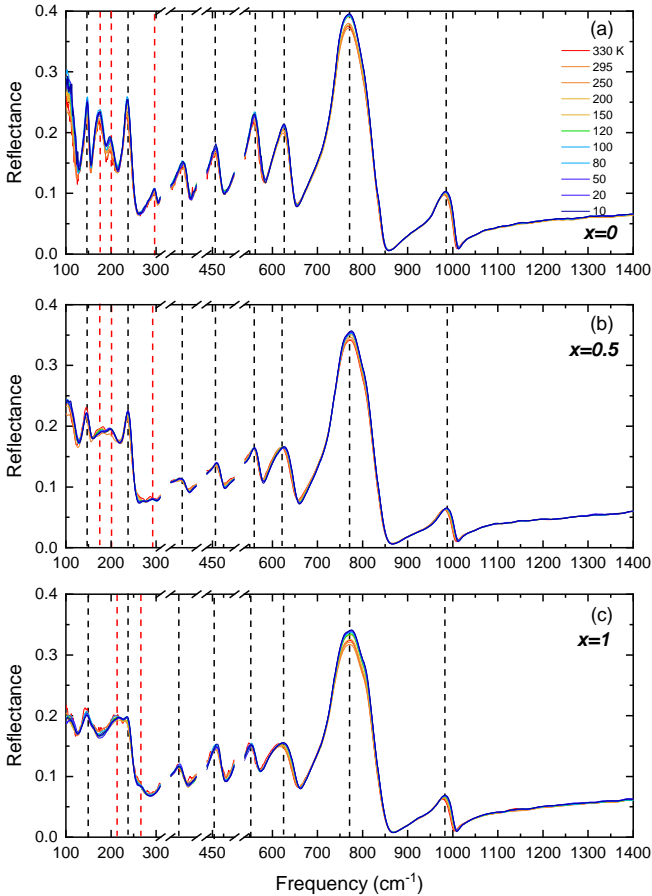


Figure 6.8: **Reflectance in the far-infrared infrared range (FTIR spectra) for selected Zn substitutions.** Several phonon modes are observed (dashed lines). In contrast to the THz phonons, the infrared modes do not show any strong temperature dependence. Slight variations with increasing Zn substitution are marked by dashed red lines while the dashed black lines represent modes that remain substitution independent. Data recorded by V. K. Kutzner under supervision of T. Biesner, first shown in [231].

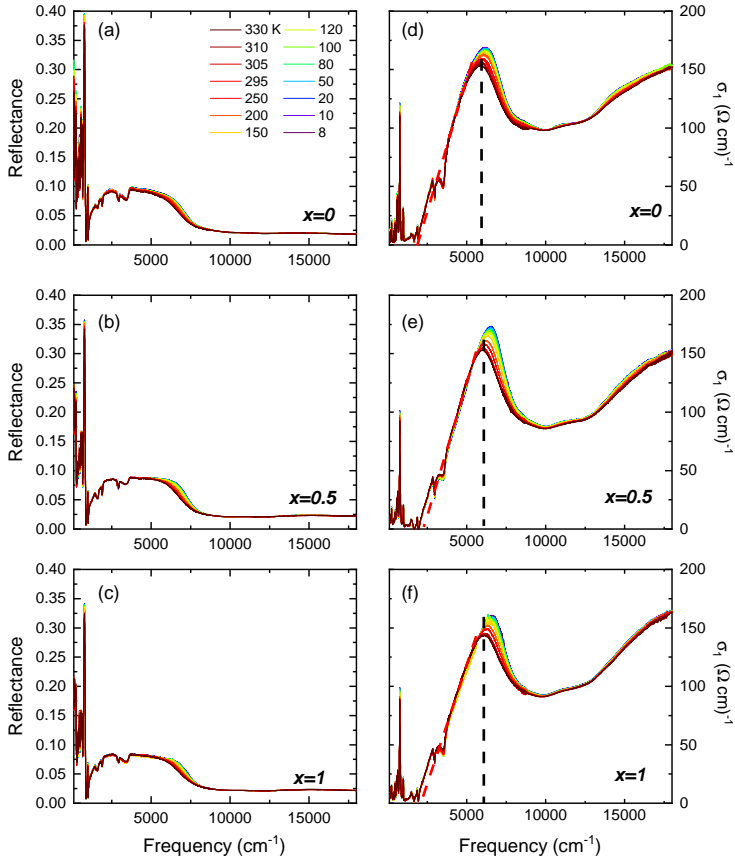


Figure 6.9: **Reflectance and optical conductivity for selected Zn substitutions.** The red dashed line represents the onset of the first electronic transition. Black dashed line: center frequency. Data recorded by V. K. Kutzner under supervision of T. Biesner, first shown in [231].

Furthermore, dielectric measurements at different frequencies (kHz to MHz) have been performed on powder samples. Fig. 6.10 shows the temperature-dependent electric permittivity at 1 MHz. For the $x = 0$ compound, a pronounced dielectric anomaly, i.e., a peaklike structure, centered at around $T = 80$ K emerges upon cooling. It shows a weak

hysteresis (cooling vs. warming). For increasing Zn substitution, the peak becomes suppressed and shifts toward lower temperatures, reaching around 30 K for $x = 1$. Note that the high-temperature response (a strong increase of the electric permittivity above 150 K) was not reproducible for different pellets/ contacts and therefore will not be discussed further. In general deviations in the high-temperature responses and a pronounced frequency dependence can be seen for samples causing an electrode polarization between the electrode/ sample interface [241, 242]; however, the reason in this case remains unknown.

The peaklike response is further analyzed with a Curie-Weiss fit of the high-temperature asymptotic (below 100 K): $\epsilon_1 = A + \frac{C}{T-T_C}$, where C is Curie-Weiss constant, T_C the transition temperature, and A a constant offset. Overall, the high-temperature asymptotic of the dielectric anomaly fits a Curie-Weiss law for $x = 0$ and lower Zn substitutions, $x < 0.75$, over an extended temperature range. However, increasing the Zn concentrations, the agreement weakens. Parameters of the fits are shown in Fig. 6.11. For increasing Zn substitution, the T_C and C decrease, i.e., the dielectric anomaly shifts to lower temperatures and loses intensity.

Fig. 6.12 shows the measurements over an extended frequency range, between 1.8 kHz and 2 MHz. In general, no pronounced dispersion is observed, but a subtle shift of the peaklike low-temperature anomaly to higher temperatures and a decrease of intensity for increasing frequency.

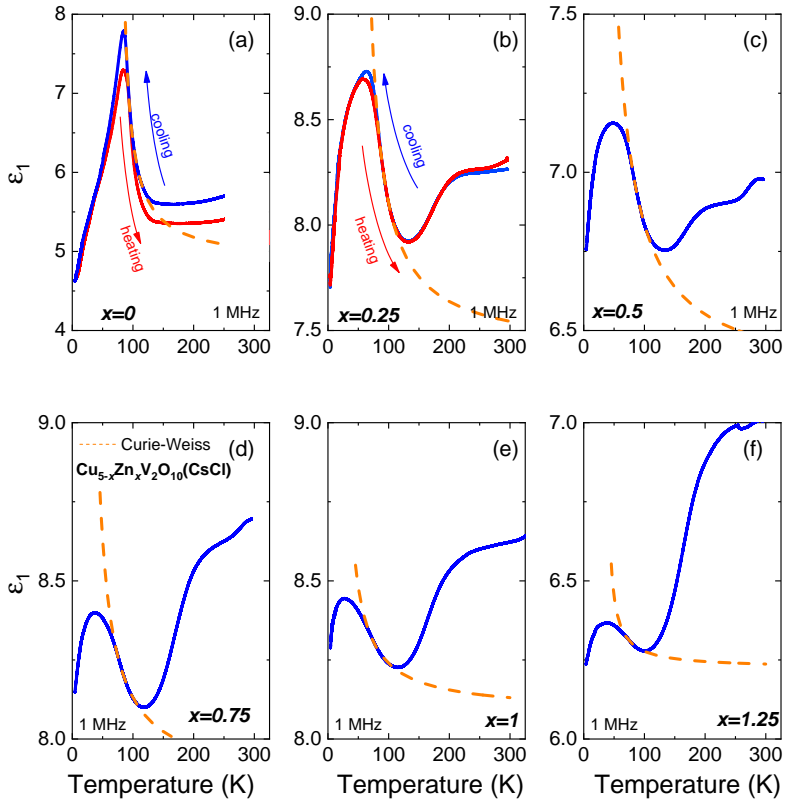


Figure 6.10: **Dielectric characterization of Averievite (temperature sweep)**. Electric permittivity as a function of temperature at 1 MHz. (a) For $x = 0$ a pronounced peak can be seen at around $T = 80$ K. As well it shows a slight hysteresis. (b-f) For higher Zn substitutions, the low-temperature peak gets strongly suppressed/ broadens and shifts to lower temperatures (around 30 K for $x = 1$). Furthermore, no hysteresis can be seen for $x > 0.25$. The orange dashed line represents a Curie-Weiss fit of the high-temperature wing.

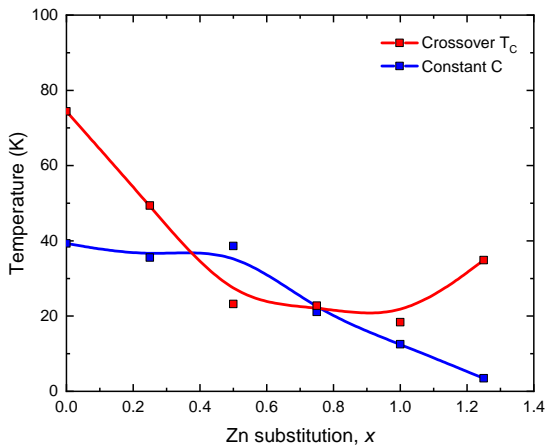


Figure 6.11: **Parameters of the Curie-Weiss fit.** With increasing Zn substitution, the crossover temperature T_C decreases, resembling a shift of the $T = 80$ K peak ($x = 0$) to lower temperatures. The reduction of the constant C can be interpreted as a reduced electric dipole moment.

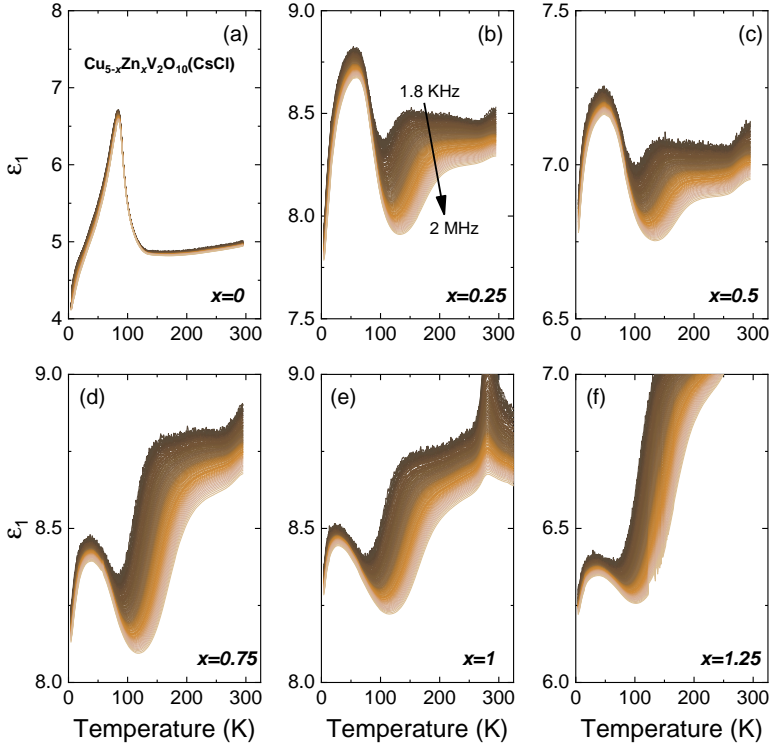


Figure 6.12: **Dielectric characterization of Averievite (frequency sweep).** (a-f) Electric permittivity as a function of temperature between 1.8 kHz and 2 MHz. In general, the low-temperature ($T = 80$ K) peak shows only a weak dispersion, in contrast to the response over 100 K.

To confirm the dielectric spectroscopy of powder samples, the measurements were repeated on single crystals ($x = 0$ and $x = 1$). Results are shown in Fig. 6.13. For $x = 0$ samples, Fig. 6.13a, the dielectric anomaly is observed as well. However, the peaklike contribution is centered at slightly lower temperatures ($T = 57$ K). Focusing on the $x = 1$ spectra, Fig. 6.13b, the feature is significantly suppressed and shifted to lower frequencies. Furthermore, the frequency dependence is analyzed for several selected temperatures. While the permittivity of $x = 0$ Averievite does only show a negligible frequency dependence, see Fig. 6.13c, the $x = 1$ compound shows a small increase in permittivity at lower frequencies ($\epsilon_1 \approx 12$ at 1 MHz compared to $\epsilon_1 \approx 14$ at 10 kHz), Fig. 6.13d. Overall, the dielectric investigation on single crystals confirms the powder results, presented above.

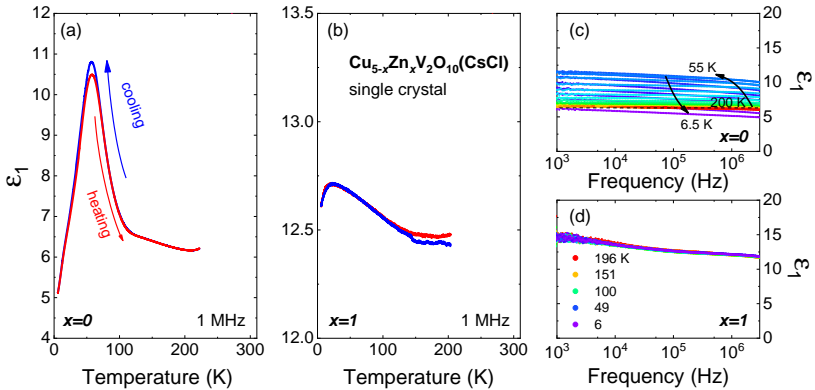


Figure 6.13: **Dielectric characterization of single-crystalline Averievite.** (a,b) Electric permittivity as a function of temperature at 1 MHz for $x = 0$ and $x = 1$ samples. Corroborating the previous measurements on powder samples (see results above), $x = 0$ single crystals show a dielectric anomaly (peaklike contribution) at around $T = 57$ K. For $x = 1$ the contribution is significantly suppressed and shifted to lower temperatures ($T = 23$ K). Frequency-dependent electric permittivity for (c) $x = 0$ and (d) $x = 1$ samples.

The observed dielectric anomaly resembles the peaklike behavior in permittivity generally observed at the ferroelectric phase transition. However, the $P2_1/c$ and $P\bar{3}m1$ phases are centrosymmetric, and thus forbid electric polarization. Nevertheless, the unknown low-temperature phase might in-

duce a distortion in $x = 0$ and $x = 0.25$ samples. In fact, such distortions are discussed for other kagome materials (see Ref. [147]). Furthermore, a dielectric anomaly is found for the case of Y-kapellasite as well (not presented). To understand the anomaly further investigations of the low-temperature structure, for instance, a comparison with single crystal XRD are necessary. This remains as an outlook for a further study.

6.5 Kagome and honeycomb copper sites: ESR characterization

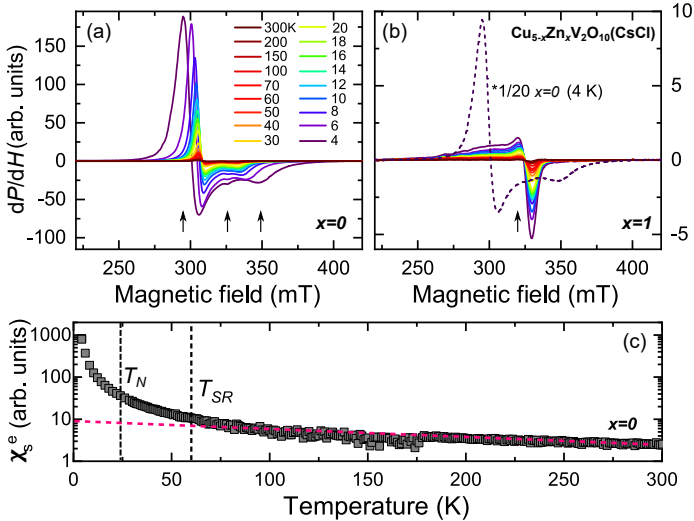


Figure 6.14: **X-band ESR spectra of Averievite with $x = 0$ and $x = 1$.** (a,b) Derivative of the absorbed microwave power with respect to the magnetic field recorded at different temperatures, as indicated. Upon cooling below 60 K, several strong Lorentzian modes are observed for $x = 0$. The spectral weight is significantly suppressed for the $x = 1$ compound. Panel (c) shows the electron-spin susceptibility $\chi_s^e(T)$ for the $x = 0$ compound obtained from ESR measurements. Vertical black dashed lines represent the $T_N = 24$ K and $T_{SR} \approx 60$ K. Colored dashed line represents the change of trend under the onset of short-range magnetic correlations. Reprinted with permission from Ref. [2]. Copyright (2022) by the American Physical Society.

To characterize the magnetism of Averievite, temperature-dependent ESR measurements in the X-band frequency were performed for $x = 0$ and $x = 1$ powders. The results are presented in Figs. 6.14a,b. In the $x = 0$ sample, three distinct Lorentzian modes can be clearly identified at $T \approx 60$ K, and their intensity strongly increases upon cooling. This splitting indicates the different magnetic contributions from kagome and honeycomb copper sites. Substituting Cu by Zn ($x = 1$) leads to an overall

suppression of spectral weight, i.e., a considerable change of magnetism for Zn-substituted samples. This result is in accord with susceptibility measurements [23], reporting a suppression of the magnetic order as the Zn concentration increases. Fig. 6.14c displays the temperature-dependent electron-spin susceptibility χ_s^e for the $x = 0$ compound, extracted from the ESR spectra. When T decreases, $\chi_s^e(T)$ starts to rise around 60 K, indicating the onset of short-range magnetic correlations/ short-range order. It further amplifies close to $T_N = 24$ K as magnetic interactions stabilize. These results yield two characteristic temperatures for magnetic properties of $x = 0$ Averievite: the onset of short-range correlations, $T_{\text{SR}} \approx 60$ K, and long-range order, $T_N = 24$ K.

6.6 Magnetic resonance in Averievite probed by THz-TDS

The frequency-dependent absorption coefficient $\alpha(\omega)$, obtained by THz-TDS, is presented in Fig. 6.15 for different Zn substitutions x . Overall, the spectra are characterized by an insulating response. At elevated temperatures, three maxima are present at around 15, 28, and 50 cm^{-1} for the $x = 0$ compound [Fig. 6.15a]. These features most likely stem from low-energy phonon modes because at THz frequencies no electronic contributions are expected due to the highly insulating nature of Averievite (see electronic responses above). Furthermore, these phonon modes are affected by Zn substitution (see Fig. 6.18). Here, the center frequencies are slightly higher compared to the unsubstituted compound. Especially, the 28 cm^{-1} peak exhibits a slight blueshift, likely due to the combined effect of Zn substitution on the lattice and different space groups of the $x = 0$ and $x = 1$ samples. The blueshift is expected due to the reduced bonding length (increased bonding force) of Zn compared to Cu. Therefore, it can be speculated that the phonons involve honeycomb and kagome sites (out-of-plane vibrations) or are associated with the distortion of the kagome lattice.

First the $x = 0$ spectra, displayed in Fig. 6.15a, are going to be discussed. It can be seen that the two latter peaks exhibit a significant temperature dependence when cooling down to $T \approx 100$ K. While the 28 cm^{-1} mode hardens, the 50 cm^{-1} feature moves to lower frequencies resulting in a

broad contribution centered at around 40 cm^{-1} . This broadening of the phonon modes upon cooling implies a lattice instability in the vicinity of the structural transition ($T_S = 127 \text{ K}$). The broad phonon contribution sustains its frequency and its intensity continuously grows with cooling down to 1.55 K .

Drastic changes are observed in $\alpha(\omega)$ when the temperature is reduced below 60 K , where short-range magnetic correlations appear: multiple well pronounced and sharp peaks emerge distributed over the entire THz range down to 19 cm^{-1} . Given the spectral form and rather abrupt temperature evolution of these features, a pure phononic origin seems very unlikely. More details will be discussed later. Interestingly, samples with intermediate substitution [$x = 0.25$ and 0.5 , presented in Figs. 6.15b,c] undergo a comparable phonon evolution implying that the structural instability still resides in these samples, possibly exhibiting a similar structural phase transition (weaker but with the same trend as in $x = 0$). The sharp resonances of the $x = 0$ sample, however, are totally absent when Zn substitution exceeds $x = 0.25$; cf. Figs. 6.15b-d. For high concentrations $x = 1$ and $x = 1.25$ [Figs. 6.15e,f], only a negligible temperature evolution of the phonon modes is observed, suggesting that no structural transition occurs with cooling. This is in accordance with the synchrotron powder diffraction [23]. These trends can also be followed in the integrated absorption coefficient, $\int \alpha(\omega, T) d\omega / \int \alpha(\omega, T = 295 \text{ K}) d\omega$, displayed in Fig. 6.15g. Indeed, for the $x = 0$ sample the temperature dependence clearly changes around $T_S = 127 \text{ K}$. Furthermore, the integrated absorption coefficient increases below $T_N = 24 \text{ K}$ indicating a close connection to the sharp peaklike features and the magnetic degree of freedom observed in the unsubstituted sample. For higher substitution rates, the absorption curves are rather monotonic without any noticeable change. This also reflects the fact that Zn substitution suppresses the structural transition as well as magnetic order.

In searching for the origin of the sharp low-temperature features of the $x = 0$ sample, the electric field of transmitted THz light in the time domain will be analyzed in more detail, Fig. 6.16a. At ambient temperature, the spectrum consists of the main pulse of the THz electric field, centered at around 3 ps . Decreasing the temperature below $T_{\text{SR}} \approx 60 \text{ K}$, additional oscillation features appear with longer periods (about 30 ps). Cooling down further to $T = 1.55 \text{ K}$, these oscillations become more prominent.

Especially below $T_N = 24$ K, an additional group of oscillations can be identified between 30 to 35 ps, increasing the sharpness of the peaklike features in Fig. 6.15a. The FFT analysis clearly shows that the phononic high-temperature response, i.e., the 15, 28, and 50 cm^{-1} features, is rather confined to the main pulse. However, the multiple sharp peaks in the low-temperature spectra correspond to the pronounced extended-time oscillation of the electric field. For the $x = 1$ sample these oscillations are absent, Fig. 6.16b, rendering a purely phonic response.

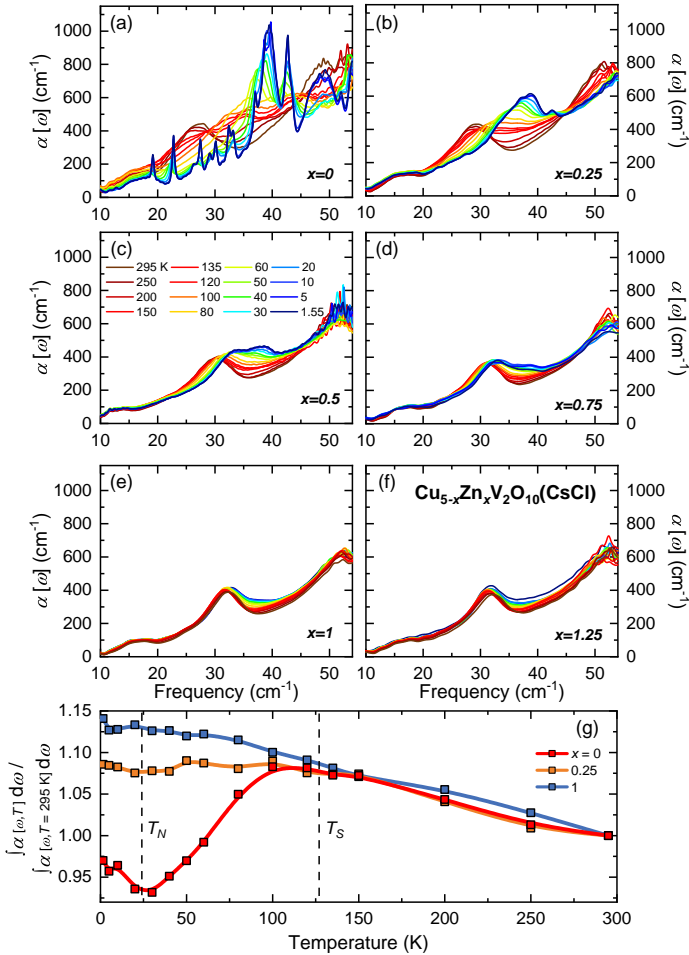


Figure 6.15: **THz-TDS spectra (absorption and IA)**. (a-f) Absorption coefficient, $\alpha(\omega)$ spectra of a series of $\text{Cu}_{5-x}\text{Zn}_x\text{V}_2\text{O}_{10}(\text{CsCl})$ powder samples with varied Zn contributions, obtained from THz-TDS. At room temperature, all compounds contain similar peaks at around 15, 28, and 50 cm^{-1} . Upon cooling through the structural transition, the lower concentrations $x < 0.75$ show pronounced changes. For $x = 0$ several sharp resonances develop below 60 K. (g) Frequency-integrated absorption coefficient (10 to 50 cm^{-1}) as a function of temperature for representative substitution, normalized by the 295 K data. Two vertical dashed lines represent T_N and T_S , respectively. Reprinted with permission from Ref. [2]. Copyright (2022) by the American Physical Society.

For the $x = 0$ compound, a three-dimensional false-color plot of $\alpha(\omega, T)$ is presented in Fig. 6.16c. Here, one can clearly separate the effects of the structural transition at $T_S = 127$ K, the spectral evolution in the vicinity of the short-range magnetic correlations, $T_{SR} \approx 60$ K, and the one related to long-range order below $T_N = 24$ K. The structural transition leads to a redistribution of spectral weight from the two phonon modes at 28 and 50 cm^{-1} to a new mode at 40 cm^{-1} . At T_{SR} the sharp peaklike contributions appear and becomes stronger toward lower temperatures. Some of the peaks (for instance, the one around 30 cm^{-1}) show additional sharpening when entering the long-range magnetically ordered phase below T_N . In general, however, only monotonic changes can be observed at T_N . This is reminiscent of the case of Y-kapllasite, presented in the previous chapter.

It is notable that the sharp spectral peaks – due to extended-time oscillations – emerge at the same temperature as magnetic short-range correlations. This fact is taken as strong evidence for the magnetic origin of these features. Indeed, THz-driven spin precession (magnetic resonance) has recently been reported in several magnetically ordered systems [66–69, 93, 235]. Here, the THz magnetic field adds a torque to the spins, resulting in a coherent precession of the magnetic moments. The emitted electromagnetic wave can be detected via a time-gated detection scheme, which allows to distinguish electronic and magnetic contributions by different timescales. Although the total magnetization vanishes for antiferromagnetic systems, the magnetic resonance is still expected to be driven by the staggered magnetic component, i.e., the Néel order \mathbf{n} [75]. The electromagnetic field emitted during the free induction decay has a distinguishable oscillation period regarding the decaying time of the precession, which is on the order of several tens of ps, whereas the electronic response of the material is confined to shorter times of the incident THz light (a few ps) [62]. The time-domain spectra of the $x = 0$ compound [Fig. 6.16a] show such a pronounced extended-time delay signal. The close temperature relation with the magnetic characteristic temperatures (T_{SR} and T_N) supports this idea.

At this point, a possible magnetoelastic coupling mechanism cannot be fully excluded from being involved. Such a scenario is used to explain splitting of the phonons under the emergence of magnetic order in other systems [243, 244]. In the present case, a lattice vibration might mod-

ulate the spin configuration, i.e., a transient change of the distortion of the kagome lattice/ coupling of kagome and honeycomb copper sites. Especially, the contributions of out-of-plane (kagome-honeycomb) modes might favor the latter. However, in distinction from a magnetic resonance, these splittings are expected to be, most likely, continuously developing from the original phonon modes, which is not the case for Averievite [cf. Fig. 6.16c]

Another possibility is Brillouin zone folding with the development of a magnetic supercell at T_N [245]. This could as well result in new THz features as the phonon wavelength increases, i.e., under unit cell doubling. Similar observations have been made, for instance, at the spin-Peierls transition [246] or charge order [247]. However, the structural/ magnetic characterizations, presented above, do not give any indications of such cases.

Furthermore, the results of the ESR measurements on the $x = 0$ compound match well with the magnetic temperature scale; the absorption starts to appear at T_{SR} and amplifies further at T_N . In addition, multiple Lorentzian contributions were observed in ESR result. In this case, the system might contain distinct magnetic contributions, i.e., multiple magnetic channels (different Cu sites). Interestingly, in the THz measurements multiple resonances were observed as well, inferring the superposition of several oscillations in the time-domain signal.

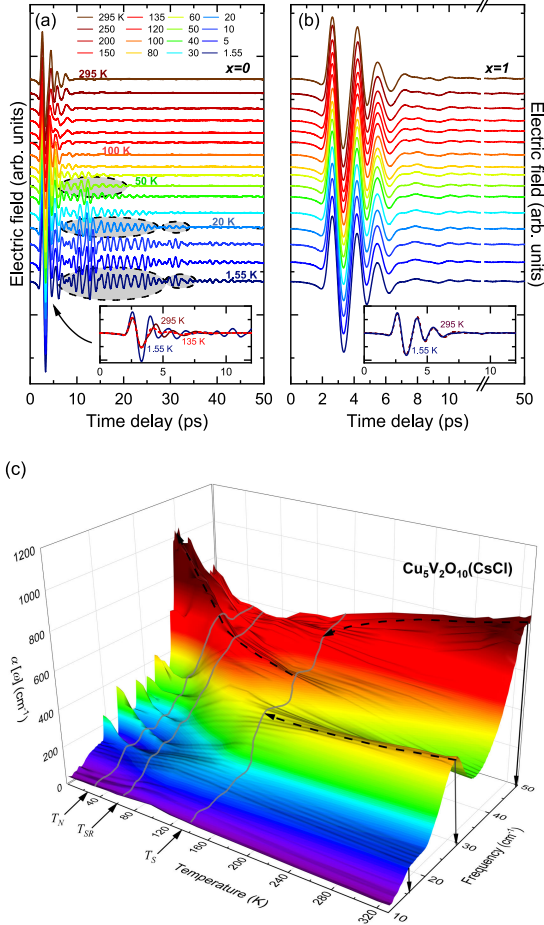


Figure 6.16: **Time-domain THz electric field and false-color plot of α .** (a) and (b) represent the $x = 0$ and $x = 1$ samples of $\text{Cu}_{5-x}\text{Zn}_x\text{V}_2\text{O}_{10}(\text{CsCl})$. The insets are the magnified views of the main echo signals. Below 60 K pronounced extended-time oscillations develop for the $x = 0$ sample [shaded area in (a)], well separated from the main pulse. For the $x = 1$ sample these oscillations are absent. (c) False-color plot of the absorption coefficient $\alpha(\omega, T)$ spectra for the $x = 0$ sample. Three lines are representing the structural transition at $T_S = 127$ K, onset of short-range magnetic correlations at $T_{SR} \approx 60$ K, and magnetic long-range order at $T_N = 24$ K, respectively. The dashed lines trace the 28 and 50 cm^{-1} modes. Reprinted with permission from Ref. [2]. Copyright (2022) by the American Physical Society.

6.6.1 Magneto-THz spectroscopy

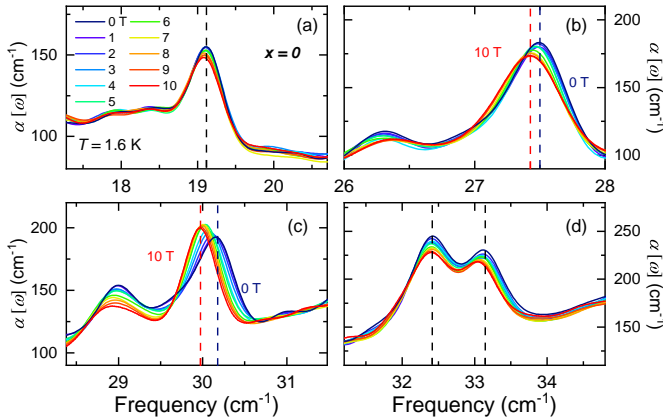


Figure 6.17: **Results of the magneto-THz measurements.** (a-d) Evolution of the frequency-dependent absorption coefficient $\alpha(\omega)$ under external magnetic field for $\text{Cu}_5\text{V}_2\text{O}_{10}(\text{CsCl})$ at $T = 1.6$ K. The black dashed lines indicate those modes which do not shift in field, but only modify their intensity. The ones with both intensity and frequency shifts are marked at the center frequency at zero field (blue) and 10 T (red) with dashed lines [panel (b,c)]. Reprinted with permission from Ref. [2]. Copyright (2022) by the American Physical Society.

To further confirm the origin of the low-temperature resonances in unsubstituted Averievite, magneto-THz measurements were carried out; the results are presented in Fig. 6.17. Some of the sharp features clearly shift to lower energies with magnetic field [see panels (b,c)]. This shift can already be concluded from modifications in the time-domain oscillations (see the appendix, Fig. 6.19). Further investigations are necessary to firmly conclude on the final reason for the redshift under external magnetic field. There are different possibilities such as enhanced magnon scattering under magnetic field [248, 249] or a slight adjustment of the internal staggered field along the external static field and thus a change in the resonance frequency and intensity. Importantly, the magneto-THz measurements confirm the magnetic origin of the sharp resonances at 27.5 and 30 cm^{-1} . Furthermore, the simultaneous appearance of multiple low-energy resonances far below the structural transition suggests a common magnetic origin of all resonances.

6.7 Discussion

Based on the comprehensive THz study understanding of the structural and magnetic properties of Averievite from a spectroscopic view is gained. Especially, with the false-color plot of $\int \alpha(\omega, T) d\omega$, Fig. 6.2d, a good agreement to previous static magnetometries and structural characterization [23] is found. The transition at $T_S = 127$ K is indeed detected in the phonon spectra, where features merge and new phonons appear for the $x = 0$ sample. For intermediate substitutions ($x = 0.25$ and 0.5), a similar phonon evolution can be revealed, reminiscent of the structural phase transition in the $x = 0$ specimen. However, the phonon modes in $\text{Cu}_4\text{ZnV}_2\text{O}_{10}(\text{CsCl})$ ($x = 1$) do not show any significant temperature dependence, providing evidence that the structural transition is absent. As far as the magnetic aspects are concerned, well pronounced magnetic resonances are detected in the THz range for the $x = 0$ Averievite. It is important to point out that these features concomitantly appear with the onset of short-range magnetic correlations, even above the temperature T_N before long-range order is established. This indicates the existence of strong magnetic interactions, i.e., paramagnons [157, 250]. The magnetic features vanish with substitution as $x > 0.25$. Increasing the Zn content further completely suppresses the magnetic order. The THz response of $x = 1$ Averievite is not susceptible to an external magnetic field (see Fig. 6.20), in conjunction with the expectation of QSLs [15, 16].

Previous DFT calculations suggest that Zn substitution specifically replaces the Cu ions within the honeycomb lattice [23]. In return, this substitution reduces the magnetic coupling between the adjacent kagome and honeycomb lattice leading to magnetically isolated kagome layers. Here, the magnetic fluctuations become stronger as the highly frustrated kagome layers decouple from each other, resulting in a suppression of magnetic order. The structural transitions are suppressed as well. Thus, the $x = 1$ system remains in the $P\bar{3}m1$ space group down to the lowest measured temperatures without magnetic ordering. These results are well corroborated by the THz measurements, revealing the entanglement of structural and magnetic factors in the phase diagram of Averievite.

6.8 Conclusion and outlook

In summary, extensive magneto-THz measurements on Averievite $\text{Cu}_{5-x}\text{Zn}_x\text{V}_2\text{O}_{10}(\text{CsCl})$ were performed. Here, magnetic resonances for the unsubstituted compound due to the spin precession induced by THz light were detected. A rather wide temperature range of magnetic short-range correlations $T_{SR} \approx 60$ K above long-range order $T_N = 24$ K was found. In fact, the THz resonances are coupled to the short-range order, similarly to paramagnons. For samples substituted with a higher Zn concentration, frustration effects of the kagome lattice take over, leading to a suppression of the magnetic resonances; they vanish when exceeding $x = 0.25$ substitution. Corroborating the magneto-THz results the ESR investigation shows a suppressed spectral weight as well. With the comprehensive information provided by THz spectra obtained in time domain magnetic and structural transitions of Averievite $\text{Cu}_{5-x}\text{Zn}_x\text{V}_2\text{O}_{10}(\text{CsCl})$ can be identified. This study sheds light on the way magnetic interactions affect THz spectra and magnetization dynamics of frustrated magnets. Moreover, tracing the magnetic resonances and their dynamics gives an augmented, spectroscopic aspect of frustrated magnetism in the vicinity of QSLs proving the efficacy of THz time-domain spectroscopy in this field.

6.9 Appendix

In this appendix additional information (mainly from Ref. [2]) are presented. This contains extended data sets of the (magneto) THz-TDS measurements, details of the pellet preparation, and information regarding the reproducibility of the measurements.

6.9.1 Zinc substitution

In order to investigate the influence of Zn substitution on the structural properties, room temperature measurements were performed. Results are shown in Fig. 6.18. Here, the phononic features are effected by substituting Cu to Zn. For instance, the 28 cm^{-1} mode shows a blueshift with increasing the Zn content. The feature at around 50 cm^{-1} sharpens for higher Zn concentrations as well. These changes are likely a combined effect of the smaller atomic diameter of Zn compared to Cu causing a stronger bonding force and the different space groups of the samples.

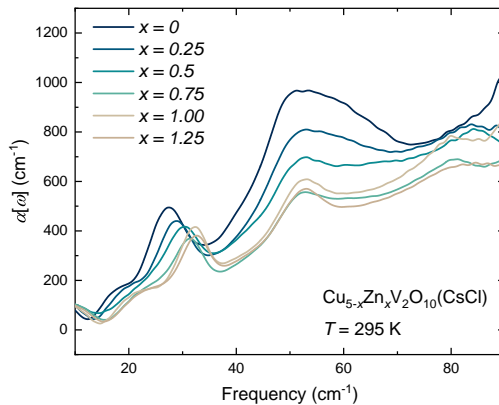


Figure 6.18: **Zn dependence of THz phonons.** Room temperature ($T = 295\text{ K}$) absorption coefficient for different Zn concentrations. Reprinted with permission from Ref. [2]. Copyright (2022) by the American Physical Society.

6.9.2 Magneto-THz measurements

Magneto-THz measurements were performed in Faraday geometry ($\vec{k} \parallel \vec{H}_{ext}$, $\vec{H}_{THz} \perp \vec{H}_{ext}$, where \vec{k} is the wave vector of the incident THz light, \vec{H}_{ext} the external magnetic field, and \vec{H}_{THz} the magnetic component of the THz light) at a base temperature of $T = 1.6$ K. The spectra are presented above. The time-domain electric fields for the $x = 0$ sample are shown in Fig. 6.19 up to the highest applied field of 10 T. While the main signal below 5 ps shows only minor intensity variations [Fig. 6.19a], systematic changes in the extended-time oscillations are observed under magnetic field [Figs. 6.19b,c]. Furthermore, results for the $x = 1$ sample are shown in Fig. 6.20 in which no changes under magnetic field are observed.

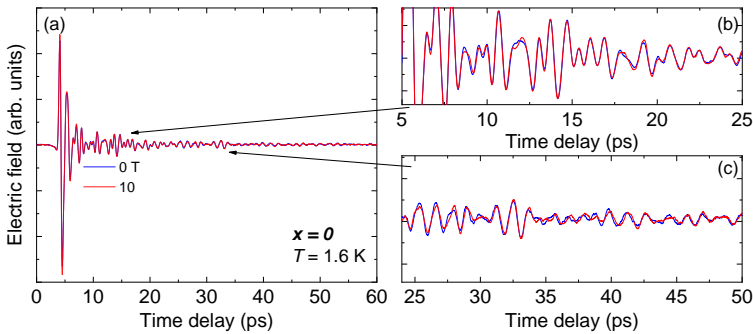


Figure 6.19: **Time-domain electric field in magneto-THz measurements.** (a-c) Electric field as a function of time delay for the $x = 0$ compound at $T = 1.6$ K. Reprinted with permission from Ref. [2]. Copyright (2022) by the American Physical Society.

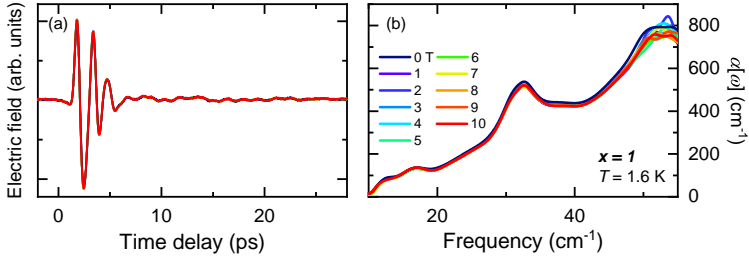


Figure 6.20: **Magneto-THz measurements of the $x = 1$ compound at $T = 1.6$ K.** (a) Time-domain spectra and (b) corresponding absorption coefficient, $\alpha(\omega)$. No systematic changes under magnetic fields up to 10 T are observed. Reprinted with permission from Ref. [2]. Copyright (2022) by the American Physical Society.

Even though, the observed shifts for $x = 0$ samples are rather small, the field dependence was systematic and reproducible (see below). In fact, an estimate of the relevant energy scales makes the small shift very plausible. A shift of roughly 0.17 cm^{-1} up to 10 T was observed for the 30 cm^{-1} resonance. This corresponds to an energy of approximately 0.021 meV, which is roughly 0.11 % of $J_1 \approx 19.63 \text{ meV}$ and 0.47 % of $J_2 \approx 4.455 \text{ meV}$ [23, 239]. Although this shift is about one order of magnitude weaker than the expected Zeeman energy ($10 \text{ T} \cdot \mu_B \approx 0.579 \text{ meV}$) the difference is not surprising. Perhaps demagnetization effects play a role for the powder samples here. The field-dependent data at $T = 13.7 \text{ K}$ and 33 K are presented below. In contrast to the observed magnetic field dependence at $T = 1.6 \text{ K}$, no significant shift in frequency can be seen at elevated temperatures. At 13.7 K the thermal energy (1.181 meV vs. 0.138 meV at $T = 1.6 \text{ K}$) is much higher than the magnetic field energy, therefore small shifts as in the low-temperature data might be very difficult to observe and remain for higher field ranges.

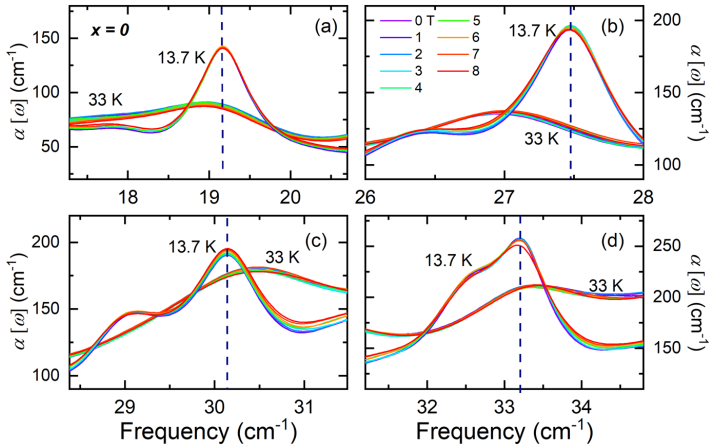


Figure 6.21: **Results of magneto-THz measurements for $x = 0$ sample for different temperatures.** (a-d) Field-dependent measurements were performed at $T = 13.7$ K and $T = 33$ K. Here, no change under magnetic field was observed.

6.9.3 Pellet preparation and reproducibility

All powders were thoroughly ground before pressing the pellets for the optical measurements. Although the grain size is small compared to the THz wavelength and therefore only negligible contribution due to scattering is expected in the probed frequency range, several pellets were compared to check the reproducibility of the spectroscopic features. As well to exclude any effect of the random crystallographic orientation within the powder, the THz measurements were repeated on differently prepared pellets (grinding, pellet size, and thickness). A picture of prepared pellets is displayed in Fig. 6.22.

In Fig. 6.23, the absorption coefficient obtained from THz-TDS measurements at 1.6 K is shown for multiple pellets. 100 and 360 μm thick pellets were measured inside the superconducting magnet. To compare with the results shown above (blue curve, 114 μm thick pellet) the spectrum has been scaled. Overall, the main features, including the assigned resonances from the main text (15 to 50 cm^{-1}), show well reproducible characteristic frequencies and lineshapes. Note that the decreased signal inside

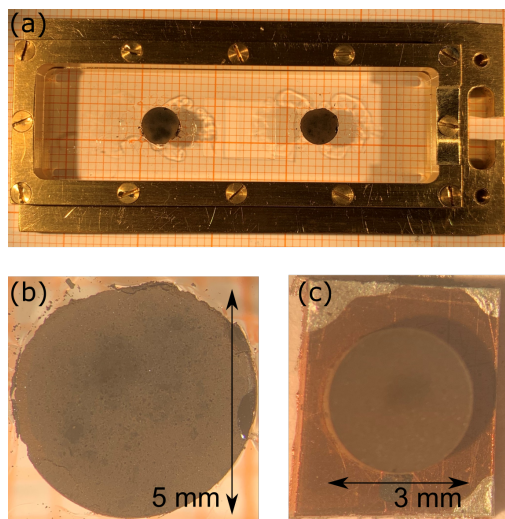


Figure 6.22: **Pressed Averievite pellets.** (a) Pellets for THz-TDS measurements on the sample holder. Thin pellets with a typical thickness of $100\ \mu\text{m}$ and a diameter of $5\ \text{mm}$ were prepared from $10\ \text{mg}$ powder. (b) Magnified view of a $100\ \mu\text{m}$ thick pellet showing a homogeneous and smooth surface. (c) Thick pellet pressed for reflectance measurements (around $4\ \text{mm}$ thickness, $18\ \text{mg}$ weight and $3\ \text{mm}$ diameter).

the magnet compared to the measurements performed in a LiHe-bath cryostat results in slight deviations at the low energies, around $10\ \text{cm}^{-1}$. Furthermore, magneto-THz measurements were repeated for the $360\ \mu\text{m}$ thick pellet (see Fig. 6.24). The behavior of the low-energy resonances in magnetic field is almost identical for the different pellets. Albeit the fact that the spectra might contain mixed responses from different crystallographic orientations, other effects from the powder can be excluded. Thus, the time-domain spectra and the absorption coefficient reflect intrinsic properties of the sample.

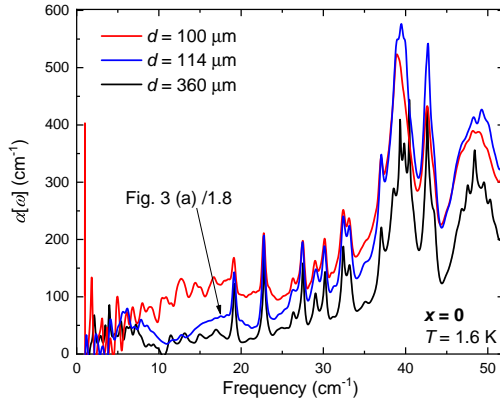


Figure 6.23: **Absorption coefficient for different pellets.** Red and black curves: 100 and 360 μm thick pellets used for magneto-THz measurements. Blue curve: 114 μm thick pellet from the main text. For comparison, data from the main text have been scaled. Reprinted with permission from Ref. [2]. Copyright (2022) by the American Physical Society.

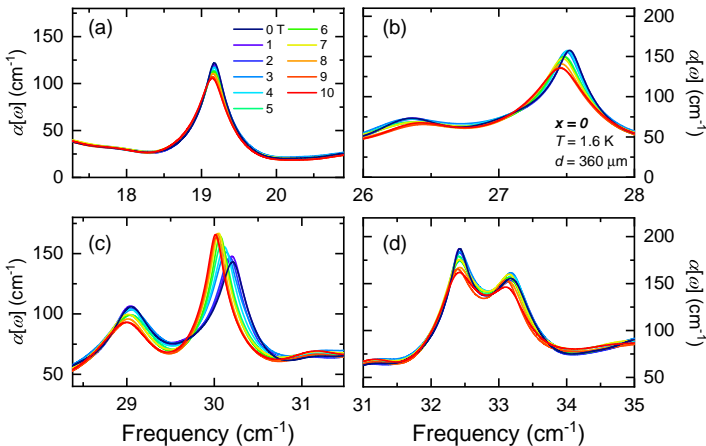


Figure 6.24: **Repetition of the magneto-THz measurements.** Spectra for a 360 μm thick pellet of the $x = 0$ compound at $T = 1.6$ K. Reprinted with permission from Ref. [2]. Copyright (2022) by the American Physical Society.

7 Conclusion

The kagome/ honeycomb lattice hosts a plethora of (frustrated) magnetic ground states and rich physics in the vicinity of the quantum spin liquid (QSL). As shown in this thesis the *THz gap* is the natural habitat for many magnetic excitations. Here, spectroscopic resolution has greatly advanced the information gained from static measurements. In combination with applied external magnetic field and low temperatures, optical spectroscopy provides versatile research opportunities. It is demonstrated that THz time-domain spectroscopy (THz-TDS) is a powerful tool to study insulating quantum magnets in a table-top experiment. Besides the sensitivity to structural and electronic properties, dynamic magnetic properties can be probed. Especially the dynamic magnetic susceptibility $\chi_m''(\omega)$ encodes the magnetic responses. In addition to the spectroscopic access, the time resolution can provide further information. However, due to the small momentum of THz photon, it is believed that only the center of the magnetic Brillouin zone can be probed ($\mathbf{q} \approx 0$). As demonstrated here, under some conditions this restriction can be released, the full magnetic Brillouin zone becomes accessible ($\Delta\mathbf{q} \approx 0$): *THz-magnetometry* can be used to probe the spin (magnon) density of states. This gives a new aspect for probing magnetic properties in quantum magnets.

In the present material class, structural distortion is an auspicious tuning parameter: it releases magnetic frustration in favor of exotic magnetic order/ spin freezing. Although, in general, external pressure might be used to tune the lattice degree of freedom, a spectroscopic investigation covering the THz range under pressure remains elusive. Here the biggest hindrance is the requirement for small samples sizes (μm range). A μm focused beam is not achieved at THz energies and the diffraction limit buries the physics. However, as presented in this work, by a systematic tuning of distortion and frustration through the present specimens Herbertsmithite $\text{ZnCu}_3(\text{OH})_6\text{Cl}_2$, Vollborthite $\text{Cu}_3\text{V}_2\text{O}_7(\text{OH})_2 \cdot 2\text{H}_2\text{O}$, Yakapellasilite $\text{Y}_3\text{Cu}_9(\text{OH})_{19}\text{Cl}_8$, and (Zn-)Averievite $\text{Cu}_{5-x}\text{Zn}_x\text{V}_2\text{O}_{10}(\text{CsCl})$, this physics can be investigated.

Starting with the undistorted quantum spin liquid candidate Herbertsmithite, the proposed spinon response (power-law absorption mechanisms [14, 15]) needs to be reconsidered. Here a clear deviation from the suggested power-law behavior was found by extending the previously investigated spectral range (Ref. [16]) to lower frequencies. Between the phonon tail, 50 cm^{-1} , down to 20 cm^{-1} the $T = 1.6 \text{ K}$ spectrum fits to a power-law conductivity with exponent $\beta = 1.47$. However, below 20

cm^{-1} down to 6 cm^{-1} , the spectrum differs significantly from this behavior. Although this observation illustrates that the previously proposed mechanisms might not be fully applicable for Herbertsmithite, it might guide further theoretical works for modeling a spinon-induced optical conductivity in the present material class.

In Volborthite the THz spectra seem to be affected by the magnetism, in particular THz integrated absorption coefficient IA resembles the temperature evolution of the susceptibility of Refs. [17, 202]. In order to expand the picture, further studies on larger single crystals, eventually yielding a better data quality, need to be performed. In addition magneto-optical THz investigation are of definite interest. Although the trimer state appears only at very low temperatures ($T_N = 1.4 \text{ K}$), measurements extending the temperature scale of the current study (6 K) could be interesting.

As the structural distortion increases, the featureless THz response is superseded by a broad, continuum-like contribution for Y-kapellasite. This contribution emerges with the onset of short range magnetic correlations (30 K) and is susceptible to external magnetic field. Comparing with the linear spin-wave theory (LSWT) the spectrum is correlated with the spin (magnon) density of states. A multi-center magnon excitation is introduced as the relevant absorption mechanism ($\Delta\mathbf{q} \approx 0$), explaining the broad, continuum-like THz response.

Further increasing the structural distortion and releasing magnetic frustration, in Averievite, sharp THz features are unveiled. They are tracked down as magnetic resonances, emerging together with the onset of short-range magnetic correlations (60 K). Furthermore, they can be slightly shifted in frequency by external magnetic field. In Zn-Averievite these resonances are switched off together with the suppression of the magnetic ground state, as the distortion vanishes, leaving only a featureless response besides the dielectric background.

In the present material class, often, a unique experimental access to the magnetism is found, even above the ordering temperature: wide ranges of short-range magnetic correlations up to intermediate temperatures (30 to 60 K). In general, the magnetic features of the THz spectra seem to be coupled to these correlations, as they show a very similar temperature scale. Surprisingly, (for the cases of Y-kapellasite and Averievite)

no pronounced qualitative changes were found below T_N , pointing to a smooth connection of the long-range ordered phase and the short-range magnetic correlations. The onset of magnetic short range correlations can be further corroborated by (quasi-) static methods, extrapolating the THz responses down to low frequencies, such as susceptibility, electron spin resonance (electron spin susceptibility χ_s^e), and nuclear magnetic resonance (spin-lattice relaxation rate $1/T_1$). As shown in this work, bringing these methods together an advanced picture, disentangling magnetic, structural, and electronic properties can be achieved.

Furthermore, these quantum magnets show a rich phononic background with unconventional temperature dependence, pointing to magnetoelastic coupling mechanisms, for instance, in Herbertsmithite and Y-kapellasite. This is natural to expect as the magnetic superexchanges could be modulated by phonons. As well structural distortion may lead to unstable lattices, introducing many structural transitions and dielectric anomalies. This is in accordance with the observation that the kagome lattice can be deformed by comparable low hydrostatic pressures, around 3 GPa.

As a general outlook, more sophisticated tuning methods for the structural distortion, such as chemical pressure, could be an interesting perspective. Especially here, manipulating Herbertsmithite might open an ideal playground to dive further into exotic magnetic phases of the distorted kagome quantum magnet. Even though increasing chemical pressure within the kagome plane is challenging, such a rigorous tuning offers improved comparability than in the present study.

The observation of a pronounced multi-center magnon feature in Y-kapellasite further calls for a refined theoretical picture to better understand the coupling mechanism between light and multi-center magnon. This includes more specific selection rules as well as further insights on the multi-center magnon itself. For instance, general questions as the magnetic/ electric dipole activity remain to be answered. As well, introducing a weighting function and taking into account the reduced probability for the contribution of states with a larger momentum could further refine the theoretically expected spectral shapes. Moreover, such an excitation should be observable in other quantum magnets hosting multiple magnetic sublattices with a low symmetry of the magnetic system. Exploiting the multi-center magnon excitation in a wider range of materials could thus yield further valuable information.

There is a plethora of closely related interesting compounds, where a spectroscopic resolution in the THz range is not achieved so far. Vesignieite ($\text{BaCu}_3\text{V}_2\text{O}_8(\text{OH})_2$) offers an intriguing multi- Q magnetic ground state [222]. Engelhauptite ($\text{KCu}_3\text{V}_2\text{O}_7(\text{OH})_2\text{Cl}$) [221] might yield a ground state similar to Volborthite. $\text{Rb}_2\text{Cu}_3\text{SnF}_{12}$ is a pinwheel valence bond solid on the kagome lattice [36]. $\text{YCu}_3(\text{OH})_6\text{Cl}_3$ harbors a 120° spin structure on an undistorted kagome lattice, possibly related to enhanced DM interaction [251]. Zn-Barlowite ($\text{ZnCu}_3(\text{OD})_6\text{FBr}$) yields spin singlet formation [174, 252]. This zoo of materials offers a great research perspective for forthcoming studies.

Acknowledgments

During the research many people contributed scientifically. I am grateful for all co-authors and collaborators making this work possible: Thank you for your input. Furthermore, I would like to thank for all possibilities to contribute to other projects: Thank you for letting me participate.

I would like to thank Prof. Dr. Martin Dressel for supervising this work. I need to thank him for the education I received during the last five years at the institute, for the always open door, and the freedom to pursue ideas. Furthermore, I would like to thank Prof. Dr. Bernhard Keimer for co-refereeing this thesis. I want to thank Prof. Dr. Hans Peter Büchler for hosting the examination.

In particular, I would like to thank Aleksandar Razpopov, Dr. Ying Li, and Prof. Dr. Roser Valentí for comprehensive theoretical contributions and the fruitful collaboration.

For the close collaboration I would like to thank Dr. Pascal Puphal and Ass. Prof. Dr. Andrej Pustogow.

Particularly I would like to thank Dr. Seulki Roh for his scientific input, many discussions, and guidance.

For the contribution of many interesting samples I would like to thank Dr. Pascal Puphal, Katharina M. Zoch, Prof. Dr. Cornelius Krellner, Dr. Pai-Chun Wei, and Dr. John F. Mitchell.

I want to thank Jannis Willwater and apl. Prof. Dr. Stefan Süllow for fruitful discussions and their input in collaboration with HLD at HZDR.

For his input at the beginning of my research I would like to thank Dr. Weiwu Li. I would like to thank Dr. Ece Uykur for sharing her knowledge in high-pressure FTIR. For further calculations I want to thank Prof. Dr. Alexander Tsirlin.

Parts of this research were carried out at SMIS 2 at SOLEIL and ID27 at ESRF. For the great beamtimes at Soleil I want to thank Dr. Francesco Capitani. For the high-pressure XRD experiment I want to thank Dr. Björn Wehinger.

For the continuous technical support during the last five years I would like to thank Gabriele Untereiner.

Acknowledgments

I want to thank all the former students contributing to this research and giving me the opportunity to practice teaching, in particular Tobias Konrad Zeh and Veit Kilian Kutzner.

Furthermore, I want to thank all members of the institute for the good working atmosphere.

I want to thank my family and my parents for their impact on my personal life.

A special thanks to my wife: Laura Torralba Díaz.

Bibliography

- [1] T. Biesner, S. Roh, A. Razpopov, J. Willwater, S. Süllow, Y. Li, K. M. Zoch, M. Medarde, J. Nuss, D. Gorbunov, et al., Multi-Center Magnon Excitations Open the Entire Brillouin Zone to Terahertz Magnetometry of Quantum Magnets, *Adv. Quantum Technol.* **5**, 2200023 (2022).
- [2] T. Biesner, S. Roh, A. Pustogow, H. Zheng, J. F. Mitchell, and M. Dressel, Magnetic terahertz resonances above the Néel temperature in the frustrated kagome antiferromagnet averievite, *Phys. Rev. B* **105**, L060410 (2022).
- [3] T. Biesner and E. Uykur, Pressure-Tuned Interactions in Frustrated Magnets: Pathway to Quantum Spin Liquids?, *Crystals* **10**, 4 (2019).
- [4] T. Biesner, W. Li, A. A. Tsirlin, S. Roh, P.-C. Wei, E. Uykur, and M. Dressel, Spectroscopic trace of the Lifshitz transition and multivalley activation in thermoelectric SnSe under high pressure, *NPG Asia Mater.* **13**, 12 (2021).
- [5] T. Biesner, S. Biswas, W. Li, Y. Saito, A. Pustogow, M. Altmeyer, A. U. B. Wolter, B. Büchner, M. Roslova, T. Doert, et al., Detuning the honeycomb of α -RuCl₃: Pressure-dependent optical studies reveal broken symmetry, *Phys. Rev. B* **97**, 220401 (2018).
- [6] L. Balents, Spin liquids in frustrated magnets, *Nature* **464**, 199 EP (2010).
- [7] M. Hering, F. Ferrari, A. Razpopov, I. I. Mazin, R. Valentí, H. O. Jeschke, and J. Reuther, Phase diagram of a distorted kagome antiferromagnet and application to Y-kapellasite, *Npj Comput. Mater.* **8**, 10 (2022).
- [8] B. Miksch, A. Pustogow, M. J. Rahim, A. A. Bardin, K. Kanoda, J. A. Schlueter, R. Hübner, M. Scheffler, and M. Dressel, Gapped magnetic ground state in quantum spin liquid candidate κ -(BEDT-TTF)₂Cu₂(CN)₃, *Science* **372**, 276 (2021).
- [9] L. Clark and A. H. Abdeldaim, Quantum Spin Liquids from a Materials Perspective, *Annu. Rev. Mater. Res.* **51**, 495 (2021).
- [10] J. Knolle and R. Moessner, A Field Guide to Spin Liquids, *Annu. Rev. Condens. Matter Phys.* **10**, 451 (2019).

- [11] M. R. Norman, Colloquium: Herbertsmithite and the search for the quantum spin liquid, *Rev. Mod. Phys.* **88**, 041002 (2016).
- [12] J. S. Helton, K. Matan, M. P. Shores, E. A. Nytko, B. M. Bartlett, Y. Yoshida, Y. Takano, A. Suslov, Y. Qiu, J.-H. Chung, et al., Spin Dynamics of the Spin-1/2 Kagome Lattice Antiferromagnet $\text{ZnCu}_3(\text{OH})_6\text{Cl}_2$, *Phys. Rev. Lett.* **98**, 107204 (2007).
- [13] T.-H. Han, J. S. Helton, S. Chu, D. G. Nocera, J. A. Rodriguez-Rivera, C. Broholm, and Y. S. Lee, Fractionalized excitations in the spin-liquid state of a kagome-lattice antiferromagnet, *Nature* **492**, 406 (2012).
- [14] T.-K. Ng and P. A. Lee, Power-law conductivity inside the mott gap: Application to κ -(BEDT-TTF) $_2\text{Cu}_2(\text{CN})_3$, *Phys. Rev. Lett.* **99**, 156402 (2007).
- [15] A. C. Potter, T. Senthil, and P. A. Lee, Mechanisms for sub-gap optical conductivity in Herbertsmithite, *Phys. Rev. B* **87**, 245106 (2013).
- [16] D. V. Pilon, C. H. Lui, T. H. Han, D. Shrekenhamer, A. J. Frenzel, W. J. Padilla, Y. S. Lee, and N. Gedik, Spin-Induced Optical Conductivity in the Spin-Liquid Candidate Herbertsmithite, *Phys. Rev. Lett.* **111**, 127401 (2013).
- [17] D. Watanabe, K. Sugii, M. Shimozawa, Y. Suzuki, T. Yajima, H. Ishikawa, Z. Hiroi, T. Shibauchi, Y. Matsuda, and M. Yamashita, Emergence of nontrivial magnetic excitations in a spin-liquid state of kagomé volborthite, *Proc. Natl. Acad. Sci. U.S.A.* **113**, 8653 (2016).
- [18] Y. Kohama, H. Ishikawa, A. Matsuo, K. Kindo, N. Shannon, and Z. Hiroi, Possible observation of quantum spin-nematic phase in a frustrated magnet, *Proc. Natl. Acad. Sci. U.S.A.* **116**, 10686 (2019).
- [19] H. Ishikawa, M. Yoshida, K. Nawa, M. Jeong, S. Krämer, M. Horvatić, C. Berthier, M. Takigawa, M. Akaki, A. Miyake, et al., One-Third Magnetization Plateau with a Preceding Novel Phase in Volborthite, *Phys. Rev. Lett.* **114**, 227202 (2015).

-
- [20] H. Yoshida, J.-i. Yamaura, M. Isobe, Y. Okamoto, G. J. Nilsen, and Z. Hiroi, Orbital switching in a frustrated magnet, *Nat. Commun.* **3**, 860 (2012).
- [21] P. Puphal, M. Bolte, D. Sheptyakov, A. Pustogow, K. Kliemt, M. Dressel, M. Baenitz, and C. Krellner, Strong magnetic frustration in $\text{Y}_3\text{Cu}_9(\text{OH})_{19}\text{Cl}_8$: a distorted kagome antiferromagnet, *J. Mater. Chem. C* **5**, 2629 (2017).
- [22] Q. Barthélemy, P. Puphal, K. M. Zoch, C. Krellner, H. Luetkens, C. Baines, D. Sheptyakov, E. Kermarrec, P. Mendels, and F. Bert, Local study of the insulating quantum kagome antiferromagnets $\text{YCu}_3(\text{OH})_6\text{O}_x\text{Cl}_{3-x}$ ($x = 0, 1/3$), *Phys. Rev. Mater.* **3**, 074401 (2019).
- [23] A. S. Botana, H. Zheng, S. H. Lapidus, J. F. Mitchell, and M. R. Norman, Averievite: A copper oxide kagome antiferromagnet, *Phys. Rev. B* **98**, 054421 (2018).
- [24] R. Feynman (Elsevier, 1955), vol. 1 of *Prog. Low Temp. Phys.*, pp. 17–53.
- [25] F. Giustino, J. H. Lee, F. Trier, M. Bibes, S. M. Winter, R. Valentí, Y.-W. Son, L. Taillefer, C. Heil, A. I. Figueroa, et al., The 2021 quantum materials roadmap, *JPhys Materials* **3**, 042006 (2021).
- [26] P. Anderson, The concept of frustration in spin glasses, *J. less-common met.* **62**, 291 (1978).
- [27] L. Savary and L. Balents, Quantum spin liquids: a review, *Rep. Prog. Phys.* **80**, 016502 (2016).
- [28] P. W. Anderson, Resonating valence bond state in La_2CuO_4 and superconductivity, *Science* **235**, 1196 (1987).
- [29] C. Broholm, R. J. Cava, S. A. Kivelson, D. G. Nocera, M. R. Norman, and T. Senthil, Quantum spin liquids, *Science* **367**, eaay0668 (2020).
- [30] G. Semeghini, H. Levine, A. Keesling, S. Ebadi, T. T. Wang, D. Bluvstein, R. Verresen, H. Pichler, M. Kalinowski, R. Samajdar, et al., Probing topological spin liquids on a programmable quantum simulator, *Science* **374**, 1242 (2021).

- [31] T. Mertz and R. Valentí, Engineering topological phases guided by statistical and machine learning methods, *Phys. Rev. Research* **3**, 013132 (2021).
- [32] C. Lacroix, P. Mendels, and F. Mila, eds., *Introduction to Frustrated Magnetism*, vol. 164 of *Springer Series in Solid-State Sciences* (Springer Berlin Heidelberg, Berlin, Heidelberg, 2011).
- [33] H. K. Yoshida, Frustrated Kagome Antiferromagnets under High Magnetic Fields, *Journal of the Physical Society of Japan* **91**, 101003 (2022).
- [34] A. A. Coker, A. Saxena, and J. T. Haraldsen, Effects of exchange distortion and spin rotation in the magnetic Kagome Lattice, *Phys. Rev. B* **103**, 054412 (2021).
- [35] M. Kohno, O. A. Starykh, and L. Balents, Spinons and triplons in spatially anisotropic frustrated antiferromagnets, *Nat. Phys.* **3**, 790 (2007).
- [36] K. Matan, T. Ono, Y. Fukumoto, T. J. Sato, J. Yamaura, M. Yano, K. Morita, and H. Tanaka, Pinwheel valence-bond solid and triplet excitations in the two-dimensional deformed kagome lattice, *Nat. Phys.* **6**, 865 (2010).
- [37] V. Baltz, A. Manchon, M. Tsoi, T. Moriyama, T. Ono, and Y. Tserkovnyak, Antiferromagnetic spintronics, *Rev. Mod. Phys.* **90**, 015005 (2018).
- [38] M. Mekata, Kagome: The Story of the Basketweave Lattice, *Physics Today* **56**, 12 (2003).
- [39] P. Mendels and F. Bert, Quantum kagome frustrated antiferromagnets: One route to quantum spin liquids, *C. R. Phys.* **17**, 455 (2016).
- [40] P. Puphal, K. M. Zoch, J. Désor, M. Bolte, and C. Krellner, Kagome quantum spin systems in the atacamite family, *Phys. Rev. Mater.* **2**, 063402 (2018).
- [41] S. Trebst, Kitaev Materials, arXiv:1701.07056 (2017).

-
- [42] R. S. W. Braithwaite, K. Mereiter, W. H. Paar, and A. M. Clark, Herbertsmithite, $\text{Cu}_3\text{Zn}(\text{OH})_6\text{Cl}_2$, a new species, and the definition of paratacamite, *Mineral. Mag.* **68**, 527 (2004).
- [43] R. S. Fishman, J. A. Fernandez-Baca, and T. R  m, *Spin-Wave Theory and its Applications to Neutron Scattering and THz Spectroscopy* (Morgan & Claypool Publishers, San Rafael, 2018).
- [44] Z. Wang, M. Schmidt, Y. Goncharov, V. Tsurkan, H.-A. Krug von Nidda, A. Loidl, and J. Deisenhofer, Terahertz spectroscopy in the pseudo-Kagome system $\text{Cu}_3\text{Bi}(\text{SeO}_3)_2\text{O}_2\text{Br}$, *Phys. Rev. B* **86**, 174411 (2012).
- [45] L. Pan, S. K. Kim, A. Ghosh, C. M. Morris, K. A. Ross, E. Kermarrec, B. D. Gaulin, S. M. Koohpayeh, O. Tchernyshyov, and N. P. Armitage, Low-energy electrodynamics of novel spin excitations in the quantum spin ice $\text{Yb}_2\text{Ti}_2\text{O}_7$, *Nat. Commun.* **5**, 4970 (2014).
- [46] N. J. Laurita, J. Deisenhofer, L. Pan, C. M. Morris, M. Schmidt, M. Johnsson, V. Tsurkan, A. Loidl, and N. P. Armitage, Singlet-Triplet Excitations and Long-Range Entanglement in the Spin-Orbital Liquid Candidate FeSc_2S_4 , *Phys. Rev. Lett.* **114**, 207201 (2015).
- [47] L. Pan, N. J. Laurita, K. A. Ross, B. D. Gaulin, and N. P. Armitage, A measure of monopole inertia in the quantum spin ice $\text{Yb}_2\text{Ti}_2\text{O}_7$, *Nat. Phys.* **12**, 361 (2016).
- [48] Z. Wang, S. Reschke, D. H  vonen, S.-H. Do, K.-Y. Choi, M. Gensch, U. Nagel, T. R  m, and A. Loidl, Magnetic Excitations and Continuum of a Possibly Field-Induced Quantum Spin Liquid in $\alpha\text{-RuCl}_3$, *Phys. Rev. Lett.* **119**, 227202 (2017).
- [49] A. Little, L. Wu, P. Lampen-Kelley, A. Banerjee, S. Patankar, D. Rees, C. A. Bridges, J.-Q. Yan, D. Mandrus, S. E. Nagler, et al., Antiferromagnetic Resonance and Terahertz Continuum in $\alpha\text{-RuCl}_3$, *Phys. Rev. Lett.* **119**, 227201 (2017).
- [50] L. Wu, A. Little, E. E. Aldape, D. Rees, E. Thewalt, P. Lampen-Kelley, A. Banerjee, C. A. Bridges, J.-Q. Yan, D. Boone, et al., Field evolution of magnons in $\alpha\text{-RuCl}_3$ by high-resolution polarized terahertz spectroscopy, *Phys. Rev. B* **98**, 094425 (2018).

- [51] X. Zhang, F. Mahmood, M. Daum, Z. Dun, J. A. M. Paddison, N. J. Laurita, T. Hong, H. Zhou, N. P. Armitage, and M. Mourigal, Hierarchy of Exchange Interactions in the Triangular-Lattice Spin Liquid YbMgGaO_4 , *Phys. Rev. X* **8**, 031001 (2018).
- [52] Z. Wang, J. Wu, W. Yang, A. K. Bera, D. Kamenskyi, A. T. M. N. Islam, S. Xu, J. M. Law, B. Lake, C. Wu, et al., Experimental observation of Bethe strings, *Nature* **554**, 219 (2018).
- [53] Y. Wan and N. P. Armitage, Resolving Continua of Fractional Excitations by Spinon Echo in THz 2D Coherent Spectroscopy, *Phys. Rev. Lett.* **122**, 257401 (2019).
- [54] K. Amelin, Y. Alexanian, U. Nagel, T. Röm, J. Robert, J. Debray, V. Simonet, C. Decorse, Z. Wang, R. Ballou, et al., Terahertz magneto-optical investigation of quadrupolar spin-lattice effects in magnetically frustrated $\text{Tb}_2\text{Ti}_2\text{O}_7$, *Phys. Rev. B* **102**, 134428 (2020).
- [55] J. Walowski and M. Münzenberg, Perspective: Ultrafast magnetism and THz spintronics, *J. Appl. Phys.* **120**, 140901 (2016).
- [56] A. Eschenlohr and U. Bovensiepen, Special issue on ultrafast magnetism, *J. Phys. Condens. Matter* **30**, 030301 (2017).
- [57] J. Lloyd-Hughes, P. M. Oppeneer, T. P. dos Santos, A. Schleife, S. Meng, M. A. Sentef, M. Ruggenthaler, A. Rubio, I. Radu, M. Murnane, et al., The 2021 ultrafast spectroscopic probes of condensed matter roadmap, *J. Phys. Condens. Matter* **33**, 353001 (2021).
- [58] J. Neu and C. A. Schmuttenmaer, Tutorial: An introduction to terahertz time domain spectroscopy (THz – TDS), *J. Appl. Phys.* **124**, 231101 (2018).
- [59] P. Němec, M. Fiebig, T. Kampfrath, and A. V. Kimel, Antiferromagnetic opto-spintronics, *Nat. Phys.* **14**, 229 (2018).
- [60] T. Kampfrath, K. Tanaka, and K. A. Nelson, Resonant and nonresonant control over matter and light by intense terahertz transients, *Nat. Photonics* **7**, 680 (2013).

-
- [61] A. V. Kimel, A. Kirilyuk, P. A. Usachev, R. V. Pisarev, A. M. Balbashov, and T. Rasing, Ultrafast non-thermal control of magnetization by instantaneous photomagnetic pulses, *Nature* **435**, 655 (2005).
- [62] A. Kirilyuk, A. V. Kimel, and T. Rasing, Ultrafast optical manipulation of magnetic order, *Rev. Mod. Phys.* **82**, 2731 (2010).
- [63] J. R. Hortensius, D. Afanasiev, M. Matthiesen, R. Leenders, R. Citro, A. V. Kimel, R. V. Mikhaylovskiy, B. A. Ivanov, and A. D. Caviglia, Coherent spin-wave transport in an antiferromagnet, *Nat. Phys.* **17**, 1001 (2021).
- [64] T. Kampfrath, A. Sell, G. Klatt, A. Pashkin, S. Mährlein, T. Dekorsy, M. Wolf, M. Fiebig, A. Leitenstorfer, and R. Huber, Coherent terahertz control of antiferromagnetic spin waves, *Nat. Photonics* **5**, 31 (2011).
- [65] C. Vicario, C. Ruchert, F. Ardana-Lamas, P. M. Derlet, B. Tudu, J. Luning, and C. P. Hauri, Off-resonant magnetization dynamics phase-locked to an intense phase-stable terahertz transient, *Nat. Photonics* **7**, 720 (2013).
- [66] F. Hansteen, A. Kimel, A. Kirilyuk, and T. Rasing, Femtosecond Photomagnetic Switching of Spins in Ferrimagnetic Garnet Films, *Phys. Rev. Lett.* **95**, 047402 (2005).
- [67] M. Nakajima, A. Namai, S. Ohkoshi, and T. Suemoto, Ultrafast time domain demonstration of bulk magnetization precession at zero magnetic field ferromagnetic resonance induced by terahertz magnetic field, *Opt. Express* **18**, 18260 (2010).
- [68] K. Yamaguchi, M. Nakajima, and T. Suemoto, Coherent Control of Spin Precession Motion with Impulsive Magnetic Fields of Half-Cycle Terahertz Radiation, *Phys. Rev. Lett.* **105**, 237201 (2010).
- [69] K. Yamaguchi, T. Kurihara, Y. Minami, M. Nakajima, and T. Suemoto, Terahertz Time-Domain Observation of Spin Reorientation in Orthoferrite ErFeO_3 through Magnetic Free Induction Decay, *Phys. Rev. Lett.* **110**, 137204 (2013).

- [70] W. Zhang, P. Maldonado, Z. Jin, T. S. Seifert, J. Arabski, G. Schmerber, E. Beaurepaire, M. Bonn, T. Kampfrath, P. M. Oppeneer, et al., Ultrafast terahertz magnetometry, *Nat. Commun.* **11**, 4247 (2020).
- [71] X. Lin, J. Jiang, Z. Jin, D. Wang, Z. Tian, J. Han, Z. Cheng, and G. Ma, Terahertz probes of magnetic field induced spin reorientation in YFeO₃ single crystal, *Appl. Phys. Lett.* **106**, 092403 (2015).
- [72] T. H. Kim, C. Kang, C.-S. Kee, J.-H. Lee, B. K. Cho, P. Gruenberg, Y. Tokunaga, Y. Tokura, and J. S. Lee, Magnetization states of canted antiferromagnetic YFeO₃ investigated by terahertz time-domain spectroscopy, *J. Appl. Phys.* **118**, 233101 (2015).
- [73] J. Guo, L. Cheng, Z. Ren, W. Zhang, X. Lin, Z. Jin, S. Cao, Z. Sheng, and G. Ma, Magnetic field tuning of spin resonance in TmFeO₃ single crystal probed with THz transient, *J. Phys. Condens. Matter* **32**, 185401 (2020).
- [74] T. Higuchi, N. Kanda, H. Tamaru, and M. Kuwata-Gonokami, Selection Rules for Light-Induced Magnetization of a Crystal with Threefold Symmetry: The Case of Antiferromagnetic NiO, *Phys. Rev. Lett.* **106**, 047401 (2011).
- [75] R. Cheng, J. Xiao, Q. Niu, and A. Brataas, Spin Pumping and Spin-Transfer Torques in Antiferromagnets, *Phys. Rev. Lett.* **113**, 057601 (2014).
- [76] H. Qiu, L. Zhou, C. Zhang, J. Wu, Y. Tian, S. Cheng, S. Mi, H. Zhao, Q. Zhang, D. Wu, et al., Ultrafast spin current generated from an antiferromagnet, *Nat. Phys.* **17**, 388 (2021).
- [77] D. N. Basov, R. D. Averitt, D. van der Marel, M. Dressel, and K. Haule, Electrodynamics of correlated electron materials, *Rev. Mod. Phys.* **83**, 471 (2011).
- [78] C. Tzschaschel, K. Otani, R. Iida, T. Shimura, H. Ueda, S. Günther, M. Fiebig, and T. Satoh, Ultrafast optical excitation of coherent magnons in antiferromagnetic NiO, *Phys. Rev. B* **95**, 174407 (2017).
- [79] A. M. Kalashnikova, A. V. Kimel, R. V. Pisarev, V. N. Gridnev, A. Kirilyuk, and T. Rasing, Impulsive Generation of Coherent

Magnons by Linearly Polarized Light in the Easy-Plane Antiferromagnet FeBO₃, *Phys. Rev. Lett.* **99**, 167205 (2007).

- [80] N. Kida, Y. Ikebe, Y. Takahashi, J. P. He, Y. Kaneko, Y. Yamasaki, R. Shimano, T. Arima, N. Nagaosa, and Y. Tokura, Electrically driven spin excitation in the ferroelectric magnet DyMnO₃, *Phys. Rev. B* **78**, 104414 (2008).
- [81] M. Dressel and G. Grüner, *Electrodynamics of Solids: Optical Properties of Electrons in Matter* (Cambridge University Press, Cambridge, 2002).
- [82] D. B. Tanner, *Optical Effects in Solids* (Cambridge University Press, Cambridge, 2019).
- [83] M. Dressel and A. Pustogow, Electrodynamics of quantum spin liquids, *J. Phys. Condens. Matter* **30**, 203001 (2018).
- [84] A. Pustogow, Ph.D. thesis, University of Stuttgart (2017).
- [85] S. Kaiser, Ph.D. thesis, University of Stuttgart (2010).
- [86] W. Li, Ph.D. thesis, University of Stuttgart (2019).
- [87] S. Miyahara and N. Furukawa, Theory of magneto-optical effects in helical multiferroic materials via toroidal magnon excitation, *Phys. Rev. B* **89**, 195145 (2014).
- [88] D. Wulferding, Y. Choi, W. Lee, and K.-Y. Choi, Raman spectroscopic diagnostic of quantum spin liquids, *J. Phys. Condens. Matter* **32**, 043001 (2019).
- [89] P. Chauhan, F. Mahmood, H. J. Changlani, S. M. Koochpayeh, and N. P. Armitage, Tunable Magnon Interactions in a Ferromagnetic Spin-1 Chain, *Phys. Rev. Lett.* **124**, 037203 (2020).
- [90] T. Gilbert, A phenomenological theory of damping in ferromagnetic materials, *IEEE Trans. Magn.* **40**, 3443 (2004).
- [91] X. Fu, X. Xi, K. Bi, and J. Zhou, Temperature-dependent terahertz magnetic dipole radiation from antiferromagnetic GdFeO₃ ceramics, *Appl. Phys. Lett.* **103**, 211108 (2013).

- [92] K. Grishunin, T. Huisman, G. Li, E. Mishina, T. Rasing, A. V. Kimel, K. Zhang, Z. Jin, S. Cao, W. Ren, et al., Terahertz Magnon-Polaritons in TmFeO_3 , *ACS Photonics* **5**, 1375 (2018).
- [93] J. Lu, X. Li, H. Y. Hwang, B. K. Ofori-Okai, T. Kurihara, T. Sue-moto, and K. A. Nelson, Coherent Two-Dimensional Terahertz Magnetic Resonance Spectroscopy of Collective Spin Waves, *Phys. Rev. Lett.* **118**, 207204 (2017).
- [94] K. Neeraj, N. Awari, S. Kovalev, D. Polley, N. Zhou Hagström, S. S. P. K. Arekapudi, A. Semisalova, K. Lenz, B. Green, J.-C. Deinert, et al., Inertial spin dynamics in ferromagnets, *Nat. Phys.* **17**, 245 (2021).
- [95] S. M. Rezende, A. Azevedo, and R. L. Rodríguez-Suárez, Introduction to antiferromagnetic magnons, *J. Appl. Phys.* **126**, 151101 (2019).
- [96] R. Loudon, Theory of infra-red and optical spectra of antiferromagnets, *Adv. Phys.* **17**, 243 (1968).
- [97] F. M. Johnson and A. H. Nethercot, Antiferromagnetic Resonance in MnF_2 , *Phys. Rev.* **114**, 705 (1959).
- [98] G. B. Wright, ed., *Light Scattering Spectra of Solids* (Springer Berlin Heidelberg, Berlin, Heidelberg, 1969).
- [99] P. A. Fleury and R. Loudon, Scattering of Light by One- and Two-Magnon Excitations, *Phys. Rev.* **166**, 514 (1968).
- [100] M. Hagiwara, K. Katsumata, H. Yamaguchi, M. Tokunaga, I. Yamada, M. Gross, and P. Goy, A Complete Frequency-Field Chart for the Antiferromagnetic Resonance in MnF_2 , *Int. J. Infrared Millim. Waves* **20**, 617 (1999).
- [101] D. A. Bas, Ph.D. thesis, West Virginia University (2016).
- [102] J. W. Halley and I. Silvera, Odd-Exciton Magnon Interaction and Explanation of Anomalous Far-Infrared Absorption in Antiferromagnetic FeF_2 , *Phys. Rev. Lett.* **15**, 654 (1965).
- [103] Y. Tanabe, T. Moriya, and S. Sugano, Magnon-Induced Electric Dipole Transition Moment, *Phys. Rev. Lett.* **15**, 1023 (1965).

-
- [104] S. J. Allen, R. Loudon, and P. L. Richards, Two-Magnon Absorption in Antiferromagnetic MnF_2 , *Phys. Rev. Lett.* **16**, 463 (1966).
- [105] M. F. Thorpe and R. J. Elliott, in *Light Scattering Spectra of Solids*, edited by G. B. Wright (Springer Berlin Heidelberg, Berlin, Heidelberg, 1969), pp. 199–206.
- [106] M. F. Thorpe, Two-Magnon Raman Scattering and Infrared Absorption in MnF_2 , *J. Appl. Phys.* **41**, 892 (1970).
- [107] D. L. Dexter, Cooperative Optical Absorption in Solids, *Phys. Rev.* **126**, 1962 (1962).
- [108] T. Moriya, Far Infrared Absorption by Two Magnon Excitations in Antiferromagnets, *J. Phys. Soc. Jpn.* **21**, 926 (1966).
- [109] J. W. Halley, Microscopic Theory of Far-Infrared 2-Magnon Absorption in Antiferromagnets. II. Second-Order Process and Application to MnF_2 , *Phys. Rev.* **154**, 458 (1967).
- [110] T. Moriya, Theory of Absorption and Scattering of Light by Magnetic Crystals, *J. Appl. Phys.* **39**, 1042 (1968).
- [111] M. E. Zhitomirsky and A. L. Chernyshev, Colloquium: Spontaneous magnon decays, *Rev. Mod. Phys.* **85**, 219 (2013).
- [112] S. M. Winter, K. Riedl, P. A. Maksimov, A. L. Chernyshev, A. Honecker, and R. Valentí, Breakdown of magnons in a strongly spin-orbital coupled magnet, *Nat. Commun.* **8**, 1152 (2017).
- [113] D. Wulferding, Y. Choi, S.-H. Do, C. H. Lee, P. Lemmens, C. Faugeras, Y. Gallais, and K.-Y. Choi, Magnon bound states versus anyonic Majorana excitations in the Kitaev honeycomb magnet $\alpha\text{-RuCl}_3$, *Nat. Commun.* **11**, 1603 (2020).
- [114] A. Sahasrabudhe, D. A. S. Kaib, S. Reschke, R. German, T. C. Koethe, J. Buhot, D. Kamenskyi, C. Hickey, P. Becker, V. Tsurkan, et al., High-field quantum disordered state in $\alpha\text{-RuCl}_3$: Spin flips, bound states, and multiparticle continuum, *Phys. Rev. B* **101**, 140410 (2020).

- [115] J. D. Thompson, P. A. McClarty, D. Prabhakaran, I. Cabrera, T. Guidi, and R. Coldea, Quasiparticle Breakdown and Spin Hamiltonian of the Frustrated Quantum Pyrochlore $\text{Yb}_2\text{Ti}_2\text{O}_7$ in a Magnetic Field, *Phys. Rev. Lett.* **119**, 057203 (2017).
- [116] T. Hong, Y. Qiu, M. Matsumoto, D. A. Tennant, K. Coester, K. P. Schmidt, F. F. Awwadi, M. M. Turnbull, H. Agrawal, and A. L. Chernyshev, Field induced spontaneous quasiparticle decay and renormalization of quasiparticle dispersion in a quantum antiferromagnet, *Nat. Commun.* **8**, 15148 (2017).
- [117] Y. Shen, Y.-D. Li, H. Wo, Y. Li, S. Shen, B. Pan, Q. Wang, H. C. Walker, P. Steffens, M. Boehm, et al., Evidence for a spinon Fermi surface in a triangular-lattice quantum-spin-liquid candidate, *Nature* **540**, 559 (2016).
- [118] Y. Huh, M. Punk, and S. Sachdev, Optical conductivity of visons in Z_2 spin liquids close to a valence bond solid transition on the kagome lattice, *Phys. Rev. B* **87**, 235108 (2013).
- [119] L. N. Bulaevskii, C. D. Batista, M. V. Mostovoy, and D. I. Khomskii, Electronic orbital currents and polarization in Mott insulators, *Phys. Rev. B* **78**, 024402 (2008).
- [120] A. Bolens, H. Katsura, M. Ogata, and S. Miyashita, Mechanism for subgap optical conductivity in honeycomb Kitaev materials, *Phys. Rev. B* **97**, 161108 (2018).
- [121] L. B. Ioffe and A. I. Larkin, Gapless fermions and gauge fields in dielectrics, *Phys. Rev. B* **39**, 8988 (1989).
- [122] P. Rao and I. Sodemann, Cyclotron resonance inside the Mott gap: A fingerprint of emergent neutral fermions, *Phys. Rev. B* **100**, 155150 (2019).
- [123] C. M. Morris, R. Valdés Aguilar, A. Ghosh, S. M. Koohpayeh, J. Krizan, R. J. Cava, O. Tchernyshyov, T. M. McQueen, and N. P. Armitage, Hierarchy of Bound States in the One-Dimensional Ferromagnetic Ising Chain CoNb_2O_6 Investigated by High-Resolution Time-Domain Terahertz Spectroscopy, *Phys. Rev. Lett.* **112**, 137403 (2014).

-
- [124] M. S. Dresselhaus, G. Dresselhaus, and A. Jorio, *Group Theory Application to the Physics of Condensed Matter* (Springer, Berlin, Heidelberg, 2008).
- [125] P. W. Atkins and J. de Paula, *Atkins' Physical chemistry* (Oxford University Press, Oxford, New York, 2006), eight ed.
- [126] D. G. Farkas, D. Szaller, I. Kézsmárki, U. Nagel, T. Röm, L. Peedu, J. Viirik, J. S. White, R. Cubitt, T. Ito, et al., Selection rules and dynamic magnetoelectric effect of the spin waves in multiferroic BiFeO₃, *Phys. Rev. B* **104**, 174429 (2021).
- [127] S. Kimura, H. Onishi, A. Okutani, M. Akaki, Y. Narumi, M. Hagiwara, K. Okunishi, K. Kindo, Z. He, T. Taniyama, et al., Optical selection rules of the magnetic excitation in the $S = \frac{1}{2}$ one-dimensional Ising-like antiferromagnet BaCo₂V₂O₈, *Phys. Rev. B* **105**, 014417 (2022).
- [128] D. Rigitano, D. Vaknin, G. E. Barberis, and E. Granado, Raman scattering from one and two magnons in magnetoelectric LiNiPO₄, *Phys. Rev. B* **101**, 024417 (2020).
- [129] T. P. Devereaux and R. Hackl, Inelastic light scattering from correlated electrons, *Rev. Mod. Phys.* **79**, 175 (2007).
- [130] T. M. H. Nguyen, L. J. Sandilands, C. H. Sohn, C. H. Kim, A. L. Wysocki, I.-S. Yang, S. J. Moon, J.-H. Ko, J. Yamaura, Z. Hiroi, et al., Two-magnon scattering in the 5d all-in-all-out pyrochlore magnet Cd₂Os₂O₇, *Nat. Commun.* **8**, 251 (2017).
- [131] S. T. Bramwell and B. Keimer, Neutron scattering from quantum condensed matter, *Nat. Mater.* **13**, 763 (2014).
- [132] T. Huberman, R. Coldea, R. A. Cowley, D. A. Tennant, R. L. Leheny, R. J. Christianson, and C. D. Frost, Two-magnon excitations observed by neutron scattering in the two-dimensional spin- $\frac{5}{2}$ Heisenberg antiferromagnet Rb₂MnF₄, *Phys. Rev. B* **72**, 014413 (2005).
- [133] R. A. Cowley, W. J. L. Buyers, P. Martel, and R. W. H. Stevenson, Two-Magnon Scattering of Neutrons, *Phys. Rev. Lett.* **23**, 86 (1969).

- [134] T. M. Holden, E. C. Svensson, W. J. L. Buyers, R. A. Cowley, and R. W. H. Stevenson, Two-Magnon Scattering of Neutrons by MnF₂, *Journal of Applied Physics* **41**, 896 (1970).
- [135] D. Pesin and L. Balents, Mott physics and band topology in materials with strong spin-orbit interaction, *Nat. Phys.* **6**, 376 (2010).
- [136] X.-G. Wen, Colloquium: Zoo of quantum-topological phases of matter, *Rev. Mod. Phys.* **89**, 041004 (2017).
- [137] Y. Zhou, K. Kanoda, and T.-K. Ng, Quantum spin liquid states, *Rev. Mod. Phys.* **89**, 025003 (2017).
- [138] M. Hermanns, I. Kimchi, and J. Knolle, Physics of the Kitaev Model: Fractionalization, Dynamic Correlations, and Material Connections, *Annu. Rev. Condens. Matter Phys.* **9**, 17 (2018).
- [139] D. Inosov, Quantum magnetism in minerals, *Adv. Phys.* **67**, 149 (2018).
- [140] H. Takagi, T. Takayama, G. Jackeli, G. Khaliullin, and S. E. Nagler, Concept and realization of Kitaev quantum spin liquids, *Nat. Rev. Phys.* **1**, 264 (2019).
- [141] J. Wen, S.-L. Yu, S. Li, W. Yu, and J.-X. Li, Experimental identification of quantum spin liquids, *npj Quantum Mater.* **4**, 12 (2019).
- [142] P. Anderson, Resonating valence bonds: A new kind of insulator?, *Mater. Res. Bull.* **8**, 153 (1973).
- [143] A. Kitaev, Anyons in an exactly solved model and beyond, *Ann. Phys.* **321**, 2 (2006).
- [144] D. P. Kozlenko, A. F. Kusmartseva, E. V. Lukin, D. A. Keen, W. G. Marshall, M. A. de Vries, and K. V. Kamenev, From Quantum Disorder to Magnetic Order in an $s = 1/2$ Kagome Lattice: A Structural and Magnetic Study of Herbertsmithite at High Pressure, *Phys. Rev. Lett.* **108**, 187207 (2012).
- [145] J. B. Goodenough, Electronic and ionic transport properties and other physical aspects of perovskites, *Rep. Prog. Phys.* **67**, 1915 (2004).

-
- [146] P. A. Mishchenko, Y. Kato, K. O'Brien, T. A. Bojesen, T. Eschmann, M. Hermanns, S. Trebst, and Y. Motome, Chiral spin liquids with crystalline \mathbb{Z}_2 gauge order in a three-dimensional Kitaev model, *Phys. Rev. B* **101**, 045118 (2020).
- [147] M. R. Norman, N. J. Laurita, and D. Hsieh, Valence bond phases of herbertsmithite and related copper kagome materials, *Phys. Rev. Res.* **2**, 013055 (2020).
- [148] A. Little, L. Wu, P. Lampen-Kelley, A. Banerjee, S. Patankar, D. Rees, C. A. Bridges, J.-Q. Yan, D. Mandrus, S. E. Nagler, et al., Antiferromagnetic Resonance and Terahertz Continuum in α - RuCl_3 , *Phys. Rev. Lett.* **119**, 227201 (2017).
- [149] L. Y. Shi, Y. Q. Liu, T. Lin, M. Y. Zhang, S. J. Zhang, L. Wang, Y. G. Shi, T. Dong, and N. L. Wang, Field-induced magnon excitation and in-gap absorption in the Kitaev candidate α - RuCl_3 , *Phys. Rev. B* **98**, 094414 (2018).
- [150] A. N. Ponomaryov, L. Zviagina, J. Wosnitza, P. Lampen-Kelley, A. Banerjee, J.-Q. Yan, C. A. Bridges, D. G. Mandrus, S. E. Nagler, and S. A. Zvyagin, Nature of Magnetic Excitations in the High-Field Phase of α - RuCl_3 , *Phys. Rev. Lett.* **125**, 037202 (2020).
- [151] Y. Huh, M. Punk, and S. Sachdev, Optical conductivity of visons in \mathbb{Z}_2 spin liquids close to a valence bond solid transition on the kagome lattice, *Phys. Rev. B* **87**, 235108 (2013).
- [152] H. O. Jeschke, F. Salvat-Pujol, and R. Valentí, First-principles determination of Heisenberg Hamiltonian parameters for the spin- $\frac{1}{2}$ kagome antiferromagnet $\text{ZnCu}_3(\text{OH})_6\text{Cl}_2$, *Phys. Rev. B* **88**, 075106 (2013).
- [153] Y. Iqbal, F. Becca, S. Sorella, and D. Poilblanc, Gapless spin-liquid phase in the kagome spin- $\frac{1}{2}$ Heisenberg antiferromagnet, *Phys. Rev. B* **87**, 060405 (2013).
- [154] Y.-F. Ma and T.-K. Ng, Nonlinear optical conductivity of U(1) spin liquids with large spinon Fermi surfaces, *Phys. Rev. B* **93**, 245109 (2016).
- [155] J. Nasu, M. Udagawa, and Y. Motome, Vaporization of Kitaev Spin Liquids, *Phys. Rev. Lett.* **113**, 197205 (2014).

- [156] T. H. Han, J. S. Helton, S. Chu, A. Prodi, D. K. Singh, C. Mazzoli, P. Müller, D. G. Nocera, and Y. S. Lee, Synthesis and characterization of single crystals of the spin- $\frac{1}{2}$ kagome-lattice antiferromagnets $\text{Zn}_x\text{Cu}_{4-x}(\text{OH})_6\text{Cl}_2$, *Phys. Rev. B* **83**, 100402 (2011).
- [157] M. Le Tacon, G. Ghiringhelli, J. Chaloupka, M. Moretti Sala, V. Hinkov, M. W. Haverkort, M. Minola, M. Bakr, K. J. Zhou, S. Blanco-Canosa, et al., Intense paramagnon excitations in a large family of high-temperature superconductors, *Nat. Phys.* **7**, 725 (2011).
- [158] J. P. Clancy, H. Gretarsson, J. A. Sears, Y. Singh, S. Desgreniers, K. Mehlawat, S. Layek, G. K. Rozenberg, Y. Ding, M. H. Upton, et al., Pressure-driven collapse of the relativistic electronic ground state in a honeycomb iridate, *npj Quantum Mater.* **3**, 35 (2018).
- [159] H. Gretarsson, J. P. Clancy, X. Liu, J. P. Hill, E. Bozin, Y. Singh, S. Manni, P. Gegenwart, J. Kim, A. H. Said, et al., Crystal-Field Splitting and Correlation Effect on the Electronic Structure of A_2IrO_3 , *Phys. Rev. Lett.* **110**, 076402 (2013).
- [160] M. Mitrano and Y. Wang, Probing light-driven quantum materials with ultrafast resonant inelastic X-ray scattering, *Commun. Phys.* **3**, 184 (2020).
- [161] S. A. Zvyagin, D. Graf, T. Sakurai, S. Kimura, H. Nojiri, J. Wosnitza, H. Ohta, T. Ono, and H. Tanaka, Pressure-tuning the quantum spin Hamiltonian of the triangular lattice antiferromagnet Cs_2CuCl_4 , *Nat. Commun.* **10**, 1064 (2019).
- [162] C. C. Homes, M. Reedyk, D. A. Cradles, and T. Timusk, Technique for measuring the reflectance of irregular, submillimeter-sized samples, *Appl. Opt.* **32**, 2976 (1993).
- [163] B. C. Smith, *Fundamentals of Fourier Transform Infrared Spectroscopy* (CRC Press, Taylor & Francis Group, Boca Raton, London, New York, 2011), 2nd ed.
- [164] T. Biesner, Fourier Transformed Infrared (FTIR) Spectroscopy, https://www.pi1.uni-stuttgart.de/research/methods_overview/fourier-transformed-infrared-spectroscopy/, Online; accessed 11-May-2022.

-
- [165] F. Datchi, A. Dewaele, P. Loubeyre, R. Letoullec, Y. L. Godec, and B. Canny, Optical pressure sensors for high-pressure-high-temperature studies in a diamond anvil cell, *High Press. Res.* **27**, 447 (2007).
- [166] A. Dewaele, M. Torrent, P. Loubeyre, and M. Mezouar, Compression curves of transition metals in the Mbar range: Experiments and projector augmented-wave calculations, *Phys. Rev. B* **78**, 104102 (2008).
- [167] A. B. Kuzmenko, Kramers-Kronig constrained variational analysis of optical spectra, *Rev. Sci. Instrum.* **76**, 083108 (2005).
- [168] TeraView, TeraPulse 4000 User's Guide No. 001-0223 Rev. 17, (2018).
- [169] C. Sirtori, Bridge for the terahertz gap, *Nature* **417**, 132 (2002).
- [170] N. M. Burford and M. O. El-Shenawee, Review of terahertz photoconductive antenna technology, *Opt. Eng.* **56**, 1 (2017).
- [171] N. J. Laurita, Ph.D. thesis, Johns Hopkins University (2017).
- [172] N. J. Laurita, G. G. Marcus, B. A. Trump, J. Kindervater, M. B. Stone, T. M. McQueen, C. L. Broholm, and N. P. Armitage, Low-energy magnon dynamics and magneto-optics of the skyrmionic Mott insulator Cu_2OSeO_3 , *Phys. Rev. B* **95**, 235155 (2017).
- [173] K. Kozuki, T. Nagashima, and M. Hangyo, Measurement of electron paramagnetic resonance using terahertz time-domain spectroscopy, *Opt. Express* **19**, 24950 (2011).
- [174] J. Wang, W. Yuan, P. M. Singer, R. W. Smaha, W. He, J. Wen, Y. S. Lee, and T. Imai, Emergence of spin singlets with inhomogeneous gaps in the kagome lattice Heisenberg antiferromagnets Zn-barlowite and herbertsmithite, *Nat. Phys.* **17**, 1109 (2021).
- [175] C. Poole, *Electron Spin Resonance: A Comprehensive Treatise on Experimental Techniques*, Dover books on physics (Dover Publications, Mineola, New York, 1996), 2nd ed.
- [176] B. A. Miksch, Ph.D. thesis, University of Stuttgart (2022).
- [177] M. Dumm, Ph.D. thesis, Universität Augsburg (1999).

- [178] R. T. Schumacher and C. P. Slichter, Electron Spin Paramagnetism of Lithium and Sodium, *Phys. Rev.* **101**, 58 (1956).
- [179] M. P. Shores, E. A. Nytko, B. M. Bartlett, and D. G. Nocera, A Structurally Perfect $S = 1/2$ Kagome Antiferromagnet, *J. Am. Chem. Soc.* **127**, 13462 (2005).
- [180] F. Bert, S. Nakamae, F. Ladieu, D. L'Hôte, P. Bonville, F. Duc, J.-C. Trombe, and P. Mendels, Low temperature magnetization of the $S = \frac{1}{2}$ kagome antiferromagnet $\text{ZnCu}_3(\text{OH})_6\text{Cl}_2$, *Phys. Rev. B* **76**, 132411 (2007).
- [181] T.-H. Han, M. R. Norman, J.-J. Wen, J. A. Rodriguez-Rivera, J. S. Helton, C. Broholm, and Y. S. Lee, Correlated impurities and intrinsic spin-liquid physics in the kagome material herbertsmithite, *Phys. Rev. B* **94**, 060409 (2016).
- [182] P. Khuntia, M. Velazquez, Q. Barthélemy, F. Bert, E. Kermarrec, A. Legros, B. Bernu, L. Messio, A. Zorko, and P. Mendels, Gapless ground state in the archetypal quantum kagome antiferromagnet $\text{ZnCu}_3(\text{OH})_6\text{Cl}_2$, *Nat. Phys.* **16**, 469 (2020).
- [183] T. Imai, E. A. Nytko, B. M. Bartlett, M. P. Shores, and D. G. Nocera, ^{63}Cu , ^{35}Cl , and ^1H NMR in the $S = \frac{1}{2}$ Kagome Lattice $\text{ZnCu}_3(\text{OH})_6\text{Cl}_2$, *Phys. Rev. Lett.* **100**, 077203 (2008).
- [184] A. Olariu, P. Mendels, F. Bert, F. Duc, J. C. Trombe, M. A. de Vries, and A. Harrison, ^{17}O NMR Study of the Intrinsic Magnetic Susceptibility and Spin Dynamics of the Quantum Kagome Antiferromagnet $\text{ZnCu}_3(\text{OH})_6\text{Cl}_2$, *Phys. Rev. Lett.* **100**, 087202 (2008).
- [185] M. Fu, T. Imai, T.-H. Han, and Y. S. Lee, Evidence for a gapped spin-liquid ground state in a kagome Heisenberg antiferromagnet, *Science* **350**, 655 (2015).
- [186] P. Mendels, F. Bert, M. A. de Vries, A. Olariu, A. Harrison, F. Duc, J. C. Trombe, J. S. Lord, A. Amato, and C. Baines, Quantum Magnetism in the Paratacamite Family: Towards an Ideal Kagomé Lattice, *Phys. Rev. Lett.* **98**, 077204 (2007).

-
- [187] M. A. de Vries, K. V. Kamenev, W. A. Kockelmann, J. Sanchez-Benitez, and A. Harrison, Magnetic Ground State of an Experimental $S = 1/2$ Kagome Antiferromagnet, *Phys. Rev. Lett.* **100**, 157205 (2008).
- [188] Q. Barthélemy, A. Demuer, C. Marcenat, T. Klein, B. Bernu, L. Messio, M. Velázquez, E. Kermarrec, F. Bert, and P. Mendels, Specific Heat of the Kagome Antiferromagnet Herbertsmithite in High Magnetic Fields, *Phys. Rev. X* **12**, 011014 (2022).
- [189] D. E. Freedman, T. H. Han, A. Prodi, P. Müller, Q.-Z. Huang, Y.-S. Chen, S. M. Webb, Y. S. Lee, T. M. McQueen, and D. G. Nocera, Site Specific X-ray Anomalous Dispersion of the Geometrically Frustrated Kagomé Magnet, Herbertsmithite, $\text{ZnCu}_3(\text{OH})_6\text{Cl}_2$, *J. Am. Chem. Soc.* **132**, 16185 (2010).
- [190] D. Wulferding, P. Lemmens, P. Scheib, J. Röder, P. Mendels, S. Chu, T. Han, and Y. S. Lee, Interplay of thermal and quantum spin fluctuations in the kagome lattice compound herbertsmithite, *Phys. Rev. B* **82**, 144412 (2010).
- [191] A. B. Sushkov, G. S. Jenkins, T.-H. Han, Y. S. Lee, and H. D. Drew, Infrared phonons as a probe of spin-liquid states in herbertsmithite $\text{ZnCu}_3(\text{OH})_6\text{Cl}_2$, *J. Phys. Condens. Matter* **29**, 095802 (2017).
- [192] A. Pustogow, Y. Li, I. Voloshenko, P. Pupal, C. Krellner, I. I. Mazin, M. Dressel, and R. Valentí, Nature of optical excitations in the frustrated kagome compound herbertsmithite, *Phys. Rev. B* **96**, 241114 (2017).
- [193] Y. Li, A. Pustogow, M. Bories, P. Pupal, C. Krellner, M. Dressel, and R. Valentí, Lattice dynamics in the spin- $\frac{1}{2}$ frustrated kagome compound herbertsmithite, *Phys. Rev. B* **101**, 161115 (2020).
- [194] J. S. Helton, K. Matan, M. P. Shores, E. A. Nytko, B. M. Bartlett, Y. Qiu, D. G. Nocera, and Y. S. Lee, Dynamic Scaling in the Susceptibility of the Spin- $\frac{1}{2}$ Kagome Lattice Antiferromagnet Herbertsmithite, *Phys. Rev. Lett.* **104**, 147201 (2010).
- [195] A. Zorko, M. Herak, M. Gomilšek, J. van Tol, M. Velázquez, P. Khuntia, F. Bert, and P. Mendels, Symmetry Reduction in

- the Quantum Kagome Antiferromagnet Herbertsmithite, *Phys. Rev. Lett.* **118**, 017202 (2017).
- [196] N. J. Laurita, A. Ron, J. W. Han, A. Scheie, J. P. Sheckelton, R. W. Smaha, W. He, J. J. Wen, J. S. Lee, Y. S. Lee, et al., Evidence for a Parity Broken Monoclinic Ground State in the $S = 1/2$ Kagome Antiferromagnet Herbertsmithite, arXiv:1910.13606 (2019).
- [197] Z. A. Kelly, M. J. Gallagher, and T. M. McQueen, Electron Doping a Kagome Spin Liquid, *Phys. Rev. X* **6**, 041007 (2016).
- [198] I. I. Mazin, H. O. Jeschke, F. Lechermann, H. Lee, M. Fink, R. Thomale, and R. Valentí, Theoretical prediction of a strongly correlated Dirac metal, *Nat. Commun.* **5**, 4261 (2014).
- [199] M. Jeong, F. Bert, P. Mendels, F. Duc, J. C. Trombe, M. A. de Vries, and A. Harrison, Field-Induced Freezing of a Quantum Spin Liquid on the Kagome Lattice, *Phys. Rev. Lett.* **107**, 237201 (2011).
- [200] P. Malavi, S. Pal, D. V. S. Muthu, S. Sahoo, S. Karmakar, and A. K. Sood, Pressure-induced tuning of quantum spin liquid state in $\text{ZnCu}_3(\text{OH})_6\text{Cl}_2$, *Phys. Rev. B* **101**, 214402 (2020).
- [201] R. Okuma, D. Nakamura, and S. Takeyama, Magnetization plateau observed by ultrahigh-field Faraday rotation in the kagome antiferromagnet herbertsmithite, *Phys. Rev. B* **102**, 104429 (2020).
- [202] Z. Hiroi, H. Ishikawa, H. Yoshida, J.-i. Yamaura, and Y. Okamoto, Orbital Transitions and Frustrated Magnetism in the Kagome-Type Copper Mineral Volborthite, *Inorg. Chem.* **58**, 11949 (2019).
- [203] O. Janson, S. Furukawa, T. Momoi, P. Sindzingre, J. Richter, and K. Held, Magnetic Behavior of Volborthite $\text{Cu}_3\text{V}_2\text{O}_7(\text{OH})_2 \cdot 2\text{H}_2\text{O}$ Determined by Coupled Trimers Rather than Frustrated Chains, *Phys. Rev. Lett.* **117**, 037206 (2016).
- [204] T. K. Zeh, Master's thesis/ Supervisor: T. Biesner, University of Stuttgart (2021).
- [205] D. I. Khomskii, *Transition Metal Compounds* (Cambridge University Press, Cambridge, 2014).

-
- [206] A. Togo, F. Oba, and I. Tanaka, First-principles calculations of the ferroelastic transition between rutile-type and CaCl_2 -type SiO_2 at high pressures, *Phys. Rev. B* **78**, 134106 (2008).
- [207] A. Togo and I. Tanaka, First principles phonon calculations in materials science, *Scr. Mater.* **108**, 1 (2015).
- [208] G. Kresse and J. Hafner, Ab initio molecular dynamics for liquid metals, *Phys. Rev. B* **47**, 558 (1993).
- [209] G. Kresse and J. Furthmüller, Efficient iterative schemes for ab initio total-energy calculations using a plane-wave basis set, *Phys. Rev. B* **54**, 11169 (1996).
- [210] G. Kresse and J. Furthmüller, Efficiency of ab-initio total energy calculations for metals and semiconductors using a plane-wave basis set, *Comput. Mater. Sci.* **6**, 15 (1996).
- [211] S. Toth and B. Lake, Linear spin wave theory for single-Q incommensurate magnetic structures, *J. Phys. Condens. Matter* **27**, 166002 (2015).
- [212] W. Sun, T. Arh, M. Gomilšek, P. Koželj, S. Vrtnik, M. Herak, J.-X. Mi, and A. Zorko, Magnetic ordering of the distorted kagome antiferromagnet $\text{Y}_3\text{Cu}_9(\text{OH})_{18}[\text{Cl}_8(\text{OH})]$ prepared via optimal synthesis, *Phys. Rev. Mater.* **5**, 064401 (2021).
- [213] Y. Skourski, M. D. Kuz'min, K. P. Skokov, A. V. Andreev, and J. Wosnitzer, High-field magnetization of $\text{Ho}_2\text{Fe}_{17}$, *Phys. Rev. B* **83**, 214420 (2011).
- [214] R. Okuma, D. Nakamura, T. Okubo, A. Miyake, A. Matsuo, K. Kindo, M. Tokunaga, N. Kawashima, S. Takeyama, and Z. Hiroi, A series of magnon crystals appearing under ultrahigh magnetic fields in a kagomé antiferromagnet, *Nat. Commun.* **10**, 1229 (2019).
- [215] J. Schulenburg, A. Honecker, J. Schnack, J. Richter, and H.-J. Schmidt, Macroscopic Magnetization Jumps due to Independent Magnons in Frustrated Quantum Spin Lattices, *Phys. Rev. Lett.* **88**, 167207 (2002).
- [216] J. Schnack, J. Schulenburg, and J. Richter, Magnetism of the $N = 42$ kagome lattice antiferromagnet, *Phys. Rev. B* **98**, 094423 (2018).

- [217] J. Schnack, J. Schulenburg, A. Honecker, and J. Richter, Magnon Crystallization in the Kagome Lattice Antiferromagnet, *Phys. Rev. Lett.* **125**, 117207 (2020).
- [218] M. I. Aroyo, J. M. Perez-Mato, D. Orobengoa, E. Tasci, G. de la Flor, and A. Kirov, Crystallography online: Bilbao Crystallographic Server, *Bulg. Chem. Commun.* **43**, 183 (2011).
- [219] F. Birch, Equation of state and thermodynamic parameters of NaCl to 300 kbar in the high-temperature domain, *J. Geophys. Res. Solid Earth* **91**, 4949 (1986).
- [220] U. S. Pracht, E. Heintze, C. Clauss, D. Hafner, R. Bek, D. Werner, S. Gelhorn, M. Scheffler, M. Dressel, D. Sherman, et al., Electrodynamics of the Superconducting State in Ultra-Thin Films at THz Frequencies, *IEEE Trans. Terahertz Sci. Technol.* **3**, 269 (2013).
- [221] H. Ishikawa, D. Nishio-Hamane, A. Miyake, M. Tokunaga, A. Matsuo, K. Kindo, and Z. Hiroi, Engelhauptite: A variant of $S = \frac{1}{2}$ kagome antiferromagnet, *Phys. Rev. Mater.* **3**, 064414 (2019).
- [222] D. Boldrin, B. Fåk, E. Canévet, J. Ollivier, H. C. Walker, P. Manuel, D. D. Khalyavin, and A. S. Wills, Vesignieite: An $S = \frac{1}{2}$ Kagome Antiferromagnet with Dominant Third-Neighbor Exchange, *Phys. Rev. Lett.* **121**, 107203 (2018).
- [223] M. Windt, M. Grüninger, T. Nunner, C. Knetter, K. P. Schmidt, G. S. Uhrig, T. Kopp, A. Freimuth, U. Ammerahl, B. Büchner, et al., Observation of Two-Magnon Bound States in the Two-Leg Ladders of $(\text{Ca, La})_{14}\text{Cu}_{24}\text{O}_{41}$, *Phys. Rev. Lett.* **87**, 127002 (2001).
- [224] M. Grüninger, D. van der Marel, A. Damascelli, A. Erb, T. Nunner, and T. Kopp, Midinfrared absorption in $\text{YBa}_2\text{Cu}_3\text{O}_6$: Evidence for a failure of spin-wave theory for spin $\frac{1}{2}$ in two dimensions, *Phys. Rev. B* **62**, 12422 (2000).
- [225] J. Lorenzana and G. A. Sawatzky, Phonon Assisted Multimagnon Optical Absorption and Long Lived Two-Magnon States in Undoped Lamellar Copper Oxides, *Phys. Rev. Lett.* **74**, 1867 (1995).
- [226] J. D. Perkins, J. M. Graybeal, M. A. Kastner, R. J. Birgeneau, J. P. Falck, and M. Greven, Mid-infrared optical absorption in undoped lamellar copper oxides, *Phys. Rev. Lett.* **71**, 1621 (1993).

-
- [227] L. L. Lohr, Spin-forbidden electronic excitations in transition metal complexes, *Coord. Chem. Rev.* **8**, 241 (1972).
- [228] Y. Tanabe and E. Hanamura, Two and Three Magnon Excitation in α -Fe₂O₃, *J. Phys. Soc. Japan* **74**, 670 (2005).
- [229] C. Cohen-Tannoudji, B. Diu, and F. Laloë, *Quantum Mechanics VOL 2 2ed* (Wiley, New York, 2019).
- [230] C. Cohen-Tannoudji, B. Diu, and F. Laloë, *Quantum Mechanics VOL 3 2ed* (Wiley, New York, 2020).
- [231] V. K. Kutzner, Bachelor's thesis/ Supervisor: T. Biesner, University of Stuttgart (2019).
- [232] C. Kittel, Theory of Antiferromagnetic Resonance, *Phys. Rev.* **82**, 565 (1951).
- [233] F. Keffer and C. Kittel, Theory of Antiferromagnetic Resonance, *Phys. Rev.* **85**, 329 (1952).
- [234] T. Kubacka, J. A. Johnson, M. C. Hoffmann, C. Vicario, S. de Jong, P. Beaud, S. Grübel, S.-W. Huang, L. Huber, L. Patthey, et al., Large-Amplitude Spin Dynamics Driven by a THz Pulse in Resonance with an Electromagnon, *Science* **343**, 1333 (2014).
- [235] J. Nishitani, K. Kozuki, T. Nagashima, and M. Hangyo, Terahertz radiation from coherent antiferromagnetic magnons excited by femtosecond laser pulses, *Appl. Phys. Lett.* **96**, 221906 (2010).
- [236] L. P. Vergasova, G. L. Starova, S. K. Filatov, and V. V. Anan'ev, Averievite Cu₅(VO₄)₂O₂.nMX - A new mineral of volcanic exhalations, *Dokl. Akad. Nauk* **359**, 804 (1998).
- [237] G. L. Starova, S. V. Krivovlchev, V. S. Fundamensky, and S. K. Filatov, The crystal structure of averievite, Cu₅O₂(VO₄)₂.nMX: comparison with related compounds, *Mineral. Mag.* **61**, 441 (1997).
- [238] L. M. Volkova and D. V. Marinin, Antiferromagnetic spin-frustrated layers of corner-sharing Cu₄ tetrahedra on the kagome lattice in volcanic minerals Cu₅O₂(VO₄)₂(CuCl), NaCu₅O₂(SeO₃)₂Cl₃, and K₂Cu₅Cl₈(OH)₄ · 2H₂O, *J. Phys. Condens. Matter* **30**, 425801 (2018).

- [239] D. Dey and A. S. Botana, Role of chemical pressure on the electronic and magnetic properties of the spin- $\frac{1}{2}$ kagome mineral averievite, *Phys. Rev. B* **102**, 125106 (2020).
- [240] M. J. Winiarski, T. T. Tran, J. R. Chamorro, and T. M. McQueen, (CsX)Cu₅O₂(PO₄)₂ (X = Cl, Br, I): A Family of Cu²⁺ $S = 1/2$ Compounds with Capped-Kagome Networks Composed of OCu₄ Units, *Inorg. Chem.* **58**, 4328 (2019).
- [241] P. B. Ishai, M. S. Talary, A. Caduff, E. Levy, and Y. Feldman, Electrode polarization in dielectric measurements: a review, *Meas. Sci. Technol.* **24**, 102001 (2013).
- [242] Y. T. Chan, S. Roh, S. Shin, T. Park, M. Dressel, and E. Uykur, Three-dimensional hopping conduction triggered by magnetic ordering in the quasi-one-dimensional iron-ladder compounds BaFe₂S₃ and BaFe₂Se₃, *Phys. Rev. B* **102**, 035120 (2020).
- [243] A. B. Sushkov, O. Tchernyshyov, W. R. II, S. W. Cheong, and H. D. Drew, Probing Spin Correlations with Phonons in the Strongly Frustrated Magnet ZnCr₂O₄, *Phys. Rev. Lett.* **94**, 137202 (2005).
- [244] Ch. Kant, J. Deisenhofer, T. Rudolf, F. Mayr, F. Schrettle, A. Loidl, V. Gnezdilov, D. Wulferding, P. Lemmens, and V. Tsurkan, Optical phonons, spin correlations, and spin-phonon coupling in the frustrated pyrochlore magnets CdCr₂O₄ and ZnCr₂O₄, *Phys. Rev. B* **80**, 214417 (2009).
- [245] T. Sekine, M. Jouanne, C. Julien, and M. Balkanski, Light-scattering study of dynamical behavior of antiferromagnetic spins in the layered magnetic semiconductor FePS₃, *Phys. Rev. B* **42**, 8382 (1990).
- [246] T. R  m, D. H  vonen, U. Nagel, Y.-J. Wang, and R. K. Kremer, Low-energy excitations and dynamic Dzyaloshinskii-Moriya interaction in α' -NaV₂O₅ studied by far-infrared spectroscopy, *Phys. Rev. B* **69**, 144410 (2004).
- [247] R. Samnakay, D. Wickramaratne, T. R. Pope, R. K. Lake, T. T. Salguero, and A. A. Balandin, Zone-Folded Phonons and the Commensurate-Incommensurate Charge-Density-Wave Transition in 1T-TaSe₂ Thin Films, *Nano Lett.* **15**, 2965 (2015).

-
- [248] Y. Mukai, H. Hirori, T. Yamamoto, H. Kageyama, and K. Tanaka, Nonlinear magnetization dynamics of antiferromagnetic spin resonance induced by intense terahertz magnetic field, *New J. Phys.* **18**, 013045 (2016).
- [249] H. Suhl, The theory of ferromagnetic resonance at high signal powers, *J. Phys. Chem. Solids* **1**, 209 (1957).
- [250] H. J. Qin, Kh. Zakeri, A. Ernst, and J. Kirschner, Temperature Dependence of Magnetic Excitations: Terahertz Magnons above the Curie Temperature, *Phys. Rev. Lett.* **118**, 127203 (2017).
- [251] A. Zorko, M. Pregelj, M. Gomilšek, M. Klanjšek, O. Zaharko, W. Sun, and J.-X. Mi, Negative-vector-chirality 120° spin structure in the defect- and distortion-free quantum kagome antiferromagnet $\text{YCu}_3(\text{OH})_6\text{Cl}_3$, *Phys. Rev. B* **100**, 144420 (2019).
- [252] J. Wang, W. Yuan, P. M. Singer, R. W. Smaha, W. He, J. Wen, Y. S. Lee, and T. Imai, Freezing of the Lattice in the Kagome Lattice Heisenberg Antiferromagnet Zn-Barlowite $\text{ZnCu}_3(\text{OD})_6\text{FBr}$, *Phys. Rev. Lett.* **128**, 157202 (2022).

Declaration of originality

Schriftliche Bestätigung der eigenständig erbrachten Leistung gemäß §6 Absatz 2 der Promotionsordnung der Universität Stuttgart:

Die eingereichte Dissertation zum Thema

Spectroscopic Investigations of Kagome - Honeycomb Quantum Magnets

stellt meine eigenständig erbrachte Leistung dar.

Ich habe ausschließlich die angegebenen Quellen und Hilfsmittel benutzt. Wörtlich oder inhaltlich aus anderen Werken übernommene Angaben habe ich als solche kenntlich gemacht.

Die Richtigkeit der hier getätigten Angaben bestätige ich und versichere, nach bestem Wissen die Wahrheit erklärt zu haben.

Stuttgart, den 12.11.2022

Tobias Biesner

Vita

Tobias Biesner was born in Bergisch Gladbach, Germany in April 1993 and raised in Hoffnungsthal, near Cologne. After receiving his Abitur (Leistungsfächer Physics and Biology) in 2012 at the Deutzer Gymnasium Schaurtstraße, he moved to Baden-Württemberg to study Physics at the Ruprecht Karl University of Heidelberg. Early in his studies he sought for experimental training in a research internship at the German Aerospace Center (DLR), Institute of Combustion Technology in the group of Dr. Wolfgang Meier (Stuttgart). Here, he later finished his Bachelor's thesis "Entwicklung und Charakterisierung eines hochauflösenden PLIF-Verfahrens zur Untersuchung der Verdunstung im Nachlauf von Acetontropfen" under supervision of Prof. Dr. Marcus Motzkus (University of Heidelberg) and Prof. Dr. Uwe Riedel (DLR). Tobias obtained his Bachelor of Science (Physics) from Ruprecht Karl University of Heidelberg in 2015.



After an extended research internship at the University of Seville, Spain, focusing on finite element simulations, he moved back to Stuttgart in 2016, starting his Master's in Physics at the University of Stuttgart. During the last year of the Master's he focused on high-pressure FTIR on the Kitaev magnet α - RuCl_3 : structural and electronic aspects, influence of external pressure on Kitaev magnetism, dimerization under pressure (thesis title "Optical Measurements on Quantum Spin Liquids") at the institute of Prof. Dr. Martin Dressel. He obtained his Master of Science (Physics) in 2018 from University of Stuttgart.

In the same year, Tobias started his dissertation (Dr. rer. nat.) at the 1. Physikalisches Institut under the supervision of Prof. Dr. Martin Dressel. At the institute he received an extensive education and training in experimental condensed matter physics and optics, including FTIR spectroscopy, THz spectroscopy, high pressure- and high magnetic field optical setups, and low-temperature cryostats. He applied these techniques in correlated electron systems and frustrated magnets. The works were done in international collaborations with theoretical and experimental colleagues, resulting in multiple peer-reviewed publications in journals

like Advanced Quantum Technologies, NPG Asia Materials, and Physical Review B. Further co-authored works were published, for instance, in Physical Review Letters and Physical Review X. Furthermore, he gained experience during multiple beamtimes at large-scale facilities (Synchrotron Soleil - France, TELBE at HZDR - Germany, ESRF - France). He further deepened his knowledge through teaching, including several laboratory courses and theses supervisions. During his thesis work, Tobias joined international conferences, including the 58th European High Pressure Research Group International Conference 2020 at Tenerife, Spain.